MANCHESTER 1824
The University of Manchester

Advanced van der Waals technologies for probing electronic properties of graphene based heterostructures

A THESIS SUBMITTED TO THE UNIVERSITY OF MANCHESTER FOR THE DEGREE OF DOCTOR OF PHILOSOPHY IN THE FACULTY OF SCIENCE AND ENGINEERING

YAPING YANG

SCHOOL OF PHYSICS AND ASTRONOMY

2020

[BLANK PAGE]

Contents

List of figures

List of tables

List of abbreviations and symbols

Abbreviations

2D	Two-dimensional	**AC**	Armchair
vdW	Van der Waals	**ZZ**	Zigzag
hBN	Hexagonal boron nitride	**LUT**	Look-up-table
AFM	Atomic force microscope	**PMMA**	Polymethyl methacrylate
QHE	Quantum Hall effects	**PMGI**	Polymethylglutarimide
TEM	Transmission electron microscopy	**PVA**	Polyvinyl acetate
3D	Three-dimensional	**PDMS**	Polydimethylsiloxane
BZ	Brillouin zone	**PPC**	Polypropylene carbonate
LLs	Landau levels	**PC**	Polycarbonate
2DEG	Two-dimensional electron gas	**S**	Stokes
DOS	Density of states	**AS**	Anti-Stokes
SdH	Shubnikov-de Haas	**A**	Acoustic
SDP	Secondary Dirac points	**O**	Optical
PDP	Primary Dirac point	**Z**	Out-of-plane
$NbSe_2$	Niobium di-selenium	**L**	Longitudinal
PT	Prandtl-tomlinson	**T**	Transverse
FFM	Friction force microscopy	**IR**	Infrared
FK	Frenkel-kontorova	**DR**	Double resonance
1D	One-dimensional	**PF**	Peak force
SG	Sine-Gordon	**DMT**	Derjaguin-muller-toporov
C-phase	Commensurate phase	**HRTEM**	High-resolution transmission electron microscopy
IC-phase	Incommensurate phase	**DF**	Dark-field
GS	Ground state	**AC**	Alternating current
TBG	Twisted bilayer graphene	**He**	Helium
SP	Saddle point	**VTI**	Variable temperature insert
STM	Scanning tunnelling microscope		

Symbols

Chapter 2

Ψ	Wave function	$.U_i.$	On-site energies of the atoms
	Expansion coefficients	q_D	Radius of spiral nodal line in the Brillouin zone of bulk rhombohedral graphite
Φ	Bloch states	Δ_{bulk}	Bulk band gap of rhombohedral graphite
ϕ	Normalised wave function	$\mathbf{B}$ or B	Magnetic field
$\mathbf{k}$	Wave vector	ω_c	Angular frequency of the cyclotron orbits of electron
$\mathbf{r}$	Position	m_e	Electron mass
H	Hamiltonian	r_c	Angular radius of the cyclotron orbits of electron
H	Transfer integral matrix	$\mathbf{J}$	Current density
S	Overlap integral matrix	$.\tau.$	Scattering time of electron collisions
E or ε	Energy	$\mathbf{v}$	Velocity
a_0	Carbon-carbon bond length	n	Charge carrier density
a	Lattice constant	$\mathbf{g}$	Conductivity tensor
$\mathbf{a}$	Bravais lattice unit vectors	$\mathbf{E}$	Electric field
$\boldsymbol{\delta}$	Nearest-neighbour vector	ρ_{xx}	Longitudinal resistivity
$\mathbf{b}$	Reciprocal-lattice vectors	ρ_{xy}	Transverse resistivity
K or K'	Dirac point	σ_{xx}	Longitudinal conductivity
ξ	Valley index	σ_{xy}	Transverse conductivity
$\mathbf{q}$	Momentum measured relatively to the Dirac points	$\mathbf{p}$	Mechanical momentum
φ	Polar angle of momentum $\mathbf{q}$	$\mathbf{A}(\mathbf{r})$	Landau gauge
$\boldsymbol{\sigma}$	Pauli matrices	l_B	Quantum magnetic length
υ_F	Fermi velocity	ϕ_0	Magnetic flux quantum
γ_i	Hopping parameters	ϕ_m	Magnetic flux

ν	Landau level filling factor	$u(\mathbf{r})$	Periodic part of Bloch wave function
n_e	Density of electrons	$S(\varepsilon)$	Area of the closed orbit in momentum space
ζ	Length scale for the electrostatic potential variation	ΔR_{xx}	Electrical resistance
$V(\mathbf{r})$	Electrostatic potential	T	Temperature
$\mathbf{r}_g$	Guiding centre of electron motion	B_F	Frequency of the sdh oscillation
I	Electric current	A	Area of the lattice unit cell
μ	Confinement potential	n_0	Carriers in a completely filled Bloch band of a unit cell
U_H	Hall voltage	t	Superlattice miniband filling index
g_0	Conductance quantum	s	Quantized Hall conductivity
β	Berry phase	θ	Twist angles between 2D layers
$\boldsymbol{\alpha}(t)$	A set of time dependent parameters	$\boldsymbol{\kappa}$	Reciprocal superlattice vectors
$Q(\boldsymbol{\alpha})$	Berry connection	λ_m	Moiré wavelength
$\lvert n(\boldsymbol{\alpha})\rangle$	Instantaneous orthonormal basis function	n_{SDP}	Carrier density of secondary Dirac points
$\boldsymbol{\Omega}$	Berry curvature		

Chapter 3

δ	Lattice mismatch	r	Distance between two interacting atoms/molecules
φ	Relative rotation angle of the moiré pattern with respect to graphene	A	Empirical parameters of the Lennard-Janes potential
$w(r)$	Interaction potential energy	B	Empirical parameters of the Lennard-Janes potential

C	Strength of particle-particle pair interaction	H	Hamiltonian
H_m	Hamaker constant	$V_{\text{int}}(x)$	Inter-particle potential
ρ	Atomic densities	$V_{sub}(x)$	Periodic potential of the substrate
F	Van der Waals force	a_A	Equilibrium distance of the inter-particle potential
F_r	Friction force	a_s	Periodicity of background sinusoidal potential
$F_\perp$	External normal force	E_{PN}	Peierls-Nabarro periodic potential
μ	Static friction coefficient	L	Length of the FK chain
S	Contact area between the 2D layers	N	Number of atoms
σ	Shear stress	ϑ	Dimensionless kink concentration
U	Potential	$K_{Aubry}(\vartheta)$	Critical value of Aubry transition
U_0	Amplitude of the potential	$\mathbf{b}$	Burgers vector
K	Effective elastic constant	$\mathbf{t}$	Tangent vector
a	Periodicity of the substrate potential	$\mathbf{u}$	Elastic displacement
v	Moving velocity	θ_t	Twist angles between graphene and top hbn
x	Displacement	θ_b	Twist angles between graphene and bottom hbn
t	Time	T_g	Glass transition temperature

Chapter 4

ω	Phonon frequency	$\mathbf{q}$	Phonon wave vector
$\mathbf{k}$	Photon wave vector	K or K'	Dirac point

$\mathbf{p}$	Phonon momentum	V_{xy}	Transverse voltage drop
$\mathbf{d_a}$	Wave vector of armchair edge	L	Length of the Hall bar channel
$\mathbf{d}_z$	Wave vector of zigzag edge	W	Width of the Hall bar channel
R	Tip end radius	I	Current
$z - z_0$	Sample deformation	R_{xx}	Longitudinal resistance
E^*	Reduced modulus	R_{xy}	Hall resistance
E_{tip}	Tip modulus	ρ_{xx}	Longitudinal resistivity
ν_{tip}	Poisson's ratio of the tip	ρ_{xy}	Transverse resistivity
ν_s	Poisson's ratio	B	Magnetic field
W	Energy dissipation	σ_{xx}	Longitudinal conductivity
$\mathbf{F}$	Interaction force between tip and sample	σ_{xy}	Hall conductivity
$\mathbf{Z}$	Displacement vector of the tip	n	Charge carrier density
$\mathbf{\upsilon}$	Tip velocity	D	Vertical displacement field
d	Spacing of the crystal lattice	V	Voltage
λ	Wavelength of electron beam	ε	Dielectric constant
θ_B	Scattering angle of electrons	h	Thicknesses of 2D layers
V_{xx}	Longitudinal voltage drop		

Abstract

Richard P. Feynman once said "when we have some control of the arrangement of things on a small scale we will get an enormously greater range of possible properties that substances can have, and of different things that we can do"[1]. This foresight has now been realized in the regime of two-dimensional (2D) materials, which could be artificially assembled into van der Waals (vdW) heterostructures with on-demand properties[2,3]. The development of ingenious experimental techniques has created a new paradigm for electronic devices with dramatic performance and enabled exploration of novel physical phenomena[4,5]. This work is dedicated to advanced vdW technologies for probing novel electronic properties of graphene based heterostructures.

The work consists of two themes. In the first theme, we focus on rhombohedral graphite, which is rarely studied yet with intrinsic fascinating electronic properties[6-11]. The lack of control of the stacking sequence limits most research to the more stable Bernal form of graphite[12]. This work presents the directional encapsulation of rhombohedral graphite crystallites with hexagonal boron nitride (hBN) along the graphite zigzag edges. Facilitated by this improved vdW technique, we obtained high-quality rhombohedral graphite devices and studied their transport properties. We observed the gap opening and quantum Hall effect of the topologically protected surface states. In the quantum Hall regime, rhombohedral graphite exhibits transition between a gapless semimetallic phase and a gapped quantum spin Hall phase with giant Berry curvature. For thinner graphite (<4nm), an insulating state at the neutrality point emerges with pronounced hysteretic behaviour in both electric and magnetic fields, which we attribute to strong electronic correlations.

In the second theme, we look into the increasingly hot research topic, the twistronics, where twist angle between successive layers in a heterostructure offers a new degree of freedom to tune its electronic properties, through the modification of moiré superlattice[13-15]. This work demonstrates an experimental technique that can achieve *in situ* dynamical rotation and manipulation of 2D materials in vdW heterostructures, thus realizing control of twist angle. The technique is mediated by a polymer patch, which is easy to operate and reproduce. Using this technique, we fabricated a heterostructure where graphene is subjected to double moiré superlattice at the two interfaces. We observed the evidence of the formation of super-moiré structures, which proves the perfect alignment of graphene with its encapsulating layer hBN and the effectiveness of the technique.

Declaration

I declare that that no portion of the work referred to in the thesis has been submitted in support of an application for another degree or qualification of this or any other university or other institute of learning.

Yaping Yang

3rd November, 2020

Copyright Statement

Acknowledgements

First and foremost, I would like to thank my main supervisor Prof. Artem Mishchenko and co-supervisor Sir Konstantin Novoselov for accepting me as one of their PhD students at the University of Manchester, even though my background was not physics. I am also thankful to Mengjian Zhu for recommending me to my supervisors. I can still remember the hard time I have been experiencing in applying for the PhD course, and how excited I was to receive the tuition-waived offer from Artem on the night that was exactly the deadline for application. Without this chance to do PhD here in Manchester, I would not have been who I am now.

I am truly lucky to have the chance to work with the great physicists and colleagues in our group. Their enthusiasm in physics and sincere attitude to science will definitely have a long term impact on my future career. I am really grateful to Prof. Artem Mishchenko for the support, patience, and expert guidance that he has provided me throughout my PhD journey. I have always been motivated by his inspiring suggestions on experiments. Every time I finished a paper draft, he would always offer insightful suggestions and detailed revisions. I truly have learnt a lot from him. In addition, he always requires a high quality work from students, either in experiments or paper work. Such a style of a supervisor proved to be beneficial to students, otherwise I would not have achieved so much during my PhD. In turn, I hope my efforts also did not disappoint my supervisors.

I am also very thankful to Dr. Shuigang Xu and Dr. Piranavan Kumaravadivel who I viewed as my mentors in terms of experimental techniques. Shuigang and Piran are very nice persons, who are skilled and always willing to teach and help whenever I came across questions and problems in doing experiments. They are also generous to share and explain what they know about physics to me. I have learnt a lot from them. I particularly admire Piran's attitude to science. He holds a critical point of view to researches and never judges a work simply by where it is published. In addition, I would like to express my sincere gratitude to other colleagues working in cleanroom and Artem's group who have helped me a lot: Jun Yin, Yanmeng Shi, Colin Woods, Seok Kyun Son, Servet Ozdemir, Jidong Li, David Perello, Yang Cao, Yuri Stebunov, Ziwei Wang, Maciej Molas and Ciaran Mullan, etc.

I certainly have to thank those awesome people I met in Manchester for their firm support to me, and for sharing happiness and sorrows throughout those stressful times: Yulia Skliueva, Yichao Zou, Omer Muhammad, Wenyu Liu, Yuan Chai, Tongcheng Yu, Junhao

Cai, Pengzhan Sun, Mengjie Feng, Wenjun Kuang, Yunzhe Du and Fan Wu, etc. Although there are too many to give due credit to all, I would like to mention my dear friend Yulia who always stands for me. Her attitude to life as well as her braveness for pursuing what she likes pretty much inspired me. Yichao, I would like to thank you for those days when we supported each other during the pandemic lockdown, and of course, for your help in TEM measurements. Omer, I appreciate your backing up whenever I was down. Wenyu, I am grateful to your comfort and encouragement during those depressing times. I appreciate and enjoy all your company in Manchester. Even though the time flies, I will keep those sweet memories in mind.

Thanks must, of course, be given to my parents for their support, patience and understanding of my choice to study abroad during these many years. Pretty much the whole family deserves acknowledgement for their support to me and my parents. I am also thankful to my friends in China, Erjiang Liu, Ge Dong and Xingyue Duan who helped a lot in dealing with my personal affairs back home.

Last but not least, I would like to express my gratitude for China Scholarship Council for providing me with the chance and fees to study abroad. During the pandemic lock down in UK, the Chinese Embassy supplied us, the overseas students, with abundant face masks, medicines and disinfectors in time, so that we could protect ourselves from getting infected. Sincere thankfulness belongs to my country for all these sufficient support.

Yaping Yang

Chapter 1: Introduction

1.1 Background and aims

Graphene research has invoked vast investigations of 2D materials, of which the atomic layers consist of covalently bonded lattices and are weakly bound to each other by vdW interactions[16]. The 2D crystals can therefore be isolated down to a-few-nanometer thick layers and reassembled into a wide range of vdW heterostructures with on-demand geometries, including a chosen sequence of semiconductors or insulators and particular relative rotation between crystals[17]. These degrees of freedom provide a platform for the investigation of various novel phenomena.

With the steady improvement in assembly techniques of vdW heterostructures, new designs of electronic devices emerge, such as van der Waals vertical transistors, optoelectronic devices, and the rising twistronics, etc. However, the vdW technique is not restricted to one-off vertical assembly. One can creatively play with the 2D layers to dynamically control their electronic properties even after assembly. Examples are tuning relative rotational angles of the crystals by an atomic force microscope (AFM) tip[18] or changing the interlayer spacing between 2D layers through hydrostatic pressure applied to the heterostructures[19], etc.

Among the vdW heterostructures, graphene/ hBN is a prototypical one, where hBN serves as a featureless insulating substrate and gate dielectrics. The encapsulating layer hBN enables graphene devices with significantly increased electronic quality[20,21] that allows access to graphene's intrinsic physics, such as the well-developed integer[22-24] and fractional[25-27] quantum Hall effects (QHE) and exotic correlated states[28,29] observed in a magnetic field. Besides, hBN modifies optical[30,31] and electronic properties[32-34] of graphene by introducing moiré superlattices. As a result, secondary Dirac points in graphene arise, accompanied by the appearance of the Hofstadter butterfly spectrum[32-34] in a magnetic field. Because of these features, hBN has been employed as an ideal encapsulating layer for 2D materials in device applications.

In the family of 2D carbon materials, rhombohedral multilayer graphene (or graphite when the number of layers is large) remains rarely investigated despite of its many theoretically predicted fascinating properties, of which the most intriguing is the topologically protected

flat surface states[35,36]. The flat surface states are expected to be a strongly correlated system[8,37] holding states with spontaneously broken symmetries, such as magnetic state[9,38] and surface superconducting state[6,10]. The reason for the lack of extensive study of rhombohedral graphite is that it can easily transform to Bernal stacking in the process of encapsulation by hBN, due to being less thermodynamically stable[39]. One of the aims of this thesis is to fabricate devices of rhombohedral graphite protected by hBN with a considerably increased success rate, using an improved vdW assembly technique. Then, with the obtained high-quality devices, explore the electronic properties of rhombohedral graphite.

On the other hand, interest in twisted vdW heterostructures is rapidly increasing after the recently discovered strongly correlated[40] and superconducting[41] phases in magic-angle twisted bilayer graphene. The twist angle provides an extra knob to tune the band structure and realize the flat band that hosts many-body interactions. The most common way to fabricate twisted vdW heterostructures is the tear and stack technique for twisted graphene layers[42], which allows an only one-off stack without further tuning of twist angle. Inspired by the superlubricity in incommensurate interfaces[43,44], we expect it is possible to dynamically manipulate 2D crystals after the heterostructure assembly, realizing tunable twist angle and displacement between 2D crystals. The aim of this idea is to devise a creative vdW technique that is non-destructive to the materials and more convenient compared to the method using AFM tips mentioned above.

The thesis discusses how the two vdW techniques mentioned above are realized. The results demonstrate that these advanced vdW techniques are able to retain the rhombohedral stacking in graphite encapsulated by hBN and manipulate 2D crystals in the heterostructure *in situ*. The device qualities prove to be good and their novel electronic properties are well studied.

1.2 Thesis structure

This thesis is organized as follows:

- **Chapter 2** provides a short overview of graphene and rhombohedral graphite. Also, the behaviour of electrons in electromagnetic fields is introduced. Finally, the motion of Bloch electrons in magnetic fields is discussed. These are the theoretical background of the electronic devices studied in the thesis.
- **Chapter 3** introduces the interfacial interactions and nanomechanics between the layers in graphene/hBN heterostructures. Also, we provide a detailed process of the vdW heterostructure assembly techniques mainly used in the thesis.

- **Chapter 4** outlines the characterization techniques and measurement set-up mainly employed in this thesis.
- **Chapter 5** puts forward the modified encapsulation process of rhombohedral graphite. We also demonstrate the variety of stacking order in graphite by Raman spectroscopy, transmission electron microscopy (TEM) and AFM, etc.
- **Chapter 6** investigates the electronic properties of rhombohedral graphite through the devices made by the vdW technology described in **Chapter 5**.
- **Chapter 7** describes the *in situ* technique to manipulate 2D crystals in the heterostructures. Using this technique, we a made heterostructure where graphene is perfectly aligned with both top and bottom hBN. The phenomena of moiré physics in turn manifest the validity of the perfect alignment, thus proving the effectiveness of the *in situ* technique.
- **Chapter 8** presents conclusions of this thesis and further prospects.

Chapter 2: Overview of graphene and graphite

In this chapter, we introduce the theoretical background of the thesis. Starting with the basic process of the tight-binding model, we present the electronic properties of monolayer graphene and rhombohedral graphite, which are the principal 2D materials across all the heterostructures studied in this thesis. Also, we reveal the variety of stacking orders in multilayer graphene and its influence on the electronic properties. Subsequently, we introduce basic concepts required to understand electron transport in electromagnetic fields. Finally, we look into the motion of Bloch electrons when magnetic length becomes commensurable with the spacing of the periodic potential.

2.1 Electronic band structures

In this section, we introduce the electronic band structures of monolayer and rhombohedral graphite derived from tight-binding model, where an electron is assumed to be tightly bound to its own atoms, while interactions between electrons and potential generated from other atoms are neglected. The wave function of electrons is therefore expressed as a linear superposition of Bloch states:

$$\Psi_{\mathrm{j}}(\mathbf{k},\mathbf{r}) = \sum_{m=1}^{M} \psi_{\mathrm{j,m}}(\mathbf{k},\mathbf{r})\Phi_m(\mathbf{k},\mathbf{r}) \tag{2.1}$$

where $\psi_{\mathrm{j,m}}(\mathbf{k},\mathbf{r})$ are expansion coefficients, and $\Phi_m(\mathbf{k},\mathbf{r})$ is the Bloch states at a given position $\mathbf{r}$ and wave vector $\mathbf{k}$, given by:

$$\Phi_m(\mathbf{k},\mathbf{r}) = \frac{1}{\sqrt{N}} \sum_{i=1}^{N} e^{i\mathbf{k}\cdot\mathbf{R}_{m,i}} \phi_m(\mathbf{r}-\mathbf{R}_{m,i}) \tag{2.2}$$

where index i labels the i-th unit cell, N is the total number of unit cells, the index m=1, 2,…,M indicates the atomic orbitals Φ_m in each unit cell, and ϕ is the normalised wave function of the carbon π-band orbital. The energy $E_j(\mathbf{k})$ of the j-th band is determined through solving the Schrödinger equation $\mathrm{H}\Phi = E\Phi$:

$$E_j(\mathbf{k}) = \langle \Psi_j | \mathrm{H} | \Psi_j \rangle / \langle \Psi_j | \Psi_j \rangle = \frac{\sum_{m,m'}^{M} \psi_{j,m} \psi^*_{j,m'} \langle \Phi_m | \mathrm{H} | \Phi_{m'} \rangle}{\sum_{m,m'}^{M} \psi_{j,m} \psi^*_{j,m'} \langle \Phi_m | \Phi_{m'} \rangle} \tag{2.3}$$

where H is the Hamiltonian, and $\langle \Phi_m | \mathrm{H} | \Phi_{m'} \rangle$ and $\langle \Phi_m | \Phi_{m'} \rangle$ are defined as the transfer integral matrix $H_{mm'}$ and overlap integral matrix $S_{mm'}$, respectively By calculating the derivative $\partial E_j / \partial \psi^*_{j,m} = 0$, the energy $E_j(\mathbf{k})$ is minimized with respect to the expansion coefficient $\psi^*_{\mathrm{j,m}}$:

$$\frac{\partial E_j}{\partial \psi^*_{j,m}} = \frac{\sum_{m'}^{M} \psi_{j,m'} H_{mm'}}{\sum_{m,m'}^{M} \psi_{j,m} \psi^*_{j,m'} S_{mm'}} - \frac{\sum_{m,m'}^{M} \psi_{j,m} \psi^*_{j,m'} H_{mm'} \sum_{m'}^{M} \psi_{j,m} S_{mm'}}{\left(\sum_{m,m'}^{M} \psi_{j,m} \psi^*_{j,m'} S_{mm'} \right)^2} = 0 . \tag{2.4}$$

This equation leads to:

$$\sum_{m'}^{M} \psi_{j,m'} H_{mm'} = \frac{\sum_{m,m'}^{M} \psi_{j,m} \psi^*_{j,m'} H_{mm'}}{\sum_{m,m'}^{M} \psi_{j,m} \psi^*_{j,m'} S_{mm'}} \sum_{m'}^{M} \psi_{j,m} S_{mm'} \tag{2.5}$$

Note that the pre-factor in the right side of the equation equals to the energy $E_j(\mathbf{k})$ itself, we then obtain the generalized eigenvalue equation:

$$H \psi_j = E_j S \psi_j \tag{2.6}$$

The band energy $E_j(\mathbf{k})$ is thus calculated by:

$$\det(H - E_j S) = 0 \tag{2.7}$$

where det denotes the determinant of the matrix.

2.1.1 Monolayer graphene

Graphene is single atomic sheet of carbon atoms arranged in a honeycomb lattice, which can be decomposed into two interpenetrating triangular sublattices (A and B) related to each other by inversion symmetry and each sublattice provides one atom in the unit cell. The crystal structure of graphene is shown in **Figure 2-1**.

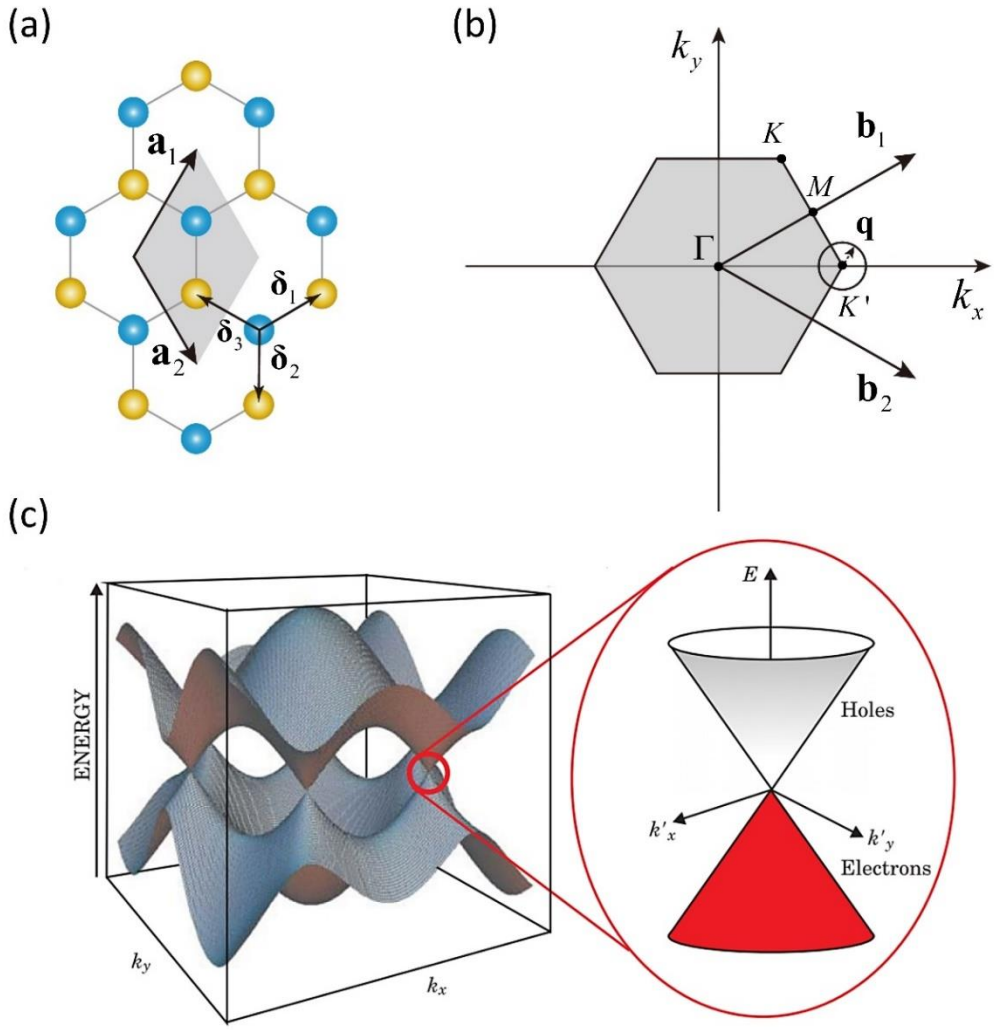

Figure 2-1 Crystal and electronic band structure of graphene. *(a) Honeycomb lattice of graphene. The blue and yellow spheres represent the A and B sublattices.* $\mathbf{a}_1$ *and* $\mathbf{a}_2$ *are the lattice unit vectors, and* $\boldsymbol{\delta}_i$ *, i=1,2,3 are the nearest-neighbor vectors (b) Corresponding Brillouin zone.* $\mathbf{b}_1$ *and* $\mathbf{b}_2$ *are the primitive reciprocal lattice vectors. (c) Band structure close to the K and K′ points showing the Dirac cones. Taken from ref* [45].

The Bravais lattice unit vectors and the three nearest-neighbour vectors in real space are given by:

$$\mathbf{a}_1 = \left(\frac{a}{2}, \frac{\sqrt{3}a}{2}\right), \quad \mathbf{a}_2 = \left(\frac{a}{2}, -\frac{\sqrt{3}a}{2}\right) \tag{2.8}$$

$$\boldsymbol{\delta}_1 = \left(\frac{\sqrt{3}a_0}{2}, \frac{a_0}{2}\right), \quad \boldsymbol{\delta}_2 = \left(0, -a_0\right), \quad \boldsymbol{\delta}_3 = \left(-\frac{\sqrt{3}a_0}{2}, \frac{a_0}{2}\right) \tag{2.9}$$

where a_0 is the carbon-carbon bond length, and $a = \sqrt{3}a_0$ is the lattice constant. The reciprocal-lattice vectors are calculated to be:

$$\mathbf{b}_1 = \frac{4\pi}{\sqrt{3}a}(\frac{\sqrt{3}}{2}, \frac{1}{2}), \quad \mathbf{b}_2 = \frac{4\pi}{\sqrt{3}a}(\frac{\sqrt{3}}{2}, -\frac{1}{2}) \tag{2.10}$$

The coordination of the corners of the graphene Brillouin zone are given by:

$$\mathbf{K} = (\frac{2\pi}{3a}, \frac{2\pi}{\sqrt{3}a}), \quad \mathbf{K}' = (\frac{4\pi}{3a}, 0) \tag{2.11}$$

In graphene, there are four valence electrons in each carbon atom, three of which fill in the hybridized sp^2 orbital, rather than the usual 2s and 2p orbitals, forming the in-plane σ bonds that construct the hexagonal lattice structure. The remaining one occupies the $2p_z$ orbital, forming the covalent π bond which is responsible for the electronic properties of graphene. The energy band structure of the π electrons can be calculated by solving Eq (2.7) [46]. First, we need to determine the two matrices H and S. For transfer integral matrix H, the diagonal H_{AA} element is calculated by:

$$H_{AA} = \langle \Phi_A | \mathrm{H} | \Phi_A \rangle \approx \frac{1}{N} \sum_{i=1}^{N} \langle \phi_A(\mathbf{r} - \mathbf{R}_{A,i}) | \mathrm{H} | \phi_A(\mathbf{r} - \mathbf{R}_{A,i}) \rangle, \tag{2.12}$$

which is the summation of a parameter $\langle \phi_A(\mathbf{r} - \mathbf{R}_{A,i}) | \mathrm{H} | \phi_A(\mathbf{r} - \mathbf{R}_{A,i}) \rangle = \varepsilon_A$ over all unit cells. The parameter ε_A takes the same value on each A site, so we have $H_{AA} \approx \varepsilon_A$. For intrinsic graphene, the two sublattices are identical, so $\varepsilon_A = \varepsilon_B$, and $H_{AA} = H_{BB}$.

The off-diagonal H_{AB} element describes processes of hopping between orbitals on the A and B sublattices. If only considering the hopping of π electrons to the nearest-neighbour atoms, H_{AB} is calculated by:

$$\begin{aligned} H_{AB} &= \langle \Phi_A | \mathrm{H} | \Phi_B \rangle \\ &\approx \frac{1}{N} \sum_{i=1}^{N} \sum_{\boldsymbol{\delta}} e^{i\mathbf{k}\cdot\boldsymbol{\delta}} \langle \phi_A(\mathbf{r} - \mathbf{R}_{A,i}) | \mathrm{H} | \phi_B(\mathbf{r} - \mathbf{R}_{A,i} - \boldsymbol{\delta}) \rangle \end{aligned}. \tag{2.13}$$

Here $\langle \phi_A(\mathbf{r} - \mathbf{R}_{A,i}) | \mathrm{H} | \phi_B(\mathbf{r} - \mathbf{R}_{A,i} - \boldsymbol{\delta}) \rangle = -\gamma_0$ is the nearest-neighbour hopping parameter and takes the same value for each neighbouring pair, thus the off-diagonal transfer integral matrix element is written by:

$$H_{AB} \approx -\frac{1}{N} \sum_{i=1}^{N} \sum_{\boldsymbol{\delta}} e^{i\mathbf{k}\cdot\boldsymbol{\delta}} \gamma_0 = -\gamma_0 f(\mathbf{k}) \; ; \quad f(\mathbf{k}) = \sum_{\boldsymbol{\delta}} e^{i\mathbf{k}\cdot\boldsymbol{\delta}} . \tag{2.14}$$

The function $f(\mathbf{k})$ describing nearest neighbour hopping is calculated by:

$$f(\mathbf{k}) = \left(e^{i\mathbf{k}\cdot\boldsymbol{\delta}_1} + e^{i\mathbf{k}\cdot\boldsymbol{\delta}_2} + e^{i\mathbf{k}\cdot\boldsymbol{\delta}_3}\right) = e^{ik_y a_0}\left[1 + 2e^{-i3k_y a_0/2}\cos\left(\frac{\sqrt{3}}{2}k_x a_0\right)\right]. \tag{2.15}$$

The other off-diagonal matrix element H_{BA} is the complex conjugate of H_{AB}:

$$H_{BA} = H^*_{AB} = -\gamma_0 f^*(\mathbf{k}). \tag{2.16}$$

Similarly, for overlap integral matrix S, assuming that the hopping between the same lattice sites dominates, we have:

$$\begin{aligned} S_{AA} &= \langle \Phi_A | \Phi_A \rangle = \frac{1}{N}\sum_{i=1}^{N}\sum_{j=1}^{N} e^{i\mathbf{k}\cdot(\mathbf{R}_{A,i}-\mathbf{R}_{A,j})} \left\langle \phi_A(\mathbf{r}-\mathbf{R}_{A,i}) \middle| \phi_A(\mathbf{r}-\mathbf{R}_{A,j}) \right\rangle \\ &\approx \frac{1}{N}\sum_{i=1}^{N} \left\langle \phi_A(\mathbf{r}-\mathbf{R}_{A,i}) \middle| \phi_A(\mathbf{r}-\mathbf{R}_{A,i}) \right\rangle \end{aligned} \tag{2.17}$$

The calculation of elements of S is similar to those of H. In this case, the overlap of an orbital with itself is equal to unity, therefore $S_{AA} = S_{BB} = 1$. If only considering the hopping of π electrons to the nearest-neighbour atoms, the off-diagonal elements are given by:

$$\begin{aligned} S_{AB} &= \langle \Phi_A | \Phi_B \rangle \\ &= \frac{1}{N}\sum_{i=1}^{N}\sum_{j=1}^{N} e^{i\mathbf{k}\cdot(\mathbf{R}_{A,i}-\mathbf{R}_{B,j})} \left\langle \phi_A(\mathbf{r}-\mathbf{R}_{A,i}) \middle| \phi_B(\mathbf{r}-\mathbf{R}_{B,j}) \right\rangle \\ &\approx \frac{1}{N}\sum_{i=1}^{N}\sum_{\boldsymbol{\delta}} e^{i\mathbf{k}\cdot\boldsymbol{\delta}} \left\langle \phi_A(\mathbf{r}-\mathbf{R}_{A,i}) \middle| \phi_B(\mathbf{r}-\mathbf{R}_{B,j}) \right\rangle \\ &= s_0 f(\mathbf{k}) \end{aligned}, \tag{2.18}$$

where $s_0 = \left\langle \phi_A(\mathbf{r}-\mathbf{R}_{A,i}) \middle| \phi_B(\mathbf{r}-\mathbf{R}_{B,i}) \right\rangle$ and $S_{BA} = S^*_{AB} = s_0 f^*(\mathbf{k})$. So the matrices H and S of graphene are written as:

$$H = \begin{pmatrix} \varepsilon_A & -\gamma_0 f(\mathbf{k}) \\ -\gamma_0 f^*(\mathbf{k}) & \varepsilon_B \end{pmatrix} \tag{2.19}$$

$$S = \begin{pmatrix} 1 & s_0 f(\mathbf{k}) \\ s_0 f^*(\mathbf{k}) & 1 \end{pmatrix} \tag{2.20}$$

where $\varepsilon_A = \varepsilon_B = 0$ for intrinsic graphene. The derived $E_j(\mathbf{k})$ is given by:

$$E_{\pm} = \frac{\pm\gamma_0 |f(\mathbf{k})|}{1 \mp s_0 |f(\mathbf{k})|} \tag{2.21}$$

where the E_+ applies to the upper conduction band and the E_- applies to the lower valance band. According to Eq (2.15), $f(\mathbf{k})$ is zero at the corners of the graphene Brillouin zone (BZ), K and K', the two Dirac points, which are generally distinguished by a valley index $\xi = \pm 1$. The energy band $E_\pm$ is therefore zero at K and K', and is exactly symmetric about the two Dirac points (**Figure 2-1c**). The energy spectrum and eigenfunctions for $\mathbf{k}$ close to a Dirac point K can be derived by the expansion of $f(\mathbf{k})$ near K to the first order:

$$f(\mathbf{k}) \approx -\frac{3a_0}{2\hbar}\left(\xi q_x - i q_y\right) \tag{2.22}$$

where $\mathbf{q} = \hbar(\mathbf{k} - \mathbf{K}) = (q_x, q_y) = q(\cos\varphi, \sin\varphi)$ is the momentum measured relatively to the Dirac points (**Figure 2-1b**), and $|\mathbf{q}| = \sqrt{q_x^2 + q_y^2} \ll |\mathbf{K}|$. So the matrix H is reduced to:

$$H = \begin{pmatrix} \varepsilon_A & \frac{3a_0\gamma_0}{2\hbar}\left(\xi q_x - i q_y\right) \\ \frac{3a_0\gamma_0}{2\hbar}\left(\xi q_x + i q_y\right) & \varepsilon_B \end{pmatrix}. \tag{2.23}$$

For intrinsic graphene, $\varepsilon_A = \varepsilon_B = 0$, so the matrix H is given by:

$$\begin{aligned} H &= \frac{3a_0\gamma_0}{2\hbar}\begin{pmatrix} 0 & \xi q_x - i q_y \\ \xi q_x + i q_y & 0 \end{pmatrix} \\ &= \upsilon_0\left(\xi q_x \boldsymbol{\sigma}_\mathbf{x} + q_y \boldsymbol{\sigma}_y\right) \\ &= \upsilon_0 \boldsymbol{\sigma}\cdot\mathbf{q} \end{aligned} \tag{2.24}$$

where $\mathbf{q} = \begin{pmatrix} \xi q_x \\ q_y \end{pmatrix}$, $\boldsymbol{\sigma} = (\boldsymbol{\sigma}_x, \boldsymbol{\sigma}_y)$, $\boldsymbol{\sigma}_\mathbf{x} = \begin{pmatrix} 0 & 1 \\ 1 & 0 \end{pmatrix}$ and $\boldsymbol{\sigma}_\mathbf{y} = \begin{pmatrix} 0 & -i \\ i & 0 \end{pmatrix}$ are the Pauli matrices, and $\upsilon_0 = \upsilon_F = \frac{3\gamma_0 a_0}{2\hbar}$ is the Fermi velocity. Taking the known values for a_0 (1.42 Å) and γ_0 (=3.16 eV)[47], υ_F is estimated to be $\approx 1\times 10^6 m/s$. The eigenvalues E of the Hamiltonian (Eq (2.24)) is then given by:

$$E(\mathbf{q}) = \pm\hbar\upsilon_F|\mathbf{q}| + O\left[(q/K)^2\right] \tag{2.25}$$

Equation (2.25) indicates that the energy bands are two circular cones touching each other at Dirac points with a linear dispersion relation with respect to momentum. The energy dispersion is analogous to the energy of ultra-relativistic particles described by the massless

Dirac equation. Thus the behaviour of π electrons in graphene is relativistic, with zero mass and the speed of light substituted by Fermi velocity υ_F.

The wave function for the momentum near K is given by:

$$\Psi_{\pm} = \frac{1}{2}\begin{pmatrix} 1 \\ \pm e^{i\xi\varphi} \end{pmatrix} e^{i\mathbf{q}\cdot\mathbf{r}} \tag{2.26}$$

where the ± denotes the conduction and valence bands respectively. Equation (2.26) indicates that the states of the system close to the Dirac point have chirality. If all the electronic densities were located on the A sublattice, then the wave function could be viewed as a pseudospin 'up' state. In contrast, if all the electronic densities lie in the B sublattice, then the wave function could be viewed as a pseudospin 'down' state. The electronic density is usually shared equally between the two sublattices so that the pseudospin is a linear combination of 'up' and 'down' states.

2.1.2 Graphite

2.1.2.1 Stacking order

Multilayer graphene, or graphite when the number of layers N is large, consists of graphene layers weakly bonded by van der Waals forces. Natural graphite is mainly composed of two relatively stable stacking orders, namely, AB stacking (hexagonal, noted 2H, also called Bernal, $P6_3$ /mmc space group), and ABC stacking (called rhombohedral, noted 3R, $R\bar{3}m$ space group)[48], as shown in **Figure 2-2**. ABC stacking is energetically less stable compared to AB stacking. The transition between the two stacking orders can happen through shifting one layer of graphene with respect to its adjacent layer by a single carbon-carbon bond along armchair directions[49]. In N-layer graphite film, in principle, there could be 2^{N-2} possible stacking sequences[50], regardless of the stacking fault energy. For Bernal stacking, the atoms of the i+2 layer lie exactly on top of the ith layer, while for rhombohedral stacking, right above the centre of the hexagons in the ith layer, the atoms of the i+1 layer and i+2 layer are of inequivalent sites. The perfect AB (or ABC) stacking corresponds to N-1 repeated Bernal (or rhombohedral) segments, whereas mixed segments of Bernal and rhombohedral stacking give rise to stacking faults (**Figure 2-2c**).

In **Figure 2-2**, we label the tight-binding couplings of multilayer graphene. The nearest-neighbour hopping parameter is γ_0, the same as that in monolayer graphene. γ_1 is the strong nearest-layer coupling parameter. γ_2 is the next-nearest-layer coupling parameter. γ_3 and

γ_4 couplings are skew, describing the weaker nearest-layer coupling. For ABC stacking, the atomic sites B_i and A_{i+1} or $B_{i+1}$and A_{i+2} (i=1,2,…N) strongly coupled by γ_1 form the dimer states. The only non-dimer sites locate at A_1 and B_N in the outer layers. For ABA stacking, the trimer sites locate at B_i, A_{i+1} or A_{i+1} and B_{i+2} (i=1,2,…N,). The rest atoms are non-dimer sites. The values of these tight-binding hopping parameters are given by: γ_0 =3.16 eV, γ_1 =0.381 eV, γ_3 =0.38 eV, γ_4 =0.14 eV, γ_2 =-0.02 eV [51].

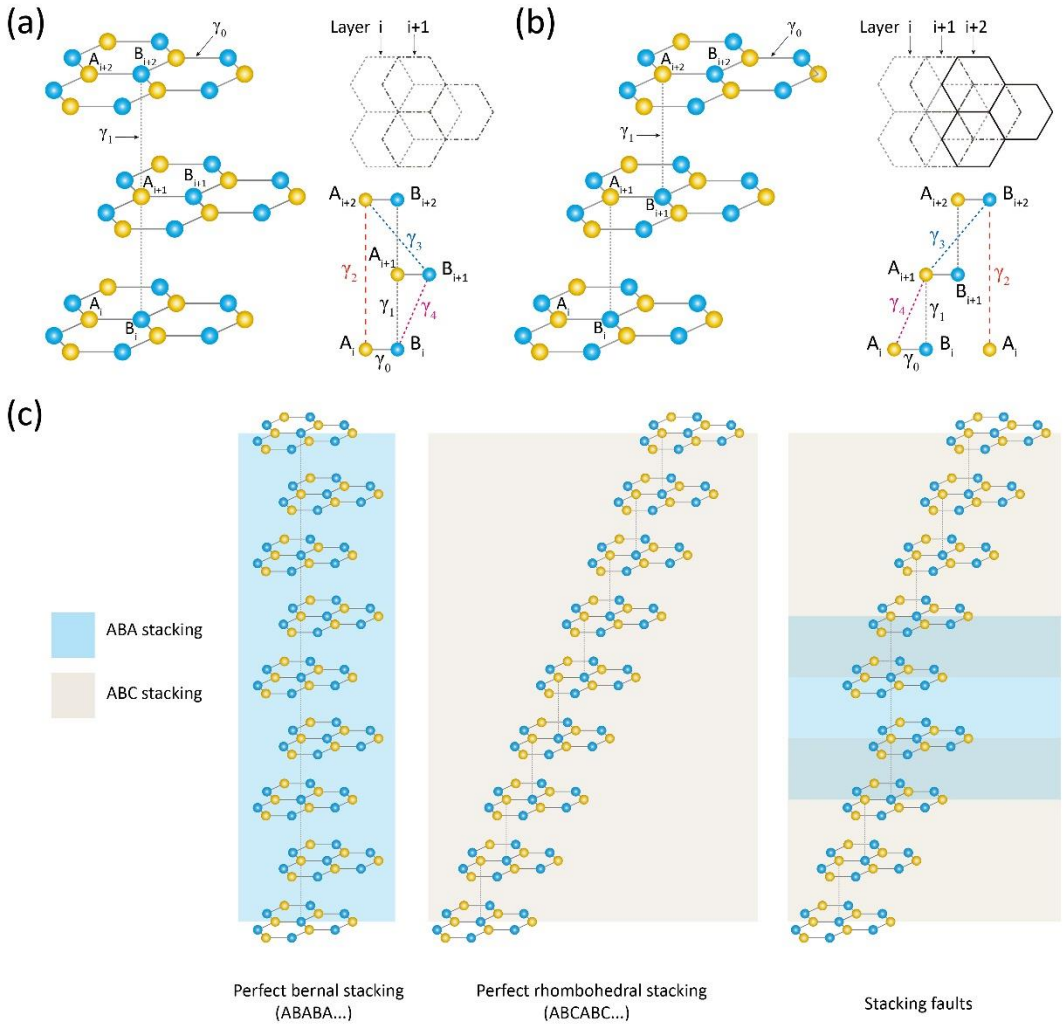

Figure 2-2 Atomic structures of ABA and ABC stacking and the schematic of stacking faults. *(a,b) Atomic structures of Bernal stacking and rhombohedral stacking, respectively, i is the layer index. The blue and yellow spheres represent the A and B sublattices of the graphene honeycomb structure. In each panel, the top right figure is the top view and the bottom right figure is the side view of the unit cell. The hopping parameters are labelled. (c) Schematics of perfect ABA stacking, perfect ABC stacking and stacking faults with Bernal and rhombohedral stacking segments. Taken from ref [52] with some modifications.*

2.1.2.2 Rhombohedral graphite

To analyse the electronic band structure of N -layer rhombohedral graphite, we modelled it as linear chains of atoms linked between the two sublattices sites. The band structure is acquired in the 2D Brillouin zone, which is the projection of the c-axis plane of the graphite stack. The Hamiltonian matrix H is based on the atomic components ψ_{A1}, ψ_{B1}; ψ_{A2}, ψ_{B2};$\cdots$; ψ_{AN}, ψ_{BN}, which reads[50,53,54]:

$$H=\begin{pmatrix} D_1 & V & W & & \\ V^{\dagger} & D_2 & V & W & \\ W^{\dagger} & V^{\dagger} & D_3 & \ddots & \ddots \\ & W^{\dagger} & \ddots & \ddots & \\ & & \ddots & & \end{pmatrix} \tag{2.27}$$

$$D_i=\begin{pmatrix} U_i & \upsilon_0\pi^{\dagger} \\ \upsilon_0\pi & U_i \end{pmatrix} \quad (i=1,2,\cdots,N) \tag{2.28}$$

$$V=\begin{pmatrix} -\upsilon_4\pi^{\dagger} & \upsilon_3\pi \\ \gamma_1 & -\upsilon_4\pi^{\dagger} \end{pmatrix},\ \mathrm{W}=\begin{pmatrix} 0 & \gamma_2/2 \\ 0 & 0 \end{pmatrix} \tag{2.29}$$

where $\upsilon_0=3a_0\gamma_0/2\hbar,\ \upsilon_3=3a_0\gamma_3/2\hbar,\ \upsilon_4=3a_0\gamma_4/2\hbar$, $\pi=\xi q_x+iq_y$, $\pi^{\dagger}=\xi q_x-iq_y$, $\mathbf{q}=\left(q_x,q_y\right)=q\left(\cos\varphi,\sin\varphi\right)$, and U_i describe on-site energies of the atoms. The block D_i describes intralayer coupling, block V describes interlayer coupling, and block W describes next-neighboring-layer coupling in the vertical direction.

In the case of N=3, i.e. trilayer ABC-stacked graphene, for no interlayer asymmetry ($U_1=U_2=U_3$), the eigenvalues for Hamiltonian matrix (Eq (2.27)) are given by $\left(\varepsilon^2-\gamma_1^2\right)^2\left(\varepsilon^2-\gamma_2^2/4\right)=0$. The four high energy bands with $\varepsilon=\pm\gamma_1$ are separated from zero energy by interlayer coupling γ_1, corresponding to dimer states. The two low energy bands with $\varepsilon=\pm\gamma_2/2$ are separated slightly from zero energy by next-nearest layer coupling γ_2, which connects the atoms A_1 and B_3 sitting at the outer layers. The low energy states near the K and K' valleys can be described using a simplified two-band model where the Hamiltonian is projected to the two pair of surface states (A_1 and B_3 sites)[55,56]. In the two-component Hamiltonian, the dimer components are thus eliminated and the interlayer couplings except γ_1 are treated as perturbations. The resulting eigenenergy of the two-

component Hamiltonian has a strong warping effect with trigonal symmetry arising from skewed interlayer coupling γ_3 and the next-nearest interlayer coupling γ_2.

Similarly, for N-layer rhombohedral graphite, all the dimer sites in the lattice contribute to high energy bands that split away from zero energy. The atoms A_1 and B_N sitting at the outer layers form the lowest-energy electron and hole bands. The effective low energy Hamiltonian based on the two-band model mentioned above in the basis ψ_{A1}, ψ_{BN} reads[53,54]:

$$H^{eff} = \begin{pmatrix} 0 & X(q) \\ X^{\dagger}(q) & 0 \end{pmatrix} + \frac{2\upsilon_0\upsilon_4 q^2}{\gamma_1}\begin{pmatrix} 1 & 0 \\ 0 & 1 \end{pmatrix} \tag{2.30}$$

$$X(q) = \sum_{n_1,n_2,n_3} \frac{(n_1+n_2+n_3)!}{n_1!n_2!n_3!} \frac{1}{(-\gamma_1)^{n_1+n_2+n_3}} \left(\upsilon_0 q e^{i\xi\varphi}\right)^{n_1} \left(\upsilon_3 q e^{-i\xi\varphi}\right)^{n_2} \left(\frac{\gamma_2}{2}\right)^{n_3} \tag{2.31}$$

where $n_1 + 2n_2 + 3n_3 = N$, n_1, n_2 and n_3 are integers. The resulting eigenenergy is given by [53]:

$$\varepsilon = \frac{2\upsilon_0\upsilon_4 q^2}{\gamma_1^2} \pm \left|X(q)\right| \tag{2.32}$$

If only considering nearest-neighbor intralayer and interlayer hopping γ_0 (=3.16 eV) and γ_1 (=0.381 eV), the model is reduced to the minimal tight-binding model, then we have $X(q) \approx \left(\upsilon_0 q e^{i\xi\varphi}\right)^N / (-\gamma_1)^{N-1}$, yielding flat surface bands which are isotropic in momentum and touch at the zero energy (**Figure 2-3a**). The nearly flat bands accommodated at the two inequivalent sublattices belonging to opposite surfaces are particularly suitable for exploring electron-electron interactions. Similar systems such as the flat bands observed in graphene layers with "magic" twist angles have proved to exhibit strongly correlated phenomena such as correlated insulating[40] and superconducting states[41].

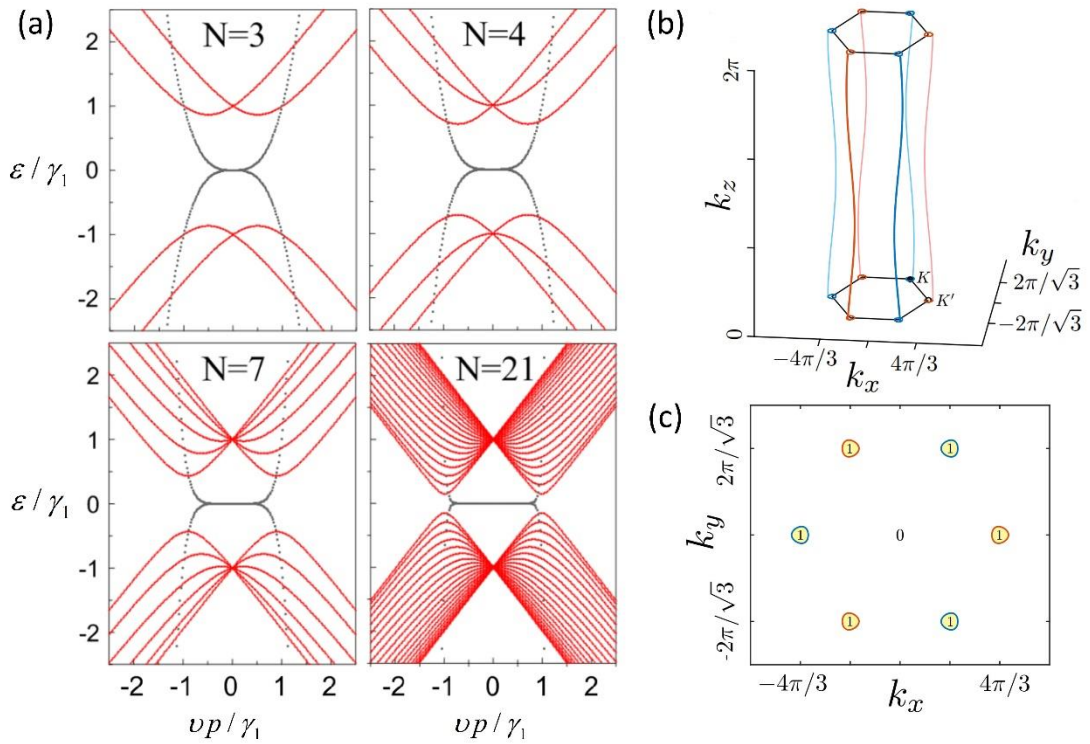

Figure 2-3 Band Structure of ABC stacked graphite and illustration of the Dirac point spirals. *(a) The band structure is acquired from the minimal tight-binding model in the 2D Brillouin zone for a finite number of layers. Grey lines are the low-energy surface subbands, which are degenerate near the* $\mathbf{K}(\xi)$ *center, but split apart at* $q = q_D$*. Red lines are bulk subbands, with* $N-1$ *series of electron-hole symmetric energies. Taken from ref [36] with some modifications. (b) Spiral nodal lines with opposite chirality (distinguished by red and blue lines) in the 3D Brillouin zone. For an infinite number of layers, the bulk subbands of rhombohedral graphite have 3D Dirac cones at the spiral nodal lines, which is discussed below and in* ***Chapter 6****. (c) Projection of the nodal lines onto the plane of* $k_z = 0$*. The numbers indicate the winding number which is a topological invariant that determines the number of zero-energy surface states. (b) and (c) are taken from ref [57].*

If the skew interlayer hopping γ_3 and next-nearest-layer hopping γ_2 are also considered, there will be trigonal warping as described in the trilayer. The presence of skew interlayer hopping γ_4 induces finite band overlap and misalignment of the energy spectrum near Dirac points. The influence of interlayer couplings on the low energy spectrum is probed by the transport gap opening effect at a critical external displacement field, which will be discussed in **Chapter 6**.

To estimate the bulk subbands, we use the minimal tight-binding model which considers only γ_0 and γ_1, with $\gamma_2 = \gamma_3 = \gamma_4 = U_i = 0$. Assuming that the low-energy bulk subbands are present near the $\mathbf{K}(\xi)$ edge lines of the Brillouin zone. For an infinite number of layers, the bulk subbands possess a gapless three-dimensional (3D) Dirac cone structure with the energy zeroes (the Dirac points) at a continuous spiral nodal line in the bulk momentum

space (**Figure 2-3b**), with the radius of the spiral equal to $q_D = \gamma_1/\upsilon_0$ [36] (**Figure 2-3c**). There are two Dirac point spirals with respect to $\mathbf{K}(\xi)$ with opposite spiral senses[36]. Due to the space and time inversion symmetry of rhombohedral graphite, the Dirac point spirals are topologically protected [57-59].

For a finite number of layers, the lowest energy eigenstates with the dispersion $\varepsilon \sim (\upsilon_0 q)^N / (-\gamma_1)^{N-1}$ in the vicinity of the Dirac point is bounded by the projection of the nodal spirals in the bulk onto the surface subspace[36,58], with $q = q_D$ (**Figure 2-3 c**). Such correspondence between the degenerate flat surface bands and nodal lines in the bulk guarantees the topological stability of the surface bands [57-59], indicating the characters of a topological semimetal[54,60,61]. The manifestation of the interplay between surface and bulk in electron transport are discussed in **Chapter 6**. The bulk gap is not fully closed up in the bulk limit. To estimate the bulk gap, the Hamiltonian matrix H (Eq (2.27)) is constructed in the simplified tight-binding model with the in-plane momentum of $\mathbf{q} = (q_D, 0) = \left(\frac{\gamma_1}{\upsilon_0}, 0\right)$ and the nearest neighbour hopping γ_1, which is written as[36,54]:

$$H = \gamma_1 \begin{pmatrix} 0 & 1 & 0 & & \\ 1 & 0 & 1 & 0 & \\ 0 & 1 & 0 & \ddots & \ddots \\ & 0 & \ddots & \ddots & \\ & & \ddots & & \end{pmatrix} \tag{2.33}$$

The resulting eigenenergy is given by $E = 2\gamma_1 \cos\left(\pi j/(2N+1)\right),\ j = 1, 2, \cdots, 2N$ which describes N series of electron-hole symmetric energies. The lowest-energy bulk band is $E_1 = 2\gamma_1 \cos\left(\pi(N-1)/(2N+1)\right) \approx 3\pi\gamma_1/2N$, thus the bulk band gap is:

$$\Delta_{bulk} = 2E_1 \approx 3\pi\gamma_1 / N \tag{2.34}$$

Equation (2.34) shows that as N increases, the bulk band gap decreases but still exists. (**Figure 2-3a**). As N goes to infinity, the bulk gap closes up with $\Delta_{bulk}^{\infty} = 0$ and the bulk band touch each other at $q = q_D = \gamma_1/\upsilon_0$.

If stacking faults reside in a rhombohedral or a Bernal film, the energy spectrum is composed of a collection of the spectra of independent sections, categorized into linear, quadratic, and higher-order bands[54,62]. Stacking faults in a rhombohedral film prove to suppress transport gap opening, which is discussed in **Chapter 6**.

2.2 Electron Dynamics in Electromagnetic Fields

In this section, we discuss the behaviour of electrons confined in two-dimensional materials in the presence of an electromagnetic field. At lower temperatures, quantum-mechanically dominated transport phenomena such as the quantum Hall effect can appear, with the energies of electrons quantized into Landau levels (LLs)[63]. In the quantum Hall regime, oscillations in longitudinal conductance appear as the Fermi level crosses successive LLs[64,65]. At high magnetic fields, transverse conductance displays plateaux with precisely quantized values[64,65]. Graphene, as an ideal two-dimensional electron gas (2DEG) system, exhibits the half-integer quantum Hall effect due to its unique electronic properties[23,24].

2.2.1 Classical Hall effect

Classically, when 2DEG is subjected to a perpendicular magnetic field B, the motion of electrons follows cyclotron orbits with the angular frequency and radius given by:

$$\omega_c = \frac{eB}{m_e}, \quad r_c = \frac{m_e v}{eB} \tag{2.35}$$

In the presence of an electric field, there will be a voltage difference (the Hall voltage) transverse to the motion of electrons and to the magnetic field. According to the Drude Model, the motion of electrons is given by:

$$m_e \frac{d\mathbf{v}}{dt} = -e\mathbf{E} - e\mathbf{v} \times \mathbf{B} - \frac{m_e \mathbf{v}}{\tau} \tag{2.36}$$

where τ is the scattering time of electron collisions. Since the current density $\mathbf{J}$ is related to the velocity by $\mathbf{J} = -ne\mathbf{v}$ (here n is the charge carrier density), at equilibrium state ($d\mathbf{v}/dt = 0$) we have:

$$\mathbf{J} = \mathbf{g}\mathbf{E} = \frac{\sigma_0}{1+\omega_c^2\tau^2}\begin{pmatrix} 1 & -\omega_c\tau \\ \omega_c\tau & 1 \end{pmatrix}\mathbf{E}, \tag{2.37}$$

where $\sigma_0 = \frac{ne^2\tau}{m}$, and $\mathbf{g} = \begin{pmatrix} \sigma_{xx} & \sigma_{xy} \\ -\sigma_{xy} & \sigma_{yy} \end{pmatrix}$ is the conductivity tensor where the off-diagonal terms are responsible for the Hall effect: in equilibrium, a current in the x-direction requires an electric field with a component in the y-direction. The resistivity can be measured from experiments and is related to $\mathbf{g}$ by:

$$\boldsymbol{\rho} = \mathbf{g}^{-1} = \begin{pmatrix} \rho_{xx} & \rho_{xy} \\ -\rho_{xy} & \rho_{yy} \end{pmatrix} = \frac{1}{\sigma_0}\begin{pmatrix} 1 & \omega_c\tau \\ -\omega_c\tau & 1 \end{pmatrix} = \begin{pmatrix} 1/\sigma_0 & B/ne \\ -B/ne & 1/\sigma_0 \end{pmatrix} \tag{2.38}$$

Equation (2.38) indicates that ρ_{xx} is independent of B and ρ_{xy} is independent of τ, which means that the sample quality does not influence ρ_{xy}. The measurement of ρ_{xy} provides an independent method to calculate the carrier density.

2.2.2 Landau levels

The quantum mechanical treatment of 2DEG in a perpendicular magnetic field B starts with the Hamiltonian:

$$H = \frac{1}{2m_e}\left[\mathbf{p} + e\mathbf{A}(\mathbf{r})\right]^2 \tag{2.39}$$

for non-relativistic electrons and:

$$H = v\left[\mathbf{p} + e\mathbf{A}(\mathbf{r})\right]\cdot\boldsymbol{\sigma} \tag{2.40}$$

for relativistic electrons, where the mechanical momentum $\mathbf{p}$ is substituted by its gauge-invariant form $\mathbf{A}(\mathbf{r})$, which is the vector potential that generates the magnetic field using Maxwell relation $\mathbf{B} = \nabla \times \mathbf{A}(\mathbf{r})$ (where $\mathbf{r} = (x, y)$), $\boldsymbol{\sigma}$ is the Pauli matrices, and m_e is the electron mass. The substitution is valid only when the lattice constant is much smaller than the quantum magnetic length:

$$l_B = \sqrt{\hbar / eB} \tag{2.41}$$

which is the fundamental length scale governing quantum phenomena in the presence of a magnetic field. The l_B is around 25nm for B=1 T, which is larger than most lattice constants. By choosing the Landau gauge $\mathbf{A}(\mathbf{r}) = B(-y, 0, 0)$ (which respects the translation invariance in the x-direction), after the quantum mechanical treatment similar to one-dimensional harmonic oscillator[64], the energy levels of the 2DEG are a sequence of discrete LLs:

$$\varepsilon_n = \hbar\omega_c\left(n + \frac{1}{2}\right) \tag{2.42}$$

for non-relativistic electrons[64] and:

$$\varepsilon_n = \mathrm{sgn}(n)\frac{\hbar \upsilon_F}{l_B}\sqrt{2|n|} = \mathrm{sgn}(n)\sqrt{2e\hbar\upsilon_F^2 |n| B} \tag{2.43}$$

for relativistic electrons[66], where $n>0$ for electron-like LLs and $n<0$ for hole-like LLs. The LLs for non-relativistic and relativistic electrons are shown in **Figure 2-4**.

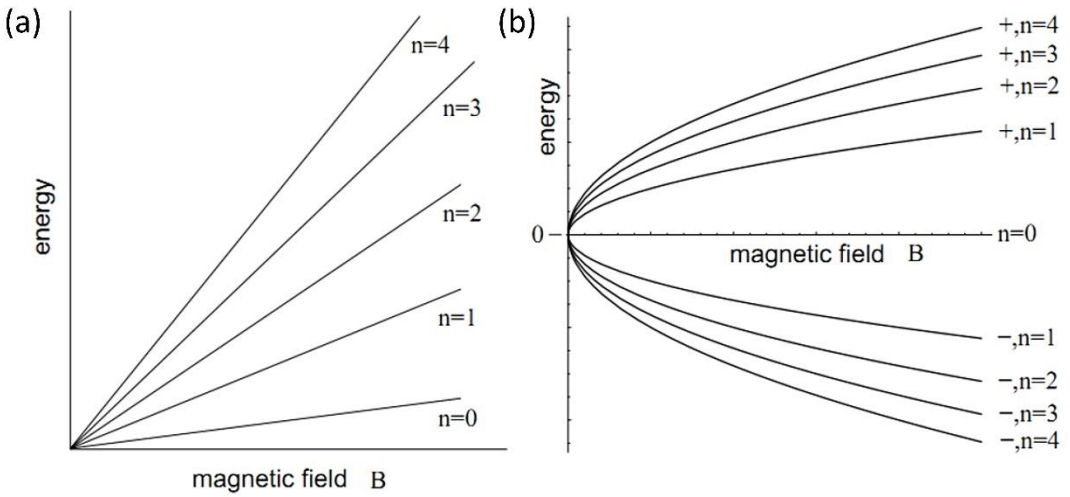

***Figure 2-4* Landau levels as a function of the magnetic field B.** *(a) Non-relativistic case. (b) Relativistic case.*

For non-relativistic electrons confined to a finite plane with length L_x and width L_y, under the Landau gauge $\mathbf{A}(\mathbf{r}) = B(-y,0,0)$, Hamiltonian (Eq (2.39)) becomes:

$$H = \frac{(p_x - eBy)^2}{2m_e} + \frac{p_y^2}{2m_e} = \frac{m_e\omega_c}{2}\left(y - kl_B^2\right)^2 + \frac{p_y^2}{2m_e} \tag{2.44}$$

The eigenstates are:

$$\psi_{n,k}(x,y) = \frac{e^{ik_x x}}{\sqrt{L_x}} H_n\left(\frac{y - k_x l_B^2}{l_B}\right) e^{-\left(y-k_x l_B^2\right)^2/4l_B^2} \tag{2.45}$$

where H_n is the nth Hermite polynomial. The Hamiltonian (Eq (2.45)) is the same as the one describing a one-dimensional oscillator centred around the position $y = y_0 = k_x l_B^2$. Using periodic boundary conditions

$$e^{ik_x(x+L_x)} = e^{ik_x x} \tag{2.46}$$

the allowed values of k and m are:

$$k_x = m\frac{2\pi}{L_x} \tag{2.47}$$

where m is an integer and is the corresponding Landau level quantum number. The state at $y=0$ corresponds to $k_x=0$, and the state at $y=L_y$ corresponds to $k_x=L_y/l_B^2$. The number of states in the plane is therefore given by:

$$N=\int_0^{L_y/l_B^2}\frac{L_x}{2\pi}dk=\frac{L_x}{2\pi}\cdot\frac{L_y}{l_B^2}=\frac{eBL_xL_y}{2\pi\hbar}=\frac{\phi}{\phi_0} \tag{2.48}$$

where $\phi=BL_xL_y$ is the total magnetic flux in the finite plane, and $\phi_0=h/e$ is the magnetic flux quantum. Equation (2.48) indicates that the number of flux quanta equals to the number of states, meaning that each state contributes to one flux quantum. The degeneracy of the Landau states is given by:

$$N/L_xL_y=B/\phi_0 \tag{2.49}$$

The filling factor ν, the number of occupied Landau levels for electrons is calculated by:

$$\nu=\frac{n_e}{B/\phi_0} \tag{2.50}$$

where n_e is the density of electrons in the finite plane.

2.2.3 Quantum Hall effect in graphene

In this section, we discuss the motion of 2DEG with an additional electric field $\mathbf{E}$ in the x-direction. We consider $L_x \gg L_y \gg \zeta \gg l_B$, where ζ is the length scale for the variation of the electrostatic potential. In a real sample, there exist disorders such as impurities and edges, which generate electrostatic potentials that alter the distribution of the electric field (**Figure 2-5a**). The Hamiltonian of 2DEG is thus modified by a potential term:

$$V(\mathbf{r})=V_{conf}(y)+V_{imp}(x,y) \tag{2.51}$$

where $V_{conf}(y)$ is the confinement potential which varies along the y-direction near the sample edges while respecting the translation invariance in the x-direction, and $V_{imp}(x,y)$ is caused by the impurities. We assume $V(\mathbf{r})$ to be smoothly varying electrostatic potential since $\zeta \gg l_B$, thus we can approximate the electron's position $\mathbf{r}$ by that of its guiding centre $\mathbf{r}_g$. Within the semi-classical picture, $\langle \dot{\mathbf{r}}_g \rangle = \frac{\mathbf{E}\times\mathbf{B}}{B^2}$, which means that the guiding centres move along the equipotential lines of the smoothly varying external electrostatic potential.

This is the so-called Hall drift, where the cyclotron orbits of electron drift in the direction of $\mathbf{E}\times\mathbf{B}$ [64]. Therefore, the electrons will turn clockwise (anticlockwise) on an equipotential line around a summit (valley) caused by a negatively (positively) charged impurity. For a closed equipotential line caused by impurities, electrons are localized (or at localized states), which does not contribute to electronic transport. For the equipotential lines near the two edges, electrons will drift along opposite directions and contribute to the electronic transport (extended states), resulting in the chirality of the edge states discussed below.

Near the edge of the sample, each Landau level is associated with a state that is a function of position, according to (Eq (2.45)). These states contribute to the transport of electrons along the edges of the sample, the so-called edge states. In the quantum mechanical treatment using the Landau gauge, the Hamiltonian (Eq (2.44)) modified by the confinement potential $V_{conf}\left(y\right)$ becomes:

$$H=\frac{\left(p_x-eBy\right)^2}{2m_e}+\frac{p_y^2}{2m_e}+V_{conf}\left(y_0^{'}\right) \tag{2.52}$$

where $y_0^{'}$ is shifted from y_0 due to the electron drift. The energy spectrum is then given by:

$$\varepsilon_n=\hbar\omega_c\left(n+\frac{1}{2}\right)+V\left(y_0^{'}\right) \tag{2.53}$$

which means that the LLs are lifted by the confinement energy $V\left(y_0^{'}\right)$, as shown in **Figure 2-5b**. **Figure 2-5b** indicates that when the Fermi level lies between the bulk levels, the bulk is insulating because the LLs are completely full, whereas the edges are conducting at quantum channels that cross the Fermi energy. The electric current of the nth LL near the edges is given by:

$$\begin{aligned} I_n^x&=\sum_{m,k}\frac{e}{L_x}v_x=\frac{e}{L_x}\sum_{m,k}\left\langle\Psi_{n,k}\left(x,y\right)\right|\frac{\partial H}{\partial x}\left|\Psi_{n.k}\left(x,y\right)\right\rangle \\ &=\frac{e}{L_x}\sum_{m,k}\left\langle\Psi_{n,k}\left(x,y\right)\right|\frac{p_x-eBy}{m_e}\left|\Psi_{n.k}\left(x,y\right)\right\rangle \\ &=\frac{e}{L_x}\sum_{m,k}\frac{1}{\hbar}\frac{\partial\varepsilon_{n,k}}{\partial k} \end{aligned} \tag{2.54}$$

where the quantum channel $\Psi_{n,k}\left(x,y\right)$ is labelled by the wave vector $k_x=2\pi m/L_x$ (Eq (2.47)), hence

$$I_n^x = \frac{e}{L_x}\sum_m \frac{1}{\hbar}\frac{L_x}{2\pi}\frac{\Delta\varepsilon_{n,m}}{\Delta m} = \frac{e}{L_x}\sum_m \frac{L_x}{h}\left(\varepsilon_{n,m+1}-\varepsilon_{n,m}\right)$$
$$= \frac{e}{h}\left(\mu_{\max}-\mu_{\min}\right) = \frac{e^2}{h}U_H \qquad (2.55)$$

where μ is the confinement potential, and U_H is the Hall voltage between the upper and the lower edge. The second line of Eq (2.55) uses the thermodynamic equilibrium between the edge states and the contact potentials (**Figure 2-5a**). Equation (2.54) and (2.55) mean that each LL contributes one conductance quantum $g_0 = e^2/h$ to electronic transport. Hence n occupied Landau levels will give rise to the conductance of $g = ne^2/h$, which is the Hall conductance.

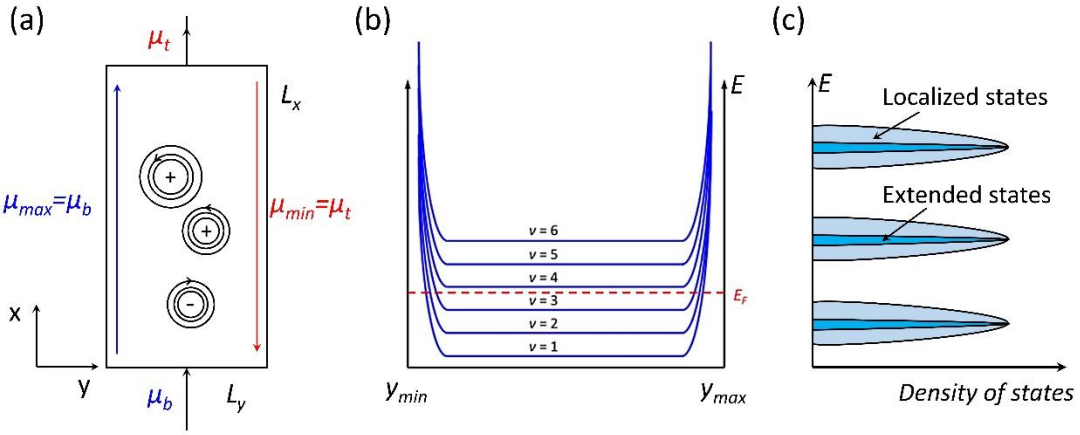

Figure 2-5 Schematic for the quantum Hall effect in a finite width sample. *(a) Localized states and edge states in the sample. For impurities in the sample, the equipotential lines are closed, while at the sample edges, the equipotential lines stretch from one side of a sample to another. (b) Schematic of Landau levels in a finite width sample, with the Fermi level lying between LLs. Taken from ref [67]. (c) Landau level density of states (DOS).*

The discussion above is the situation of n completely filled LLs, where Fermi level lies between LLs. The longitudinal conductivity vanishes since there are no states available for carriers. When LLs get partially filled by electrons (as shown in **Figure 2-5c**) either by varying magnetic field or carrier density, the electrons will populate the localised states. Since these states do not contribute to the transport, the Hall conductivity remains unchanged. As the LLs get further filled, the longitudinal conductivity peaks at the bulk extended states, and the Hall conductivity jumps to the next plateau, at some critical value of magnetic field or carrier density. This plateau transition is related to percolation transition, where electrons start to percolate between the opposite sample edges beyond a certain threshold of the filling[68]. The longitudinal conductivity displays oscillations as the Fermi level fills successive LLs, which is the so-called Shubnikov-de Haas (SdH) oscillation.

In a 2D massless Dirac fermion system such as graphene, the Hall conductivity plateaux appear at:

$$\sigma_{xy} = 4\left(n+1/2\right)e^2/h \tag{2.56}$$

where $4\left(n+1/2\right)$ is the filling factor for LLs (**Figure 2-6**). The pre-factor 4 is due to two valley and two spin degeneracies of each LL in graphene. The 1/2 shift is caused by the Berry phase of π, arising from the band degeneracy point[23,24].

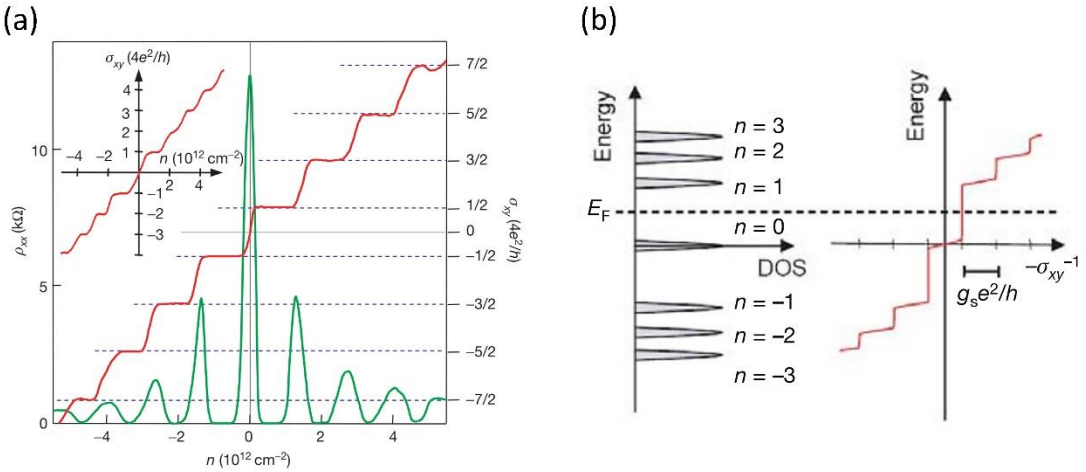

Figure 2-6 Quantum Hall effect in graphene. *(a) Hall conductivity σ_{xy} and longitudinal resistivity ρ_{xx} as a function of carrier density at B= 14 T and T= 4 K. Taken from ref [23]. (b) Schematic of Landau level DOS and corresponding quantum Hall conductance as a function of energy. Taken from ref [24].*

2.3 Basics of Berry phase

Berry phase of the electronic wave function can have a profound effect on electronic dynamics [69-71] and is responsible for exotic phenomena such as the anomalous and spin Hall effects[72-76], etc. The exceptional topology of the rhombohedral graphite band structure is characterized by the Berry phase and Berry curvature, which is investigated experimentally in **Chapter 6**. In this section, we introduce the basic concepts of the Berry phase and its physical significance, as well as the manifestation of the Berry phase in the magneto-oscillation effects.

2.3.1 Berry phase and Berry curvature

When a quantum state, of which the Hamiltonian H depends on time through a set of parameters $\boldsymbol{\alpha} = \boldsymbol{\alpha}(t) = (\alpha_1, \alpha_2, \alpha_3, ...)$, undergoes adiabatic evolution along a loop C in the parameter space, it will acquire a geometrical phase called Berry phase in addition to the

dynamical phase. Berry phase β can be expressed as an integral along the loop C in the parameter space[76,77]:

$$\beta_n = \oint_C d\boldsymbol{\alpha} \cdot Q_n(\boldsymbol{\alpha}), \tag{2.57}$$

where $Q_n(\boldsymbol{\alpha})$ is a vector-valued function called the Berry connection or the Berry vector potential:

$$Q_n(\boldsymbol{\alpha}) = i\left\langle n(\boldsymbol{\alpha})\right|\frac{\partial}{\partial \boldsymbol{\alpha}}\left|n(\boldsymbol{\alpha})\right\rangle \tag{2.58}$$

where $\left|n(\boldsymbol{\alpha})\right\rangle$ is the instantaneous orthonormal basis function from the eigenstates of $H(\boldsymbol{\alpha})$. Vector $Q_n(\boldsymbol{\alpha})$ is gauge dependent whereas β is a gauge-invariant quantity with physical significance for a closed path. The Eq (2.57) shows that the Berry phase only depends on the geometric of the closed path and is independent of how $\boldsymbol{\alpha}(t)$ varies with time.

The Berry curvature is a gauge-field tensor derived from the Berry vector potential. If the parameter space is three dimensional, the Berry curvature is given by:

$$\boldsymbol{\Omega}_n(\boldsymbol{\alpha}) = \nabla_{\boldsymbol{\alpha}} \times Q_n(\boldsymbol{\alpha}) \tag{2.59}$$

Berry curvature is gauge invariant and provides a local description of the geometric properties of the parameter space. According to Stokes's theorem, the Berry phase can be written as a surface integral:

$$\beta_n = \int_M d\mathbf{M} \cdot \boldsymbol{\Omega}_n(\boldsymbol{\alpha}) \tag{2.60}$$

where M is an arbitrary surface enclosed by the path C.

2.3.2 Berry phase in Bloch bands and its manifestation

Now we consider the realization of the Berry phase in crystalline solids. Remember that the Bloch wave function of the electron in a crystal index by n is given by:

$$\Psi_{\mathbf{k}n}(\mathbf{r}) = e^{i\mathbf{k}\mathbf{r}} u_{\mathbf{k}n}(\mathbf{r}) \tag{2.61}$$

where $u_{\mathbf{k}n}(\mathbf{r})$ is the periodic function of position $\mathbf{r}$ and $\hbar\mathbf{k}$ is the crystal momentum. Within the independent electron approximation, the Hamiltonian of the system is given by:

$$H = \frac{\hat{p}^2}{2m} + V(\mathbf{r}), \tag{2.62}$$

which is $\mathbf{k}$ independent. Through the following unitary transformation:

$$H(\mathbf{k}) = e^{-i\mathbf{k}\cdot\mathbf{r}} H e^{i\mathbf{k}\cdot\mathbf{r}} = \frac{\left(\hat{\mathbf{p}} + \hbar\mathbf{k}\right)^2}{2m} + V(\mathbf{r}), \tag{2.63}$$

the Hamiltonian Eq (2.62) becomes $\mathbf{k}$ dependent. Thus one can identify the Brillouin zone as the parameter space of the transformed Hamiltonian $H(\mathbf{k})$ and $u_n(\mathbf{k})$ as the basis function. The Berry connection is thus given by $Q_n(\mathbf{k}) = i\langle u_{n\mathbf{k}}(\mathbf{r})|\nabla_{\mathbf{k}}|u_{n\mathbf{k}}(\mathbf{r})\rangle$. According to the concept of the Berry phase, if $\mathbf{k}$ varies along a closed path C in the momentum space, then the Bloch state will gain a Berry phase:

$$\beta_n = \oint_C d\mathbf{k}\cdot\langle u_{n\mathbf{k}}(\mathbf{r})|i\nabla_{\mathbf{k}}|u_{n\mathbf{k}}(\mathbf{r})\rangle, \tag{2.64}$$

which is a gauge-invariant physical quantity. Correspondingly, the Berry curvature is given by:

$$\mathbf{\Omega}_n(\mathbf{k}) = \nabla_{\mathbf{k}} \times \langle u_{n\mathbf{k}}(\mathbf{r})|i\nabla_{\mathbf{k}}|u_{n\mathbf{k}}(\mathbf{r})\rangle \tag{2.65}$$

which describes the intrinsic property of the energy band structure of the crystal.

To generate a closed path in the momentum space, one common way is to apply a magnetic field to the crystal. In the presence of a magnetic field $\mathbf{B}$ which is perpendicular to the plane where the electron moves, for a semi-classical approach, the variation rate of the momentum is equal to the Lorentz force:

$$\hbar\dot{\mathbf{k}} = -e(\mathbf{v}\times\mathbf{B}). \tag{2.66}$$

Since the Lorentz force is normal to $\mathbf{v}$, the electron will move with constant energy. Integration of Eq (2.66) with respect to time gives:

$$\mathbf{k}(t) - \mathbf{k}(0) = -\frac{eB}{\hbar}(\mathbf{r}(t) - \mathbf{r}(0)) \times \hat{\mathbf{B}}, \tag{2.67}$$

which displays the correspondence between the electron trajectory in a crystal and its orbit in $\mathbf{k}$ space. The orbit in $\mathbf{k}$ space is given by the intersection of the constant energy surface with planes of constant $\mathbf{k}_z$ (z is the direction of the magnetic field $\mathbf{B}$) and it is also the closed path C in the momentum space needed to generate the Berry phase. If orbit C surrounds the contact between the energy bands which are separated linearly in the vicinity

of the band contact, then a non-trivial Berry phase of $\beta = \pm\pi$ will be obtained [78]. Such a situation can be well fulfilled in graphene, as will be discussed below.

Berry phase can manifest itself in magneto-oscillation effects[24,70,79], which can be detected experimentally. For Bloch electrons in magnetic fields, the semiclassical quantization condition for energy levels of the closed and nonintersecting orbits is given by the Onsager relation [80,81]:

$$S(\varepsilon_n) = (n+\gamma)2\pi eB/\hbar \tag{2.68}$$

where $S(\varepsilon_n)$ is the area of the closed orbit in $\mathbf{k}$ space mentioned above, n is an integer and γ is a constant which can be expressed by Berry phase [78]:

$$\gamma - \frac{1}{2} = -\frac{1}{2\pi}\oint_C d\mathbf{k}\cdot\langle u(\mathbf{k})|i\nabla_{\mathbf{k}}|u(\mathbf{k})\rangle = -\frac{1}{2\pi}\beta \tag{2.69}$$

As described in **Section 2.1.1** and **2.2.2**, graphene possesses massless Dirac fermion with a linear energy band dispersion relation near Dirac points according to Eq (2.25) $\varepsilon(\mathbf{k}) \approx \pm\hbar\upsilon_F|\mathbf{k}|$, and with the LLs given by Eq (2.43): $\varepsilon_n = \mathrm{sgn}(n)\sqrt{2e\hbar\upsilon_F^2|n|B}$ in the presence of a magnetic field. The nth LL corresponds to a circular orbit with radius of $k_n = \varepsilon/\hbar\upsilon_F$. Thus the area of the circular orbit of the nth LL can be calculated from Eq (2.25) and (2.43):

$$S(\varepsilon_n) = \pi k_n^2 = 2\pi eB|n|/\hbar \tag{2.70}$$

Comparison between Eq (2.68) and (2.70) implies that $\gamma = 0$, which means that β equals π for graphene. Recall that in graphene the electrons are of chiral nature, where the electronic states possess a pseudospin degree of freedom (see **Section 2.1.1**). As the electronic states undergoes the adiabatic rotation of 2π in $\mathbf{k}$ space, the pseudospin states obtain a Berry phase of π, which is characteristic of a real spinor that gains a Berry phase of π after a 2π adiabatic rotation.

The constant γ manifests itself to be the semiclassical SdH oscillation phase [82,83], which can be probed experimentally by measuring the electrical resistance [24]:

$$\Delta R_{xx} = R(B,T)\cos\left[2\pi\left(B_F/B - \gamma\right)\right] \tag{2.71}$$

where $R(B,T)$ is the SdH oscillation amplitude, T is temperature and B_F is the frequency of the SdH oscillation in $1/B$. Berry phase thus results in the π shift in SdH oscillation and a half-integer shift in the Hall conductivity plateau (**Figure 2-6**).

2.3.3 Nπ Berry phase in ABC-stacked multilayer graphene

The effective low energy Hamiltonian for N layer ABC-stacked multilayer graphene is given by Eq (2.30) in **Section 2.1.2.2**, where the first term describes a family of Hamiltonians H_N. In the minimal tight-binding model, H_N can be written as[36,50]:

$$H_N = g_N \begin{pmatrix} 0 & (\pi^\dagger)^N \\ (\pi)^N & 0 \end{pmatrix} \tag{2.72}$$

where $g_1 = \upsilon_F$ for graphene, $g_2 = -1/2m$ for bilayer graphene[55] and $g_3 = \upsilon^3/\gamma_1^2$ for trilayer ABC-stacked graphene [84]. The quasiparticles described by Hamiltonians H_N will acquire a Berry phase of $N\xi\pi$ upon an adiabatic propagation along an equienergy contour in $\mathbf{k}$ space [53]. Although the trigonal warping effect leads to several band touching points or Dirac points, the total Berry phase summed over all Dirac points is always $N\xi\pi$, the same as the value without trigonal warping [53]. The Nπ Berry phase in ABC-stacked multilayer graphene and the corresponding Berry curvature are investigated by the magneto-oscillation effects, which is further discussed in **Chapter 6**.

2.4 Graphene in a periodic potential and magnetic field

The motion of electrons in a periodic potential, e.g. a crystal lattice, can be described by Bloch's state which is delocalized over the entire crystal lattice. In the presence of magnetic fields, as discussed in **Section 2.2**, Bloch electrons are localized in cyclotron orbits with quantised energies. However, the electrons can obtain delocalized Bloch states as if without the presence of a magnetic field (effective magnetic field $B_{eff} = 0$) when the translational symmetry is restored in the Hamiltonian. This is the case when values of magnetic field satisfies[85,86]

$$\frac{\phi_m}{\phi_0} = \frac{p}{q} \tag{2.73}$$

where $\phi_m = BA$ is the magnetic flux piercing the unit cell (with the area of A) of the periodic potential, p and q are co-prime integers and $\phi_0 = h/e$ is the magnetic flux quantum. For common crystals, the period of the lattice is a few angstroms. Thus the necessary magnetic field required to reach $\phi_m / \phi_0 = 1$ exceeds 10,000 T. For the achievable lab magnetic field, the period of the lattice should be tens of nanometres, i.e. it is commensurable to the scale of the magnetic length l_B.

On the other hand, when the condition of Eq (2.73) is satisfied, the Bloch band clusters into precisely q distinct energy bands, which themselves cluster into larger groups of bands, forming a quasicontinuous distribution of quantum states with a self-similar recursive structure, the Hofstadter butterfly (right panel of **Figure 2-7a**), where the spectral gaps occur along the lines $\phi_m / \phi_0 = p/q$[87,88]. By integrating density of states over energy, the Hofstadter energy spectrum can be transformed into a diagram of charge carrier density versus magnetic field (Wannier diagram), where the spectral gaps are constrained to linear trajectories described by a Diophantine equation[89]:

$$n / n_0 = t\left(\phi_m / \phi_0\right) + s \tag{2.74}$$

Here t and s are integers, denoting the superlattice miniband filling index and quantized Hall conductivity of the gapped state, respectively. n is the carrier density, and $n_0 = 1/A$ is carriers in a completely filled Bloch band in a unit cell of the periodic potential.

One of the experimental techniques to realize the lattice periodicity of the order tens of nanometres is to obtain artificial moiré superlattices formed in graphene/hBN heterostructure with a small rotation angle θ. This is possible because of the near-lattice matching of the two crystals, as discussed in **Section 3.1.2**. The moiré potential leads to multiple minibands and the generation of massless secondary Dirac-like spectra in graphene at the supercell Brillouin zone boundaries[90,91] (left panel of **Figure 2-7a**). The secondary Dirac points (SDP) occurs at an energy of $E = \pm\hbar v_F |\boldsymbol{\kappa}| / 2 = 2\pi\hbar v_F / \sqrt{3}\lambda_m$, where $\boldsymbol{\kappa}$ is the reciprocal superlattice vectors and λ_m is the moiré wavelength related to the rotation angle θ by Eq (3.5). The SDPs manifest themselves as additional peaks in the resistance symmetrically situated at the carrier density of $n_{SDP} = 8/\sqrt{3}\lambda_m^2$ relative to the primary Dirac point (PDP), accompanied by the reversal of the Hall effect due to Van Hove singularities[32-34,92] (**Figure 2-7b**).

In the presence of a magnetic field, the Landau levels of graphene evolve into Hofstadter minibands separated by a hierarchy of self-similar minigaps occurring at $\phi_m / \phi_0 = p / q$, leading to the Brown-Zak oscillations[93]. For the usual quantum Hall effect, the Hall conductivity is quantized according to the relation $\sigma_{xy} = \nu e^2 / h$, where ν is a filling factor of a particular LL. In the fan diagram, the quantum oscillations emerging from PDP follow the trajectories $B = n\phi_0 / \nu$. For the Hofstadter spectrum, the Hall conductivity is quantized according to the relation $\sigma_{xy} = te^2 / h$. According to the Diophantine equation, the quantized Hall conductivity associated with each minigap will appear at linear trajectories as a function of magnetic field[32-34] (**Figure 2-7c**). Detailed explanations are also presented in **Section 7.2**.

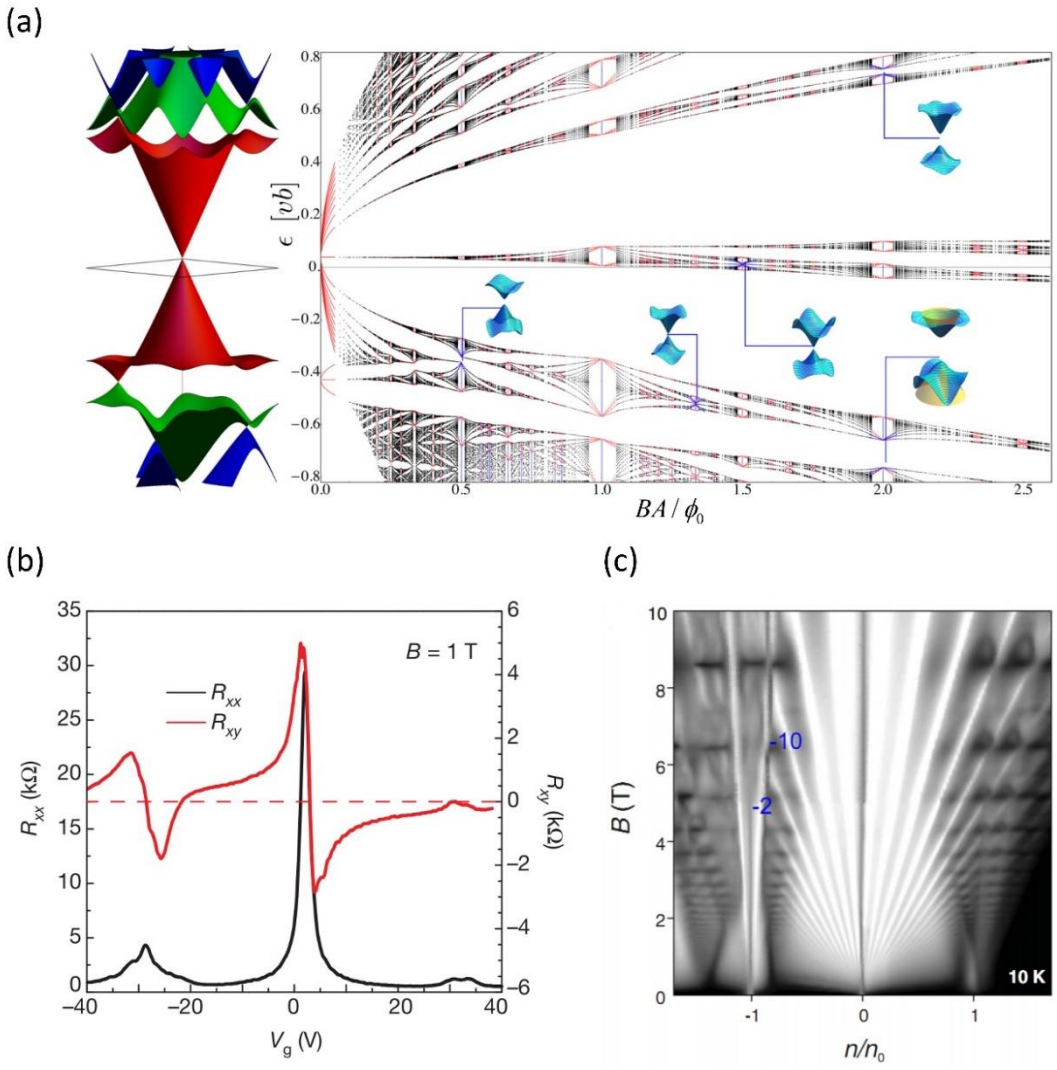

Figure 2-7 Graphene in moiré superlattice. *(a) Energy spectrum of graphene in moiré superlattice. The left panel shows the minibands with a distinct SDP in the valence band. THE right panel shows the Hofstadter butterfly spectrum in a non-zero magnetic field. The insets show examples of magnetic minibands at* $B = p\phi_0 / qA$ *. Taken from ref* [93] *with some modifications. (b) Longitudinal resistance and Hall resistance versus gate voltage at non-quantised B. The Hall resistance changes sign and passes through zero at the same gate voltage as the satellite peaks of the longitudinal resistance, indicating that the Fermi level passes from the electron-like to the hole-like band of the mini-Brillouin zone band. Taken from ref* [32]*. (c) Concentration and field dependence of Brown-Zak oscillations. The numbers -10 and -2 indicate quantum oscillations emerging from PDP and SDP, with v = -10 for PDP and t = -2 for SDP. Here v is the Landau level filling factor, and t represents the prefactor of quantized Hall conductivity of the gapped state in the fractal spectrum. The horizontal streaks in the diagram imply the Brown-Zak oscillations. Taken from ref* [94]*.*

Chapter 3: Graphene/hBN van der Waals heterostructures

Graphene/hBN heterostructure is the prototypical one in a large family of 2D van der Waals heterostructures, where the hBN not only serves as a featureless insulating substrate[95-98] but also modifies the electronic properties of graphene[4]. This chapter is dedicated to understanding the interfacial interactions and nanomechanics acting between the layers in graphene/hBN heterostructures, which is the key to designing on-demand geometries of the electronic devices and controlling the emergent device properties resulting from relative rotation angles between the layers. We also introduce a detailed fabrication procedure for graphene/hBN heterostructures, where creative modifications can be introduced to tune the desired electronic and optical device properties.

3.1 Basics of graphene/hBN heterostructures

In this section, we describe the atomic structures of hBN and common stacking configurations, as well as the formation of moiré superlattice in graphene/hBN heterostructures. We also explain the origin of hBN as an excellent substrate for graphene and the interaction between the two crystals.

3.1.1 Hexagonal boron nitride

Hexagonal boron nitride (hBN) is a layered material whose atomic structure is analogous to graphite. It has weak van der Waals interaction between crystal layers and a hexagonal lattice in each layer, with alternating boron and nitrogen atoms in the A and B triangular sublattices. The lattice mismatch δ between graphene and hBN is small, approximately 1.8%[99] since boron, carbon and nitrogen are next to each other on the periodic table. Lattice mismatch is calculated using:

$$\delta = \frac{a_{hBN} - a_{gr}}{a_{gr}} \approx 1.8\% \tag{3.1}$$

where $a_{hBN} \approx 2.50$ Å[99] and $a_{gr} \approx 2.46$ Å are lattice constants of hBN and graphene, respectively. Bulk hBN typically adopts AA' stacking sequence[100,101] with an interlayer spacing of around 3.33Å[99], where alternating boron and nitrogen atoms are arranged along the c axis, in contrast to AA stacking, where nitrogen (boron) atoms eclipse over nitrogen (boron) atoms. The crystal symmetry of hBN relies on the total number of layers N. If N is even, BN crystal belongs to the centrosymmetric D_{3d} point group, whereas for odd N, it belongs to the non-centrosymmetric D_{3h} point group (**Figure 3-1**).

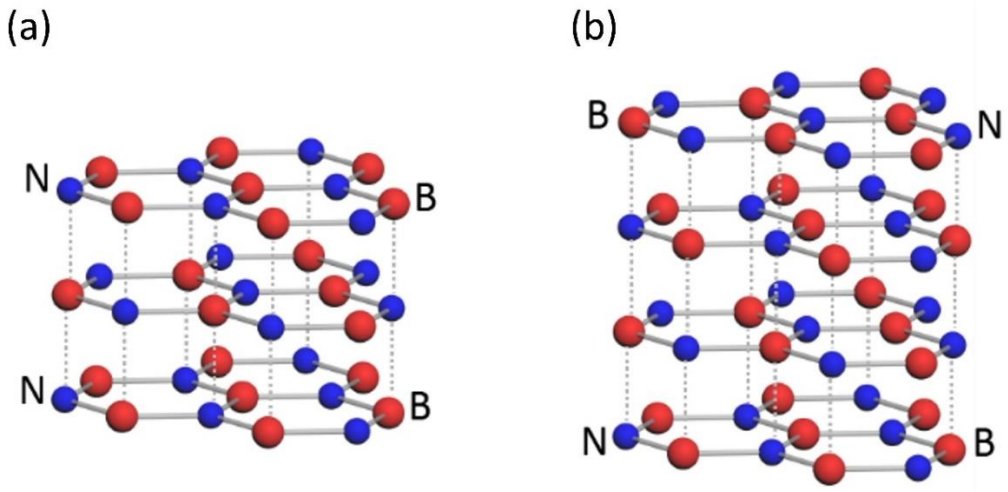

Figure 3-1 Atomic structure of hBN. *(a) hBN with odd numbers of layers. (b) hBN with even numbers of layers. The stacking order is AA'. The structure has been scaled to see the layer parity in crystal symmetry clearly.*

Hexagonal boron nitride has been a fundamental building block for vdH heterostructures. It protects air-sensitive 2D materials, such as black phosphorus and niobium di-selenium ($NbSe_2$)[102,103], against degradation caused by exposure to air. It also proves to be an exceptional substrate for graphene because of the following features. First, hBN is a relatively inert wide-gap (bandgap of around 6 eV) semiconductor[95,96], as a result of the asymmetry between the potential energies of the A and B sublattice sites, thus hBN can also serve as a gate dielectric. Second, the weak van der Waals interaction between layers allows easy exfoliation of hBN crystals, even down to a-few-nanometers-thick flakes with atomically flat surfaces[97]. Such an ultra-flat surface avoids detrimental rippling in graphene that can easily occur since graphene tends to conform to its substrate[20]. Third, the strong in-plane B-N bond of hBN is polar covalent, leaving the surface free of dangling bonds and charge traps[97,98]. As a result, encapsulated hBN/graphene/hBN heterostructure devices show unprecedented performance in graphene with high mobility roughly one order of magnitude larger than that of the best devices on SiO_2 [20,104]. Crucially, the encapsulation by hBN also enables ballistic transport of electrons in graphene at cryogenic temperatures, with an electronic mean free path limited by device size (typically <20 μm) rather than impurity scattering [104,105].

3.1.2 Moiré Superlattice

Moiré patterns are large-scale interference patterns generated by superimposing similar templates with slight displacement, rotation or pitch. Since graphene and hBN share similar lattice structures with a small lattice mismatch, a small relative rotation between the layers (which can be introduced in the heterostructure fabrication procedure) will lead to the formation of a moiré superlattice at the graphene/hBN interface. In the reciprocal space, the wavevector of the resultant moiré superlattice $\boldsymbol{\kappa}$ is given by the difference between the wave vectors of the two lattices (**Figure 3-2a**):

$$\boldsymbol{\kappa} = \mathbf{k}_2 - \mathbf{k}_1 . \tag{3.2}$$

Therefore, the absolute value of $\boldsymbol{\kappa}$ is derived by:

$$|\boldsymbol{\kappa}| = \sqrt{k_1^2 + k_2^2 - 2k_1 k_2 \cos\theta} . \tag{3.3}$$

Since the wavevectors can be expressed through the corresponding periods $\mathbf{k}_{1,2} = \frac{2\pi}{\lambda_{1,2}}$, $\boldsymbol{\kappa} = \frac{2\pi}{\lambda_m}$, we have:

$$\lambda_m = \frac{\lambda_1 \lambda_2}{\sqrt{\lambda_1^2 + \lambda_2^2 - 2\lambda_1 \lambda_2 \cos\theta}} , \tag{3.4}$$

or

$$\lambda_M = \frac{\lambda_1 (1+\delta)}{\sqrt{2(1+\delta)(1-\cos\theta) + \delta^2}} , \tag{3.5}$$

where δ is the lattice mismatch between two lattices. The relative rotation angle φ of the moiré pattern with respect to the $\mathbf{k}_1$ lattice can be found using the sine rule $|\boldsymbol{\kappa}| \sin\varphi = |\mathbf{k}_2| \sin\theta$, so φ is given by:

$$\tan\varphi = \frac{\sin\theta}{(1+\delta) - \cos\theta} \tag{3.6}$$

For the graphene/hBN interface, if graphene is aligned with hBN ($\theta = 0^\circ$), there still exists a moiré pattern since the lattice mismatch ($\delta \approx 1.8\%$) is nonzero. The corresponding wavelength is the maximum, approximately 14 nm. Plots of the period and the relative rotation angle φ of the moiré pattern as functions of the twist angle θ are shown in **Figure 3-2b**.

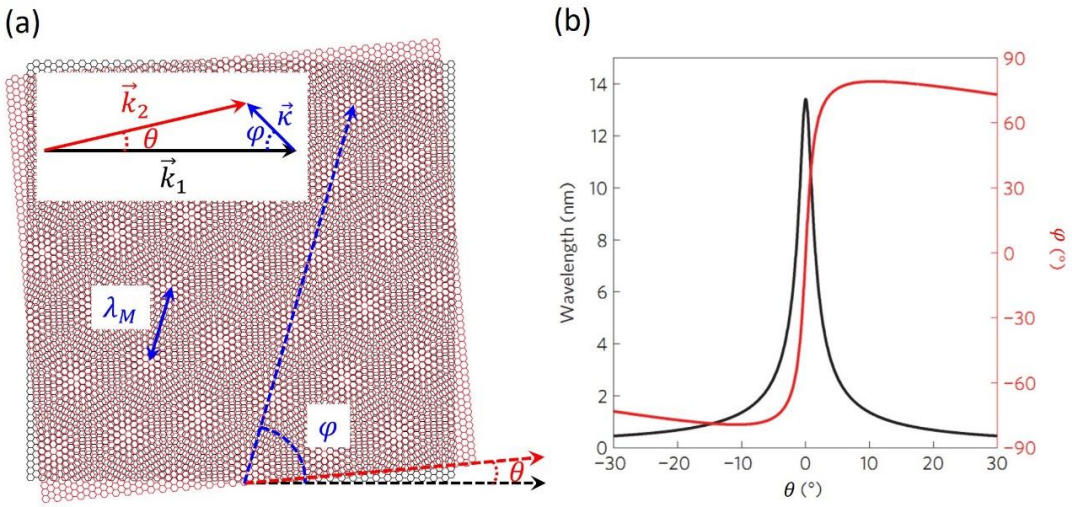

Figure 3-2 Illustration of moiré pattern formed at the graphene/hBN interface. *(a) Illustration of the moiré pattern. The top inset shows reciprocal lattice vectors for graphene (black), hBN (red), and the moiré pattern (blue), respectively. θ is the twist angle between graphene and hBN lattices. φ indicates the orientation of the moiré pattern with respect to graphene. (b) Superlattice wavelength (black) and relative rotation angle φ (red) as a function of the twist angle θ between graphene and hBN lattices, modified from ref [92].*

3.1.3 Van der Waals forces

In inert gases and also many organic molecules, there exists a straightforward electrostatic interaction between the atoms, i.e. the vdW interaction, which arises from the dipole-dipole interaction[106,107]. The dipoles are either permanent or induced, resulting in three types of contributions to van der Waals forces:

- **Keesom forces**, or the orientation interaction, is a Boltzmann-averaged interaction between two freely rotating permanent dipoles over all orientations. The strength of the interaction depends on the relative orientation between the two dipoles and the maximum attraction occurs when the two dipoles are in line. This is a polar interaction
- **Debye forces**, or the induction interaction, where a permanent dipole leads to polarization of a nearby molecule, inducing a dipole in this nearby molecule. The permanent dipole and induced dipole are mutually attracted in a polar interaction.
- **London dispersion forces**, or the induced dipole-dipole interaction, is the interaction between the dipoles induced by the instantaneous electric fields generated by fluctuations in the electron distribution around an atom or molecule. The London forces contribute to the most important part of the total vdW forces and are responsible for phenomena such as adhesion, surface tension and physical adsorption, etc.

In the model of the interaction (described by potential energy $w(r)$) between two atoms/molecules separated by r, we only consider the London dispersion forces since they are the most significant parts of vdW forces. When r is large, the London forces contribute to the interaction energy since they are long-range forces. We have:

$$w(r) = -\frac{A}{r^6} \tag{3.7}$$

and when r is small, the charge distributions of the atoms/molecules will overlap and the electrostatic energy of the system is therefore changed. At sufficiently small r, the energy overlap is repulsive, in large part because of the Pauli exclusion principle. The $w(r)$ can be described by an empirical repulsive potential:

$$w(r) = \frac{B}{r^{12}} \tag{3.8}$$

The total potential energy of the system is thus expressed as:

$$w(r) = 4\varepsilon\left[\left(\frac{\sigma}{r}\right)^{12} - \left(\frac{\sigma}{r}\right)^{6}\right] \tag{3.9}$$

where $4\varepsilon\sigma^6 = A$, $4\varepsilon\sigma^{12} = B$, A and B are empirical parameters. Equation (3.9) is known as the Lennard-Janes potential (**Figure 3-3**). By integrating the energies of all the atoms over two interacting bodies, one can obtain the "two-body" potential for an atom near a surface, based on the interatomic vdW pair potential of the form

$$w(r) = -\frac{C}{r^6} \tag{3.10}$$

in which C describes the strength of particle-particle pair interaction, and can be determined by the Hamaker constant H_m:

$$H_m = \pi^2 C \rho_1 \rho_2 \tag{3.11}$$

where $\rho_{1,2}$ are the atomic densities in the respective materials. The resulting vdW interaction potential w and the vdW force F between two flat surfaces are then given by:

$$w = -H_m / 12\pi d^2 \tag{3.12}$$

$$F = -H_m / 6\pi d^3 \tag{3.13}$$

where d is the separation between two surfaces.

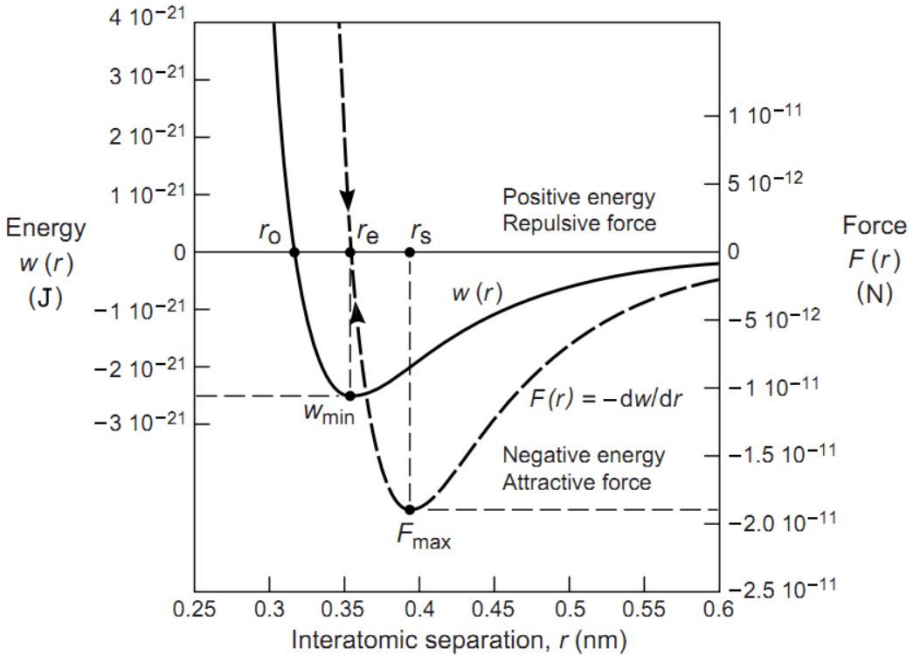

Figure 3-3 Lennard-Janes potential function $w(r)$ ***and force function*** $F(r) = -dw/dr$ ***of two inert gas atoms.*** *The separation* r_e *is the equilibrium separation, where the force is zero and the energy is at the minimum. The separation* r_s *is the point at which the two atoms are separated from* r_s *when pulled apart by the force* F_{max} *. Taken from ref [106].*

3.2 Nanomechanics

The weak van der Waals forces between the atomic planes in 2D materials make it possible to slide or rotate the vdW heterostructures in situ, which allows further modification of the vdW heterostructures after assembly. Such nanomechanical manipulation of vdW heterostructures is based on the extremely low friction or 'superlubricity' when the two contacting 2D layers are stacked with a relative twist to form an incommensurate interface. Understanding the nanotribological phenomena is the key to the application of vdW heterostructures in device engineering, nanomotors, moveable components in micro-electro-mechanical systems, and research of twistronics, etc.

In this section, we introduce the origin of friction and adhesion forces that dominate the sliding of two interfaces. We also present two models, i.e. the Prandtl-Tomlinson model and the Frenkel-Kontorova model, which describe the relative motion of two interfaces and how the friction force is influenced within the two models. The in situ manipulation of 2D layers in the vdW heterostructure discussed in **Chapter 7** is based on the relative motion mechanism of two interfaces demonstrated by these two models.

3.2.1 Origin of friction and adhesion forces

Frictional forces arise as a reaction to motion or another force and are one type of energy dissipating forces associated with the transfer of mechanical, potential, or kinetic energy to heat. The energy transfer process happens through the collision between atoms which interact with each other through the Lennard-Jones potential. In a vdW heterostructure, when the 2D materials are subjected to continuing normal and lateral forces which allow for off-axis collisions (**Figure 3-4**), the friction force is given by:

$$F_r = \mu F_\perp + \sigma A \tag{3.14}$$

where $F_\perp$ is the external normal force, μ is the static friction coefficient, S is the contact area between the 2D layers defined by the number of atoms within the range of interatomic forces, and σ is the shear stress. In Eq (3.14), the first term is a lateral force needed to initiate lateral motion, which is the load-controlled contribution and is proportional to the load. The second term is the adhesion-controlled contribution which represents the force to overcome the interlayer adhesion. It is proportional to the number of bonds broken when the top layer moves laterally by a distance of x across the bottom layer. In the case of lateral displacement, since the interface between the layers is not mathematically flat, the top layer will rise by a distance d from the initial position (**Figure 3-4**), a phenomenon called dilation, which happens when relative motion is induced in a system initially at rest. When the motion continues, the friction coefficient will be the kinetic coefficient, which is smaller than the static coefficient. Energy dissipation happens when a fraction $\varepsilon (0 < \varepsilon < 1)$ of the kinetic energy of the atoms in the moving 2D layer transfers to the bottom layer.

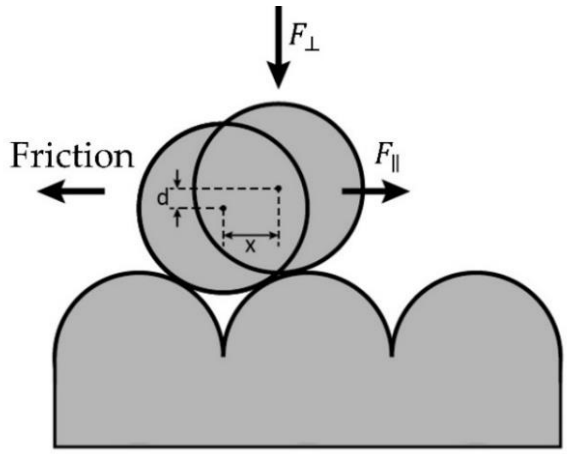

Figure 3-4 Schematic showing the origin of the friction. *When subjected to a lateral force $F_\parallel$, the top atom or molecule needs to rise by a distance d when it moves laterally by a distance of x across the bottom surface.*

Frictional and adhesion forces are qualitatively different. The frictional force is sensitive to the topography of the material surface whereas the adhesion force is not. The adhesion force comes from the vdW forces between the 2D material layers. Whether the surface is flat or not does not change the adhesion energy required to separate the 2D layers from each other. In contrast, the surface topography determines the finite dilation d in the lateral motion, thus changing the shear strength of an interface. If the interface between the materials was mathematically flat, the dilation would be zero and no energy would be dissipated in the lateral motion. As a result, the friction force would be zero even if the adhesion force is high.

3.2.2 Prandtl-Tomlinson model

The Prandtl-Tomlinson (PT) model describes the nonuniform relative motion between two surfaces. In the simplified PT model, a point mass m (e.g., the AFM tip) is subjected to a one-dimensional sinusoidal potential, and simultaneously it is attached to a spring whose potential energy function is a parabola. The total potential experienced by the point mass is:

$$U(x,t) = U_0 \cos\left(\frac{2\pi}{a}x\right) + \frac{K}{2}(x - vt)^2 \tag{3.15}$$

where U_0 is the amplitude and a is the periodicity of the substrate potential, K is the effective elastic constant of the spring which arises from the lateral stiffness of the contact between the two surfaces, and v is the constant velocity driven by the external force. The total potential energy is shown by the wavy curve in **Figure 3-5b**.

There are two modes for the point mass motion, i.e. the stick and slip motion modes. Initially, at time t = 0, the point mass rests at a potential energy minimum. When the driver starts moving with velocity v, the point mass is subjected to the wavy potential curve (**Figure 3-5b**). The friction force keeps increasing when the point mass is stuck to the potential minimum. At some critical point where the spring force equals the maximum friction force, the local potential minimum becomes a stationary point and the point mass starts to "slip" to another potential energy minimum (**Figure 3-5b**), where the friction force suddenly decreases, leading to a sawtooth-like evolution (**Figure 3-5c**). The critical point corresponds to the changeover where $d^2U/dx^2 = 0$ and $dU/dx = 0$, and it depends on the potential corrugation U_0 and the lateral contact stiffness K, both of which are influenced by many factors such as the normal load on the contact, the substrate material, etc. The stick-slip motion corresponds to jumps of the point mass between successive minima of U, which is the most common origin of non-uniform friction and the main energy dissipation channel.

Such a phenomenon is commonly seen in the tip-sample relative motion in the measurement of friction forces using friction force microscopy (FFM), as shown in **Figure 3-5c**.

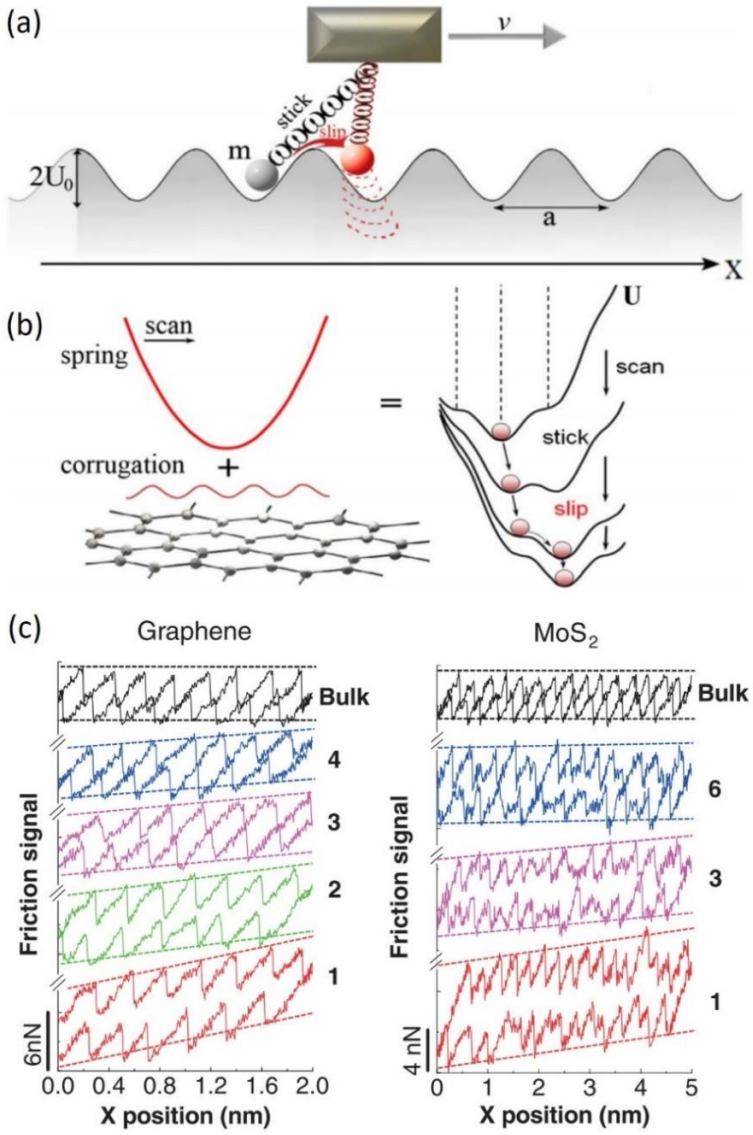

Figure 3-5 Illustration of stick-slip motion in Prandtl-Tomlinson model. *(a)Schematic of PT model. (b) The total potential landscape, which is comprised of harmonic spring and sinusoidal substrate potential, exhibits different metastable minima, giving rise to stick-slip behaviour. Taken from ref [108]. (c) Friction force traces showing typical stick-slip behaviour of graphene and MoS_2 with different thicknesses measured by FFM. Taken from ref [109].*

3.2.3 Frenkel-Kontorova model

As discussed in **Section 3.2.2**, the stick-slip motion of the probing tip in FFM measurement can be well described by the PT model, where the tip is atomically sharp with a radius less than 10 nm and therefore it can be approximated by only one atom. However in systems where a periodic surface slide on another periodic surface, the role of commensurability becomes essential and these systems can be described by a more universal model, the Frenkel-Kontorova (FK) model. The one-dimensional (1D) FK model describes a one-

dimensional chain of classical particles modified by background sinusoidal potential (**Figure 3-6a**), which can be applied to modelling the structure and dynamics of crystal lattices with competing incommensurate spatial periodicities[108,110,111]. The standard Hamiltonian for the FK model is:

$$H=\sum_i\left[\frac{p_i^2}{2m}+\frac{K}{2}\left(x_{i+1}-x_i-a_A\right)^2+\frac{U_0}{2}\cos\frac{2\pi x_i}{a_s}\right] \tag{3.16}$$

where the first term is the kinetic energy of the chain, the second term is the harmonic interaction between the nearest neighbours of the chain with elastic constant K and equilibrium distance (a_A) of the inter-particle potential ($V_{\text{int}}(x)$), and the last term is the interaction of the chain with the external periodic potential ($V_{sub}(x)$) of magnitude U_0 and periodicity a_s. The FK model is inherently discrete and nonintegrable. In the continuum approximation, it can be reduced to an integrable sine-Gordon (SG) equation, which is a fundamental nonlinear model. The solutions of the SG equation are in the form of nonlinear excitations, namely phonons, kinks (topological solitons, which appear due to an inherent degeneracy of the system ground state), and breathers (dynamical solitons).

In the FK model, kinks (antikinks) corresponding to extra atoms (vacancies) are responsible for the physical characteristics of the one-dimensional chain (**Figure 3-6c** and **d**). The motion of kinks is strongly affected by the discreteness-induced Peierls-Nabarro periodic potential (E_{PN}), which is the smallest energy barrier that the kink should overcome in order to start moving in the lattice, determined by the potential energy difference between two stationary configurations of kinks, the stable and unstable ones. The energy barrier E_{PN} is always smaller or much smaller than the amplitude U_0 of the substrate potential, therefore the mass transport along the chain is mainly through kink motion.

In the FK chain, the competition between the substrate potential and the interatomic interaction between the atoms results in the relaxation of the atoms into a configuration which exhibits two distinct types of phases, that is the commensurate (C-phase, also crystalline phase) and incommensurate (IC-phase). Generally, $a_A \neq a_s$, while at the trivial commensurate ground state (GS) of an FK chain, each minimum of the substrate potential is occupied by one particle and a_A equals to a_s (**Figure 3-6b**). In the case of an infinite FK chain where the length L and the number of atoms N tend to infinity, the equilibrium means spacing between the atoms in the chain $a_A = L/N$. It is useful to introduce the following parameter:

- **Dimensionless kink concentration** ϑ, or the coverage parameter, determined by $\vartheta = a_s / a_A$.

There are two distinct situations of the FK chain, the 'fixed-density' and the 'free-end' chains. For 'free-end' chains, L is not fixed and is of open-end boundary condition. An example of 'free-end' chains is the FK system where the substrate is in contact with a 'vapour phase' chains so that the number of atoms N is not fixed. For 'fixed-density' chain, L and N are fixed and it is of fixed boundary condition. Here only the 'fixed-density' chain is considered because it fits for vdW heterostructures. For rational concentration ϑ ($\vartheta = s/q$, with s and q being relative prime), the GS configuration of the chain is C-phase with the period $qa_s = sa_A$ and there are s atoms per unit cell of the commensurate configuration. The nonlinear kink excitations (or antikinks, the topological solitons) are topologically stable in the commensurate configuration owing to fixed boundary condition but do not exist in IC configuration. The kinks (or antikinks) link two commensurate ground states in the infinite FK chain, which realize the minimal contraction (extension) of the commensurate configuration. Kinks are localized quasi-particles that can move along the chain and any equivalent FK configurations can be obtained through kink motion (**Figure 3-6c** and **d**).

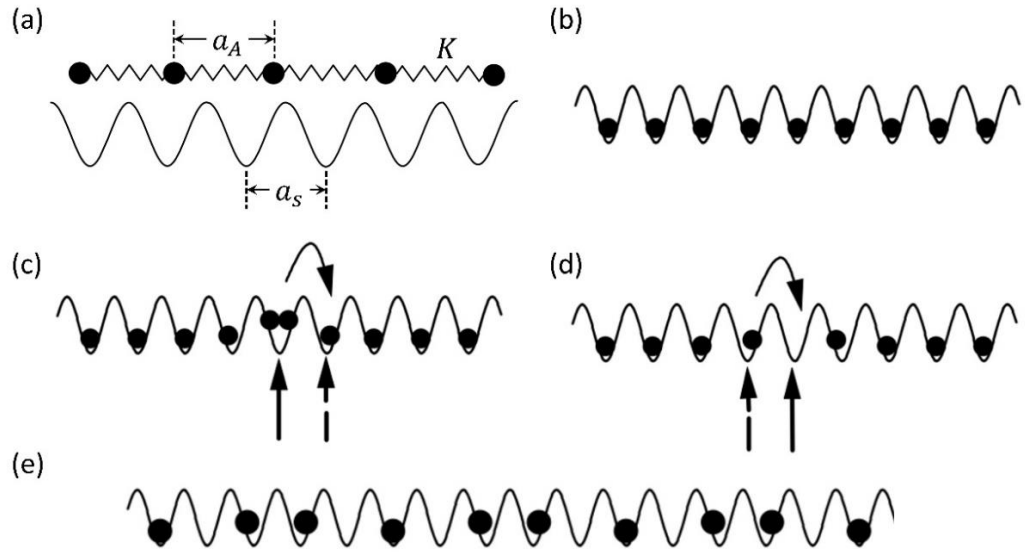

Figure 3-6 Schematic of the Frenkel-Kontorova model. *(a) A chain of particles interacting via harmonic springs with elastic constant K is subjected to an external periodic potential with period a_s. (b) Configuration of trivial commensurate ground state, with $\vartheta = 1$. (c,d), Kink and antikink in a commensurate structure with $\vartheta = 1$. The arc arrow indicates the motion of the kink (antikink). Solid (dashed) arrow shows the displacement of an atom to the right before (after) the kink motion. (e) Configuration of a commensurate structure with $\vartheta = 3/5$. Taken from ref [110].*

For irrational concentration ϑ, the GS configuration of the system is IC-phase. For the discrete FK chain with strictly convex potential, the incommensurate GS can be described by the hull function. If the elastic constant K is above a certain critical value $K_{Aubry}(\vartheta)$, the hull function is continuous and the motion of incommensurate GS is "frictionless" (or superlubrication)[112], which means that the chain can be moved freely when a small force is applied to each atom. In this case, the interactions between atoms in the chain dominate over substrate potential and some of the atoms may occupy the substrate potential maxima. When the atomic chain is translated over the substrate, some atoms go down in the potential while others go up. There exist no barriers to the translation of the chain and the system exhibits superlubricity. Alternatively, to understand the superlubricity in the motion of incommensurate GS, the IC-phase can be considered as the limit of a sequence of C-phases in the infinite FK chain. The motion of the IC-phase can thus be regarded as the motion of a single kink with the width tending towards infinity and E_{PN} tending towards zero in the sequence of C-phases.

In contrast, if the elastic constant K is smaller than $K_{Aubry}(\vartheta)$, the hull function becomes discontinuous and consists of discrete incommensurate structures, forming the devil's staircase [111,112] which could be either complete or incomplete. Such a transition of hull function by the breaking of analyticity is the Aubry transition. For the incomplete devil's staircase where there are IC-phases between the C-phases, the atoms in the chain need to cross the discontinuity of the hull function and go over the maxima of the $V_{sub}(x)$ for the chain motion. Thus the incommensurate GS is pinned by the substrate potential and the atoms tend to stay near the potential minima. A nonzero depinning force must be applied so that the atoms can be moved over the potential maxima, which is expected to be stick-slip motion as described in **Section 3.2.2**. For the complete devil's staircase, C-phase fills up the whole range of the hull function and the GS of the system is at C-phase.

3.2.4 Applications of Frenkel-Kontorova model

The FK model is one of the most fundamental and universal tools of low-dimensional nonlinear physics and can be generalized to two-dimensional systems. The difference between the 2D model and the 1D model lies in the motion of atoms in all directions for the 2D model and the construction of the 2D potential[110]. The 2D FK model can be applied to explain the reconstruction of 2D material interfaces with matched lattice periods, the formation of stacking faults in graphite crystal, and superlubricity at incommensurate interfaces, etc, since 2D materials have perfectly rigid crystalline structures, and provide

periodic potential as well as discrete lattice array which plays the role of effective atoms in the FK model.

3.2.4.1 Superlubricity

In this section, we discuss superlubricity, which is the underlying mechanism of the phenomena that 2D materials can rotate or slide freely in the vdW heterostructures as described in **Chapter 7**. The definition of superlubricity is that the kinetic friction coefficient, defined as the local derivative of the friction force with respect to the applied normal load, should be below 10^{-3}. Superlubricity has been observed in incommensurate interfaces, such as the sliding of graphene nano-flakes on a graphene surface at incommensurate state[43,113], on gold surfaces[44], on the diamond like carbon coated counterface (with the friction coefficient of ~0.004)[114] and on hexagonal boron nitride surface (**Figure 3-7a** and **b**)[115]. It also exists in two incommensurately stacked single layers of MoS_2 (with the friction coefficient in the range of 0.8×10^{-4}-2.6×10^{-4})[116]. These rigid crystalline interfaces normally exhibit rotational frictional anisotropy with the symmetry consistent with that of the crystal lattices. The frictional anisotropy displays the rotational transition from incommensurate state to commensurate state, where the two contacted surfaces can be locked or characterized by pronounced stick-slip motion (**Figure 3-7b**). The extent of the frictional anisotropy depends on the intrinsic lattice constant misfit of the two surfaces (**Figure 3-7b** and **c**). Such phenomena can be well understood by the Aubry transition in the incommensurate case as discussed in **Section 3.2.3**.

Even though the incommensurability of two periodic interfaces cancels the lateral forces so that the friction force is substantially reduced, it only cancels one energy dissipation channel which comes from the low-speed stick-slip instability. Other energy dissipation channels, such as the linear waves (phonons) generated by the kink motion[110], still exist, so the friction force does not vanish in the superlubric regime.

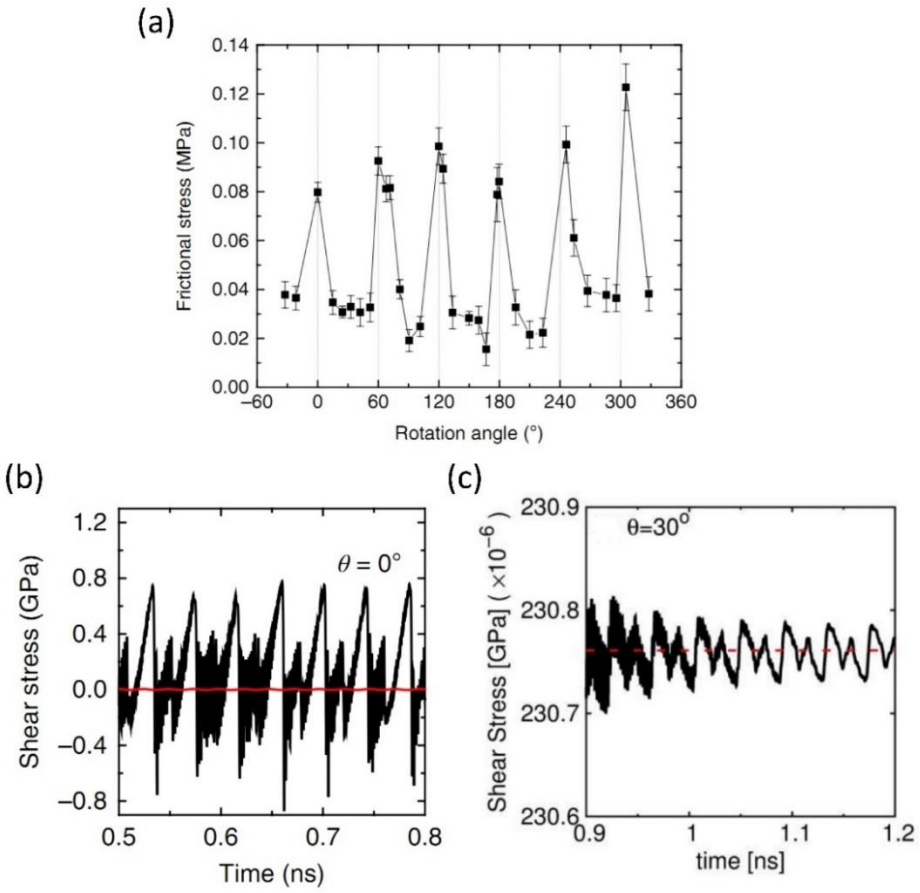

Figure 3-7 Friction traces in different heterostructures. *(a) Dependence of the frictional stress on the relative rotation angle between graphite and hBN surfaces measured under ambient conditions. (b) Simulated friction traces in the aligned graphene/hBN interface (red line) and graphene/graphene interface (black line). (c) Simulated friction traces in misaligned (θ=30°) graphene/graphene interface. The red dashed line is the average kinetic frictional-stress. Taken from ref [115].*

3.2.4.2 Dislocations

In this section, we discuss dislocations, of which the motion leads to the formation of stacking faults and deformation in graphite crystal, as well as the structural reconstruction of twist graphene layers and graphene/hBN interface in the small twist regime. As discussed in **Section 3.2.3**, in the FK model, kink motion plays an important role in the mass transport of the system. In the 1D FK model, kinks are 1D topological solitons. In the 2D FK model, the kinks could be either edge or screw type. Kinks reaction results in the formation of dislocations or domain walls [110]. Depending on the type of kinks, the dislocation may be either edge or screw types, the former is similar to the domain wall. Dislocation is characterized by the topological invariant, Burgers vector **b** and the tangent vector **t** [117]. The tangent vector **t** is a unit vector that points along the dislocation line, defining the line sense. The mathematical definition of Burgers vector **b** is given by the line integral of the elastic displacement **u**:

$$\mathbf{b} = \oint_C \frac{\partial \mathbf{u}}{\partial l} dl \,, \tag{3.17}$$

where the closed contour C is defined in a right-hand sense around $\mathbf{t}$ (**Figure 3-8a**). The Burgers vector $\mathbf{b}$ reflects the magnitude and displacement direction of the crystalline lattice distortion in dislocations which could be viewed as a stacking-fault ribbon with the width of $|\mathbf{b}|$. Screw dislocation has $\mathbf{b} \cdot \mathbf{t} = \pm b$, where the ± represents the right-handed and left-handed sense, respectively. Screw dislocation only involves shear strain (left panel of **Figure 3-8c**). Whereas for edge dislocation, $\mathbf{b} \cdot \mathbf{t} = 0$ and it only involves tensile strain (right panel of **Figure 3-8c**). In a general case, a dislocation has both edge and screw components.

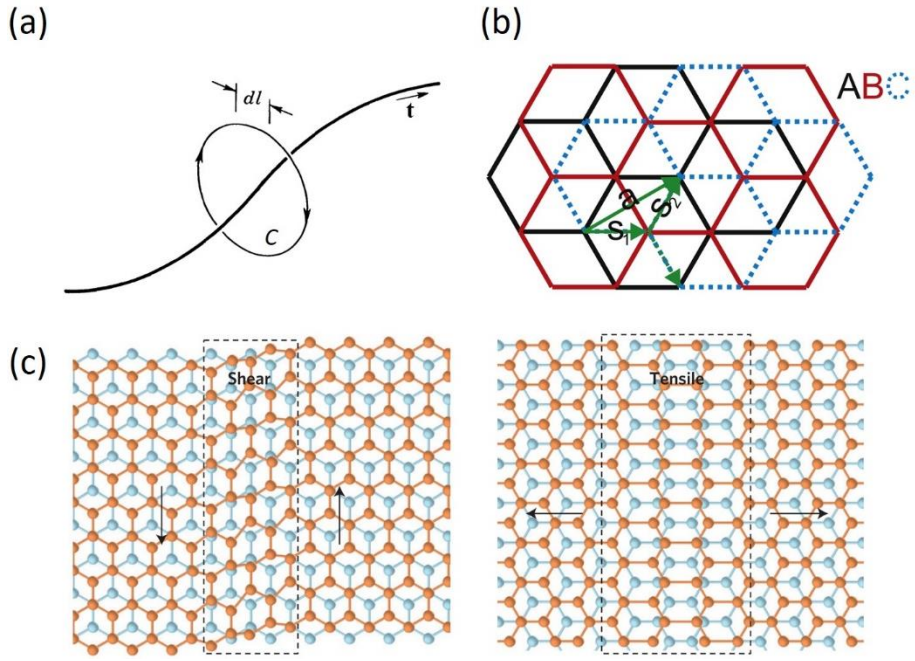

Figure 3-8 Schematic of the Burgers vector and dislocations. *(a) Schematic showing the definition of Burgers vector. Modified from ref [117]. (b) Atomic structure of ABC stacked trilayer graphene with the three layers coloured differently and the Burgers vectors of dislocations. The dislocation labelled 'a' can be dissociated into two Shockley partial dislocations labelled by 'S1' and 'S2'. A partial dislocation can transform the ABC stacking into ABA stacking. The third possible direction of a partial dislocation is shown by the dashed green arrow. Taken from ref [118]. (c) Schematics of the screw (left) and edge (right) dislocations. The dashed lines outline the dislocation region through which the AB-stacking region smoothly transits to the BA-stacking region. In screw dislocation which only involves shear strain, the Burgers vector* $\mathbf{b}$ *(indicated by the arrows) is parallel with the tangent vector* $\mathbf{t}$ *(parallel with the dislocation). In edge dislocation which only involves tensile strain, the Burgers vector* $\mathbf{b}$ *is perpendicular to the tangent vector* $\mathbf{t}$*. Taken from ref [119].*

Theory of dislocation well explains the formation of stacking faults and deformation in graphite[118], as well as atomic reconstruction at the interface of two crystals with small lattice misfit[120,121]. For layered materials such as graphite, dislocation movement is mainly restricted to the basal plane since it has weak interlayer interaction. In graphite, the Burgers vector with

the smallest $|\mathbf{b}|$ connecting two crystallographically equivalent structures is the translation of the atomic layer with one lattice constant length along the zigzag direction (or $<11\bar{2}0>$ direction)[122], as shown in **Figure 3-8b**. Such a perfect basal-plane dislocation can be dissociated into pairs of energetically more favourable Shockley partial dislocations (partials), which are the along armchair direction (or $<10\bar{1}0>$ direction) [122], as shown in **Figure 3-8b**. For trilayer graphene, single partials can directly cause a change in the stacking order transition from Bernal stacking to rhombohedral stacking (ABA↔ABC) [119,123,124]. Thereby in graphite, the existence of partials can result in stacking faults[125]. This could explain the emergence of the domains of different stacking order observed in exfoliated graphite flakes in **Chapter 5**. Shifting of graphene layers caused by the external mechanical stress during flake exfoliation leads to large amounts of dislocations in the graphite basal plane, thus resulting in the formation of these stacking domains. If the dislocations are arranged in a periodic array, they will form grain boundaries at the interfaces of grains with different crystallographic orientations[126], such as twin boundary, where the grains on each side of the interface are of mirror symmetry[127]. The folds, bends and kink bands that appear in exfoliated graphite films are all associated with dislocation movement when graphite is under stress [125,128].

For twisted vdW heterostructure systems such as twisted bilayer graphene (TBG) where there exist rotational misfit between the crystals, the lattice will undergo structural reconstruction when the twist angle is below a certain crossover value[120,121], due to the balance between interlayer commensurability and intralayer lattice distortion [129-131]. When the twist angle is below 1° [120], the lattice of TBG will relax into alternating AB/BA stacking domains separated by a triangular network of line (saddle point,SP) solitons joint by the point (AA stacking) solitons [132,133] (**Figure 3-9a** and **b**). These stacking domain walls prove to be partial dislocations with three different directions $<10\bar{1}0>$ [134-136], of which the crossing points are the nodes corresponding to AA stacking. For graphene/hBN interface, due to a small lattice mismatch between graphene and hBN, the lattice relaxation also happens when the twist angle is small, however, it reconstructs into a structure of a hexagonal network of dislocations with both screw and edge components[137,138] (**Figure 3-9c** and **d**). The graphene lattice tends to relax toward an hBN lattice and the AB stacking regions where carbon (C) atoms are located above the boron (B) atoms is the most energetically favourable configuration compared to the BA or AA stacking regions[138,139], thus the AB stacking region increases its size in the structural relaxation and AB stacking is at the center of the hexagonal moiré pattern.

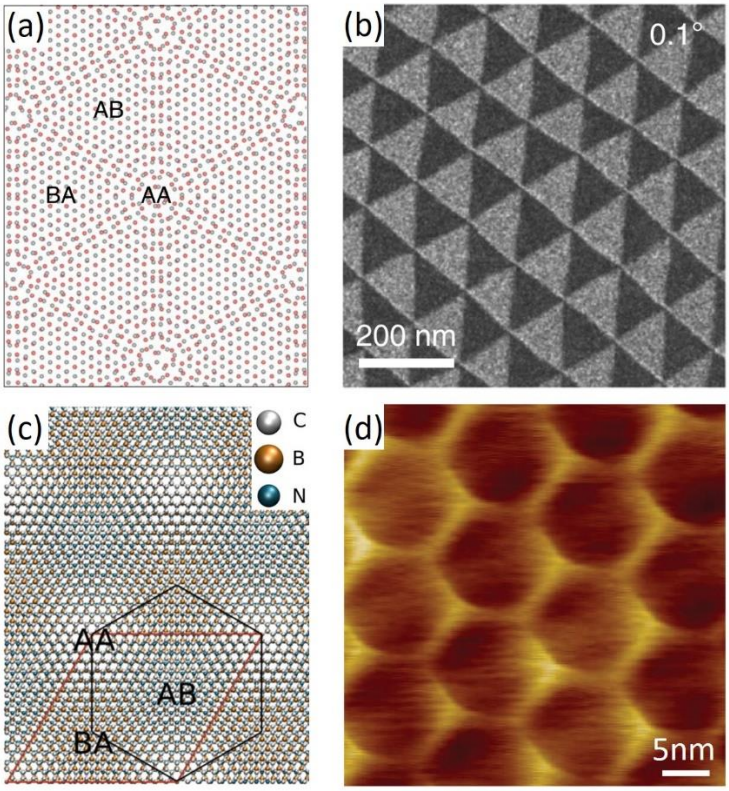

Figure 3-9 Structural reconstruction of TBG and graphene/hBN interface. *(a) Atomic structure of TBG after lattice relaxation. (b) Transmission electron microscopy dark-field image obtained by selecting the graphene diffraction peak (*$\mathbf{g}=[10\bar{1}0]$*) in TBG with the twist angle of 0.1°, showing the triangular network in the TBG moiré superlattice. (a) and (b) are taken from ref [120]. (c) Atomic structure of graphene/hBN moiré superlattice. The supercell is highlighted by red and the moiré pattern by black. Taken from ref [139]. (d) Scanning tunnelling microscope (STM) topography image showing the graphene/hBN moiré superlattice with a hexagonal network. Taken from ref [92].*

3.3 Assembly

Two-dimensional crystals can be assembled into heterostructures by van der Waals forces. Efforts have been dedicated to devising creative solutions to van der Waals assembly and improving device qualities. The well-developed assembly techniques can be classified as wet and dry transfer methods, which are used under different circumstances. The wet transfer technique involves the procedures where 2D layers are in direct contact with the solvents for dissolving the substrates that hold the materials; this method is common for transferring synthesised 2D layers. In contrast, the dry transfer method avoids direct contact between 2D layers and solutions; this method is commonly used for transferring mechanically exfoliated crystals. Here, we focus only on dry transfer methods since wet transfer potentially introduces contaminations to van der Waals heterostructures and thus degrades the device properties.

3.3.1 Crystal exfoliation

Mechanical exfoliation of 2D materials flourished since 2004 with Andre Geim and Konstantin Novoselov's work[140], in which graphene was first isolated and tested using SCOTCH tape. The technique is primitive but effective because of its evident simplicity: the crystals are pealed several times using tapes until a reasonable coverage is achieved. Then the piece of tape with the remaining flakes is pressed firmly and evenly onto a Si substrate (usually with an oxide layer of 90 or 290 nm thick) which is pre-heated. There are several factors that are critical to obtaining clean flakes with required thickness, area and even specific stacking order:

First, the type of tapes. The adhesive layers of different tapes mainly differ in the adhesion strength and the number of polymer residues remaining on the exfoliated crystals and substrates. Different tapes are appropriate for different 2D materials due to the strength of their interlayer interaction. The frequently used tapes include SCOTCH tape, NITTO DENKO tapes of BT-150E-CM, BT-130E-SL and BT-150E-KL type, etc. According to the exfoliation of thousands of flakes with different tapes, together with the experience from other colleagues, I summarized the comparison of different tapes regarding their exfoliation effectiveness, as shown in **Table 3-1**.

Table 3-1 Comparison among different tapes for crystal exfoliation*.

Tapes	Adhesion strength	Residues on substrate	Flakes on substrate	Cleanness of flakes	Suitable 2D materials
Scotch tape	★★★★	★★★	★★★★	★★★	Graphene
BT-150E-CM	★★★	★★	★★★	★★★	Graphene and hBN
BT-130E-SL	★★★	★★	★★★	★★★	hBN
BT-150E-KL	★★★★★	★	★	★★★★	TMDCs

**The numbers of symbol ★ indicate the degree or amount in each column.*

Second, the exfoliation times of the crystal. Ideally, 10 times bifurcation would reduce the thickness of the crystal down to a few nanometers. However, in practice, too many peeling attempts will not only smash the crystals into flakes with a size smaller than a few microns but also contaminate the crystal surface with the adhesive polymer residues. The key to obtaining thin and large 2D layers on a substrate is to leave shiny and fresh surfaces of the crystals exposed to the substrate (**Figure 3-10**).

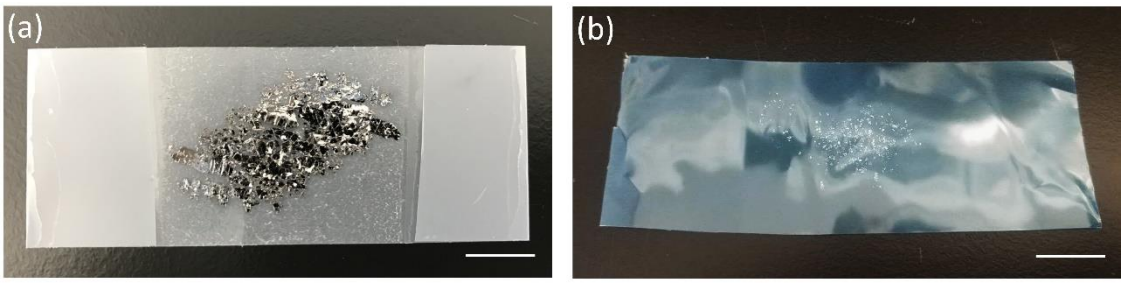

Figure 3-10 Crystals exfoliated on tapes. *(a) Graphite crystals exfoliated on Scotch tape. (b) hBN crystals exfoliated on BT-130E-SL tape. The scale bars are 1cm.*

Third, the pre-heating temperature of the Si substrate. Pre-heating of Si substrate higher than 150 °C for more than 10 minutes can efficiently remove the adsorbed water molecules on the substrate and somehow increase the adhesion between the crystals and the substrate. The thickness, size and amount of the flakes on the substrate depend on the balance between the adhesion at the tape/crystal surface, crystal/substrate surface and interlayer interaction strength of the crystals. To further increase the adhesion at the crystal/substrate surface, the Si substrate can be pre-cleaned by oxygen plasma.

Among the exfoliated graphite flakes, we found that 176 out of 617 flakes contained ABC-stacked regions (29%), as mentioned in **Chapter 5**. Both SCOTCH tape and NITTO DENKO tape of BT-150E-CM type worked well in yielding graphite flakes containing ABC stacking. Interestingly, when the SCOTCH tape is used, the obtained flakes with ABC-stacked regions normally contained different stacking domains, probably due to stronger adhesion strength which favoured relative movement of the graphene layers and thus caused stacking transition.

3.3.2 Flake selection

The initial selection of flakes on SiO_2/Si substrate is mainly based on the flake thickness, geometry and cleanness using reflected light optical microscopy (Nikon Eclipse Lv150 series with DS-Ri2 Camera).

The flake thickness is determined by the optical contrast (**Figure 3-11a** and **c**), which is generated by the interference of the incident light and the light reflected at the interfaces of air/flake, flake/SiO_2, and SiO_2/Si. The SiO_2 thickness of 90nm or 290 nm gives good optical contrast for graphene[141], whereas a few-layer hBN flake is hardly visible on 290 nm SiO_2 but visible on 85 nm SiO_2[142]. For particular transfer processes where flakes need to be exfoliated on a spin-coated polymer layer on SiO_2/Si substrate, the optical contrast of flakes will be changed. In this case, using narrow band pass filters of different ranges could enhance the contrast of the flakes.

For certain devices, specific flake geometries may be needed. The crystallographic alignment between graphene and hBN is an example of this. In this case, graphene flakes with angles between adjacent straight edges being multiples of 30° are selected for crystalline alignment. Such edges normally take either zigzag or armchair structures, which indicate the crystalline orientation of graphene flakes[143]. If the angle between adjacent edges is 60° or 120°, both edges have the same chirality, either armchair (AC) or zigzag (ZZ). If the angles are 30°, 90°, or 150°, the two edges have different chirality, i.e., one AC and the other ZZ (**Figure 3-11c** and **d**). The edge chirality can be further determined by Raman spectroscopy, which is further discussed in **Section 4.1.3**. Without additional Raman characterization, theoretically, there is only a 50% chance that the edge chirality of graphene is known. Similarly, hBN crystal also possesses edges of different chirality which requires further characterization for its determination. The hBN flakes with angles between adjacent straight edges being multiples of 30° are selected for crystalline alignment.

For the alignment of graphene with one hBN crystal, either top or bottom hBN crystal, there is no difference between 0° and 60° alignment since graphene is of D_{6h} point group symmetry. In contrast, for alignment of graphene with both top and bottom hBN crystals, 0° and 60° alignment will result in different rotational offset between the top and bottom hBN layers, since monolayer hBN is of D_{3h} point group symmetry. Specifically, if graphene/top hBN and graphene/bottom hBN interfaces are both of 0° or 60° alignment, the top and bottom hBN layers will be of 0° alignment and the overall heterostructure is three-fold rotationally symmetric without inversion symmetry (**Figure 3-11g**). Whereas if one of the graphene/ hBN interfaces is of 0° and the other 60° alignment, the top and bottom hBN layers will be of 60° alignment and the overall heterostructure is six-fold rotationally symmetric with inversion symmetry (**Figure 3-11h**).

As described above, to determine the exact alignment between graphene and the top and bottom hBN layers, one needs to know about the crystal orientation of hBN. The solution is to use top and bottom hBN flakes from the same exfoliated crystal. Note that for bulk hBN, an odd or even number of layers in hBN will lead to different symmetry between the top and bottom atomic layers (**Figure 3-1**). Thus flakes from the same exfoliated crystal cannot determine the crystal orientation of hBN, unless the parity of the number of layers is known. This ambiguity can, in principle, be circumvented by using the same surface, either top or bottom, of the original hBN crystal for alignment. For this purpose, hBN fakes that are fractured into pieces during mechanical exfoliation are selected as top and bottom hBN

layers. The related assembly process is described in detail in Supplementary information of **Section 7.2**.

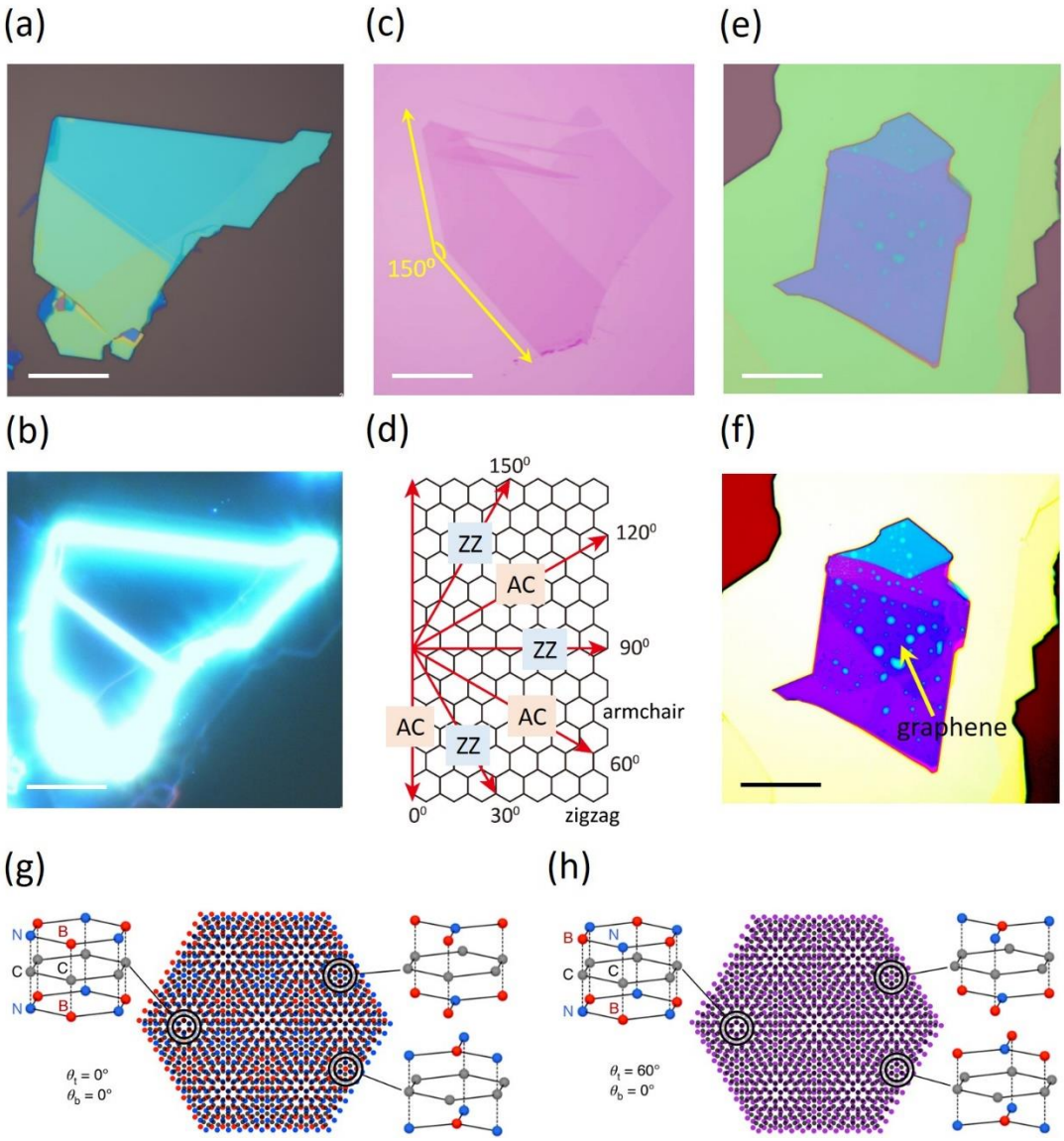

Figure 3-11 Optical images and atomic structure of flakes and stacks. *(a) Optical image of an hBN flake with the yellow part being around 50nm thick, blue part being around 30nm thick. (b) Dark field image corresponding to (a), which shows the step of the flake. (c) Optical image of a graphene flake with monolayer and trilayer region. The flake has two adjacent edges with an angle of 150° between them. (d) Graphene lattice showing the relationship between angles and the edge chiralities. AC and ZZ stand for armchair and zigzag, respectively. (e) Optical image of hBN/graphene/hBN stack. (f) LUT image corresponding to (e), with the shape of graphene under the hBN clearly seen. The scale bars are 20 μm. (g) and (h) Schematics of hBN/graphene/hBN heterostructures with a different alignment. θ_t and θ_b are the twist angles between graphene and top hBN and bottom hBN, respectively. (g) Both θ_t and θ_b are 0°. (h) θ_t is 0°and θ_b is 60°. Panels of lattice models show the atomic alignment for each high symmetry points of the moiré pattern. Purple shading in (h) denotes perfect overlap of boron and nitrogen in the top and bottom BN layers respectively. Taken from ref [144].*

The flake cleanness and flatness can be distinguished by dark field imaging, or adjusting the Look-Up-Table (LUT) values in the microscopy software. Dark field images only collect light

diffracted by flake edges, cracks and contaminants, etc. Thus, it is useful to select clean and flat flakes using dark field images (**Figure 3-11b**). Look-Up-Table stores the information of the red, green and blue light coming out from the sample by a transfer function. Contributions of different colour channels can be modified by altering this transfer function. Therefore it is possible to selectively enhance the contrast of the features on a sample by focusing on a certain colour channel (**Figure 3-11f**).

A further selection of flakes includes characterization by Raman spectroscopy and atomic force microscopy, etc. to distinguish the stacking order, edge chirality and thickness of the flakes, which will be further discussed in the next chapter.

3.3.3 Transfer methods

Dry transfer methods avoid direct contact between interior surfaces and the polymers, thus significantly reducing the contaminations in the 2D materials stack. There are two main categories that are widely used for stacking 2D crystals, the polymer membrane and polymer stamp mediated methods. The polymer membrane and stamp are normally supported by plectrum and glass slide (**Figure 3-12**), respectively. Here we introduce the transfer techniques mainly used in this thesis. Note that the possible procedures are not strictly restricted to what is presented here. There is a large room for flexibility and creativity depending on the desired geometry of the heterostructures fabricated. For example, different transfer techniques can be combined to improve device quality (further discussed in the experimental part of **Chapter 7**).

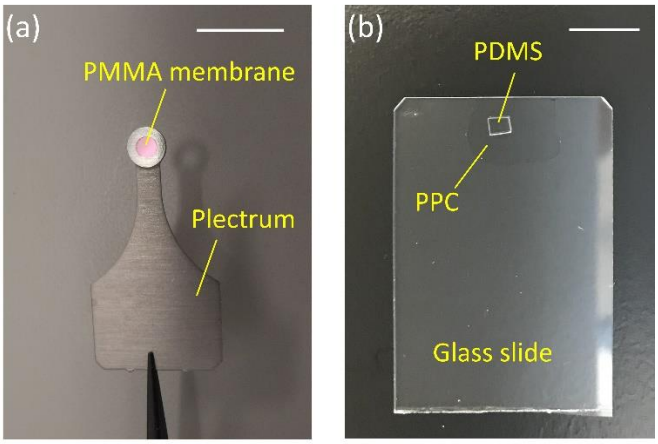

Figure 3-12 Support for polymer membrane and stamp. *(a) Plectrum for supporting the polymer membrane. (b) Glass slide with polymer stamp. The scale bars are 1 cm.*

The transfer processes are based on the transfer system which allows alignment of crystals with high accuracy within a micron. The transfer system consists of a transfer arm fixed by

a vacuum to an xyz micro-manipulator, a rotatable hotplate sitting on an xy sample holding stage, with a vacuum control (**Figure 3-13**). The whole system lies below a microscope with 5×, 10×, 20× and 50× magnifications.

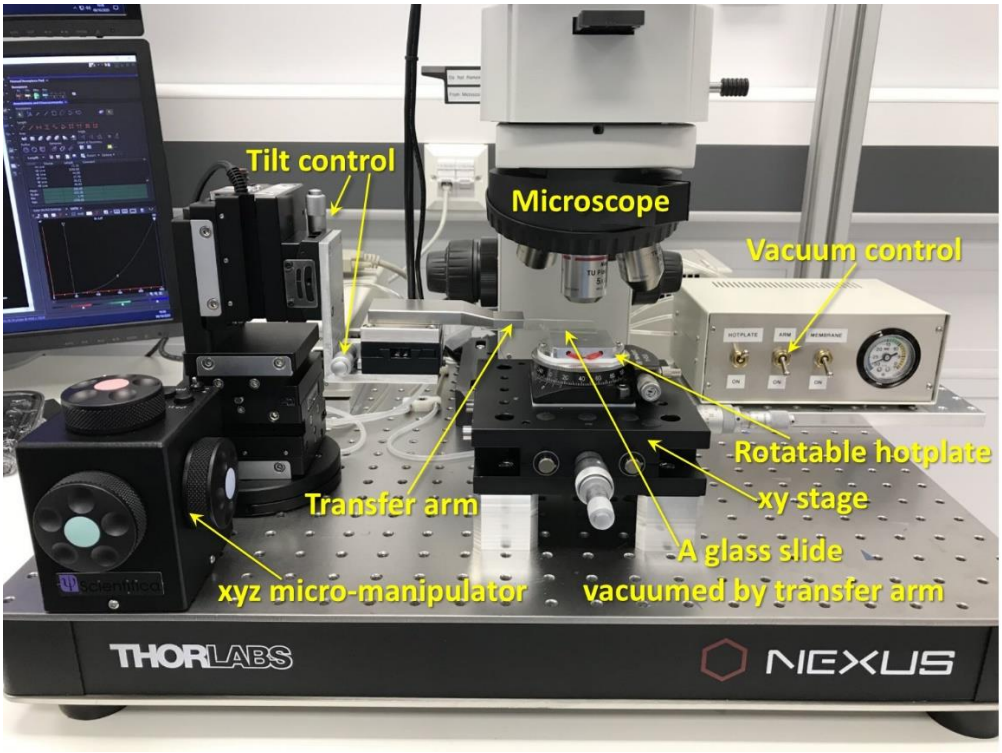

Figure 3-13 Transfer system. *The polymer membrane supported by plectrum and polymer stamp fixed onto a glass slide would be stuck to the end of the transfer arm. The target flake on SiO_2/Si substrate would be fixed on the hotplate by vacuum. The microscope would be used to align the flake on the plectrum or stamp with the flake on the substrate below. The transfer arm can be adjusted by tilt control in the xz and yz plane. The accuracy of the xyz manipulator and the xy stage is within 1μm.*

3.3.3.1 Membrane mediated method

In the membrane mediated method, Polymethyl methacrylate (PMMA) is typically used as the carrier membrane for target flakes, with the assistance of a sacrificial layer that can be dissolved in specific solvents. The sacrificial layer used is commonly polymethylglutarimide (PMGI)[145] or Polyvinyl acetate (PVA)[146], with the corresponding solvents being MF319 or water, respectively. The transfer procedure is as follows and shown in **Figure 3-14**.

Step 1, the flakes are exfoliated onto spin-coated polymer layers on SiO_2/Si substrate. The polymer layers contain one sacrificial layer and one flake carrier layer PMMA. **Step 2**, polymer layers are cut around the region of the target flake. **Step 3**, the sacrificial layer is dissolved by the solvent and then the carrier layer with the target flake is floated in the water. **Step 4**, the carrier layer/flake is fished out from water using the plectrum followed by baking at around 100 °C to evaporate water on the other side of the carrier layer (**Figure 3-12a**).

Step 5, the plectrum with carrier layer/flake is fixed onto the transfer arm by vacuum. The flake on the carrier layer is then aligned and placed onto another target flake on the SiO_2/Si substrate at the temperature of around 70 °C. **Step 6**, the carrier layer is cut and removed by dissolving with acetone. **Step 7**, the final stack remains on the substrate and is ready for device fabrication.

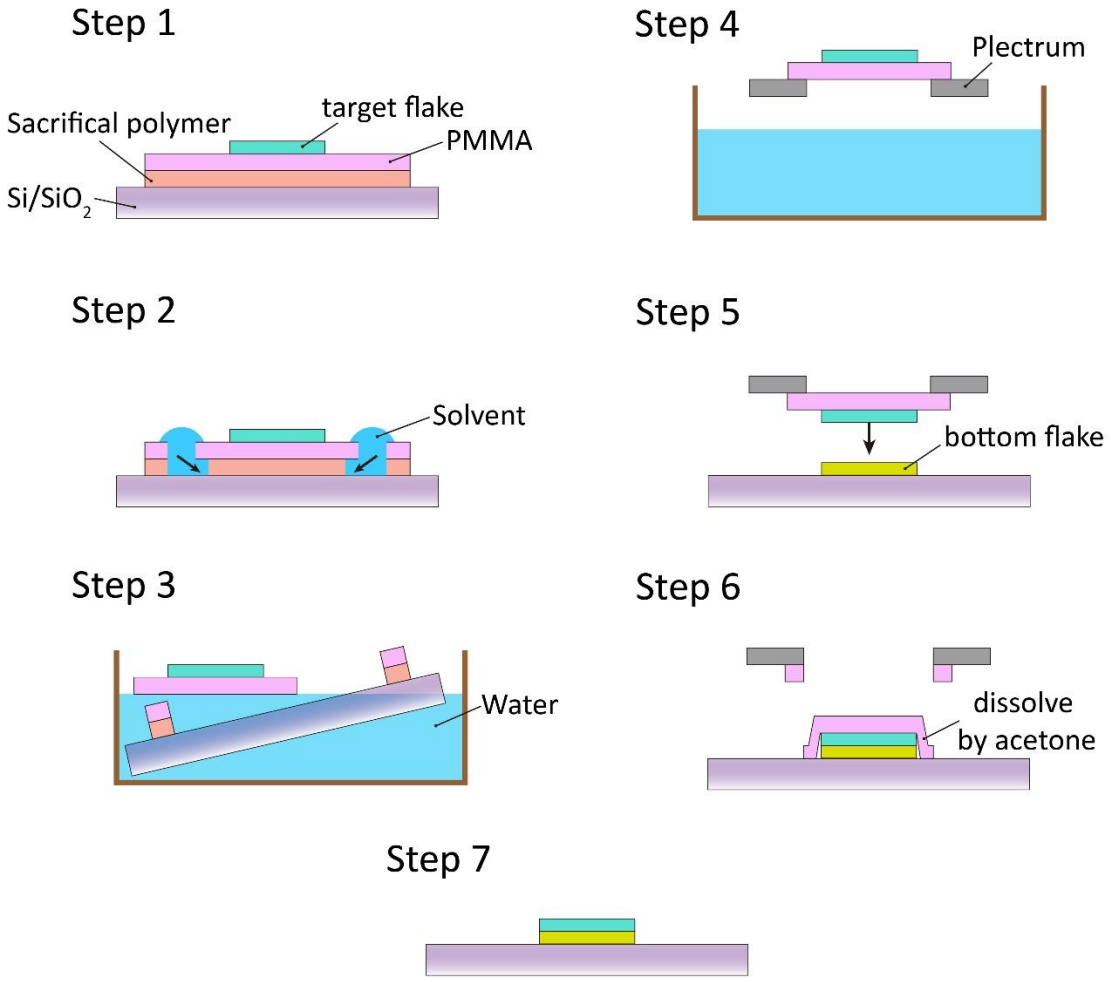

Figure 3-14 Process of membrane mediated transfer method. *The panels correspond to the transfer steps described in the text. The last panel shows the final heterostructure stack.*

3.3.3.2 Stamp mediated method

In the stamp mediated method, Polydimethylsiloxane (PDMS) spin-coated with polymers is used as the stamp for picking up the target crystal flakes. Before spin coating, PDMS is pre-treated by oxygen plasma to increase the adhesion between PDMS and the polymer layer. The polymers used can be PMMA[147], Polypropylene carbonate (PPC)[148], and Polycarbonate (PC)[149,150], etc. This method utilizes the viscoelastic properties of PDMS and the vdW forces

at the interfaces between the 2D materials used. The transfer procedure is as follows and shown in **Figure 3-15**.

Step 1, the PDMS stamp spin-coated with polymers is mounted onto a glass slide (**Figure 3-12b**), which is fixed onto the transfer arm by vacuum. **Step 2**, the target flake is picked up by PDMS/polymer at a temperature lower than the glass transition temperature T_g of the polymer. Increasing the pick-up temperature helps to enhance the adhesion strength between the crystal and the stamp. **Step 3**, with the temperature slowly increased to a relatively high temperature (still below T_g), another target flake on the substrate is picked up by the first flake through vdW interaction. The viscoelasticity of PDMS allows a slow pressing down process, which can push away contaminants, leaving a clean interface without bubbles. **Step 4**, at a relatively high temperature below the polymer T_g, the sequentially picked-up flakes are released onto the bottom flake by slowly peeling off the polymer; or, alternatively, **Step 5**, at a temperature higher than T_g, releasing the polymer/stack onto the substrate and then dissolving away the polymer with acetone. **Step 6**, the final stack remains on the substrate and is ready for device fabrication.

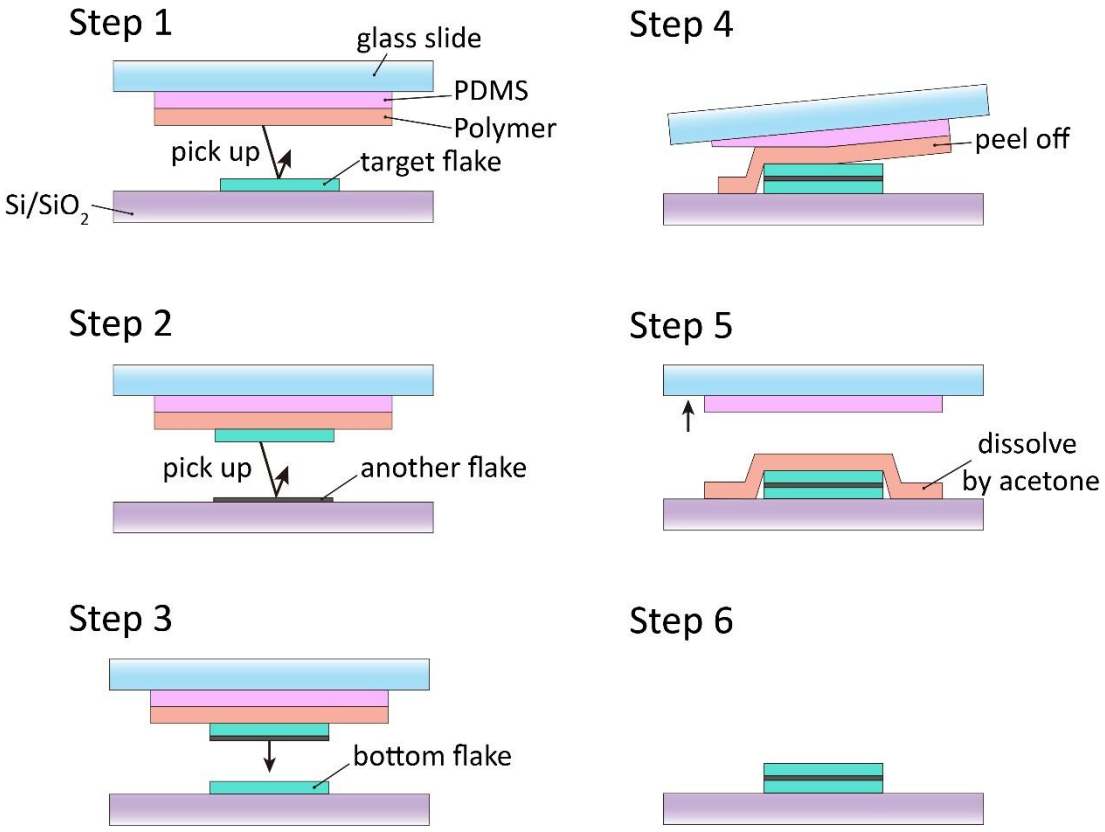

Figure 3-15 Process of stamp mediated transfer method. *The panels correspond to the transfer steps described in the text. The last panel shows the final heterostructure stack.*

As described above, it is explicit that the pick-up and releasing steps in the transfer process play a key role in heterostructure assembly. The factor that influences pick-up and releasing processes is the balance between adhesion at three types of interface, i.e. the polymer/2D layer, 2D layers and 2D layers/SiO_2 substrate interfaces. The adhesion depends not only on the hot plate temperature but also on the type of interfaces. Generally speaking, according to my experience of transfer during the past few years' works in cleanroom, below T_g, the ranking of adhesion at different interfaces is as follows in ascending order: graphene/polymer < SiO_2 substrate/hBN < SiO_2 substrate/graphene < graphene/hBN < hBN/polymer < plasma-treated SiO_2 substrate/graphene. According to the ranking, the adhesion between graphene and polymers is much smaller than that between graphene and SiO_2 substrate, so it is difficult for most of the polymers to pick up graphene on SiO_2 substrate directly, however, the case is inverse for hBN. Below T_g, most of the polymers can pick up hBN flakes easily. The factors that influence adhesion at SiO_2 substrate/2D flake interface include the type of the exfoliation tape, the pre-heating temperature of the SiO_2 substrate, the thickness of the flakes remaining on the substrate and operation of the researchers, etc. Among these factors, the last two ones cannot be well controlled. Normally, the thinner the flake is, the stronger the adhesion is at the SiO_2 substrate/flake interface. The last factor is the most uncontrollable. Even for skilled and experienced researchers, the adhesion between 2D flakes and SiO_2 substrate could vary in each exfoliation process. As such, sometimes the adhesion at SiO_2 substrate/graphene interface could be larger than that at hBN/polymer interface, resulting in the hBN fallen onto the graphene rather than picking it up.

As the temperature goes up, the adhesion at the three types of interface all increase and the order of the ranking varies. Increasing the temperature facilitates the polymer to pick up the flakes or the hBN flakes to pick up graphene. For temperature higher than 100°C, the adhesion at polymer/hBN and graphene/hBN interfaces dominate over that between graphene and plasma-treated SiO_2 substrate, so one can use polymer/hBN stack to pick up graphene on plasma-treated SiO_2 substrate.

The process of releasing the top hBN/graphene stack onto the bottom hBN could be slightly different for a specific polymer. Below T_g, it is possible that the polymer picks up the whole hBN/graphene/hBN stack while peeling off the polymer from the stack. This is because, at the temperature of **Step 4**, the adhesion at the bottom hBN/polymer interface also increases. To solve this problem, before **Step 4**, one can pre-heat up hBN on SiO_2 substrate to the temperature of around 200°C. Such a high temperature leads to strong adhesion between

hBN and SiO_2 substrate, which becomes larger than that at the hBN/polymer interface. Thus at the temperature of **Step 4**, the top hBN/graphene stack could be released onto the bottom hBN without the whole stack being picked up. This is the case with a success rate of around 100% only when the size of the top hBN and graphene are smaller than the bottom hBN. When the temperature goes above T_g, the polymer transits from a relatively hard "glassy" state to a viscous state, at which the polymers like PMMA and PC would be stuck to the SiO_2 substrate. In this case, the polymer has to be dissolved away by acetone. For PPC, it will not adhere to SiO_2 substrate even when the temperature is above T_g, so it applies to the process of **Step 4** instead of **Step 5**.

The temperature of the transfer steps is different for each polymer because T_g differs for a different polymer. The T_g of PMMA, PPC and PC are 105°C, 45°C and 150°C, respectively. For PPC and PC, below T_g, the wavefront of the contact area between the polymer and SiO_2 substrate normally moves in discrete jumps while increasing the temperature, whereas above T_g, it can move continuously, allowing greater control over its lateral movement. In contrast, for PMMA the wavefront can move continuously at any temperature, regardless of T_g. The temperature of the pick-up process for PMMA, PPC, and PC is approximately 60°C-90°C, 40°C-45°C, and 60°C-90°C, respectively. For **Step 5**, the temperature of releasing process for PMMA, PPC, and PC is approximately 120°C -150°C, 50°C -60°C and 150°C -180°C.

Temperature not only affects the adhesion at the interfaces but also plays an important role in the formation and motion of bubbles at the interfaces of the heterostructure. The bubbles come from trapped contaminants that are absorbed on the sample interfaces. At low temperature, the trapped contaminants cannot form visible bubbles. As the temperature goes up, the contaminants aggregate into bubbles, which further become increasingly mobile at a temperature above ~70°C[148]. Therefore, compared to PMMA and PC, there are more bubbles in the final stack using PPC for transfer. At a temperature above ~70°C, the process of pressing down the polymer stamp allows pushing of the mobile bubbles across the stack, during which the bubbles will collide, aggregate and finally stop at cracks and wrinkles or be eliminated at the heterostructure edges[148,150].

In conclusion, in this section, we described in detail the process of stamp mediated transfer method and discussed the factors that influence the transfer process, as well as the comparison of different polymers. Temperature plays a key role in a successful assembly of the heterostructure. The setting of temperature at each step depends on what polymer is

chosen. Each polymer has its merits and demerits for transfer. One has to carefully select the polymer depending on what heterostructure is to be made. In brief, transfer using PPC is convenient while it could introduce more bubbles in the stack. PMMA allows more controllable movement of the wavefront. Transfer using PC can be carried out at a relatively high temperature which favours clean interfaces without bubbles.

3.3.3.3 Comparison between different transfer methods

The two transfer methods demonstrated above both include two parts, i.e. preparation before transfer and transfer itself. The steps of the transfer process are similar to each other for both methods and the main difference lies in the preparation steps. In this section, a comparison between the two transfer methods is presented in four aspects, based on my experience of transfer and related review articles[3,151,152]. First, how easy it is to implement the transfer process. For the membrane mediated method, the preparation needs one spin-coating step for exfoliation of flakes onto the polymer layers and the procedure of attaching polymer membranes to plectrums. For the stamp mediated method, the preparation also needs one spin-coating step, whereas it is for making PDMS/polymer stamp. The preparation steps are easy to implement for both methods.

Second, how fast it is to finish the assembly. Membrane mediated method has more preparation steps than the stamp mediated method. However in the transfer process, the stamp mediated method requires slowly increasing of transfer temperature to carefully press down the polymer and push away contaminants, so it takes a much longer time to finish the assembly than the membrane mediated method.

Third, how clean are the as-fabricated heterostructures. Heterostructures fabricated by membrane mediated method normally has much more bubbles than those made by the stamp mediated method, because it lacks the process of slowly pushing away contaminants. In the final step of peeling off the polymer layer from the stack, both the membrane mediated method and the stamp mediated method with **Step 5** requires the dissolution of the polymer by acetone, which results in direct contact of the heterostructures with chemicals. Nevertheless, post-transfer baking at a temperature above 200°C or thermal annealing up to 500°C can remove the chemical residues adhere to the heterostructures.

Fourth, what situation the method applies to. Membrane mediated method works better for transferring flakes onto the substrate which has a weak interaction with the flakes, especially those with curved and uneven surfaces. Stamp mediated method is superior to the membrane mediated method in assembling multi-heterostructures with a large area of contaminant-free regions. For thin flakes, the membrane mediated method is more favourable to flake

alignment since PMMA membranes are much thinner than PDMS/polymer stamp and have higher transmittance of light, allowing a much larger optical contrast of the flakes. Besides, the viscoelasticity of PDMS introduces stress in the pressing down process, which could easily lead to cracks, folds and wrinkles in thin flakes. In this thesis, samples, where thin films of 2D materials are supported by SiN_x grids, were prepared by the membrane mediated method, as presented in **Chapter 5**. All the hBN/graphene (graphite)/hBN heterostructures in this thesis were fabricated by stamp mediated method.

Comparison between the two methods is summarized in **Table 3-2**.

Table 3-2 Comparison between different transfer methods*

Methods	Easiness	Speed	Bubbles	Suitable cases
Membrane mediated	★★★	★★★	★★★	Thin films, such as few layer hBN films that are difficult to pick up by the polymer; substrates with curved and uneven surfaces
Stamp mediated	★★★	★	★	Almost all 2D crystals, except those difficult to pick up

**The numbers of symbol ★ indicate the degree or amount in each column.*

3.3.3.4 Tear and stamp technique

In this section, we introduce the tear and stamp technique which is a ubiquitous method for making heterostructures with twisted graphene layers. Even though in this thesis we did not use this method for twistronics, the method is presented for comparison to our in situ manipulation technique presented in **Chapter 7**.

In the tear and stamp technique, graphene flake is split into two sections which are sequentially picked up by hBN attached to the PDMS/polymer stamp or PDMS hemisphere spin-coated with polymer[42,153]. Splitting of graphene is achieved by partially picking it up using hBN, which requires a good control of the contact area between hBN and the target region of graphene. Before the second pick-up step of graphene, the substrate is rotated by a small angle with accuracy reaching 0.1°. Since the two graphene sections come from the same crystal, the crystal orientation is known for each section and the twist angle can be well controlled by substrate rotation to yield the moiré superlattice. A schematic of the tear and stamp technique is shown in **Figure 3-16**.

In contrast, our in situ manipulation technique is mediated by a polymer resist patch deposited on target 2D crystals and a handle made by glass slide with PDMS hemisphere. When the PDMS hemisphere is brought in contact with the PMMA patch, one can easily move or rotate the target 2D crystals on the surface of the bottom flake. The technique can precisely and dynamically control the rotation and positioning of 2D materials, which is demonstrated in detail in **Chapter 7**.

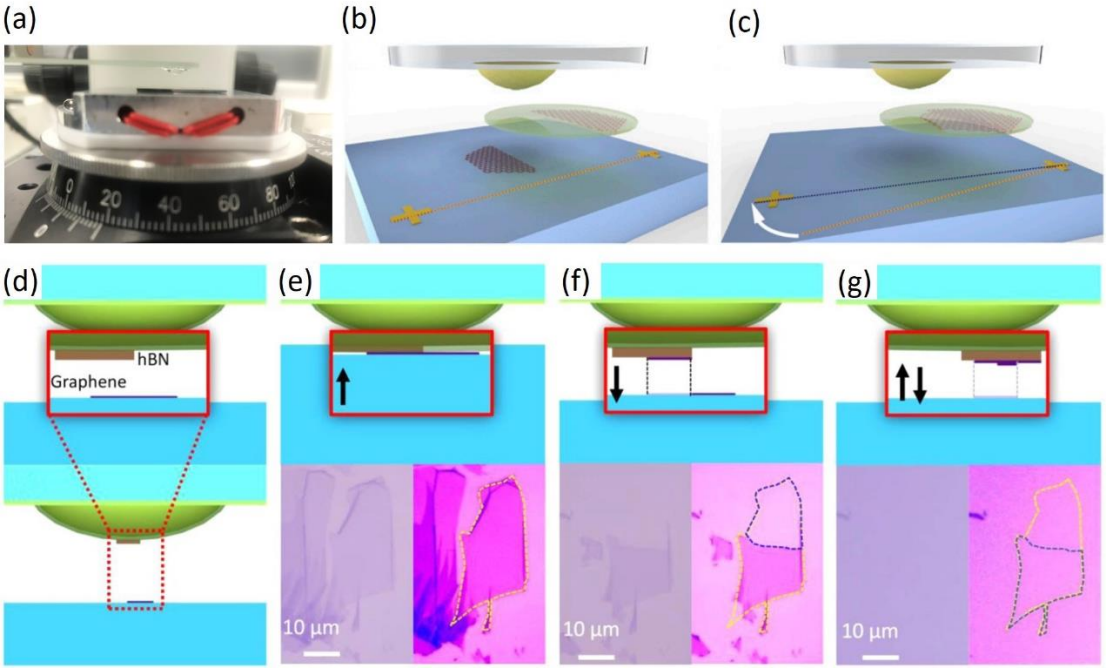

Figure 3-16 Schematic of tear and stack technique. *(a) Photograph of PDMS hemisphere handle and the transfer system. The PDMS hemisphere can be used in the tear and stack technique or as a manipulator in the in-situ manipulation technique discussed in* ***Chapter 7****. (b) The first graphene section is torn and picked up by hBN. (c) The second graphene section is picked up after the substrate is rotated by a small angle, as indicated by the white arrow. Since the two graphene sections come from the same crystal, the small rotation angle yields moiré superlattice between the graphene layers. (b) and (c) are taken from ref [153]. (d-g) Schematic side view of successively picking up graphene sections. The bottom panels of (e-g) are the optical images of the successive stacking steps. Taken from ref [42].*

3.3.4 Challenges to high quality heterostructure

In **Section 3.3**, a detailed process of vdW heterostructure assembly is presented, starting from the crystal exfoliation and flake selection to the assembly techniques. Creating an electronic device includes the building of vdW heterostructures and several steps of standard processes, i.e. lithography, etching and metal deposition for contacts. The former is the key to making a device with excellent performance, whereas the latter involves standard and mature techniques. In this thesis, we focus on the assembly of vdW heterostructures, which is also the most difficult part of device fabrication.

Generally, the common obstacle to a high-quality device is the issue of interlayer contaminants introduced in each step of the heterostructures assembly, from the very beginning procedure of crystal exfoliation and flake selection to stack assembly. The existence of interlayer contaminants, normally in the form of bubbles with trapped hydrocarbons[154], degrades the quality of the device by way of doping and changing the permittivity of the dielectric layers, blocking up access to the intrinsic properties of 2D materials. For specific devices, the challenges to high-quality performance may differ. In particular, for devices of hBN/rhombohedral graphite/hBN heterostructure, the main problem is to retain the rhombohedral stacking of graphite during assembly since it is energetically less stable compared to Bernal stacking. For devices involving moiré superlattice structure, accurate control of the twist angle between 2D layers is the main issue to be solved.

In this section, we mainly discuss how to avoid introducing contaminants for each step of **Section 3.3**. The issues of preserving rhombohedral stacking of graphite during assembly and control of twist angle are fully demonstrated later in **Chapter 5** and **Chapter 7**. In terms of crystal exfoliation, apart from choosing suitable tapes that introduce less organic residues, it is important to do the transfer as soon as possible after flake exfoliation, or rather, to use newly exfoliated flakes for heterostructure assembly and better to keep them for no more than 3 days. The longer the flakes are kept, the more adsorbates there are. Alternatively, keeping flakes in an oxygen- and the moisture-free environment is also a good choice, especially for sensitive 2D materials such as black phosphorus, niobium diselenide and indium monoselenide, etc.

Regarding flake selection, with the help of dark field images, it is efficient to screen out large numbers of flakes with cracks and contaminants. Obviously, it is favourable to use flakes without any contaminants and cracks. Cracks in flakes will bring in uncertainty factors such as folds in the heterostructure during transfer, making it less controllable in the transfer process.

For transfer techniques, the stamp mediated method is commonly used for creating heterostructures with a large clean area. Comparison of the different polymers has been fully discussed in **Section 3.3.3.2**. Using PMMA and PC favours a large area of clean interfaces without bubbles since they allow a high transfer temperature at which the contaminants become mobile. On the other hand, an ultraslow velocity of pressing down the flakes is necessary so that there is enough time for contaminants to be squeezed out of the closing interface and avoid being trapped.

Chapter 4: Characterization methods

In this chapter, we outline the characterization techniques and measurement set-up mainly employed in this thesis, covering characterization of graphene stacking order and its mechanical properties, surface topography of van der Waals heterostructure, and the measurement and quantification of the electronic properties of the finished devices.

4.1 Raman spectroscopy

Raman spectroscopy is a fast, non-destructive, high-resolution and versatile tool for understanding the behaviour of electrons and phonons in 2D materials, which allows the determination of the number of layers, stacking order, defects, and strains in graphene. Raman spectrum is based on the light-matter interaction, which reflects the atomic vibrations in a crystal lattice, exhibiting peaks with a varying position, line shape, and intensity depending on the atomic, electronic and phonon structures of the 2D materials. In this thesis, the characterization of stacking order and edge chirality of graphite films is performed by Raman spectroscopy, which is fully discussed in **Chapter 5**. In **Chapter 7**, we use the Raman spectrum for the determination of monolayer and bilayer graphene, as well as studying the effect of moiré superlattices on the Raman response of graphene.

4.1.1 Principles of Raman Spectroscopy

When light is shed on materials, most of the light is transmitted or reflected, and the rest is scattered. The scattering process is classified as Rayleigh scattering and Raman scattering, which is further divided into several processes, depending on the initial state of the system and the state after the scattering (**Figure 4-1**).

Rayleigh scattering is an elastic scattering because there is no energy loss in the system. The incident photon and the emitted one might change the propagation direction but with the same frequency, and the system returns to its initial state after scattering.

In contrast, Raman scattering involves a change in the incident and emitted photon energy in the electron-phonon interaction process. The incident photon $\hbar\omega_L$ excites an electron to a virtual energy state, creating the electron-hole pair, and then the electron interacts with a

phonon $\hbar\omega_{ph}$ before recombining with the hole, which emits a photon with energy $\hbar\omega_{sc}$. For Stokes (S) scattering, the electron loses part of the energy $\hbar\omega_L$ to generate a phonon:

$$\hbar\omega_L - \hbar\omega_{ph} = \hbar\omega_{sc} \qquad \mathbf{k}_L - \mathbf{q} = \mathbf{k}_{sc} \tag{4.1}$$

where $\mathbf{k}_{L,sc}$, and $\mathbf{q}$ are the wave vector of the photons and phonon, respectively, and $\omega_{L,sc,ph}$ is the frequency. While for anti-Stokes (AS) scattering, the electron absorbs a phonon to an excited vibrational state before being excited by the photon:

$$\hbar\omega_L + \hbar\omega_{ph} = \hbar\omega_{sc} \qquad \mathbf{k}_L + \mathbf{q} = \mathbf{k}_{sc} \tag{4.2}$$

Raman process is resonant when the virtual energy state matches a specific energy level, e.g. a stationary state. More importantly, the phonon involved in the Raman process must have the vibration mode that changes the polarizability of the material so that it can be detected by Raman spectroscopy.

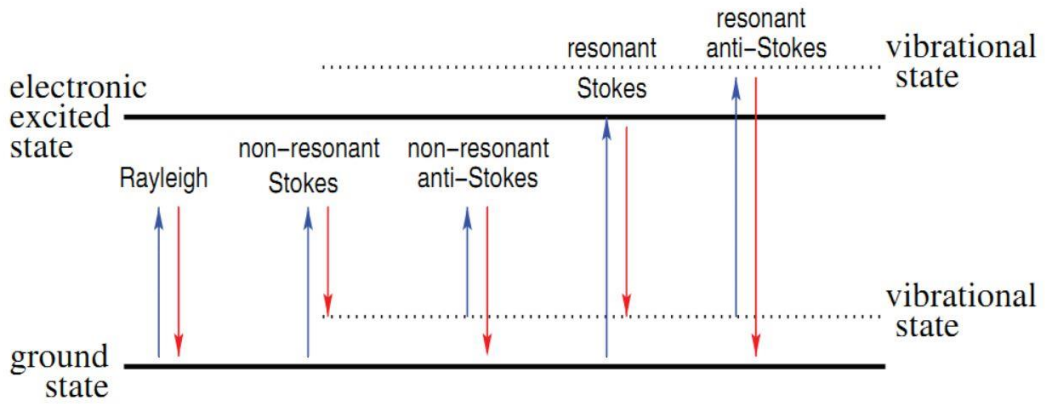

Figure 4-1 Rayleigh and Raman scattering in resonant and non-resonant conditions. *Taken from ref [155].*

In the Raman process, the frequency and momentum are conserved, as derived by Eq (4.1) and (4.2):

$$\omega_L = \omega_{sc} \pm \omega_{ph} \qquad \mathbf{k}_L = \mathbf{k}_{sc} \pm \mathbf{q} \tag{4.3}$$

where $k = c\omega$ and c is the light speed. Since the Raman experiments normally use light in the range of 229-758 nm, for graphene, the magnitude of a zone boundary wave vector for crystal lattice is much larger than the incident (or scattered) photon wave vector, $k \ll 2\pi / a$. According to Eq (4.3), the phonon wave vector also has the relation $q \ll 2\pi / a$, which means that the phonon is restricted to near the centre of the Brillouin zone.

4.1.2 Phonon dispersion and Raman processes in graphene

Phonon dispersions and Raman processes are relevant for the interpretation of the Raman spectra of graphene[156]. Monolayer graphene contains two atoms per unit cell, thus there are six phonon dispersion bands (**Figure 4-2**) including three acoustic (A) and three optical (O) branches inherited from the six vibration modes at the Γ point. In each acoustic and optical branch, one vibration mode is out-of-plane (Z), while the other two are in-plane modes, which are further classified as longitudinal (L) or transverse (T) according to vibrations parallel with or perpendicular to the propagation direction. Along the high symmetry $\Gamma - M$ and $\Gamma - K$ directions in the first Brillouin zone of graphene, the six phonon dispersion curves are assigned to LO, TO, ZO, LA, TA, and ZA phonon modes.

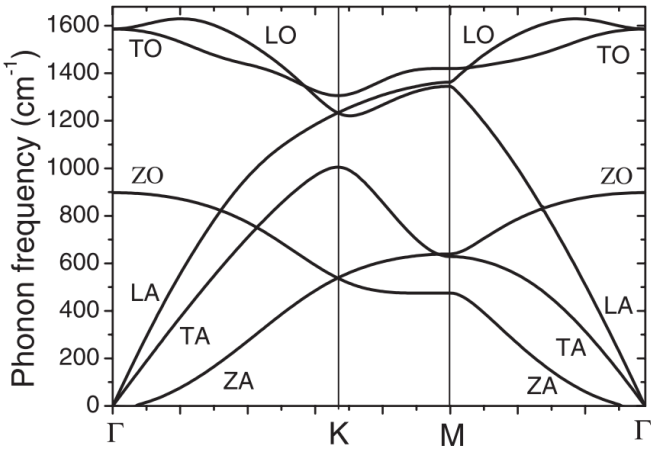

Figure 4-2 Phonon dispersions for monolayer graphene. *Taken from ref [156].*

The Raman spectrum of graphene mainly consists of three basic sets of peaks, that is D (around 1350 cm^{-1}), G (around 1580 cm^{-1}) and 2D (around 2700 cm^{-1}) bands (**Figure 4-3a**). Other bands include the shear (C) modes[157], the layer-breathing modes (LBMs)[158] and the G* band (around 2450 cm^{-1}). The G band comes from first order Raman scattering process, involving the doubly degenerate high-frequency TO and LO phonon mode (E_{2g} symmetry) at Γ. G band is a characteristic peak of graphene-related materials, of which the peak position is sensitive to the number of layers, stacking order, defect and strain, etc.

D band comes from a second-order process, which corresponds to the breathing modes of six-carbon-atom rings and involves defects and one TO phonon near K which couple preferentially to the electronic states in the intervalley double resonance (DR) process (**Figure 4-3b**). Therefore, the appearance of D band means the existence of defects in graphene. The 2D band is the D band overtone, which involves two TO phonons near K in the intervalley DR process and no defects are required for scattering (**Figure 4-3b**). The

G* band is a combination mode involving one TO phonon around K and one LA phonon in the intervalley double resonance process.

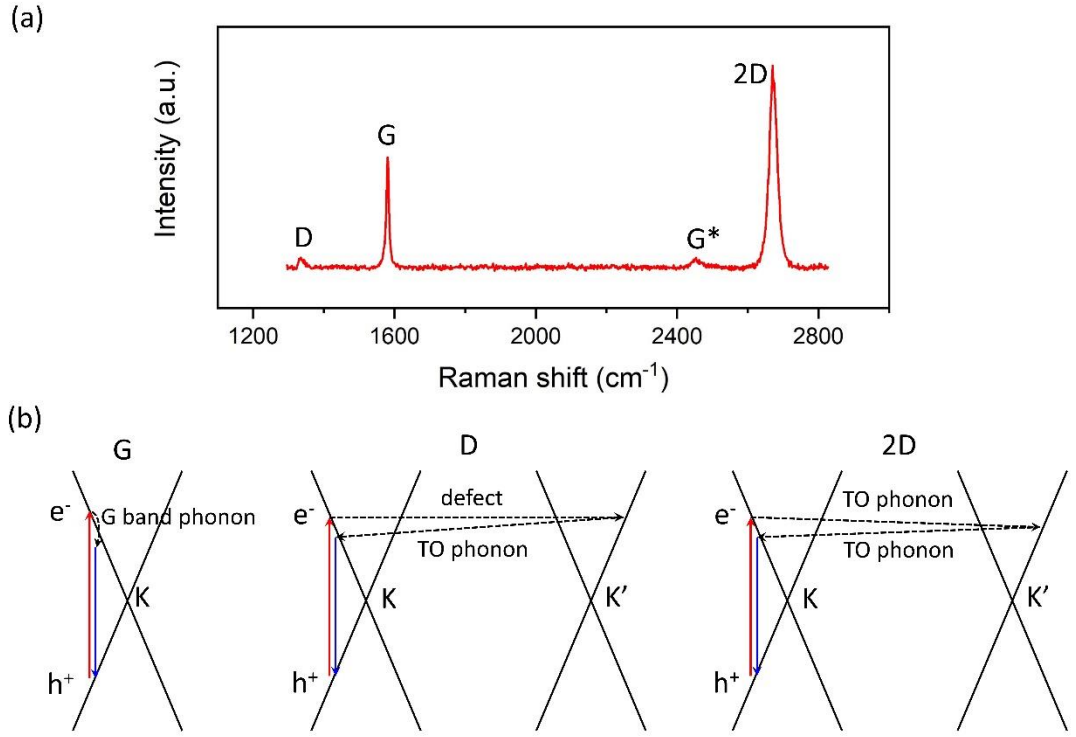

Figure 4-3 Raman spectrum and Raman processes in graphene. *(a) Raman spectrum of graphene. (b) Raman processes of G, D and 2D bands. Modified from ref [159].*

4.1.3 Influence of stacking order and edges on Raman spectrum of graphite

In this section, we discuss how the three basic sets of Raman peaks, i.e. G band, 2D band and D band, respond to the graphite stacking order and edges. To understand the influence of stacking order on the Raman response of graphite, one needs to know about the phonon dispersion and electronic band structure of graphite. Phonon dispersions for AB bilayer, ABA trilayer, and ABC trilayer graphene are given in **Figure 4-4** [156]. On one hand, as is shown in **Figure 4-4b**, at Γ the doubly degenerate E_{2g} branch in the monolayer graphene splits into two (three) doubly degenerate branches for bilayer (trilayer) graphene with a small energy window, due to the coupling of each intralayer modes through interlayer interactions. On the other hand, as the number of layers increase, the different stacking order of graphite leads to the change of point group symmetries. Graphene is of D_{6h} symmetry, while AB bilayer and ABC trilayer are of D_{3d} symmetry, and ABA trilayer is of D_{3h} symmetry[159]. As such, the corresponding Γ phonons evolve from E_{2g} mode into different mode symmetries, which could be Raman or infrared (IR) active. Take bilayer graphene as an example, the E_{2g} mode of graphene evolves into E_u mode and E_g mode, corresponding to the in-phase and out-of-phase vibrations of the atoms in the two different layers respectively[156,159]. The E_g

mode is Raman active and E_u mode is IR active, therefore, only E_g mode can be detected in the Raman response, exhibiting a shift in G band frequency. The case is similar for ABA and ABC trilayer. The shift of G band frequency induced by branch splitting could explain the observed different G band frequencies in domains of the different stacking order in **Chapter 5**. Such a branch splitting also gives rise to an enhanced intensity of the corresponding Raman mode due to the increased number of phonon modes as the number of layer increases[156,160].

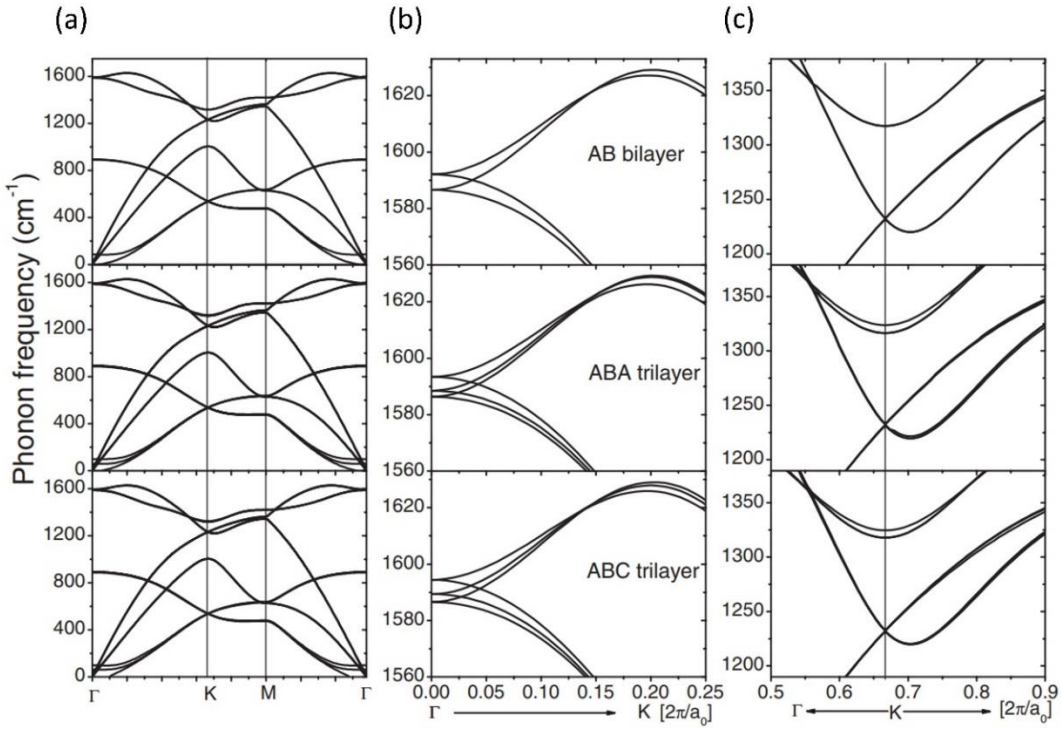

Figure 4-4 Phonon dispersions for few-layer graphene with different stacking order. *From top to bottom: AB bilayer, ABA trilayer, and ABC trilayer. (a) Full phonon dispersions. (b) Dispersions near* Γ *. (c) Dispersions near* K *. Taken from ref* [156].

Similarly, for the highest phonon branches at K which are associated with D band and 2D band, there also exists mode splitting (**Figure 4-4c**) that leads to the shift of phonon frequencies and intensity enhancement of the bands. D band and 2D band originate from the DR process, where the evolution of the electronic bands plays the key factor in Raman response[161]. In particular, the 2D band displays a complicated line shape change with the evolution of the number of layers and stacking order. To analyse the influence of the number of layers and stacking order on 2D band, here we start from the DR process of graphene, which is the simplest case. The intervalley DR process of graphene is as follows (**Figure 4-5a**)[161,162]: the incident photon excites an electron with wave vector $\mathbf{k}$, creating a hole near K point (A $\rightarrow$ B vertical transition in **Figure 4-5a**), with the photon energy in resonance with the $\pi \leftrightarrow \pi^*$ transition. Next, the excited electron is inelastically scattered by a TO phonon with momemtum $\mathbf{p}$ (B $\rightarrow$ C) to a point near K' with wave vector $\mathbf{k}'$, and then inelastically

scattered back to the state of $\mathbf{k}$ by another TO phonon (C → B) with momentum $-\mathbf{p}$. Finally, the electron recombines with the hole and emits a photon (B → A). The DR condition is reached when the energy is conserved in these transitions.

For bilayer graphene, the splitting of the electron dispersion near K leads to four different possible processes, as shown in **Figure 4-5b**. The vertical transitions of $\pi_1 \leftrightarrow \pi_2^*$ and $\pi_2 \leftrightarrow \pi_1^*$ are forbidden while $\pi_1 \leftrightarrow \pi_1^*$ and $\pi_2 \leftrightarrow \pi_2^*$ are allowed[159,163,164]. For each vertical transitions there are two possible electron-phonon scattering processes, giving rise to four components in 2D band (with frequencies of ω_{11}, ω_{12}, ω_{21} and ω_{22} and the corresponding phonon momenta $\mathbf{p}_{11}$, $\mathbf{p}_{12}$, $\mathbf{p}_{21}$ and $\mathbf{p}_{22}$). The two components of the lowest (ω_{22}) and highest (ω_{11}) frequencies have relatively lower intensity than the other two in the experimental data[161].

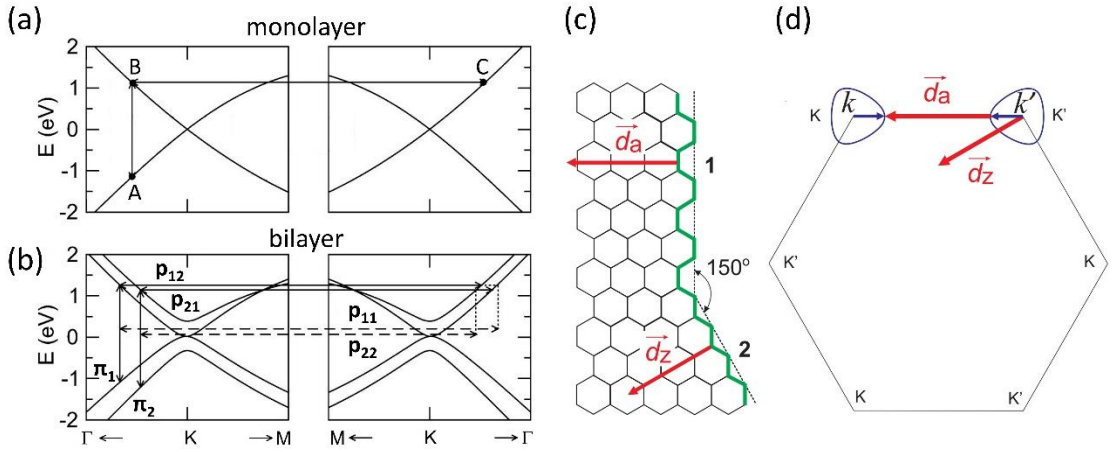

Figure 4-5 Double resonance processes of 2D band and D band. *(a) DR process for monolayer graphene. (b) DR process for bilayer graphene. Vertical arrows denote transitions from a valence (π) band to a conductance (π^*) band. Horizontal arrows denote electron-phonon scattering processes with the phonons of wave vectors* $\mathbf{p}_{11}$, $\mathbf{p}_{12}$, $\mathbf{p}_{21}$ *and* $\mathbf{p}_{22}$. *The scattering processes are drawn horizontally for simplicity since the energy of the phonons is much smaller compared to the incident photon energy. (a) and (b) are modified from ref [164].(c) Schematic of the atomic structure of the edges. The bold green lines highlight the edge structures, armchair for edge 1 and zigzag for edge 2. The wave vectors of the armchair and zigzag edges are* $\mathbf{d}_a$ *and* $\mathbf{d}_z$, *respectively. (d) The first Brillouin zone of graphene showing the top view of the DR process. The circles near* K *and* K' *are the equienergy contours. (c) and (d) are taken from ref [165].*

For bulk graphite, both phonon and electronic band disperse in the first BZ of 3D graphite, however, the phonon dispersion does not change much along k_z direction[166], therefore the effect of π electron dispersion to the evolution of 2D band dominates. Since the electronic band disperses in the 3D BZ, the DR processes giving rise to 2D band can take place along entire k_z direction. The 2D band is thus formed by a convolution of an infinite number of components with different intensities and frequencies ranging from ω_{22} to ω_{11} [163], resulting in

a complicated 2D band line shape. As described in **Section 2.1.2.2**, the electron dispersion of 3D graphite is determined by the stacking order, thus the 2D band line shape bears the stacking order information of graphite. Based on the theoretical calculation[163] and experimental data in **Chapter 5**, for Bernal graphite, the strongest component of 2D band at higher frequency mainly comes from the $\mathbf{p_{11}}$ scattering process. While for rhombohedral graphite, the intensity of lower frequency components competes with that of $\mathbf{p_{11}}$ process. This is obviously due to the distinct electronic band structures of Bernal and rhombohedral graphite, which result in electron-phonon scattering processes with different frequencies and intensity. For ABC stacked graphite, there exists energy separation between the surface and bulk subbands [36,167], whereas there is no such energy separation for ABA stacked graphite [167]. According to ref [163,164], the splitting between the two valence bands and between the two conduction bands in bilayer graphene gives rise to the four scattering processes and determines the phonon frequencies of ω_{12}, ω_{21} and ω_{22}. In the same way, it can be inferred that the energy separation between the surface and bulk subbands in rhombohedral graphite will also result in additional scattering processes, which probably contribute to the lower frequency components in 2D band, resulting in a distinct line shape compared to that of Bernal graphite as shown in **Chapter 5**. For quantitative understanding of the relative intensity of the lower and higher components of 2D band in ABC stacked graphite, further theoretical Raman calculations will be needed.

Graphene edges can be viewed as defects, which activates D band. Similar to 2D band, D band also originates from the intervalley DR process, but one electron-phonon scattering process is substituted with the elastic electron-defect scattering (**Figure 4-3b**). **Figure 4-5d** shows the top view of the intervalley DR process in the first BZ, where the excited electron with wave vector $\mathbf{k}$ forms a circle centered at K since the electronic band structure of graphene is symmetric around K. As described in **Section 3.3.2**, there are two types of edge structures, i.e. armchair and zigzag. The corresponding wave vectors are $\mathbf{d_a}$ and $\mathbf{d_z}$ in the reciprocal space, respectively, which are in the direction perpendicular to the edges. It is clearly shown in **Figure 4-5d** that only $\mathbf{d_a}$ is able to connect the electron wave vector $\mathbf{k}$ near the two inequivalent K and K' points, but $\mathbf{d_z}$ is not since the circles around K and K' points is not large enough for momentum conservation in the intervalley DR process[168,169]. Therefore, a perfect zigzag edge cannot activate a D peak. For mechanically exfoliated flakes, the microscopically sharp edges are found to be imperfect at the atomic level[170,171]. Thus the zigzag edges of the flakes also exhibit D band, but with weaker intensity compared to that of armchair edges which can be distinguished by the Raman intensity

map[143]. These features of D band for different edge chirality is used for distinguishing the crystal orientation of graphite flakes in **Chapter 5**.

4.2 Atomic force microscopy

Atomic force microscopy emerged after the invention of the scanning tunnelling microscope (STM), with the tunnelling tip replaced by a force sensing cantilever. So they share the key components and principles. AFM is now a powerful and versatile tool for characterizing and manipulating surfaces at the atomic level and studying surface interactions quantitatively. AFM is indispensable in the process of device fabrication for the following reasons. First, the fabrication of a high-quality electronic device requires the information of the surface morphology and heights of each 2D layers in the stack, which can be provided by AFM characterization. Second, for devices with complex architectures which need numbers of fabrication steps, the size of specific geometries of the device in certain critical steps and heights of the metal contacts need to be detected by AFM. Apart from device fabrication, AFM allows for the detection of Young's modulus, adhesion and deformation of the material surfaces, which provides spatial visualization of mechanical properties. The main usage of AFM in this thesis is to probe the mechanical properties of multilayer graphene, as well as the measurement of thickness and surface topography characterization of van der Waals heterostructures.

4.2.1 Principles of atomic force microscopy

The core of AFM is that the sample surface is probed by a tip fabricated onto a cantilever (**Figure 4-6**). Tip and sample are moved relative to each other in a raster fashion with quantities measured at discreet locations (pixels). The tip-surface interaction causes deflection or torsion in the cantilever, which can be detected by several schemes, including beam-bounce, capacitive sensor and interferometry. The most used one is the beam-bounce scheme, in which a laser beam on the backside of the cantilever is reflected into a quartered photodiode which converts the signal to the controller. The displacement of the cantilever and sample stage in the x, y, and z directions is controlled by a piezoelectric transducer. A set of controller regulates, collects, and processes data from the detection system and drives the piezo scanner. During the scanning process, the tip-sample interaction is maintained by a classical closed-loop feedback system.

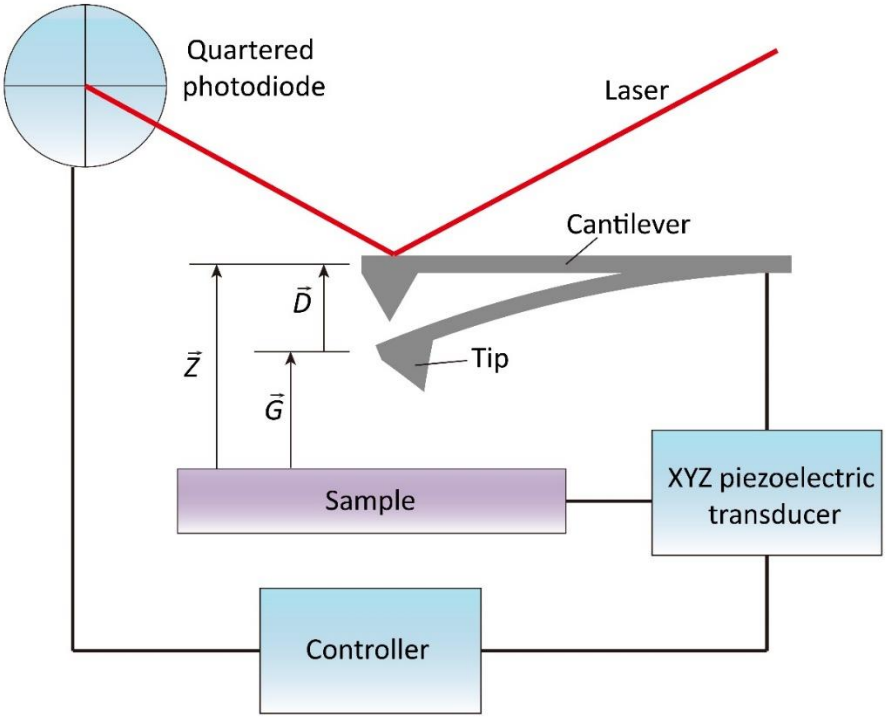

Figure 4-6 Schematic of basic components of AFM with the light-lever detection system. *$\vec{D}$ is the deflection of the free end of the lever caused by tip-sample interactions. $\vec{Z}$ is the Z piezo position. $\vec{G}$ is the tip-sample gap, which equals to $\vec{Z}-\vec{D}$.*

4.2.2 Atomic force microscopy modes

There are three typical modes of AFM, i.e. contact mode, tapping mode and Peak Force (PF) tapping mode developed by Bruker company. Understanding the working principle of each mode is fundamental to obtaining high-quality AFM images of the heterostructures, as one needs to carefully set and monitor the scanning parameters before and during the scanning process. Different modes apply to different samples and purposes, which are described as follows.

- **Contact mode**

Contact mode is a basic working paradigm of AFM. **Figure 4-7** shows the force-distance curve of the contact mode. The cantilever is driven by a z-piezo applied with a triangular waveform. When the cantilever approaches the surface, it deflects through the tip-sample interaction force. Further movement to the surface will cause an upward deflection of the lever and/or sample deformation. The cantilever is retracted at the set point deflection, which is maintained by the feedback loop while raster scanning the tip on the sample. Point 2 and 4 are the turning points where the balance between tip-sample interaction and restoring

force of the cantilever breaks. The setpoint deflection is the primary parameter that needs to be carefully monitored so that the sample will not be damaged.

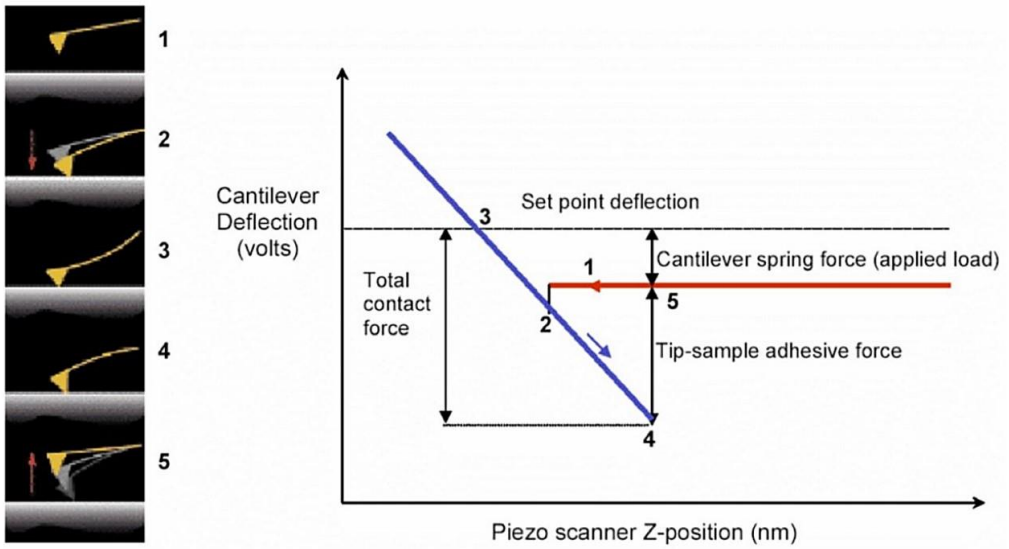

Figure 4-7 Force distance curve in contact mode. *The approach (red) and withdraw (blue) curves are shown on the right. Taken from ref [172].*

- **Tapping mode**

Tapping mode overcomes the disadvantage of contact mode. In contact mode, the feedback loop needs adjustment to guarantee that it responds to the changes in sample topography fast enough but slow enough to avoid oscillations of the system, so the sample and the tip can easily suffer a high lateral force, thus leading to damage. In contrast, in tapping mode, the cantilever is oscillated normal to the sample at or near its resonance frequency, with the amplitude in the range of tens of nanometers. When it approaches the sample, the tip-sample interaction results in a shift of the resonance to lower frequency and a drop in its amplitude (**Figure 4-8**). The change in cantilever oscillation amplitude is recorded as the sample topography. The main parameter that needs to be monitored is thus the cantilever amplitude set point during the experiment.

Tapping mode significantly decreases the contact time between tip and sample as well as the lateral forces, thus it is much less destructive to sample. However, it is inherently unstable due to two main reasons. First, a high amplitude error caused by rough surfaces, especially those with sharp edges, or surfaces with high adhesion forces, will lead to high interaction force that can damage the cantilever. Second, the cantilever dynamics are relatively complicated, depending strongly on the amplitude set-point and sample properties, etc.

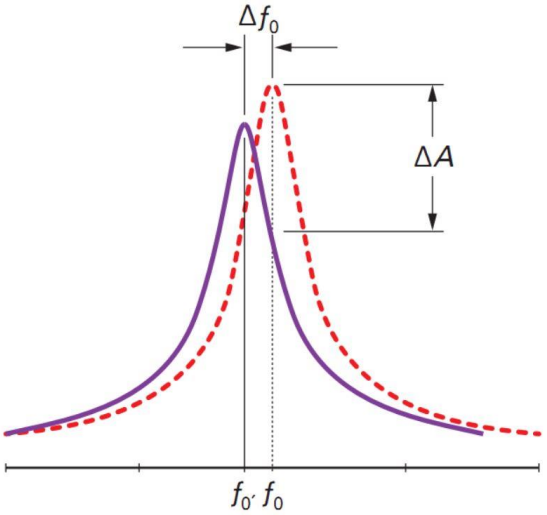

Figure 4-8 Resonance curve of a Tapping Mode cantilever above (red dash) and close to the surface (purple). *The resonance shifts to lower frequencies and exhibits a drop in amplitude. Taken from ref* [172].

- **Peak Force tapping mode**

Peak Force (PF) tapping mode combines the benefits of contact and tapping mode. PF tapping operates similarly to tapping mode but differs in two ways. First, the cantilever oscillates at frequencies well below the cantilever resonance. Second, the cantilever is retracted at the peak force, which is the triggering mechanism for the feedback loop. In contrast to contact mode, the z-piezo which drives the cantilever is modulated by a sine wave instead of a triangular one so that unwanted resonances at the turnaround points are avoided. These features protect the tip and sample from damage while allowing the tip-sample contact area to be minimized. **Figure 4-9a** shows the Force vs. Time curve, with the initial contact of the probe with the sample (B), peak force (C) and adhesion (D) points labelled. Using the Z-position information, the Force vs. Time curve can be transformed into a Force vs. Z position curve (**Figure 4-9b**), which can be analysed to obtain the peak interaction force and mechanical properties of the sample (**Figure 4-9c**), including modulus, adhesion, dissipation, and deformation.

Elastic Modulus is obtained by fitting the retract curve (**Figure 4-9c**) using the Derjaguin-Muller-Toporov (DMT) model:

$$F - F_{adh} = \frac{4}{3} E^* \sqrt{R\left(z - z_0\right)^3} \tag{4.4}$$

where R is the tip end radius, $z - z_0$ is the sample deformation, and E^* is the reduced modulus. If the sample's Poisson's ratio is known, the elastic modulus of the sample can be obtained by:

$$E^* = \left[\frac{1-\nu_s^2}{E_s} + \frac{1-\nu_{tip}^2}{E_{tip}} \right]^{-1}, \tag{4.5}$$

where E_{tip} is the tip modulus, ν_{tip} is Poisson's ratio of the tip, and ν_s is Poisson's ratio of the sample.

Adhesion force is the minimum force in **Figure 4-9c**. For an unfunctionalized tip, the adhesion reflects the chemical interaction between the tip and sample, including van der Waals forces, electrostatic forces, and forces due to the formation of a capillary meniscus. Notably, the adhesion typically increases proportionally to the tip end radius.

Energy dissipation is shown in yellow area in **Figure 4-9c** and calculated by:

$$W = \int \mathbf{F} \cdot d\mathbf{Z} = \int_0^T \mathbf{F} \cdot \mathbf{v} dt \tag{4.6}$$

where W is the energy dissipated in a cycle of interaction, $\mathbf{F}$ is the interaction force and $d\mathbf{Z}$ is the displacement vector. The energy dissipation comprises the work of adhesion, which is the area below the zero force reference and above the withdrawing curve, and the non-elastic energy dissipation, which is the hysteresis above the zero force reference.

Deformation is the separation between the point where the force is zero and the point corresponding to the peak force. Deformation reflects penetration of the tip into the surface at the peak force. Pure elastic deformation can be converted to the hardness of the material with a known tip shape and contact area.

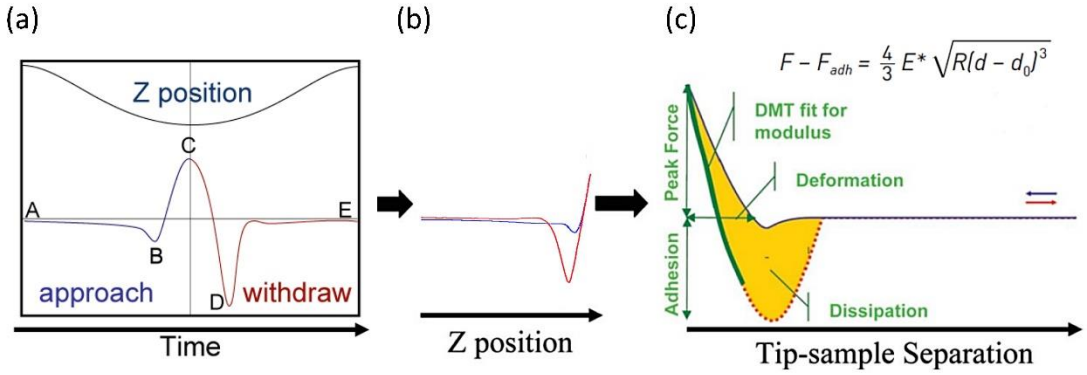

Figure 4-9 Force curves in PF tapping mode. *(a) Plot of force and piezo Z position as a function of time, including (B) jump-to-contact, (C) peak force, (D) adhesion. (b) Force vs. Z piezo position curve, transformed from the Force vs. Time curve. (c) Force vs. separation curve, transformed from the Force vs. Z piezo position. Taken from ref [173].*

In the device fabrication process throughout the thesis, we mainly used contact mode or tapping mode for the measurement of sample thickness and surface topography. For

interested regions of the sample where the devices are made, we chose tapping mode for surface topography characterization. In **Chapter 5**, we characterized the mechanical properties of graphite films using PF tapping mode. The AFM images show that mechanical properties differ for domains of different stacking orders among the graphite flakes. Thus, in addition to the Raman map, the AFM images of mechanical properties can serve as an alternative method to the visualization of the spatial distribution of different stacking orders in graphite films.

4.3 Transmission electron microscopy

Transmission electron microscopy (TEM) is one of the most direct observation techniques to elucidate the atomic structural information of crystals. TEM utilizes the wave-particle duality of electrons. It operates on a similar principle to that of optical microscopy, with the light replaced by electrons and glass lenses replaced by electromagnetic lenses. The electron beam travelling through a vacuum column of the microscope is focused by electromagnetic lenses and directed through the specimen. Then the electrons passing through the specimen are collected by the detector.

The main components of the microscope are electron source, condenser lenses, specimen holder, objective lens, intermediate and projector lenses and phosphor screen/camera (**Figure 4-10**). The electron source generates electron beams of good stability, brightness and coherence. For a perfectly coherent beam, electrons have the same wavelength and phase and originate from one point. The condenser lenses control the spot size and the intensity of the electron beam. The objective lens further controls the electron beam and magnifies the image. The diffraction lens passes the image of the diffraction pattern of the specimen from the back focal plane. The intermediate and projector lenses are magnifying lenses, all of which are electromagnetic lenses.

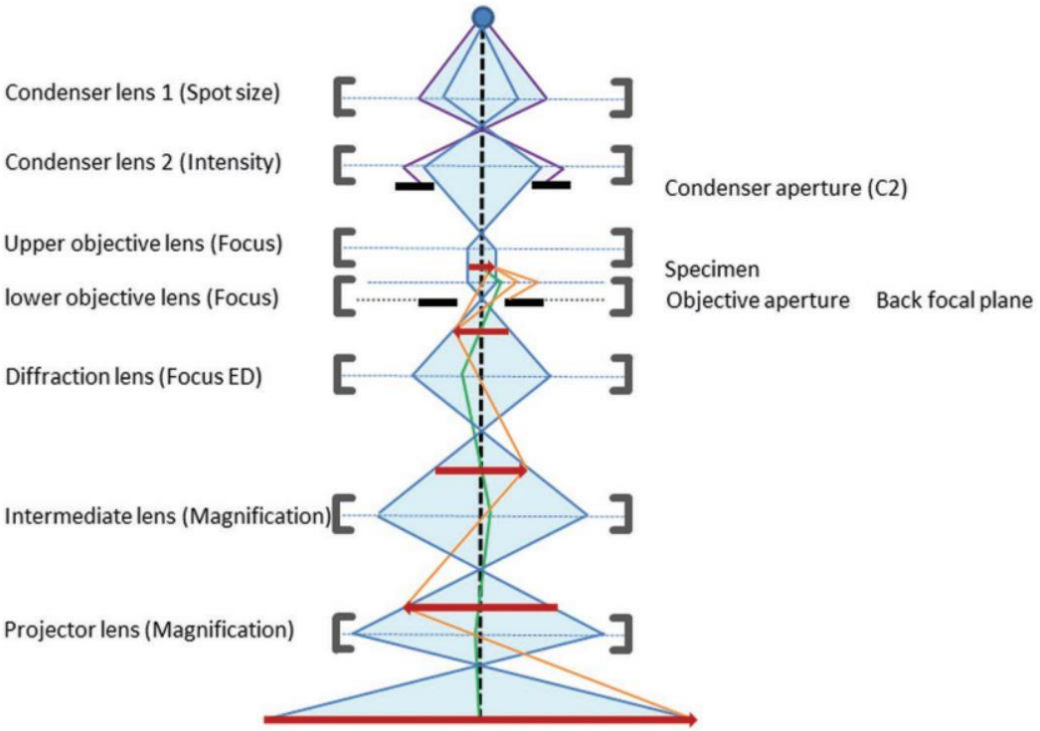

Figure 4-10 Schematic of an electron microscope. *The beam is shown in blue; grey brackets represent lenses, labelled with their names and the microscope function that controls them; black bars are apertures, and; the red arrow is the specimen and its (intermediate) images. The paths of scattered electrons are drawn in orange and green. Taken from ref [174].*

TEM imaging includes real space imaging and diffraction pattern imaging. When passing through the specimen, most electrons penetrate through the specimen, while some are scattered. For scattered electrons, the specimen serves as gratings. The scattered electrons are focused to a point in the back focal plane (**Figure 4-11**), forming a diffraction pattern by electron wave interference, which is described by the Bragg's law[174]:

$$2d \sin \theta_B = \lambda \tag{4.7}$$

where d is the spacing of the crystal lattice, λ is the wavelength of electron beam and θ_B is the scattering angle. The beam diffracted by angle $2\theta_B$ produces a spot, marked G. The distance between a diffracted (G) and transmitted (O) spot is inversely proportional to the corresponding lattice spacing in the sample. A specimen should contain all levels of spacing d. The real space image is formed at the image plane. Both the image plane and back focal plane can be projected onto the screen to be seen. An objective aperture or phase plate can be inserted into the back focal plane to increase the image contrast. A selected area aperture in the image plane allows the formation of diffraction patterns from a specific area of an image. Bright field and dark field images are formed using objective aperture and beam tilt to select unscattered beams or scattered beams.

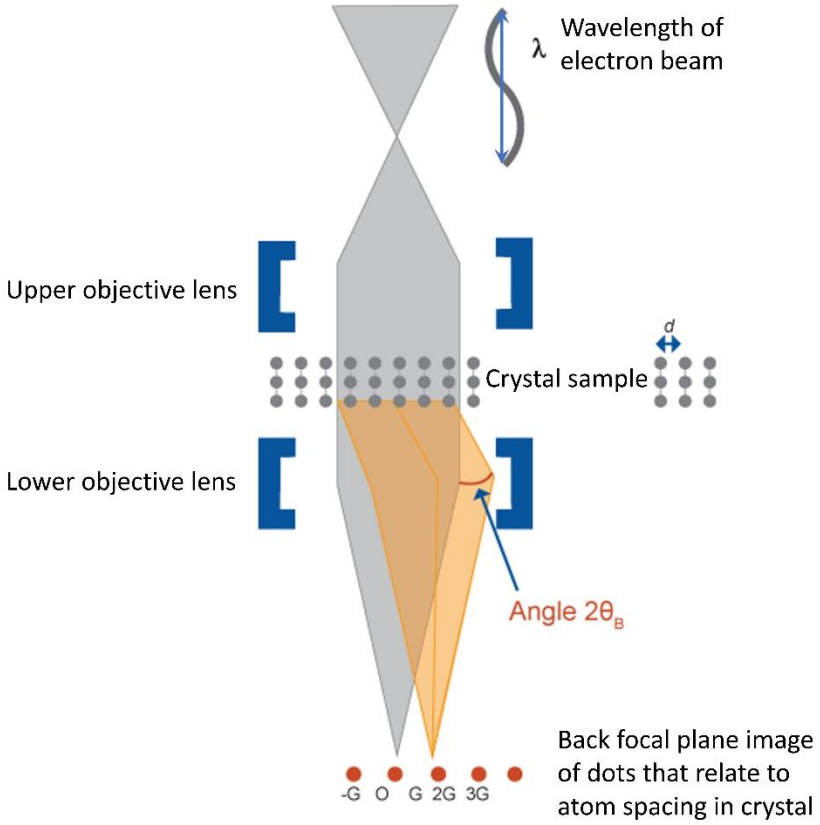

Figure 4-11 Simplified imaging system of TEM. *Electrons passing through the specimen are shown by the grey line. Electrons scattered by the specimen are shown by the orange line. Taken from ref [175] with modifications.*

Using different TEM techniques, we revealed atomic structural information of graphite, including different stacking orders that existed in thick graphite films and their cross-sectional structure, which are discussed in detail in **Chapter 5**. Specifically, high-resolution transmission electron microscopy (HRTEM) images using monochromatic illumination enables direct visualization of the lattice structure in graphite with atomic resolution. Using dark-field TEM (DF-TEM) imaging where electrons are scattered through selected diffraction angles, we distinguished between regions of different graphite crystallographic symmetry. Electron diffraction patterns, combined with DF-TEM imaging, allow us to quantify the contributions of different stacking order and the interlayer spacing in graphite films.

4.4 Electronic transport measurements

The electron transport study of the graphene/graphite devices in **Chapter 6** and **7** is based on the data acquired from electronic transport measurement, which provides abundant information of the electronic band structure and behaviour of electrons in the sample. The transport measurements were performed in a cryogenic measurements system, mainly using

standard low-frequency alternating current (AC) measurement with Lock-in amplifiers. The cryogenic measurements system generally consists of the cryostat, superconducting magnet, measurement and communication set up. There are several types of cryostats, including continuous flow cryostats, closed-cycle cryostats, and dilution cryostats, etc. The measurement performed in this thesis is in a dilution (10 mK), ^{3}He (300 mK), or dry ^{4}He (1.6 K) cryostat, depending on the required temperature.

The flow-cryostat comprises helium Dewar, variable temperature insert (VTI) and a sample insert. The Dewar is filled with liquid helium, which is pumped into the sample space through a small capillary with a valve (needle valve) that controls the flow of liquid helium. Temperature control of the sample is performed by the flow rate of liquid helium together with the VTI equipped with a sensor and heater, which monitors and regulates the temperature. The superconducting magnets in the helium bath wrap around the VTI, offering magnetic fields of up to 18 T.

In contrast, the closed-cycle cryostat needs not to be refilled with helium. It consists of a helium vapour chamber, where helium vapour is pumped and then cooled and recycled by an external mechanical refrigerator. The sample is held by a metallic cold plate inside a vacuum chamber which is in thermal contact with the helium vapour chamber.

By employing a dilution refrigerator, the cryostat can achieve temperature lower than liquid helium, down to 2 mK. The dilution refrigerator uses a mixture of helium-3 (^{3}He) and helium-4 (^{4}He) isotopes. The endothermic process of moving ^{3}He from the concentrated phase (practically 100% ^{3}He) into the dilute phase (about 6.6% ^{3}He and 93.4% ^{4}He) is the cooling power of the refrigerator.

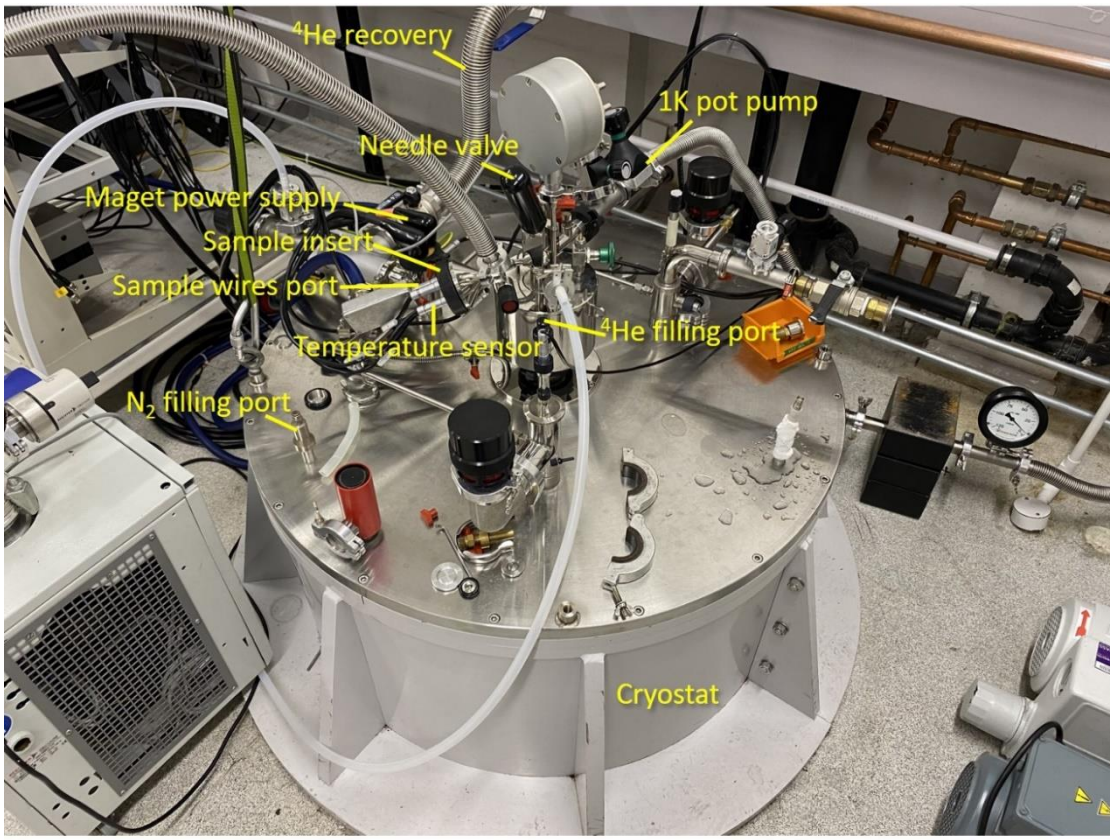

Figure 4-12 The flow-cryostat.

The electronic properties of the samples in this thesis are primarily probed by the four-terminal method, using a low-frequency (below 30 Hz) standard lock-in technique (SR830 lock-in amplifier). An AC current of around 0.1 to 1 μA sourced from the lock-in amplifier is supplied to the sample by placing a large resistor R_B (usually 10 MΩ) which bears the majority of the voltage drops. Schematics of the measurement is shown in **Figure 4-13**. In **Figure 4-13a**, the four-terminal geometry of measuring the sample's sheet resistance is given. In this configuration, we measure the longitudinal voltage drop V_{xx} in the channel when current I is applied to it. In the 2D system, the longitudinal resistance is given by $R_{xx} = V_{xx} / I = \rho_{xx} \cdot L / W$, where L and W are the length and width of the channel respectively, and ρ_{xx} is the longitudinal resistivity. In **Figure 4-13b**, the geometry of measuring the Hall effect is given. In this configuration, we measure the transverse voltage drop V_{xy} when current I is applied to the channel at a finite magnetic field B. Hall resistance is given by $R_{xy} = V_{xy} / I = \rho_{xy}$. In **Section 2.2.1** we relate ρ_{xy} to the carrier density $\rho_{xy} = -B / ne$ (Eq (2.38)), where one can extract the carrier density to calculate the hall mobility. The longitudinal and Hall conductivity are calculated from the tensor relation:

$$\sigma_{xx} = \rho_{xx} / \left(\rho_{xx}^2 + \rho_{xy}^2 \right) \tag{4.8}$$

$$\sigma_{xy} = \rho_{xy} / \left(\rho_{xx}^2 + \rho_{xy}^2 \right) \tag{4.9}$$

Since graphene has pronounced electric field effect[140], we can control the vertical displacement field strength and the carrier doping independently by varying both the top and bottom gate voltages (**Figure 4-13c**) in an hBN/graphene/hBN heterostructure[176], which is a ubiquitous method for transport measurement. The vertical displacement field D across the sample is $D = \left(D_b + D_t \right) / 2$ and the charge carrier density is determined by $n = \left(D_b - D_t \right) / e$. Here $D_b = \varepsilon_b \left(V_b - V_{b_0} \right) / h_b$ and $D_t = -\varepsilon_t \left(V_t - V_{t_0} \right) / h_t$, where $\varepsilon_{t,b}$ and $h_{t,b}$ are the dielectric constants and thicknesses of the top and bottom dielectric layers, respectively, and V_{b_0} and V_{t_0} are the effective offset voltages caused by environment-induced doping.

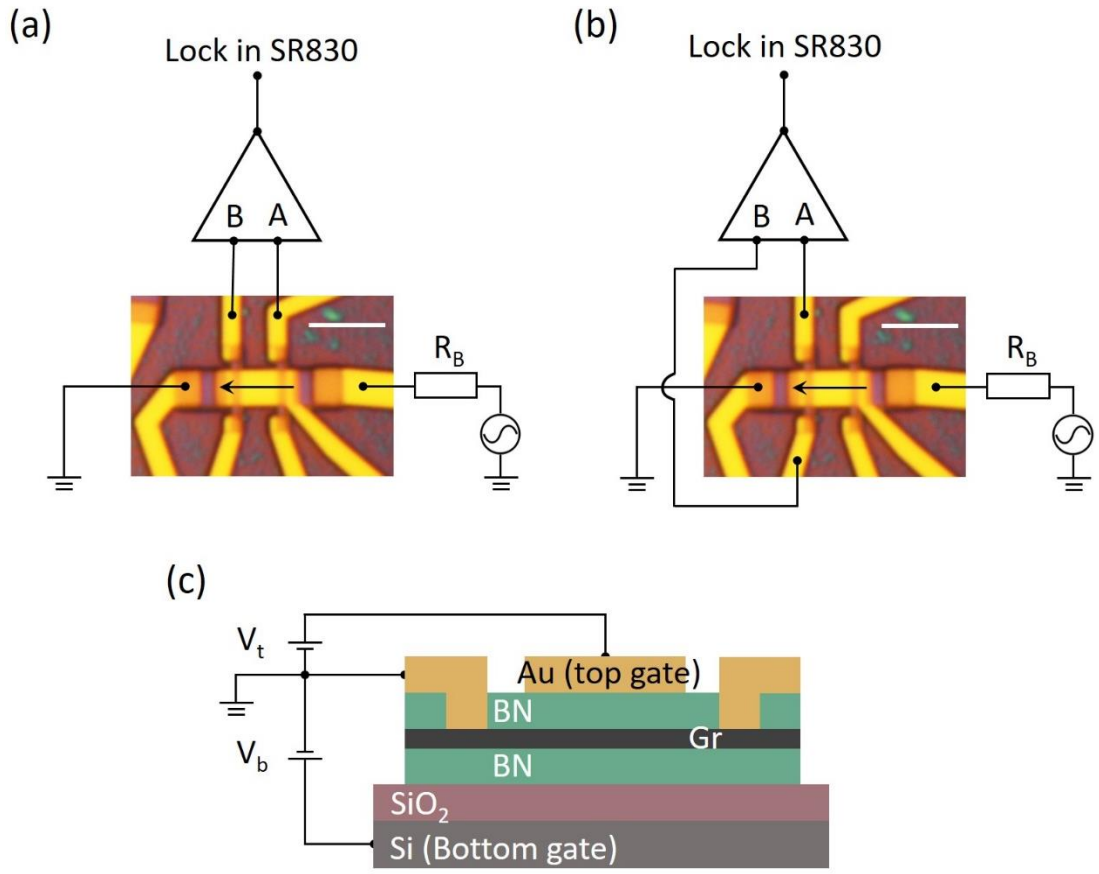

Figure 4-13 Measurement geometries.*Schematics for AC measurement of longitudinal resistance (a) and Hall effect (b). (c) The schematic cross-sectional view of the device shown in (a) and (b). The Au bar and doped Si serve as the top and bottom gate, respectively.*

Results

Chapter 5: Stacking order in graphite and directional encapsulation technique

5.1 Introduction

The ABC-stacked or rhombohedral graphite attracts significant attention because numerous theoretical works predict fascinating electronic properties due to many-body interactions within special topological states on the surfaces of rhombohedral graphite. At the same time, experimental works are limited to just an ABC trilayer, owing to challenges in the fabrication of this less stable form of graphite. In this chapter, we present a strategy to distinguish and control the stacking order (ABA or ABC) in graphite crystals tens of layers thick, using van der Waals technology.

First, we demonstrate the existence of domains composed of rhombohedral and Bernal stacking segments in mechanically exfoliated graphite films. These domains exhibit different responses in the Raman modes, mechanical properties, and infrared plasmon reflection. Then, after careful analysis and identification of these domains, we used the vdW stacking technique for directional (along zigzag or armchair edges) encapsulation of graphite with hBN. We found that performing hBN encapsulation along zigzag edges enables high-quality rhombohedral graphite films facilitating research of its yet undiscovered properties. This technique presents a new strategy in designing materials with novel electronic properties, which will have a significant effect on the research community, similar to that triggered by the development of crystallographic rotational alignment of 2D materials.

5.2 Stacking Order in Graphite Films Controlled by van der Waals Technology

Publication: Stacking Order in Graphite Films Controlled by van der Waals Technology

Journal reference: Nano Letters, 2019, 19, 12, 8526-8532.

DOI: 10.1021/acs.nanolett.9b03014

My contribution: discovered domains of different stacking orders in graphite by Raman spectroscopy, developed the idea of directional encapsulation of ABC-stacked graphite, prepared all the samples, performed Raman spectroscopy and atomic force microscopy measurement, analysed the data, prepared the figures and wrote the manuscript.

Full author list: Yaping Yang, Yi-Chao Zou, Colin R. Woods, Yanmeng Shi, Jun Yin, Shuigang Xu, Servet Ozdemir, Takashi Taniguchi, Kenji Watanabe, Andre K. Geim, Kostya S. Novoselov, Sarah J. Haigh and Artem Mishchenko.

Author contributions: A.M. directed and supervised the project. Y.Y. carried out sample preparation, performed Raman measurement and atomic force microscopy, developed the presented idea, analysed the data and wrote the manuscript. Y.Z. and S.J.H. performed transmission electron microscopy measurement. C.R.W. helped with the measurement of atomic force microscopy and carried out near field infrared nanoscopy measurement. Y.S., S.X., J.Y. and S.O. gave important suggestions to the project. T.T. and K.W. synthesized the hBN crystals. A.K.G and K.S.N. advised on the experiments. All authors discussed the results and commented on the manuscript.

NANO LETTERS
Cite This: Nano Lett. 2019, 19, 8526−8532
Letter
pubs.acs.org/NanoLett

Stacking Order in Graphite Films Controlled by van der Waals Technology

Yaping Yang,[†,‡] Yi-Chao Zou,[§] Colin R. Woods,[†,‡] Yanmeng Shi,[†,‡] Jun Yin,[†] Shuigang Xu,[‡] Servet Ozdemir,[†] Takashi Taniguchi,[∥] Kenji Watanabe,[∥] Andre K. Geim,[†,‡] Kostya S. Novoselov,[†,‡,⊥,○] Sarah J. Haigh,[§] and Artem Mishchenko*[,†,‡]

[†]School of Physics and Astronomy, University of Manchester, Oxford Road, Manchester, M13 9PL, United Kingdom
[‡]National Graphene Institute, University of Manchester, Oxford Road, Manchester, M13 9PL, United Kingdom
[§]School of Materials, University of Manchester, Manchester M13 9PL, United Kingdom
[∥]National Institute for Materials Science, 1-1 Namiki, Tsukuba, Ibaraki 305-0044, Japan
[⊥]Centre for Advanced 2D Materials, National University of Singapore, 117546, Singapore
[○]Chongqing 2D Materials Institute, Liangjiang New Area, Chongqing 400714, China

Supporting Information

ABSTRACT: In graphite crystals, layers of graphene reside in three equivalent, but distinct, stacking positions typically referred to as A, B, and C projections. The order in which the layers are stacked defines the electronic structure of the crystal, providing an exciting degree of freedom which can be exploited for designing graphitic materials with unusual properties including predicted high-temperature superconductivity and ferromagnetism. However, the lack of control of the stacking sequence limits most research to the stable ABA form of graphite. Here, we demonstrate a strategy to control the stacking order using van der Waals technology. To this end, we first visualize the distribution of stacking domains in graphite films and then perform directional encapsulation of ABC-rich graphite crystallites with hexagonal boron nitride (hBN). We found that hBN encapsulation, which is introduced parallel to the graphite zigzag edges, preserves ABC stacking, while encapsulation along the armchair edges transforms the stacking to ABA. The technique presented here should facilitate new research on the important properties of ABC graphite.

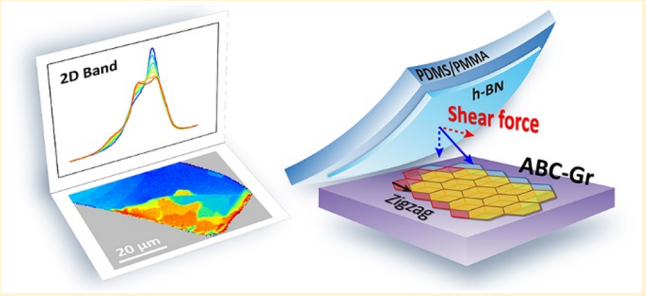

KEYWORDS: *Stacking order, rhombohedral graphite, domains, zigzag, van der Waals assembly*

The possible atomic stacking arrangements for the basal planes in *N*-layer graphite films encompasses 2^{N-2} different stacking sequences.[1] The two limiting cases are Bernal stacking (ABABAB...) and the rhombohedral stacking (ABCABCABC...) with very distinct electronic band structures.[2−5] The ABC-stacked graphite has attracted significant attention because of the promise for fascinating electronic properties. For instance, ABC trilayer, which was the main focus of research on the ABC-stacked allotrope, was shown to have a semiconducting behavior with a tunable band gap,[6,7] insulating quantum Hall states,[8] tunable Mott[9] and Chern[10] insulating states at a partially filled moiré minibands, the Lifshitz transition induced by a trigonal warping,[11,12] and the presence of chiral quasiparticles with cubic dispersion.[8,11] The band structure of bulk rhombohedral graphite hosts 3D Dirac cones, which are gapped out in finite-*N* ABC graphite films,[13] thus uncovering topologically protected surface states with nearly flat band dispersions.[13,14] These nearly flat bands at the surfaces are conducive to strongly correlated phenomena, giving rise to states with spontaneously broken symmetries, such as magnetic ordered states[15,16] and surface superconducting states.[17,18] Despite the promise of interesting physics, there are no experimental works on electronic transport in ABC-stacked graphite films thicker than tri- or tetralayer. This is due to the difficulty of producing the ABC allotrope on demand and of high quality. Here, we show that the probability of producing high-quality encapsulated ABC-stacked graphite can be greatly increased through the directional micromechanical assembly of graphite-hexagonal boron nitride (hBN) heterostructures.

Using bulk natural graphite crystals as a starting material, we exfoliated graphite films onto oxidized silicon substrates and used Raman spectroscopy to identify the presence of ABC stacking[19] (for optical transparency, we limited the thickness of flakes to 10 nm). The optical micrograph of one of the exfoliated flakes (Flake 1) is shown in Figure 1a. Despite the

Received: July 23, 2019
Revised: September 30, 2019
Published: October 30, 2019

DOI: 10.1021/acs.nanolett.9b03014
Nano Lett. 2019, 19, 8526−8532

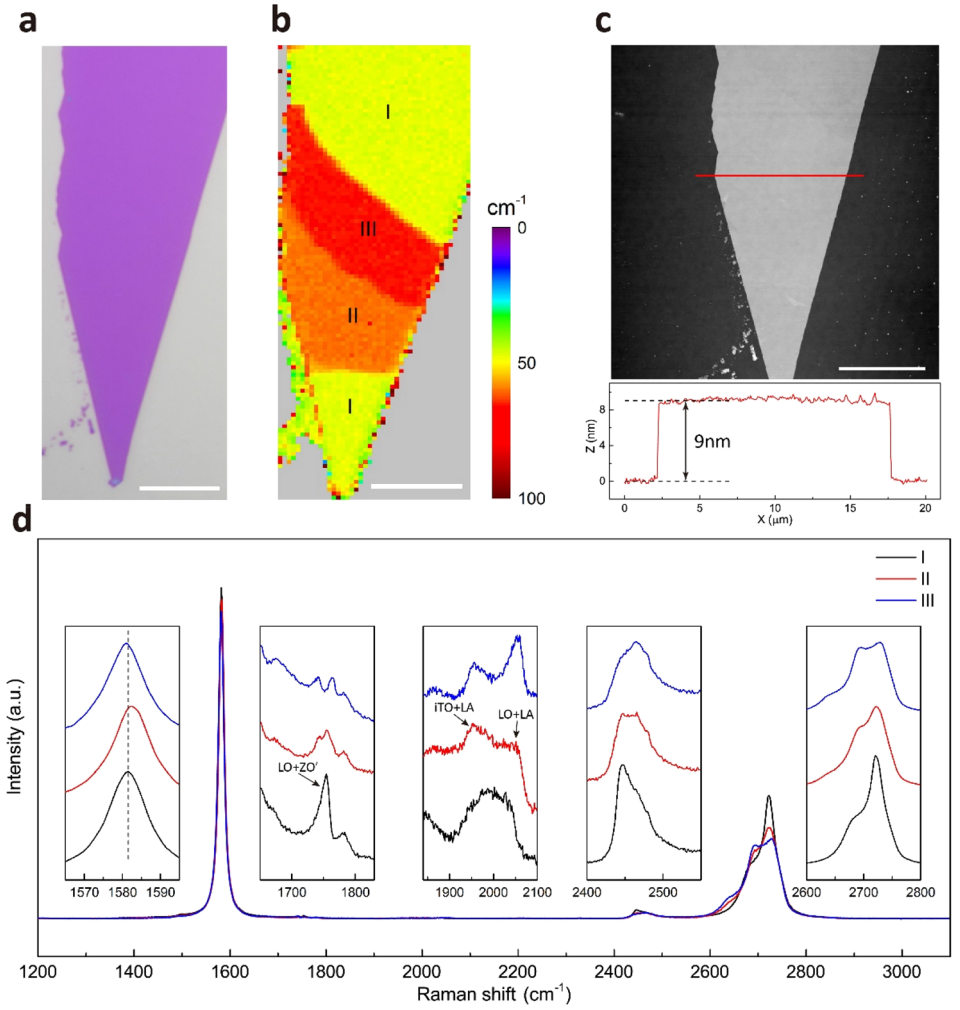

Figure 1. Raman spectroscopy of a 9 nm-thick graphite flake with different stacking domains. (a, b) Optical micrograph (a) and Raman map (b) of the 2D bandwidth of the flake. The step size of the map is 0.5 μm. (c) AFM image and height profile of the flake. The scale bars in (a−c) are 10 μm. (d) Raman spectra of different regions shown in (b). Insets are the magnified spectra of the G band (1565−1595 cm^{-1}), intermediate frequency modes (1650−1830 and 1840−2100 cm^{-1}), G* band (2400−2550 cm^{-1}), and 2D band (2600−2800 cm^{-1}). G band corresponds to the high-frequency E_{2g} phonon at the Γ point. The intermediate frequency modes are related to out-of-plane layer breathing phonons. Both G* band and 2D bands originate from the intervalley double resonance process. All these modes are sensitive to layer number and stacking order.

uniform thickness (≈9 nm or 27 ± 1 graphene layers) and nearly featureless topography, as shown by the atomic force microscopy (AFM) in Figure 1c, the Raman map of the 2D peak bandwidth exhibits three regions with strikingly different contrast, Figure 1b. According to previous reports,[20−23] these distinct regions should arise from the different stacking order in graphite. To further understand the origin of these three regions, we probed the detail of the Raman spectrum of each region, as shown in Figure 1d. In regions I and III, the 2D band shows the line shape characteristic of ABA and ABC stacking, respectively.[20,23] Also, the G band of region III is ≈1 cm^{-1} red-shifted compared to that of region I, which is also characteristic of ABC stacking.[21,23] For region II, the line shape of the 2D band displays a shape characteristic of mixed ABA and ABC stacking. Specifically, the intensity of the low-frequency shoulders of the 2D band (one ranging from 2600 to 2650 cm^{-1} and another ranging from 2675 to 2705 cm^{-1}) in region II is weaker than that in region III, while stronger than that in region I. Besides 2D and G modes, we also found a distinct Raman behavior for regions I, II, and III in the intermediate frequency range (multiple modes between 1650 and 2500 cm^{-1}); see insets in Figure 1d and the Supporting Information for details.

In our further study, we have focused on the 2D and G bands, since they have strong signals and both contain information about the stacking order. We observed a remarkable richness of different domains with distinct Raman scattering responses in another exfoliated graphite film (Flake 2), presented in Figure 2. We focused on the region encompassed by the dashed line in Figure 2a,c,d, which shows homogeneous thickness (see also Figure S1). According to refs 20 and 23 and supported by our measurements of the 2D band of Flake 1, the relative intensity of the lower frequency component (≈2680 cm^{-1}) to the higher frequency component (≈2725 cm^{-1}) changes with the stacking order. Thus, for Flake 2, we mapped the ratio of the integral area of the 2D band ranging from 2675 to 2705 cm^{-1} (indicated by blue rectangle in Figure 2b) to the area in the range of 2705 to 2735 cm^{-1} (indicated by the gray rectangle in Figure 2b). In the ratio map, plotted in Figure 2a, we can identify 7 regions with distinct ratios, indicating at least 7 domains with different stacking orders. The Raman maps of the 2D bandwidth and

DOI: 10.1021/acs.nanolett.9b03014
Nano Lett. 2019, 19, 8526−8532

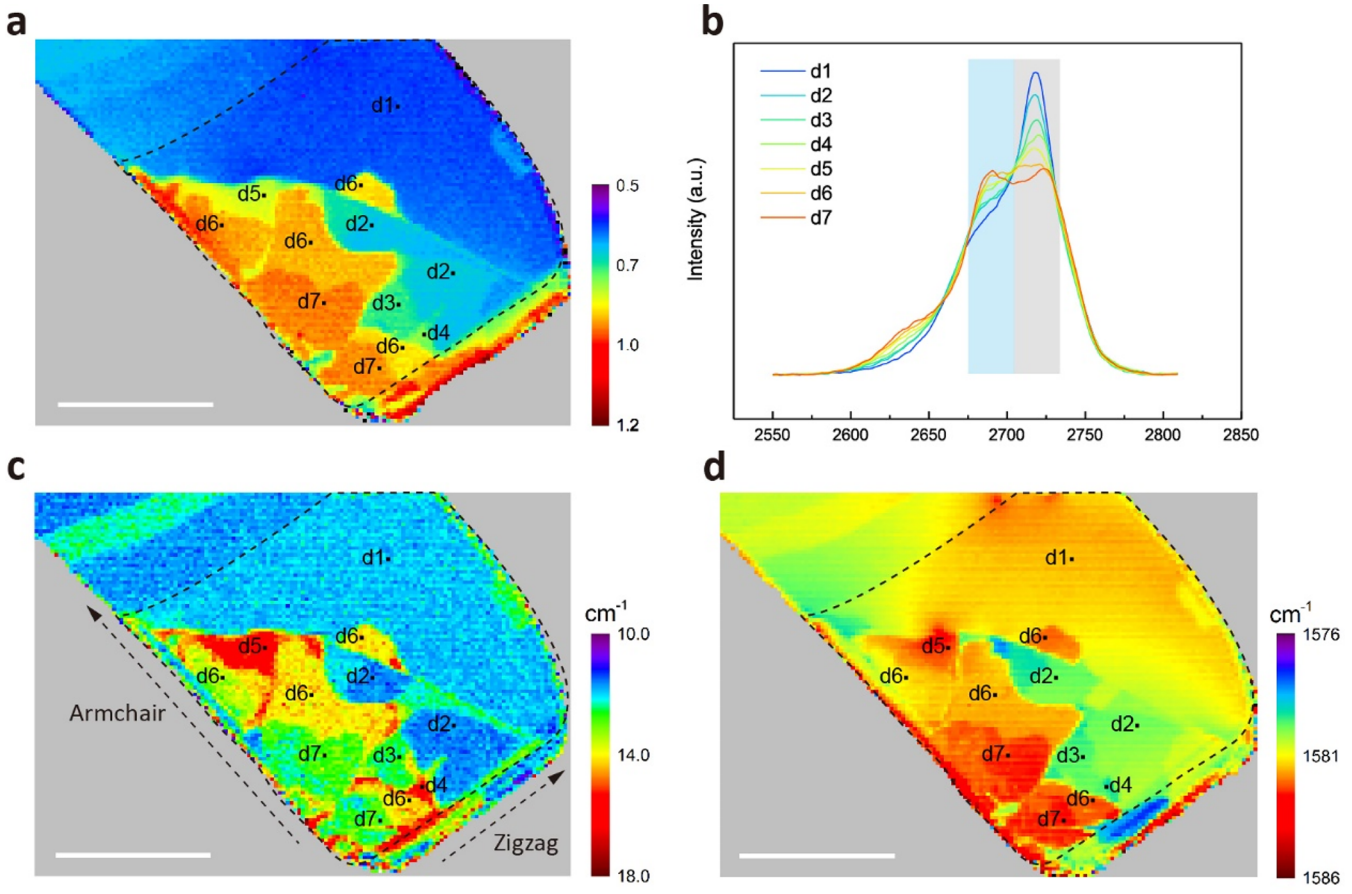

Figure 2. Evolution of 2D and G bands among different domains in a 6.5 nm-thick graphite flake. (a) Raman map of the ratio of the integral area of the 2D band ranging from 2675 to 2705 cm^{-1} (indicated by a blue rectangle) to that ranging from 2705 to 2735 cm^{-1} (indicated by a gray rectangle). (b) 2D band regions corresponding to domains d1 to d7 shown in (a). (c, d) Raman maps of the G bandwidth and position. The two orthogonal black dashed arrows in (c) indicate the edge chirality of the flake, confirmed by the D band intensity map (Figure S2c). The scale bars are 20 μm.

position (Figure S2a,b) also show consistent shape and distribution of the domains. The 2D mode (a D mode overtone) arises from a double resonance process, which makes it sensitive to electronic band structure and, thus, to the stacking sequence.[24,25] This suggests that the evolution of the 2D band line shape in regions d1 to d7 in Figure 2 reflects the increasing proportion of ABC stacking, from perfect ABA (region d1) to perfect ABC stacking (region d7).

The G mode originates from doubly degenerate optical phonons at the center of the Brillouin zone and is not affected by the electronic structure; the frequency and width of the G band reflect the changes in phonon dispersion due to the difference in the stacking sequence.[20,26] In the G bandwidth and position maps (Figure 2c,d), the distribution and shape of the domains match those in the ratio map and 2D bandwidth map (Figures 2a and S2a), also confirming the different stacking order of these domains. However, the trend of the G bandwidth and position among these domains is slightly different from the ratio map (Figure 2a), which we attribute to the influence of local strain.[27] We noticed three special regions where local mechanical deformation of the flake allows us to investigate the effect of the strain. There is a wrinkle diagonally across Flake 2 (seen in the dark field image and AFM in Figure S1), where an out of plane crease leads to increased strain in the graphite. For region d1, the G band position gradually decreases along the direction from the top of the flake to the edge of the wrinkle. A similar behavior can also be seen in the 2D band position map (Figure S2b). For region d5, where the wrinkle vanishes and therefore the strain should also be reasonably high, both the G bandwidth and position are higher than that of the adjacent regions. For region d7, there is a contamination bubble between the two domains (shown in Figure S1a), and thus, the strain induced broadening and softening of the G band also occur near the bubble.

Diffraction in the transmission electron microscope (TEM) allows one to measure the fraction of ABA and ABC stacking from the relative intensity of the first order diffraction peaks, and cross-sectional TEM imaging is able to directly show the local stacking order in different domains (shown in Figures 3 and S9). To further examine the stacking order present in plan-view ABC/ABA graphite specimens, selected-area electron diffraction (SAED) and dark field imaging (Figure 3) were used. For ABC graphite, the intensity of the first-order diffraction peaks is close to zero, whereas for ABA stacking the first-order diffraction peaks are more prominent.[28] Figure 3a shows an optical image taken from a typical ABC/ABA graphite flake (Flake 3, ≈6 nm thick), which was transferred onto the TEM grid; the corresponding 2D Raman map is shown in Figure 3b. Regions $1^{\#}$ and $2^{\#}$, ABC and ABA stacking, respectively, were further examined by electron diffraction, and the result is shown in Figure 3d,e. The fraction of ABC stacking can be evaluated by calculating the intensity ratio (R)

DOI: 10.1021/acs.nanolett.9b03014
Nano Lett. 2019, 19, 8526−8532

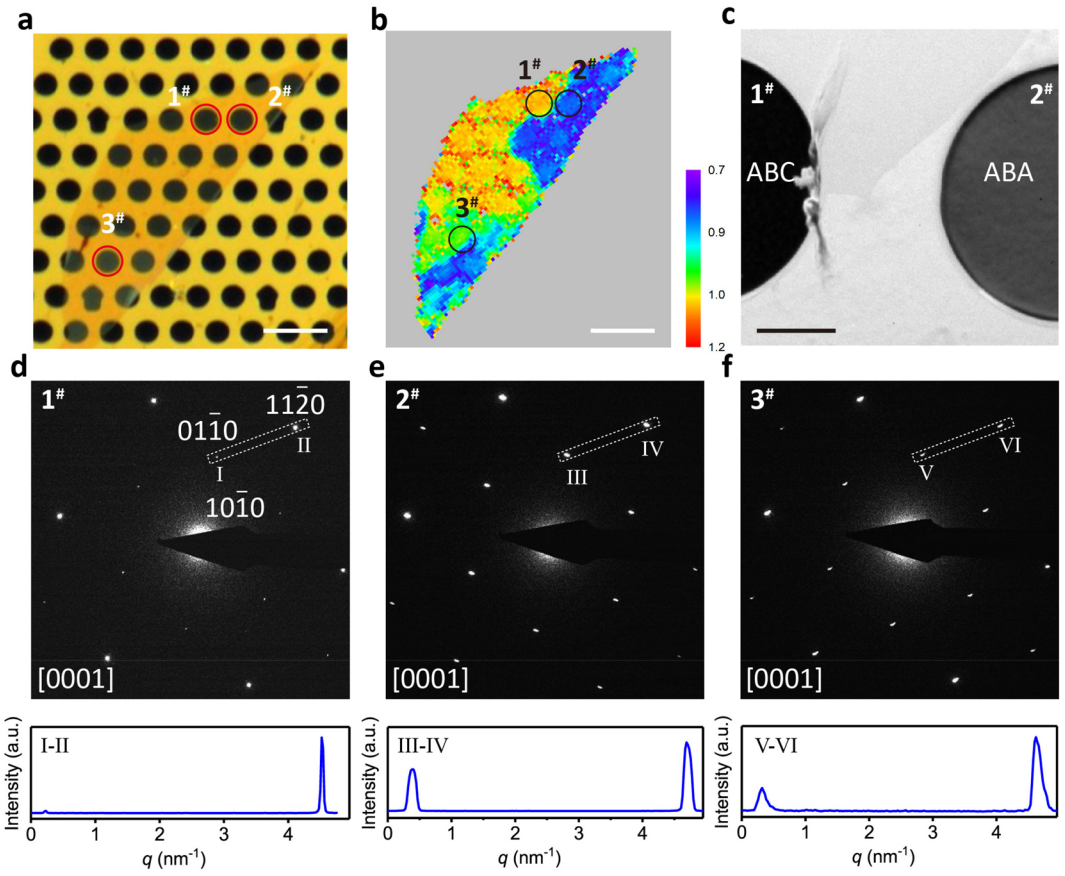

Figure 3. Plan-view TEM imaging and diffraction of an ABC/ABA graphite flake. (a) Optical micrograph of Flake 3 suspended on a TEM grid. (b) Corresponding Raman map of the ratio of the integral area of the 2D band ranging from 2675 to 2705 cm^{-1} to that ranging from 2705 to 2735 cm^{-1}. (c) Dark field TEM image showing the different domains in holes $1^{\#}$ and $2^{\#}$ obtained using the intensity from the $(10\bar{1}0)$ diffraction peak, which is much stronger for ABA domains. (d, e) SAED taken from region $1^{\#}$ and $2^{\#}$ and beneath these the line intensity profile measured along line I−II and III−IV, respectively, allowing comparison of the intensity of the first order $10\bar{1}0$ and second order $11\bar{2}0$ diffraction spots. (f) SAED patterns taken from region $3^{\#}$ with the bottom inset showing the line intensity profile taken along line V−VI. Scale bars, 10 μm for panels (a) and (b) and 1 μm for panel (c).

between the six innermost first-order $\{10\bar{1}0\}$ spots and the six second-order $\{11\bar{2}0\}$ spots[28] (see the Supporting Information). The calculated fraction of ABC for regions $1^{\#}$ and $2^{\#}$ are 96% and 8%, respectively, in excellent agreement with the Raman analysis.

Figure 3c shows the TEM dark field images performed with the $(10\bar{1}0)$ selected diffraction peak, where one can easily distinguish between the ABA and ABC stacked domains. The greater intensity in the dark field for region $2^{\#}$ indicates the presence of a high level of ABA stacking consistent with the Raman analysis. The holey SiN_x support also appears bright in the dark field image due to its large thickness. It is interesting to see that some ABC/ABA mixing regions (e.g., region $3^{\#}$) can still be preserved after the flake transfer according to the Raman map (Figure 3b). Figure 3f shows a diffraction pattern taken from region $3^{\#}$, and the calculated F_{ABC} is 81%, confirming a mixed region of ABC and ABA stacking. Such TEM analysis is too time-consuming to measure large numbers of flakes, but the correlation between our Raman and TEM analysis provides excellent calibration for large Raman data sets.

We exfoliated 617 flakes in total and found that 176 of them contained ABC-stacked regions (29%). We did not observe any effect of the flake thickness or tape peel direction on the success rate of production of ABC-stacked flakes. Among the flakes with ABC-stacked regions that have been Raman mapped (24 in total), 21 contained different stacking domains (88%). We found that domains with different stacking sequences in graphite films also have a distinct mechanical response and exhibit marked contrast in near-field infrared nanoscopy imaging, as shown in Figures S5 and S6. Generally, rhombohedral stacking in graphite is quite rare as it is energetically less stable compared to Bernal stacking; it was previously reported that in the exfoliated samples around 15% of the total area displays rhombohedral stacking.[20] However, our results demonstrate that, within almost all the graphite films containing regions of rhombohedral stacking, there exist domains with various proportions of rhombohedral stacking. The formation of these domains is most likely related to the slip-induced transformation of stacking order during micromechanical exfoliation, due to the unavoidable presence of shear force applied to graphite crystallites through a soft polymer stamp used for exfoliation (see the Supporting Information for details).

A shear force applied to graphite leads to a displacement of the graphene planes in a "stick−slip" fashion.[29] If the displacement occurs along zigzag edge directions, it preserves the stacking order, while displacement parallel to armchair edges alternates stacking order between ABA and ABC. This effect is illustrated in Figure 4a (using ABC trilayer as an

DOI: 10.1021/acs.nanolett.9b03014
Nano Lett. 2019, 19, 8526−8532

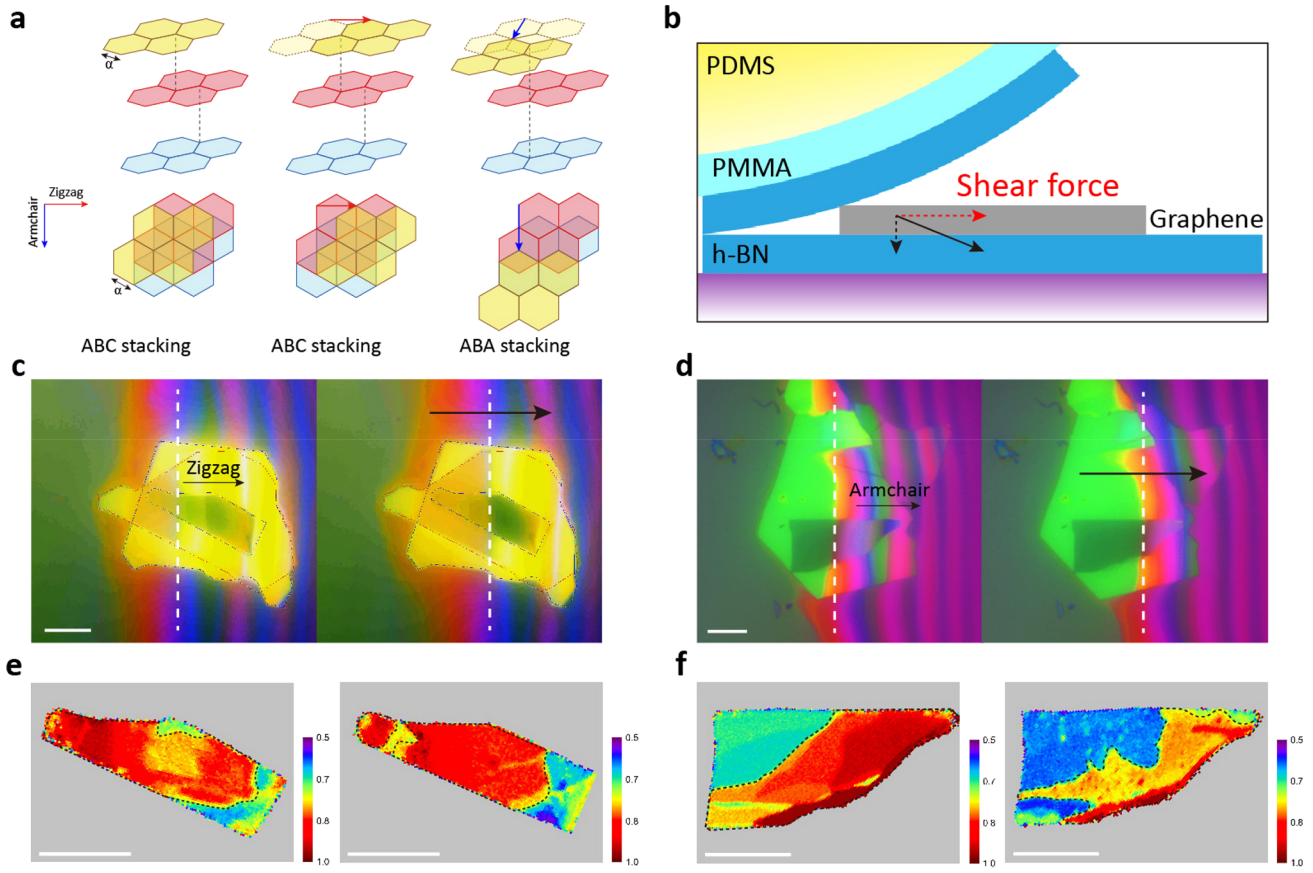

Figure 4. Stacking order control in graphite films. (a) Crystal structure and top view of the stacking order transformation of a model trilayer graphene. The top, middle, and bottom layers are labeled yellow, red, and blue, respectively. The left figure is the original ABC stacking trilayer. The middle and right figures are the final stacking order after the energetically favorable displacement of the top layer along zigzag (red arrow) and armchair (blue arrow) directions, respectively. α is the C−C bond length. (b) Schematic of the shear force applied to the flakes during micromechanical transfer. (c, d) Optical images of the pressing down process of PDMS during transfer along zigzag (Flake 4) or armchair (Flake 5) directions, respectively. The approximate edge of the contact area is marked by the white dashed line (note that the wavefront is actually an arc with a small curvature, which is approximated as a straight line although small deviations may result due to local contamination, etc.). The black arrows indicate the expansion direction of the edge. (e, f) Maps of the ratio of the integral area of the 2D band ranging from 2675 to 2705 cm^{-1} to that ranging from 2705 to 2735 cm^{-1} before (left) and after (right) encapsulation for Flakes 4 and 5, respectively. The outline of the ABC stacking region is marked by the black dashed line. The scale bars are 20 μm.

example); all the stacking orders of trilayer graphene after the relative movement of the top graphene layer with different displacement vectors are summarized in Table S1. The shear force along the armchair directions causes the movement of the graphene layers, leading to a transition of the stacking order. These shear-induced basal plane dislocations cause the graphene layers to wrinkle and kinks to arise.[30] This coincides with the reported result that the formation of kink bands can induce local stacking faults in layered crystals.[31] As the number of graphene layers increases, it is harder for the thicker flakes to fold since they have larger bending moduli, thus the need to induce stacking faults to accommodate bending explains the formation of the observed domains in graphite films.[31] The domain size is governed by a balance between stacking fault energy and dislocation energies, and the dislocations could be split into lower energy partial dislocations, which have stacking faults between them.[32] Interestingly, the number of observed different domains remains rather low. For instance, the sample in Figure 2 is approximately 18 layers-thick, which could lead to tens of thousands of domains with distinct stacking orders covering all the spectrum between pure ABA and pure ABC types, but just around seven were observed. Although some of the 7 regions shown in Figure 2 could perhaps be separated into smaller subdomains, our experimental results clearly demonstrate a preference for relatively large areas of uniform stacking (Figure S3).

Inspired by this mechanism of stacking transformation, we modified the encapsulation protocol for ABC-stacked graphite, aiming to significantly increase the chance of the survival of this energetically less stable stacking allotrope. We used the PDMS (polydimethylsiloxane) transfer technique,[33] in which viscoelastic PDMS enables precise control of the contact area between the PMMA (poly(methyl methacrylate)) adlayer and the substrate, including the contact area expansion direction while pressing down PDMS and the expansion speed. During the transfer process, there is a stress force while pressing down the top h-BN/PMMA/PDMS stack, which can be resolved into two components, the vertical one and the horizontal one that is parallel to the surface of the substrate, denoted as the shear force, as shown in Figure 4b. As discussed above, the transformation of the stacking order is mainly caused by the shear force applied to the exfoliated flakes. If the direction of this shear force is aligned with the zigzag edge direction of graphite crystal, then its stacking order will remain unchanged.

DOI: 10.1021/acs.nanolett.9b03014
Nano Lett. 2019, 19, 8526−8532

Therefore, the key is to distinguish the edge chirality of graphite films. If the angle between two adjacent edges of a graphite film is 30°, 90°, or 150°, the two edges have different chiralities, i.e., one armchair and the other zigzag. This edge chirality could be determined by Raman spectroscopy using the D band intensity. A perfect zigzag edge cannot produce a D peak, whereas the armchair edges contribute to the D band.[19,34] Thus, the intensity of the D band near the armchair edge is always stronger than that near the zigzag edge.[34] Alternatively, the rotational anisotropy of nonlinear optical second harmonic generation (SHG) offers another method to determine the crystal orientation of graphene layers.[35]

Using this modified van der Waals assembly process, we encapsulated an ABC-stacked graphite film (Flake 4) in which the angle between two of its edges is 150° (Figure S7a). The D band intensity map reveals the edge chirality (Figure S6b). During the transfer, we carefully pressed down the PDMS along the zigzag edge in order to align the shear force with the zigzag direction, as shown in Figure 4c. The Raman maps of Flake 4 before and after encapsulation (Figure 4e) clearly show that the ABC stacking order was successfully preserved. As a comparison, we also made another encapsulated ABC stacked graphite film (Flake 5) with the PDMS pressed down along the armchair edge of the graphite film during the transfer process. The result shows that after transfer the ABC stacking region has almost disappeared (Figure 4f). Our technique proved to be reproducible: we made five encapsulated samples using zigzag shear transfer, and for these flakes, large ABC stacking regions of the graphite films were preserved (Figure S11). Interestingly, we found that, among our encapsulated graphite samples where the whole flake was of ABC stacking order, this was more likely to be preserved after transfer, compared to flakes with mixed domains of a different stacking order. Our approach to micromechanical control of the crystal structure of graphite enables the preparation of high-quality hBN-encapsulated rhombohedral graphite films and should greatly promote electronic transport studies in this exciting material.

■ ASSOCIATED CONTENT

Supporting Information

The Supporting Information is available free of charge on the ACS Publications website at DOI: 10.1021/acs.nanolett.9b03014.

Experimental methods including exfoliation and van der Waals assembly, Raman, AFM, near-field infrared nanoscopy, TEM diffraction and cross-sectional imaging; demonstration of the distinct behavior of the three regions of Flake 1 in the combination Raman modes; optical and AFM images and Raman maps of Flake 2; description of the stacking order of the domains in graphite films; the distinct response of the domains in mechanical properties and near-field infrared plasmon reflection; determination of the edge chirality in graphite films using Raman spectroscopy; demonstration of the consistency of the Raman signal measured on the opposite surfaces of the graphite film; calculation of the fraction of ABC stacking and the cross-sectional TEM; optical images and Raman maps of samples encapsulated along the zigzag direction; optical images and Raman maps of samples encapsulated along arbitrary nonzigzag directions (PDF)

■ AUTHOR INFORMATION

Corresponding Author

*E-mail: artem.mishchenko@gmail.com.

ORCID

Yaping Yang: 0000-0002-4335-8518
Sarah J. Haigh: 0000-0001-5509-6706
Artem Mishchenko: 0000-0002-0427-5664

Notes

The authors declare no competing financial interest.

■ ACKNOWLEDGMENTS

A.M. and J.Y. acknowledge the support of EPSRC Early Career Fellowship EP/N007131/1. S.J.H. and Y.-C.Z. acknowledge financial support from the ERC H2020 Starter Grant EvoluTEM and EPSRC (EP/P009050/1) and assistance in diffraction analysis from Mr. Eupin Tien.

■ REFERENCES

(1) Min, H. K.; MacDonald, A. H. Chiral decomposition in the electronic structure of graphene multilayers. *Phys. Rev. B: Condens. Matter Mater. Phys.* **2008**, *77* (15), 155416.

(2) Mak, K. F.; Shan, J.; Heinz, T. F. Electronic structure of few-layer graphene: experimental demonstration of strong dependence on stacking sequence. *Phys. Rev. Lett.* **2010**, *104* (17), 176404.

(3) Bao, C.; Yao, W.; Wang, E.; Chen, C.; Avila, J.; Asensio, M. C.; Zhou, S. Stacking-Dependent Electronic Structure of Trilayer Graphene Resolved by Nanospot Angle-Resolved Photoemission Spectroscopy. *Nano Lett.* **2017**, *17* (3), 1564−1568.

(4) Koshino, M. Interlayer screening effect in graphene multilayers with ABA and ABC stacking. *Phys. Rev. B: Condens. Matter Mater. Phys.* **2010**, *81* (12), 125304.

(5) Avetisyan, A. A.; Partoens, B.; Peeters, F. M. Stacking order dependent electric field tuning of the band gap in graphene multilayers. *Phys. Rev. B: Condens. Matter Mater. Phys.* **2010**, *81* (11), 115432.

(6) Lui, C. H.; Li, Z. Q.; Mak, K. F.; Cappelluti, E.; Heinz, T. F. Observation of an electrically tunable band gap in trilayer graphene. *Nat. Phys.* **2011**, *7* (12), 944−947.

(7) Zou, K.; Zhang, F.; Clapp, C.; MacDonald, A. H.; Zhu, J. Transport studies of dual-gated ABC and ABA trilayer graphene: band gap opening and band structure tuning in very large perpendicular electric fields. *Nano Lett.* **2013**, *13* (2), 369−73.

(8) Bao, W.; Jing, L.; Velasco, J.; Lee, Y.; Liu, G.; Tran, D.; Standley, B.; Aykol, M.; Cronin, S. B.; Smirnov, D.; Koshino, M.; McCann, E.; Bockrath, M.; Lau, C. N. Stacking-dependent band gap and quantum transport in trilayer graphene. *Nat. Phys.* **2011**, *7* (12), 948−952.

(9) Chen, G.; Jiang, L.; Wu, S.; Lyu, B.; Li, H.; Chittari, B. L.; Watanabe, K.; Taniguchi, T.; Shi, Z.; Jung, J.; Zhang, Y.; Wang, F. Evidence of a gate-tunable Mott insulator in a trilayer graphene moiré superlattice. *Nat. Phys.* **2019**, *15* (3), 237−241.

(10) Chen, G.; Sharpe, A. L.; Fox, E. J.; Zhang, Y.-H.; Wang, S.; Jiang, L.; Lyu, B.; Li, H.; Watanabe, K.; Taniguchi, T.; Shi, Z.; Senthil, T.; Goldhaber-Gordon, D.; Zhang, Y.; Wang, F. Tunable Correlated Chern Insulator and Ferromagnetism in Trilayer Graphene/Boron Nitride Moiré Superlattice. 2019, *arXiv:1905.06535*. arXiv.org. e-Print archive. https://arxiv.org/abs/1905.06535.

(11) Zhang, L.; Zhang, Y.; Camacho, J.; Khodas, M.; Zaliznyak, I. The experimental observation of quantum Hall effect of l = 3 chiral quasiparticles in trilayer graphene. *Nat. Phys.* **2011**, *7* (12), 953−957.

(12) Koshino, M.; McCann, E. Trigonal warping and Berry's phase Nπ in ABC-stacked multilayer graphene. *Phys. Rev. B: Condens. Matter Mater. Phys.* **2009**, *80* (16), 165409.

(13) Ho, C. H.; Chang, C. P.; Lin, M. F. Evolution and dimensional crossover from the bulk subbands in ABC-stacked graphene to a three-dimensional Dirac cone structure in rhombohedral graphite. *Phys. Rev. B: Condens. Matter Mater. Phys.* **2016**, *93* (7), 075437.

DOI: 10.1021/acs.nanolett.9b03014
Nano Lett. 2019, 19, 8526−8532

(14) Xiao, R. J.; Tasnadi, F.; Koepernik, K.; Venderbos, J. W. F.; Richter, M.; Taut, M. Density functional investigation of rhombohedral stacks of graphene: Topological surface states, nonlinear dielectric response, and bulk limit. *Phys. Rev. B: Condens. Matter Mater. Phys.* **2011**, *84* (16), 165404.
(15) Olsen, R.; van Gelderen, R.; Smith, C. M. Ferromagnetism in ABC-stacked trilayer graphene. *Phys. Rev. B: Condens. Matter Mater. Phys.* **2013**, *87* (11), 115414.
(16) Pamuk, B.; Baima, J.; Mauri, F.; Calandra, M. Magnetic gap opening in rhombohedral-stacked multilayer graphene from first principles. *Phys. Rev. B: Condens. Matter Mater. Phys.* **2017**, *95* (7), 075422.
(17) Kopnin, N. B.; Ijäs, M.; Harju, A.; Heikkilä, T. T. High-temperature surface superconductivity in rhombohedral graphite. *Phys. Rev. B: Condens. Matter Mater. Phys.* **2013**, *87* (14), 140503.
(18) Muñoz, W. A.; Covaci, L.; Peeters, F. M. Tight-binding description of intrinsic superconducting correlations in multilayer graphene. *Phys. Rev. B: Condens. Matter Mater. Phys.* **2013**, *87* (13), 134509.
(19) Ferrari, A. C.; Basko, D. M. Raman spectroscopy as a versatile tool for studying the properties of graphene. *Nat. Nanotechnol.* **2013**, *8* (4), 235−46.
(20) Lui, C. H.; Li, Z.; Chen, Z.; Klimov, P. V.; Brus, L. E.; Heinz, T. F. Imaging stacking order in few-layer graphene. *Nano Lett.* **2011**, *11* (1), 164−9.
(21) Cong, C.; Yu, T.; Sato, K.; Shang, J.; Saito, R.; Dresselhaus, G. F.; Dresselhaus, M. S. Raman characterization of ABA- and ABC-stacked trilayer graphene. *ACS Nano* **2011**, *5* (11), 8760−8.
(22) Graf, D.; Molitor, F.; Ensslin, K.; Stampfer, C.; Jungen, A.; Hierold, C.; Wirtz, L. Spatially resolved Raman spectroscopy of single- and few-layer graphene. *Nano Lett.* **2007**, *7* (2), 238−42.
(23) Henni, Y.; Ojeda Collado, H. P.; Nogajewski, K.; Molas, M. R.; Usaj, G.; Balseiro, C. A.; Orlita, M.; Potemski, M.; Faugeras, C. Rhombohedral Multilayer Graphene: A Magneto-Raman Scattering Study. *Nano Lett.* **2016**, *16* (6), 3710−6.
(24) Maultzsch, J.; Reich, S.; Thomsen, C. Double-resonant Raman scattering in graphite: Interference effects, selection rules, and phonon dispersion. *Phys. Rev. B: Condens. Matter Mater. Phys.* **2004**, *70* (15), 155403.
(25) Cançado, L. G.; Reina, A.; Kong, J.; Dresselhaus, M. S. Geometrical approach for the study ofG′band in the Raman spectrum of monolayer graphene, bilayer graphene, and bulk graphite. *Phys. Rev. B: Condens. Matter Mater. Phys.* **2008**, *77* (24), 245408.
(26) Yan, J. A.; Ruan, W. Y.; Chou, M. Y. Phonon dispersions and vibrational properties of monolayer, bilayer, and trilayer graphene: Density-functional perturbation theory. *Phys. Rev. B: Condens. Matter Mater. Phys.* **2008**, *77* (12), 125401.
(27) Huang, M. Y.; Yan, H. G.; Chen, C. Y.; Song, D. H.; Heinz, T. F.; Hone, J. Phonon softening and crystallographic orientation of strained graphene studied by Raman spectroscopy. *Proc. Natl. Acad. Sci. U. S. A.* **2009**, *106* (18), 7304−7308.
(28) Latychevskaia, T.; Son, S.-K.; Yang, Y.; Chancellor, D.; Brown, M.; Ozdemir, S.; Madan, I.; Berruto, G.; Carbone, F.; Mishchenko, A.; Novoselov, K. S. Stacking transition in rhombohedral graphite. *Frontiers of Physics* **2019**, *14* (1), 13608.
(29) Dienwiebel, M.; Verhoeven, G. S.; Pradeep, N.; Frenken, J. W.; Heimberg, J. A.; Zandbergen, H. W. Superlubricity of graphite. *Phys. Rev. Lett.* **2004**, *92* (12), 126101.
(30) Soule, D. E.; Nezbeda, C. W. Direct Basal-Plane Shear in Single-Crystal Graphite. *J. Appl. Phys.* **1968**, *39* (11), 5122−5139.
(31) Rooney, A. P.; Li, Z.; Zhao, W.; Gholinia, A.; Kozikov, A.; Auton, G.; Ding, F.; Gorbachev, R. V.; Young, R. J.; Haigh, S. J. Anomalous twin boundaries in two dimensional materials. *Nat. Commun.* **2018**, *9* (1), 3597.
(32) Gong, L.; Young, R. J.; Kinloch, I. A.; Haigh, S. J.; Warner, J. H.; Hinks, J. A.; Xu, Z.; Li, L.; Ding, F.; Riaz, I.; Jalil, R.; Novoselov, K. S. Reversible loss of Bernal stacking during the deformation of few-layer graphene in nanocomposites. *ACS Nano* **2013**, *7* (8), 7287−94.
(33) Uwanno, T.; Hattori, Y.; Taniguchi, T.; Watanabe, K.; Nagashio, K. Fully dry PMMA transfer of graphene onh-BN using a heating/cooling system. *2D Mater.* **2015**, *2* (4), 041002.
(34) Cancado, L. G.; Pimenta, M. A.; Neves, B. R.; Dantas, M. S.; Jorio, A. Influence of the atomic structure on the Raman spectra of graphite edges. *Phys. Rev. Lett.* **2004**, *93* (24), 247401.
(35) Shan, Y.; Li, Y.; Huang, D.; Tong, Q.; Yao, W.; Liu, W. T.; Wu, S. Stacking symmetry governed second harmonic generation in graphene trilayers. *Sci. Adv.* **2018**, *4* (6), eaat0074.

DOI: 10.1021/acs.nanolett.9b03014
Nano Lett. 2019, 19, 8526−8532

Supporting Information

Stacking order in graphite films controlled by van der Waals technology

Yaping Yang[1,2], Yi-Chao Zou[3], Colin R. Woods[1,2], Yanmeng Shi[1,2], Jun Yin[1], Shuigang Xu[2], Servet Ozdemir[1], Takashi Taniguchi[4], Kenji Watanabe[4], Andre K. Geim[1,2], Kostya S. Novoselov[1,2,5,6], Sarah J. Haigh[3], Artem Mishchenko[1,2,]*

[1]*School of Physics and Astronomy, University of Manchester, Oxford Road, Manchester, M13 9PL, United Kingdom*

[2]*National Graphene Institute, University of Manchester, Oxford Road, Manchester, M13 9PL, United Kingdom*

[3]*School of Materials, University of Manchester, Manchester M13 9PL, United Kingdom*

[4]*National Institute for Materials Science, 1-1 Namiki, Tsukuba, 305-0044, Japan*

[5]*Centre for Advanced 2D Materials, National University of Singapore, 117546, Singapore*

[6]*Chongqing 2D Materials Institute, Liangjiang New Area, Chongqing, 400714, China*

**e-mail: artem.mishchenko@gmail.com*

1. Experimental methods

1.1. Exfoliation and van der Waals assembly

Graphite films were obtained by mechanical exfoliation of bulk graphite (NGS naturgraphit, Graphenium Flakes 25-30mm) onto the SiO_2 (290 nm)/Si substrate cleaned by oxygen plasma. During the exfoliation, the shear force mainly originates from peeling off the water-soluble tape. Whether the extra shear force is applied on top of the tape or not did not make a difference in getting ABC stacking flakes.

The transfer process (van der Waals assembly) can be briefly divided into three main steps: (i) The PMMA/PDMS/glass slide was prepared to pick up the h-BN which was mechanically exfoliated onto a Si/SiO_2 (290 nm) wafer; (ii) Then we used the h-BN/PMMA/PDMS/glass slide to pick up graphite flakes; (iii) Finally the graphite flake/h-BN was released onto the bottom h-BN on Si/SiO_2 (290 nm) wafer by peeling off the PMMA from the top h-BN.

1.2. Raman characterization

The Raman spectra were acquired by Renishaw Raman system with 1800 lines/mm grating, using linearly polarized laser radiation at the wavelength (photon energy) of 532 nm (2.33 eV). The laser power was kept below 3 mW on the sample surface to avoid laser-induced heating. The Raman spatial maps were taken with a step size of 0.5 µm. To extract the peak width, position and intensity of different bands, we fit the spectrum at each pixel in the spatial mapping to a single Lorentzian function. For the intermediate frequency range, the acquisition time was increased to 10 min because of the weak signal.

1.3. Atomic Force Microscopy (AFM)

The AFM images were taken by Bruker AFM system. The nanomechanical images were obtained by PeakForce Quantitative Nanoscale Mechanical (QNM) mode. The Scanasyst-Fluid+ cantilever with the silicon tip on nitride lever is used. The spring constant of the cantilever is 0.7 N/m.

1.4. Near-field infrared nanoscopy

The near-field infrared nanoscopy imaging was carried out by scattering-type Scanning Near-Field Optical Microscopy (sSNOM), based on tapping mode AFM, using Bruker Anasys nanoIR3 system. The Quantum Cascade Laser with the wavelength of 9090 nm (narrow-band) was focused onto the apex of the tip with Platinum Iridium coating and the resonant frequency of ≈350 kHz. Near-field optical images with spatial resolution better than 100 nm were taken simultaneously with the topography images. The enhanced optical near field interaction between the tip and sample depends on the electronic properties of the sample. Thus ABA- and ABC-stacked domains give different infrared responses due to their different electronic band structures.

1.5. Transmission electron microscope diffraction and cross-sectional imaging

For high resolution scanning transmission electron microscope (STEM) imaging, a probe side aberration corrected FEI Titan G2 80-200 S/TEM microscope was used with an acceleration voltage of 200 kV, probe convergence angle of 21 mrad, an annular dark field (ADF) inner angle of 48 mrad and a probe current of ≈80 pA. To ensure the electron probe was parallel to the basal planes, the cross-sectional sample was aligned to the relevant Kikuchi bands of the graphite crystal. The electron diffraction experiment was conducted using the same microscope but operated in TEM mode with an accelerating voltage of 80 kV.

Cross-sectional TEM specimens were prepared from graphite flakes on SiO_2/Si substrate covered by boron nitride, using Ga^+ focused ion beam (FIB) scanning electron microscope (SEM) (FEI Helios 660). The region of interest (ROI) was deposited with a narrow Pt strap (1 µm thick) to avoid charging and being damaged by the ion beam when creating the cross-sectional lamella. The ROI contains ABA and ABC stacked domains, confirmed by Raman measurement before FIB milling. Cross section lamellae were prepared

perpendicular to the armchair or zigzag edges of the graphite flakes, to facilitate orienting the crystal to perform atomic resolution STEM imaging. Then the lamella was cut from the substrate and transferred to a pillar on a specialist OmniProbe™ TEM grid, followed by 30 kV, 16 kV, 5 kV and 2 kV ion beam milling and polishing for electron transparency.

2. The distinct behavior of the three regions of Flake1 in the combination Raman modes (ranging 1650 cm^{-1} to 2500 cm^{-1})

The intensity of the combination modes in the range from 1650 cm^{-1} to 2100 cm^{-1} is very weak, roughly two orders of magnitude smaller than that of the G mode. These modes are related to out-of-plane layer breathing phonons, and have a direct sensitivity to layer number and stacking order.

In the range of 1650-1850 cm^{-1}, it is reported that the M band at ≈1750 cm^{-1} is attributed to LO+ZO' (in-plane longitudinal optical phonon and the out-of-plane interlayer breathing phonon) combination mode, based on an intravalley double-resonant Raman scattering process[1-5]. For ABA stacked multilayer graphene thicker than 6 layers, M band appears as a strong peak near 1750 cm^{-1}, while for ABC stacked graphene, M band splits into subpeaks with narrower widths as the number of layer increases[1, 6]. Our results in Figure 1d in the main text show consistent fingerprints of M band. In region I and III, M band exhibits the characters of ABA and ABC stacking, respectively, while in region II, M band splits into two subpeaks, displaying the transition line shape between ABA and ABC stacking. In the range of 1850-2100 cm^{-1}, there are two combinational modes, the iTO+LA (in-plane transverse optical phonon and longitudinal acoustic phonon) at ≈1950 cm^{-1} and LO+LA at ≈2050 cm^{-1} [2, 5]. From the bottom region I to region III, this band gradually splits into two subbands, corresponding to the two combinational modes, indicating the transition of the ABA stacking to ABC stacking.

In terms of the Raman band at ≈2450 cm^{-1}, named G* (or D+D'') band, it is assigned as the combination of one iTO phonon around the Brillouin zone corner K and one LA phonon in the intervalley double resonance process[7, 8]. In our results, G* band shows unique line shape in each region.

Among these Raman bands arising from the double resonance scattering process, there are two main reasons for their sensitivity to the stacking order. On one hand, the electronic structures of different stacking orders result in different values of the phonon wave vectors required to satisfy the double resonance process. On the other hand, the stacking order directly influences the phonon dispersions, thus affects the electron-phonon coupling processes. These stacking-order-dependent modes showing unique line shapes for different regions again verify the different stacking orders among these three regions.

3. Optical and AFM images and Raman maps of Flake2

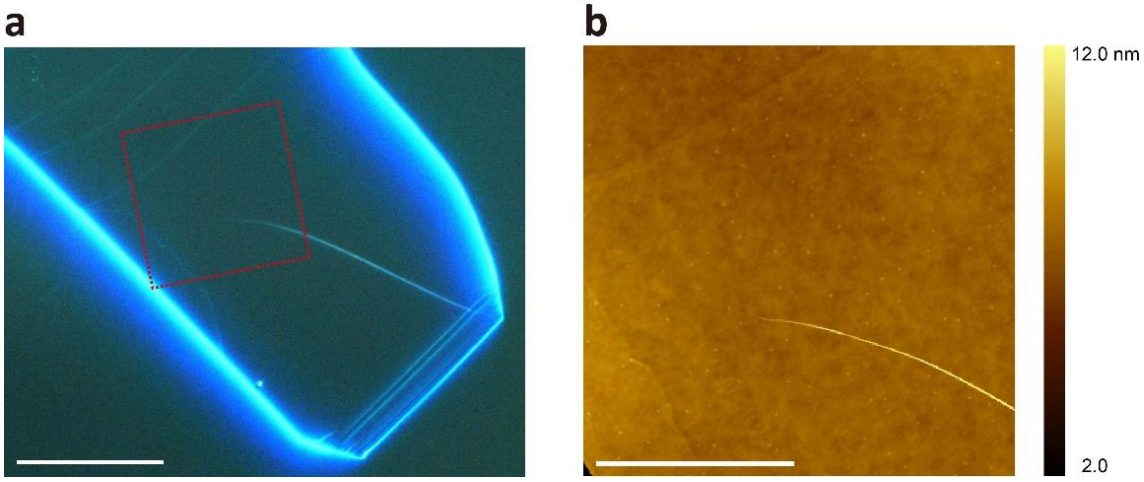

Figure S1. Optical and AFM images of Flake2. (a) Optical micrograph, scale bar is 20 μm. (b) AFM image of the dashed area in (a). The scale bar is 10 μm.

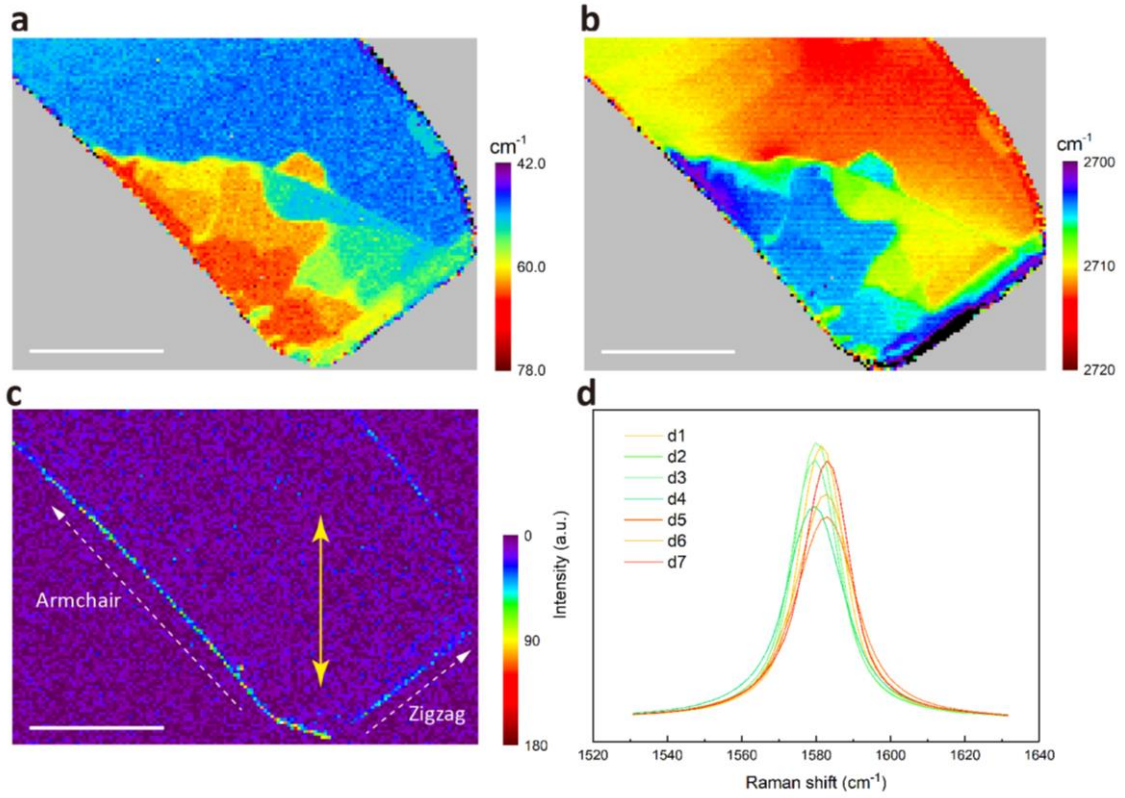

Figure S2. Raman maps of Flake2. (a) 2D band width map. (b) 2D band position map. (c) D band intensity map. The yellow arrow indicates the direction of laser polarization. The scale bars are all 20 μm. (d) G bands corresponding to the d1 to d7 domains shown in Figure 2d of the main text.

Apart from strain, the factors that also influence the line width and peak positions of G band and 2D band include the presence of doping or defects. The samples measured in our study are all freshly exfoliated flakes, which reduces the effect of doping. The D band intensity map (e.g., Figure S2c) indicates that our flakes are defect-free[9].

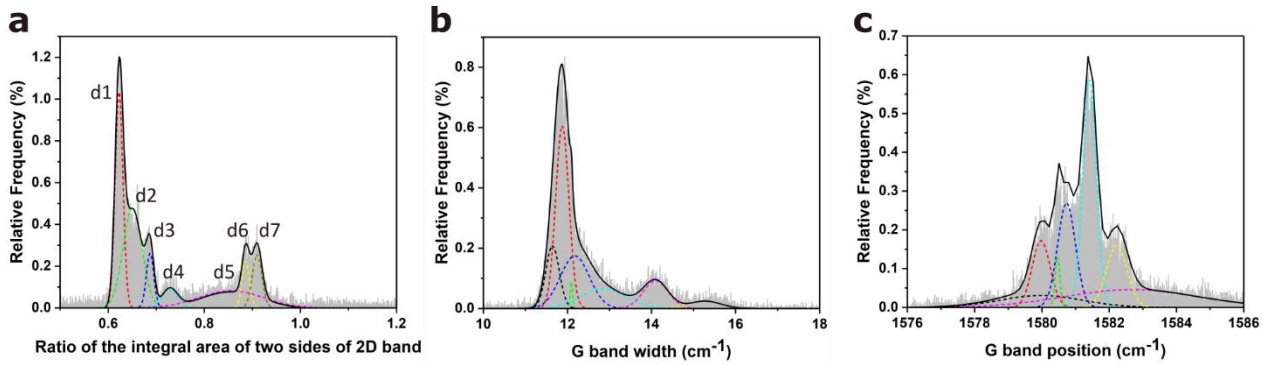

Figure S3. Histograms of the Raman maps presented in Fig.2 of the main text. Histogram of (a) Raman map of the ratio of the integral area of 2D band ranging 2675-2705 cm^{-1} (indicated by a blue rectangle) to that ranging 2705-2735 cm^{-1} (indicated by a gray rectangle), labels "d1" to "d7" mark the domains presented in Fig. 2 of the main text, (b) G band width and (c) position. The bin size of (a)-(c) is 0.001, 0.01 cm^{-1} and 0.01 cm^{-1}, respectively.

We plotted the histograms of each Raman map in Figure 2 of the main text. They clearly demonstrate a preference for relatively large areas of uniform stacking, which is consistent with the domains shown in the Raman maps. The histograms further verify the existence of the domains and show that only a small fraction of domains can be observed from large numbers of possible stacking orders.

4. The stacking order of the domains in graphite films

The layer arrangements of the two allotropes of graphite films (≥ 3 layers) are shown in Figure S4a,b. We labelled the two sets of inequivalent atoms in each layer with A and B, representing the two sublattices of the hexagonal structure. For Bernal stacking, the atoms of the i+2 layer lie exactly on top of the i^{th} layer, while for rhombohedral stacking, right above the center of the hexagons in the i^{th} layer, the atoms of the i+1 layer and i+2 layer are of inequivalent sites. In N-layer graphite film, as shown in Figure S4c, an alternating AB and BA stacking makes perfect Bernal stacking, while the repeated AB (or BA) stacking generates perfect rhombohedral stacking. For stacking faults, there are mixed segments of Bernal and rhombohedral stacking. In principle, for an N-layer graphite film there should be 2^{N-2} possible stacking sequences and the perfect ABA (or ABC) stacking corresponds to N-2 repeated Bernal (or rhombohedral) segments. The proportion and distribution of rhombohedral stacking segments in the stacking sequence of graphite film are the two important factors that affect its electronic structure, thus changing the Raman scattering response. For Flake2, the stacking orders of regions d1 and d7 should be perfect ABA and ABC stacking respectively. For regions d2 to d6, each of these domains has its specific proportion and distribution of Bernal and rhombohedral stacking segments.

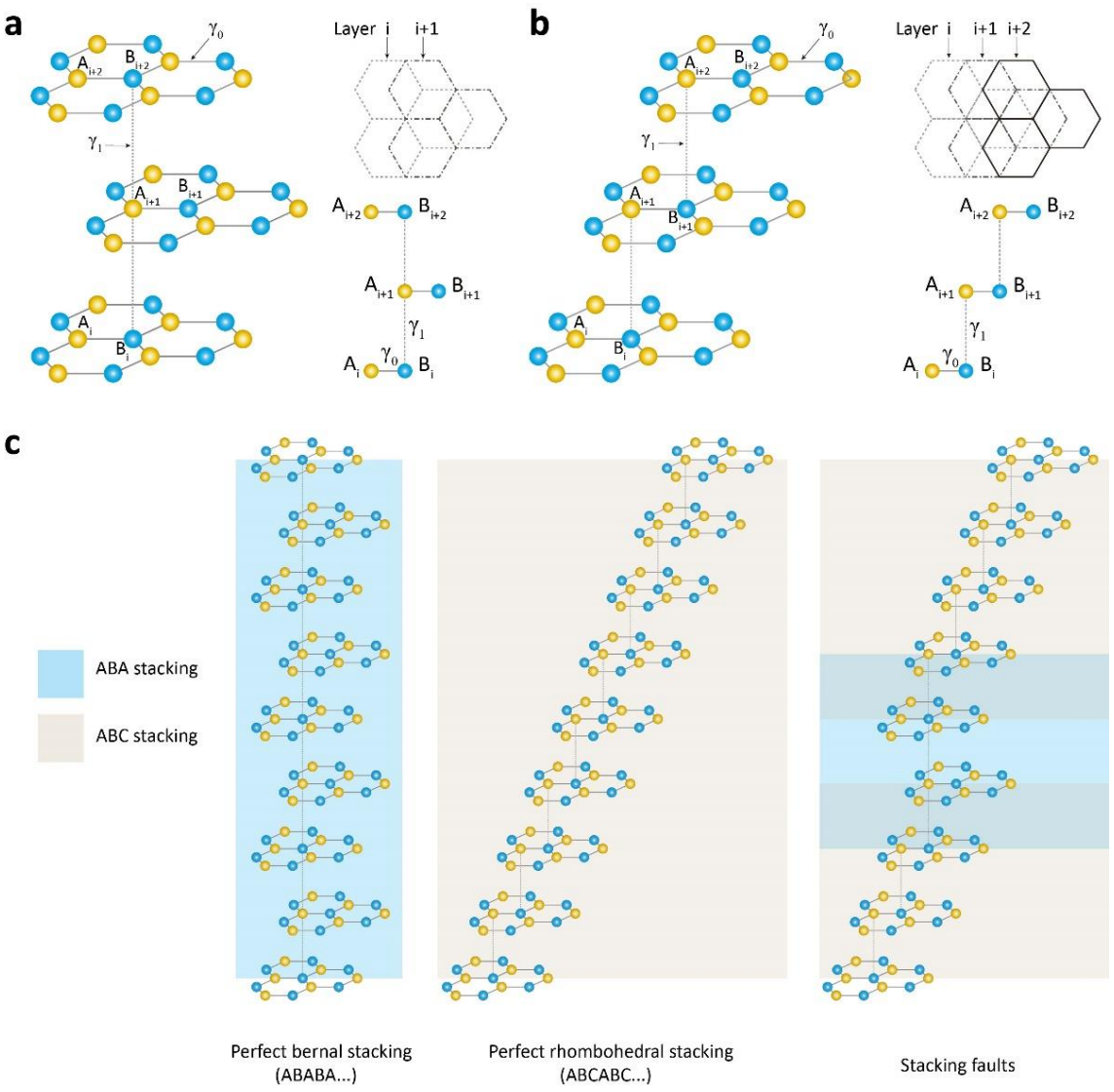

Figure S4. Atomic structures of ABA and ABC stacking and the schematic of stacking faults. (a,b) Atomic structures of Bernal stacking and rhombohedral stacking, i is the layer index. The blue and yellow spheres represent the A and B sublattices of the graphene honeycomb structure. In each panel, the top right figure is the top view and the bottom right figure is the side view of the unit cell. The hopping parameters γ_0 and γ_1 describe the nearest neighbor coupling within each layer and the coupling of the interlayer vertical bonds respectively. (c) Schematics of perfect ABA stacking, perfect ABC stacking and stacking faults with Bernal and rhombohedral stacking segments.

5. The distinct response of the domains in mechanical properties and near-field infrared plasmon reflection

We performed Quantitative Nanoscale Mechanical mode of AFM on another exfoliated graphite film (Flake6), as shown in Figure S4. The Raman map of the ratio of the integral area of 2*D* band ranging 2675-2705 cm^{-1} to the area ranging 2705-2735 cm^{-1} (Figure S5a) indicates the existence of different domains. In the AFM topography image (Figure S5b), the flake shows the homogeneous thickness and no domains are visible. Nevertheless, the mechanical channels of AFM (Figures S5c-f), which reflect the elastic modulus of the sample, exhibits several regions with distinctly different contrasts and matched shape and dimensions compared to the Raman map.

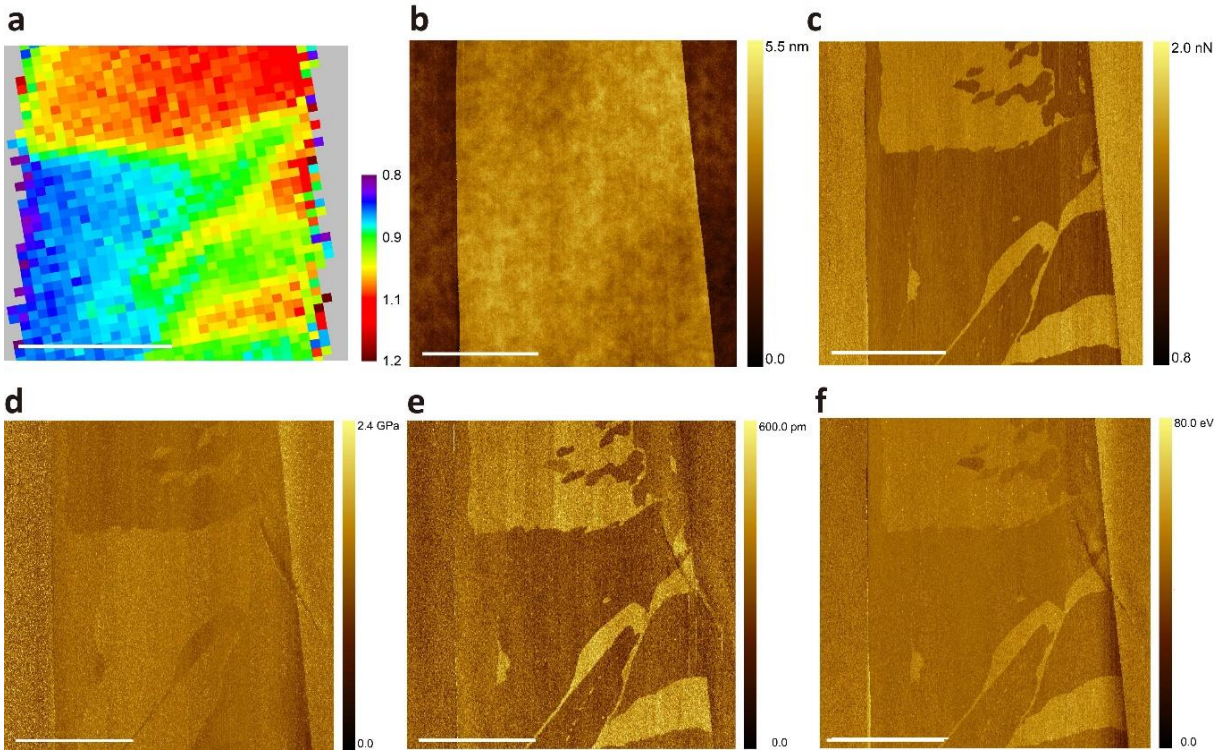

Figure S5. The correspondence between Raman map and mechanical response in AFM of graphite film with different domains. (a) Raman map of the ratio of the integral area of 2D band ranging 2675-2705 cm^{-1} to that ranging 2705-2735 cm^{-1}. (b) AFM topography of Flake6. (c-f) The adhesion, Derjaguin-Muller-Toporov (DMT) modulus, deformation and dissipation channels of the flake taken at Quantitative Nanoscale Mechanical mode. The flake is ≈1.5 nm in thickness. The scale bars are 5 μm.

We performed near-field infrared nanoscopy on another exfoliated graphite film (Flake7) with different domains (Figure S6c). In the AFM topography image (Figure S6a), the flake shows the homogeneous thickness and no domains are visible whereas the near-field infrared nanoscopy image exhibits patterns which match those in Raman map.

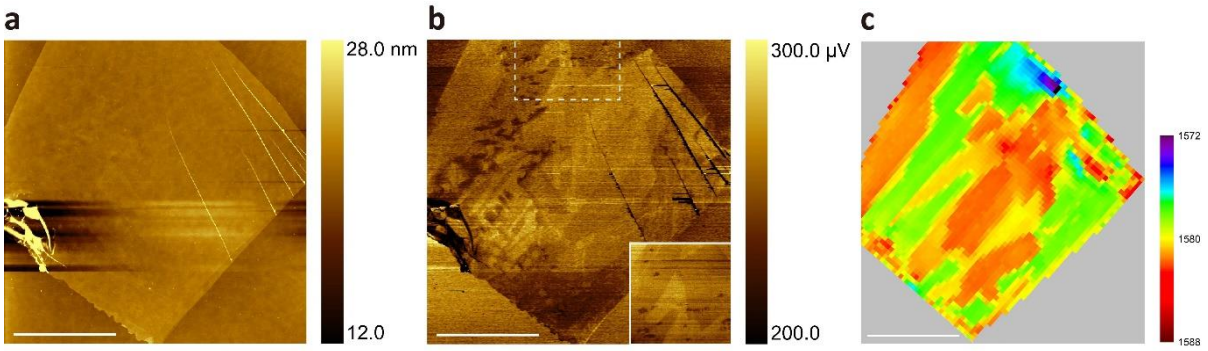

Figure S6. The correspondence between Raman map and near-field infrared nanoscopy image of graphite film with different domains. (a) AFM topography of Flake7. (b) The NF2-R channel of near-field infrared nanoscopy. (c) Raman map of the *G* band position. The flake is ≈1.5nm in thickness. The scale bars are 10 μm.

6. Edge chirality determination of graphite films by Raman spectroscopy

It is reported that D band in the Raman spectrum can be used to determine the chirality of the graphene edges[10-12]. A perfect zigzag edge cannot produce a D peak in the double resonance process, whereas the boundary conditions of the double resonance scattering process are only satisfied by the armchair edges[10, 13]. Thus the intensity of the D band near the armchair edge is always stronger than that near the zigzag edge[11, 13-15]. Another feature of D band is that its intensity shows a strong polarization dependence: $I(D) \propto \cos 2\theta$ or $\cos 4\theta$, where θ is the angle between laser polarization and the flake edge[12, 15].

If the angle between two adjacent edges is 30° (modulo 60°), the two edges should be armchair and zigzag respectively. We selected the graphite flakes with these special angles (30°, 90°, or 150°) and then put them in a way that the direction of laser polarization lies in the angular bisector of the angle between the adjacent edges, as shown in Figure S7, in order to diminish the influence of polarization dependence of different edges. According to the different responses of edge chirality to the D band, the edge with a stronger D band intensity should be armchair, and the other should be zigzag. Even though the edges of graphite flakes are not always perfectly smooth, they are on average predominantly either zigzag or armchair in nature, allowing to determine the edge chirality by Raman characterization.

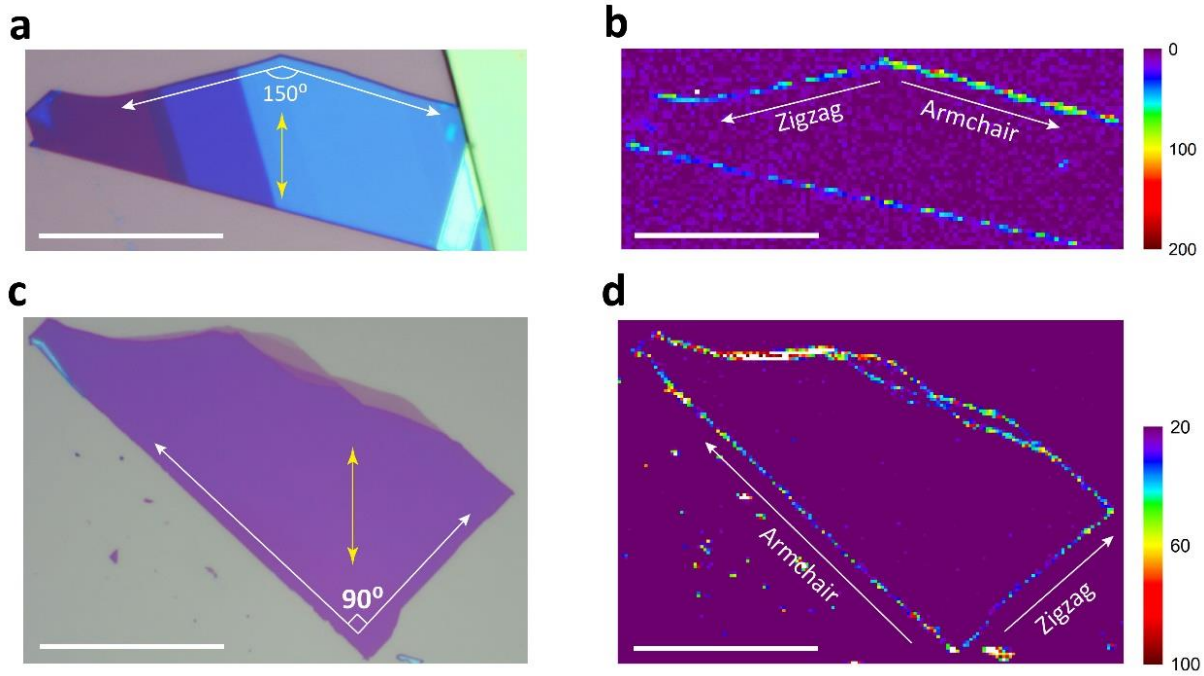

Figure S7. Edge chirality determination from Raman D band. (a) Optical micrograph of Flake3. (b) D band intensity map of Flake3. (c) Optical image of Flake4. (d) *D* band intensity map of Flake4. The yellow arrows in (a) and (c) indicate the direction of laser polarization. The scale bars are 20 μm.

Table S1. Transformation of the stacking order of trilayer graphene along the displacement vector (d is the distance of energy favorable displacement, α is the C-C bond length, and n is an integer).

Edge type along the dislocation vector			zigzag	armchair	
Origin stacking type	ABC	d	√3nα	(3n+1) α or (3n+2) α	3nα
		Final stacking type	ABC	ABA	ABC
	ABA	d	√3nα	3nα	(3n+1)α or (3n+2)α
		Final stacking type	ABA	ABA	ABC

7. Consistency of the Raman signal measured by both sides of the graphite film

To confirm that the Raman signal comes from the entire graphite flake rather than the first few layers of the flake, we carried out the Raman spectroscopy on both sides of a suspended graphite flake (Flake8) with the thickness of around 9 nm (Figure S8b). The graphite flake was transferred onto a MoS_2/Si_3N_4 grid with the diameter of the holes being around 2 μm, Figure S8a. Figures S8c and S8d show the 2D band width maps of the suspended region measured while the top side and back side of the sample were facing upwards, respectively. The two Raman maps again show different stacking order in the suspended region among the flake and the distribution of the domains are consistent between the two maps, which means that the laser can penetrate through the flake with the thickness of at least 9nm.

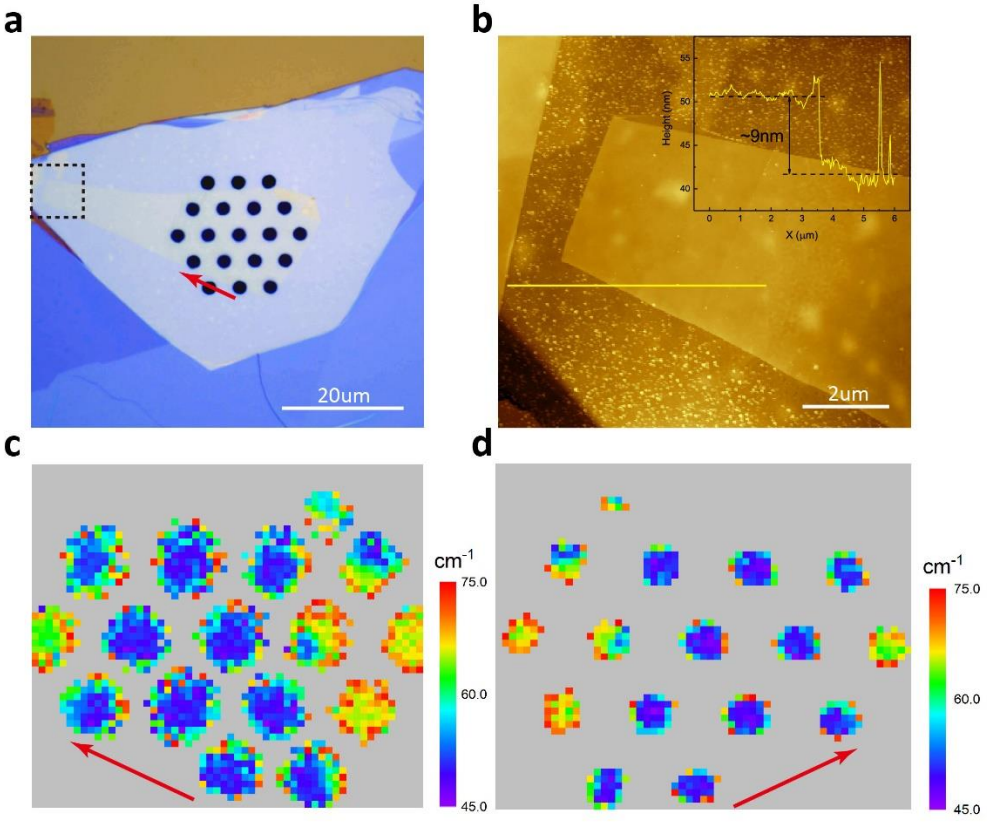

Figure S8. 2D band width Raman maps measured by both sides of the graphite film. (a) Optical micrograph of Flake8 suspended on MoS_2/Si_3N_4 grid. (b) AFM image of the dashed line region in (a) and height profile of the flake. (c) 2D width Raman maps of Flake5 with the top side facing upwards and (d) with the back side facing upwards. The red arrows in panels (a,c,d) indicate the layout of the holes covered by graphite film. Panels (c) and (d) are of mirror symmetry and the distribution of the domains in each panel match each other.

8. Calculation of the fraction of ABC stacking and the cross sectional TEM

To evaluate the fraction of ABC stacking, the intensity ratio (R) between the six inner-most first-order $\{10\bar{1}0\}$ spots and the six second-order $\{11\bar{2}0\}$ spots is firstly calculated by:

$$R = \frac{\sum_{i=1}^{6} I_i^{(1)}}{\sum_{i=1}^{6} I_i^{(2)}},$$

where $I_i^{(1)}$ and $I_i^{(2)}$ are the intensity of each of the first- and second-order peaks. The fraction of ABA stacking and ABC stacking can then be calculated by: [16]

$$F_{ABA} = \frac{R}{0.444} - 0.005\,,$$
$$F_{ABC} = 1 - F_{ABA}.$$

According to the method above, the calculated R for hole 1# and 2# are 0.02±0.01 and 0.41±0.01 respectively, giving the fraction of ABC for hole 1# and 2# as 96% and 8%, respectively.

For atomic-resolution cross-sectional S/TEM imaging, a dual-beam FIB/SEM instrument was used to prepare an electron transparent cross-sectional TEM specimen (see Methods section). The region of interest (ROI) contains both ABA and ABC stacked domains, confirmed by Raman mapping (black dashed region in Figure S9c). The ROI is then covered by BN flake as a protection layer, and located by correlating its optical image and Raman mapping (Figures S9a and c) with SEM imaging inside the FIB/SEM facility (Figure S9b) for cross-section specimen preparation. In the high-resolution STEM image (Figure S9d), individual atomic layers of the graphite flake are clearly resolved and the number of layers (9 layers for graphite) can be easily counted. As shown in Figure S9d, cross-sectional imaging reveals the existence of different stacking sequences in the selected region, which contains regions of both ABA and ABC stacking.

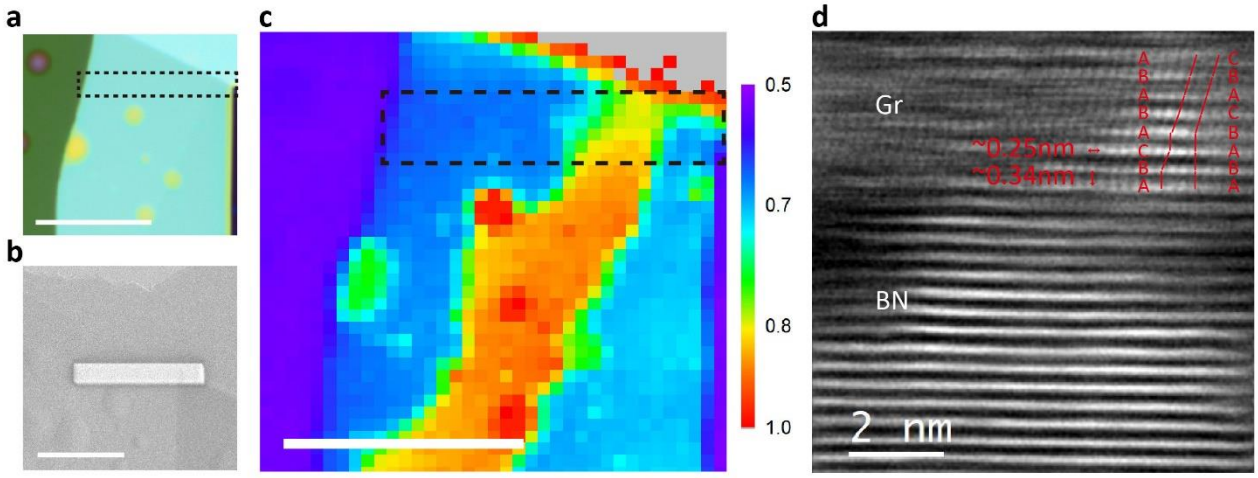

Figure S9. Cross-sectional STEM specimen preparation and imaging of a graphite flake containing both ABA and ABC domains. (a) Optical image taken from the flake on SiO_2/Si substrate, please note that the flake was covered by hBN to protect it during STEM specimen preparation. (b) Corresponding SEM image showing the region of interest in the FIB-SEM. (c) Corresponding 2D ratio Raman map of the flake. The scale bars of (a-c) are 10μm. (d) High-resolution STEM ADF image taken from the ABC/ABA graphite flake. The variation in the atomic positions indicates different basal plane stacking sequences are present in the graphite flake.

By combining the TEM results and the Raman mapping of the ratio of the two sides of 2D band of Flake3 (≈ 6 nm thick), we depicted the relation between the proportion of ABC/ABA stacking and the measured ratio of the two sides of 2D band, as shown in Figure S10. This relation can be used as a reference to judge the proportion of ABC/ABA stacking by Raman spectroscopy. Note that the Raman mapping was done on the flake suspended on TEM grid, the ratio of the two sides of 2D band would be slightly different from what was measured on Si/SiO_2 wafer. For flakes of other thickness, similar methodology can be carried out.

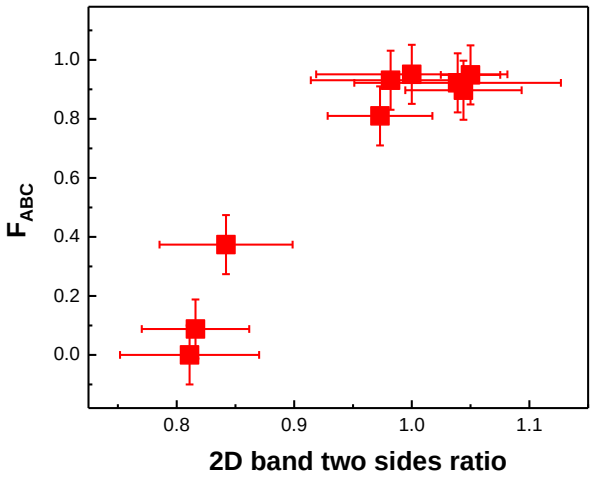

Figure S10. Comparison of the Raman and TEM results on ABC/ABA stacking ratio in graphite films. The ratio of the integral area of 2D band ranging 2675-2705 cm^{-1} to that ranging 2705-2735 cm^{-1} versus the fraction of ABC stacking estimated from TEM analysis.

9. Optical images and Raman maps of samples encapsulated along zigzag direction

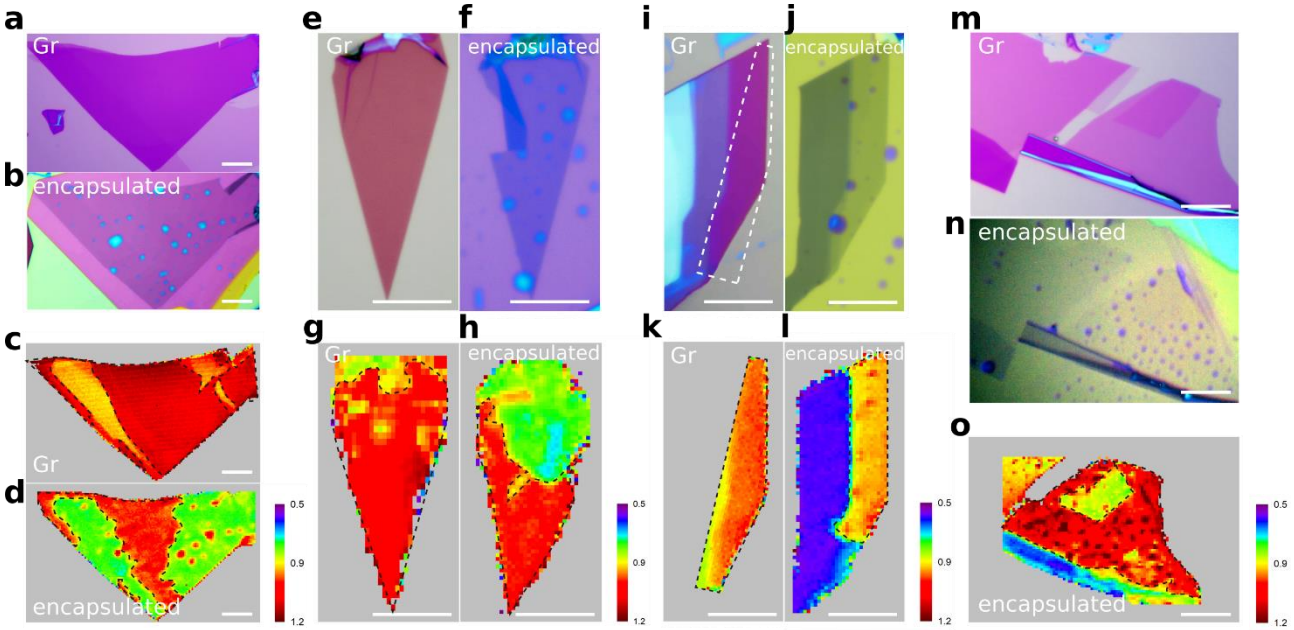

Figure S11. hBN/ABC-stacked graphite/hBN samples encapsulated along zigzag direction. (a–b), Optical images (≈3.5 nm) and Raman maps of the ratio of the integral area of 2D band ranging 2675-2705 cm^{-1} to that ranging 2705-2735 cm^{-1} of a graphite flake before (a, c) and after (b, d) encapsulation. (e–h), Optical images and the ratio maps of a graphite flake (≈2.7 nm) before (e, g) and after (f, h) encapsulation. (i–l), Optical images and the ratio maps of a graphite flake (≈6 nm) before (i, k) and after (j, l) encapsulation. (m–o), optical images before (m) and after (n) encapsulation of a graphite flake (≈2.1 nm), and the ratio Raman map after encapsulation (o). The black dashed line regions in (c), (d), (g), (h), (k), (l) and (o) indicate the ABC stacking region. The white dashed line region of (i) shows the Raman mapping region of the flake. The scale bars are 10 μm.

10. Optical images and Raman maps of samples encapsulated along arbitrary non-zigzag directions

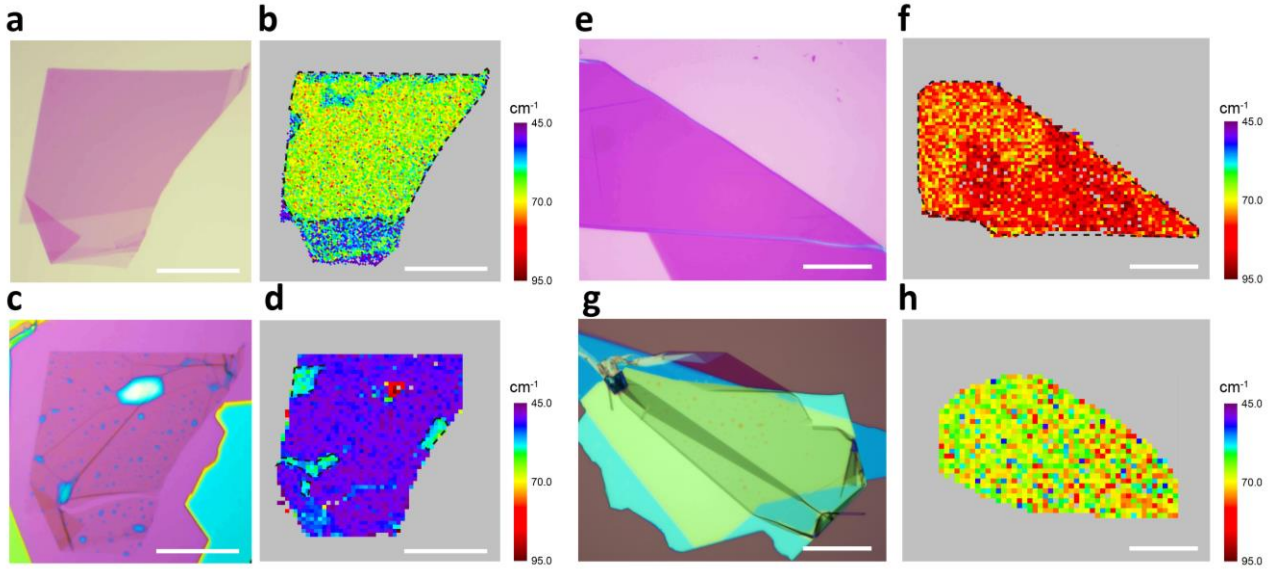

Figure S12. hBN/ABC-stacked graphite/hBN samples encapsulated along arbitrary direction. (a) and (b), Optical image and 2D band width map of a graphite flake (≈2 nm) before encapsulation. (c) and (d), Optical image and 2D band width map of the graphite flake after encapsulation. (e) and (f), Optical image and 2D band width map of a graphite flake (≈6 nm) before encapsulation. (g) and (h), Optical image and 2D band width map of the graphite flake after encapsulation. The black dashed lines in (b), (d) and (f) indicate the ABC stacking region. The scale bars are 20μm.

References

1. Lui, C. H.; Malard, L. M.; Kim, S.; Lantz, G.; Laverge, F. E.; Saito, R.; Heinz, T. F. Observation of layer-breathing mode vibrations in few-layer graphene through combination Raman scattering. *Nano Lett* **2012,** 12, (11), 5539-44.
2. Cong, C.; Yu, T.; Saito, R.; Dresselhaus, G. F.; Dresselhaus, M. S. Second-order overtone and combination Raman modes of graphene layers in the range of 1690-2150 cm(-1). *ACS Nano* **2011,** 5, (3), 1600-5.
3. Herziger, F.; May, P.; Maultzsch, J. Layer-number determination in graphene by out-of-plane phonons. *Physical Review B* **2012,** 85, (23).
4. Rao, R.; Podila, R.; Tsuchikawa, R.; Katoch, J.; Tishler, D.; Rao, A. M.; Ishigami, M. Effects of layer stacking on the combination Raman modes in graphene. *ACS Nano* **2011,** 5, (3), 1594-9.
5. Cong, C.; Yu, T.; Sato, K.; Shang, J.; Saito, R.; Dresselhaus, G. F.; Dresselhaus, M. S. Raman characterization of ABA- and ABC-stacked trilayer graphene. *ACS Nano* **2011,** 5, (11), 8760-8.
6. Nguyen, T. A.; Lee, J. U.; Yoon, D.; Cheong, H. Excitation energy dependent Raman signatures of ABA- and ABC-stacked few-layer graphene. *Sci Rep* **2014,** 4, 4630.
7. Mafra, D. L.; Samsonidze, G.; Malard, L. M.; Elias, D. C.; Brant, J. C.; Plentz, F.; Alves, E. S.; Pimenta, M. A. Determination of LA and TO phonon dispersion relations of graphene near the Dirac point by double resonance Raman scattering. *Physical Review B* **2007,** 76, (23).
8. Maultzsch, J.; Reich, S.; Thomsen, C. Double-resonant Raman scattering in graphite: Interference effects, selection rules, and phonon dispersion. *Phys. Rev. B* **2004,** 70, (15).
9. Eckmann, A.; Felten, A.; Mishchenko, A.; Britnell, L.; Krupke, R.; Novoselov, K. S.; Casiraghi, C. Probing the nature of defects in graphene by Raman spectroscopy. *Nano Lett.* **2012,** 12, (8), 3925-3930.
10. Ferrari, A. C.; Basko, D. M. Raman spectroscopy as a versatile tool for studying the properties of graphene. *Nat Nanotechnol* **2013,** 8, (4), 235-46.
11. You, Y.; Ni, Z.; Yu, T.; Shen, Z. Edge chirality determination of graphene by Raman spectroscopy. *Applied Physics Letters* **2008,** 93, (16), 163112.
12. Gupta, A. K.; Russin, T. J.; Gutierrez, H. R.; Eklund, P. C. Probing graphene edges via Raman scattering. *ACS Nano* **2009,** 3, (1), 45-52.
13. Cancado, L. G.; Pimenta, M. A.; Neves, B. R.; Dantas, M. S.; Jorio, A. Influence of the atomic structure on the Raman spectra of graphite edges. *Phys Rev Lett* **2004,** 93, (24), 247401.
14. Begliarbekov, M.; Sasaki, K.; Sul, O.; Yang, E. H.; Strauf, S. Optical control of edge chirality in graphene. *Nano Lett* **2011,** 11, (11), 4874-8.
15. Casiraghi, C.; Hartschuh, A.; Qian, H.; Piscanec, S.; Georgi, C.; Fasoli, A.; Novoselov, K. S.; Basko, D. M.; Ferrari, A. C. Raman spectroscopy of graphene edges. *Nano Lett* **2009,** 9, (4), 1433-41.
16. Latychevskaia, T.; Son, S.-K.; Yang, Y.; Chancellor, D.; Brown, M.; Ozdemir, S.; Madan, I.; Berruto, G.; Carbone, F.; Mishchenko, A.; Novoselov, K. S. Stacking transition in rhombohedral graphite. *Frontiers of Physics* **2018,** 14, (1).

Chapter 6: Electronic properties of rhombohedral graphite

6.1 Introduction

Electrons in flat bands of solid-state systems are susceptible to correlation effects, with magic-angle twisted bilayer graphene being the recent celebrity. In this chapter, we studied a completely new experimental platform: films of rhombohedral graphite – to explore strong correlations, quantum criticality, and other many-body phenomena, free from moiré structuring or spin-orbit interactions.

Rhombohedral graphite (RG) is predicted to host topological nearly-flat-band surface states and emergent quantum phases such as superconductivity or ferromagnetism. In this chapter, we provide the first experimental realisation of high-quality films of RG up to tens of graphene layers thick, using the van der Waals technique discussed in **Chapter 5**. We found that RG films show intricate quantum Hall effect with phase transitions between a trivial gapless semimetal and a gapped quantum spin Hall insulator accompanied by a giant Berry curvature phase. We also observed a spontaneous gap opening that emerges in thinner graphite films. In this insulating state, we found hysteretic behaviour as a function of carrier density, and also both perpendicular and parallel magnetic fields, which signifies electronic phase separation. The *B*-*T* phase diagram implies a strong correlation nature of this insulating state.

6.2 Electronic phase separation in multilayer rhombohedral graphite

Publication: Electronic phase separation in multilayer rhombohedral graphite

Journal reference: Nature, volume 584, pages 210–214 (2020).

DOI: 10.1038/s41586-020-2568-2

My contribution: conceived the idea that stacking faults in graphite affect its electronic properties quite a lot, fabricated large portions of the rhombohedral graphite samples using the technique discussed in **Chapter 5**, including those with stacking faults, discussed and analysed the data in close collaboration with Y.S. and S.X. (we equally contributed to this work), wrote fabrication parts of the supplementary information.

Full author list: Yanmeng Shi, Shuigang Xu, Yaping Yang, Sergey Slizovskiy, Sergey V. Morozov, Seok-Kyun Son, Servet Ozdemir, Ciaran Mullan, Julien Barrier, Jun Yin, Alexey I. Berdyugin, Benjamin A. Piot, Takashi Taniguchi, Kenji Watanabe, Vladimir I. Fal'ko, Kostya S. Novoselov, A. K. Geim & Artem Mishchenko.

Author contributions: A.M. conceived the presented idea and directed the project. Y.S., S.V.M., S.O., C.M., J.B., J.Y., A.I.B. and B.A.P. performed transport measurement. S.X., Y.Y. and S.-K.S. fabricated devices. Y.S., S.O., C.M. and J.Y. performed data analysis. S.S. and V.I.F. developed the theory and performed theoretical calculations. Y.S., S.O., A.K.G., V.I.F. and A.M. contributed to the interpretation of data. K.W. and T.T. grew hBN single crystals. A.M., Y.S., A.K.G., S.S., V.I.F. and K.S.N. contributed to the writing of the manuscript. All authors discussed the results and commented on the manuscript.

Article

Electronic phase separation in multilayer rhombohedral graphite

https://doi.org/10.1038/s41586-020-2568-2

Received: 11 November 2019

Accepted: 5 May 2020

Published online: 12 August 2020

Check for updates

Yanmeng Shi[1,10], Shuigang Xu[2,10], Yaping Yang[1,2,10], Sergey Slizovskiy[1,2], Sergey V. Morozov[3], Seok-Kyun Son[1,2,9], Servet Ozdemir[1], Ciaran Mullan[1], Julien Barrier[1,2], Jun Yin[1,2], Alexey I. Berdyugin[1], Benjamin A. Piot[4], Takashi Taniguchi[5], Kenji Watanabe[5], Vladimir I. Fal'ko[1,2,6], Kostya S. Novoselov[1,2,7,8], A. K. Geim[1,2] & Artem Mishchenko[1,2]✉

Of the two stable forms of graphite, hexagonal and rhombohedral, the former is more common and has been studied extensively. The latter is less stable, which has so far precluded its detailed investigation, despite many theoretical predictions about the abundance of exotic interaction-induced physics[1–6]. Advances in van der Waals heterostructure technology[7] have now allowed us to make high-quality rhombohedral graphite films up to 50 graphene layers thick and study their transport properties. Here we show that the bulk electronic states in such rhombohedral graphite are gapped[8] and, at low temperatures, electron transport is dominated by surface states. Because of their proposed topological nature, the surface states are of sufficiently high quality to observe the quantum Hall effect, whereby rhombohedral graphite exhibits phase transitions between a gapless semimetallic phase and a gapped quantum spin Hall phase with giant Berry curvature. We find that an energy gap can also be opened in the surface states by breaking their inversion symmetry by applying a perpendicular electric field. Moreover, in rhombohedral graphite thinner than four nanometres, a gap is present even without an external electric field. This spontaneous gap opening shows pronounced hysteresis and other signatures characteristic of electronic phase separation, which we attribute to emergence of strongly correlated electronic surface states.

Films of rhombohedral graphite (RG; also described as chirally stacked ABC graphene multilayers) are predicted to possess nearly flat bands localized at the surfaces; these bands are particularly suitable for exploring electron–electron interactions[3]. In RG, interlayer hopping (parameterized by γ_1; see Fig. 1a) dimerizes the electronic states of the opposite sublattices of all contiguous graphene layers in the bulk, shifting their energies away from the Fermi level[9,10]. Electrons of only two sublattices, one in the top layer, and the other in the bottom layer, remain at low energies. These surface states are considered to be equivalent to topological edge states in the 'polyacetylene' Su–Schrieffer–Heeger model[11]. The surface states residing on the inequivalent sublattices of the opposite surfaces of N-layer-thick samples are expected to form nearly flat bands with approximate energy dispersion relations of the form $E \propto \pm p^N$ (refs. [3,9,12]), where p is the in-plane momentum. These surface states are further theorized to have strong electron–electron interactions, hypothetically leading to spontaneous quantum Hall states, ferromagnetism and superconductivity[1–6,13]. When considering other hopping parameters (γ_0–γ_4 are shown in Fig. 1a; Methods), the surface flat bands acquire a finite bandwidth of the order of $2\gamma_4\gamma_1/\gamma_0$ as well as electron–hole asymmetry, and trigonal warping due to γ_2 and γ_3 (Fig. 1b), which could affect electron–electron interactions, spontaneous symmetry breaking and the opening of a bandgap (Fig. 1c). Owing to the metastable nature of RG, the reported transport experiments have been limited to ABC trilayer and ABCA tetralayer graphene, either in suspended two-terminal devices, or with the spectrum modified by moiré superlattices[14–17]; longer ABC sequences have been studied using magneto-Raman[18] and ARPES[19]. Here we report electronic transport in high-quality RG of up to $N \approx 50$ graphene layers thick, where we observe strong electronic correlations and phase separation, phenomena typically reserved for unconventional superconductors and heavy fermion materials. Eight RG devices were studied in detail in this work, with thicknesses ranging from about 2.3 nm ($N = 7$) to about 16.5 nm ($N \approx 50$).

We identified the stacking order of graphite films using Raman spectroscopy and, to retain their high electronic quality, we encapsulated the exfoliated films with hexagonal boron nitride (hBN) crystals using the directional dry transfer technique[7] (Methods). Figure 1d compares low-temperature ($T = 20$ mK) resistivity ρ_{xx} of RG and hexagonal graphite (HG) devices of the same thickness (device 1, about 3 nm thick, 9 graphene layers) as a function of total carrier density $n = \frac{C_t V_t + C_b V_b}{e}$. (Here V_t and V_b are the gate voltages, and C_t and C_b are the unit-area capacitances, of the top and bottom gates, respectively, and e is the

[1]Department of Physics and Astronomy, University of Manchester, Manchester, UK. [2]National Graphene Institute, University of Manchester, Manchester, UK. [3]Institute of Microelectronics Technology and High Purity Materials, Russian Academy of Sciences, Chernogolovka, Russia. [4]Université Grenoble Alpes, Laboratoire National des Champs Magnétiques Intenses, UPS-INSA-EMFL-CNRS-LNCMI, Grenoble, France. [5]National Institute for Materials Science, Tsukuba, Japan. [6]Henry Royce Institute for Advanced Materials, Manchester, UK. [7]Centre for Advanced 2D Materials, National University of Singapore, Singapore, Singapore. [8]Chongqing 2D Materials Institute, Chongqing, China. [9]Present address: Department of Physics, Mokpo National University, Muan, South Korea. [10]These authors contributed equally: Yanmeng Shi, Shuigang Xu, Yaping Yang. ✉e-mail: artem.mishchenko@gmail.com

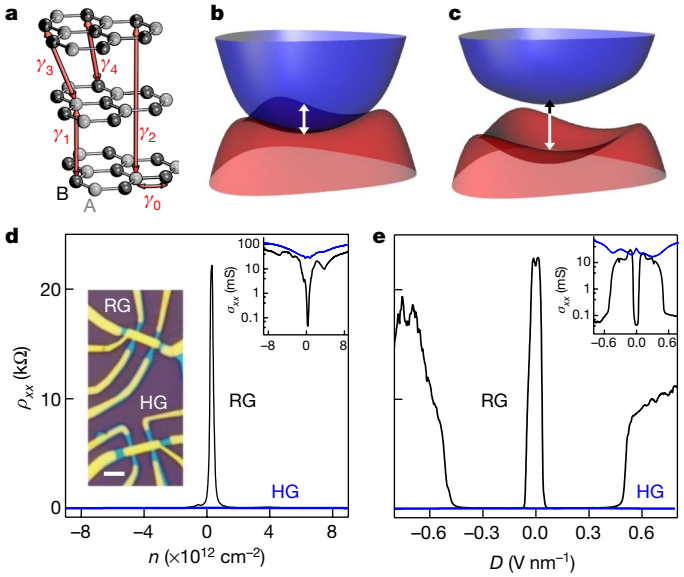

Fig. 1 | Transport characteristics of thin RG films. a, Schematic of RG hopping parameters, γ_i. Light- and dark-grey spheres represent carbon atoms of sublattices A and B, respectively. **b**, Dispersion of the surface states including all the hopping parameters in **a**. The vertical axis is energy, E, and horizontal axes are in-plane momenta, p. Skew hopping γ_4 adds an appreciable bandwidth $2\gamma_4\gamma_1/\gamma_0$ to the otherwise flat surface state bands, and introduces electron–hole asymmetry. The presence of γ_2 and γ_3 leads to trigonal warping. Blue and red colours indicate conduction and valence bands, respectively, and the double-headed arrow shows the finite band overlap between conduction and valence bands. **c**, Scenario when a bandgap $\Delta > 2\gamma_4\gamma_1/\gamma_0$ spontaneously opens in the RG spectrum. The double-headed arrow indicates the size of the bandgap. **d**, ρ_{xx} as a function of total carrier density $n = n_t + n_b$ measured at $D = 0$ for device 1 with rhombohedral (black curve) and hexagonal (blue curve) crystal structures (both are nine graphene layers thick). n_t (n_b) is the charge density induced by top (back) gate voltage. Left inset, optical micrograph of device 1; scale bar, 2 μm. **e**, ρ_{xx} as a function of the displacement field D; $n = 0$, $T = 20$ mK. Inset graphs in **d** and **e** show the corresponding σ_{xx} curves on a logarithmic scale.

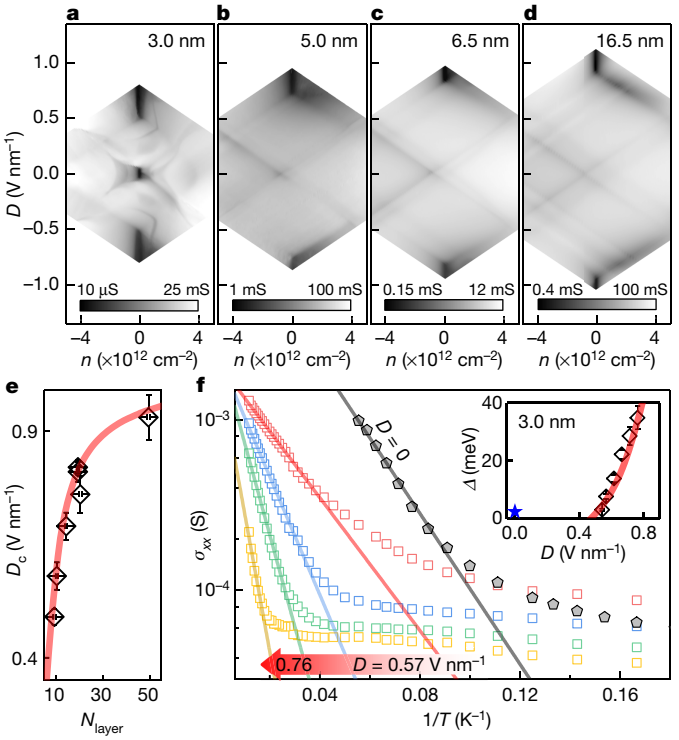

Fig. 2 | Thickness dependence of the transport characteristics of multilayer RG. a–**d**, Conductivity maps $\sigma_{xx}(n, D)$ for RG devices 1 to 4, respectively, of different thicknesses as specified in the panels. **e**, Thickness dependence of the critical field D_c, above which the transport gap is opened (black diamonds); thickness is expressed as number of layers, N_{layer}. D_c values were extracted from linear fits of $\sigma_{xx}(D)$ at $n = 0$ near the insulating states in the maps shown in **a**–**d**. Error bars represent uncertainties of the fitting procedure. The red curve is the self-consistent model (Methods). **f**, Arrhenius plot of σ_{xx} for RG device 1 at $D = 0.57$ V nm^{-1} (red squares), 0.62 V nm^{-1} (blue squares), 0.66 V nm^{-1} (green squares) and 0.76 V nm^{-1} (yellow squares). The grey pentagons are the data for $D = 0$. Linear fits of high-T regions (solid lines) give the bandgap Δ presented in the inset. The red curve in the inset is the bandgap estimation using the self-consistent screening model (Methods). For comparison, the thermal activation energy of the high-resistance state at $D = 0$ V nm^{-1} is also plotted in the inset (blue star).

elementary charge.) The RG device shows much stronger modulation of $\rho_{xx}(n)$ as compared to the reference HG device, such that ρ_{xx} of the former spans 10 Ω to 23 kΩ and exhibits a profound high-resistivity region near $n = 0$. At the same time, the HG device displays metallic behaviour over the entire range of carrier densities (ρ_{xx} varies only from 8 Ω to 63 Ω), similarly to the reported dual-gated devices of tetralayer and hexalayer Bernal-stacked graphene[20,21].

Figure 1e shows three distinct high-resistance regions for RG device 1 (which are absent in the HG device) as a function of displacement field $D = \frac{C_t V_t - C_b V_b}{2\varepsilon_0}$ measured at $n = 0$ (ε_0 is the vacuum permittivity). The appearance of the high-resistivity region at the neutrality point ($n = 0$, $D = 0$) suggests that an energy gap opens in the surface states spectrum, whereas the ρ_{xx} value close to the resistance quantum h/e^2 hints at edge-state transport caused possibly by topological character of the insulating state. The resistivity peak at the neutrality point was observed only in sufficiently thin (<4 nm) RG devices and cannot be explained within a free-particle model (Methods). Before discussing this high-resistivity feature, we consider states induced by a large displacement field. These regions of high resistivity, observed in all RG devices, emerging above a critical displacement field, $|D| > D_c$ (see Fig. 2a–d), are in agreement with the theoretical prediction that a high enough D opens an energy gap in the surface state spectrum of RG[22]. The effect is similar to that observed in bilayer graphene under displacement but has much stronger nonlinear screening of charges at the two RG surfaces (Methods). Note that the observation of these displacement-induced gaps requires a gapped bulk of multilayer RG (Methods). The resistivity of our fully gapped RG film (both surface and bulk states are gapped) is of the order of 20 kΩ for the thin RG sample at 20 mK (device 1), and 2–3 kΩ for the 16.5-nm-thick sample (device 4) at 1.5 K.

The effect of RG thickness on the displacement-field-induced bandgap is shown in Fig. 2a–d, which shows $\sigma_{xx}(n, D)$ maps for four RG devices with thicknesses ranging from 3 nm to 16.5 nm (devices 1 to 4). Figure 2e summarizes how the critical displacement field D_c increases with sample thickness. The solid line is the self-consistent theory (see Methods). From the T dependence of σ_{xx} of 3-nm-thick RG device 1, we extracted the sizes of thermally activated gaps Δ at different D (Fig. 2f), which are plotted in Fig. 2f inset. The bandgap observed in RG at $|D| > D_c$ is in stark contrast to the HG response to the displacement field where D causes the resistivity to decrease (Fig. 1e) due to the growing size of the Fermi surfaces of the top and bottom surface states[22,23]. The behaviour of $\sigma_{xx}(D)$ presented in Fig. 2a–d is characteristic of the uniform ABCABC… stacking in our RG samples. We note that, if mixed ABC/ABA stacking were present in our devices, this should have prevented gap opening by the displacement field (Methods), which provides complementary evidence for complete ABC stacking in our RG devices (Extended Data Figs. 1 and 2).

Next we explore electron transport in multilayer RG using magnetic field B applied perpendicular to the plane. Longitudinal (ρ_{xx})

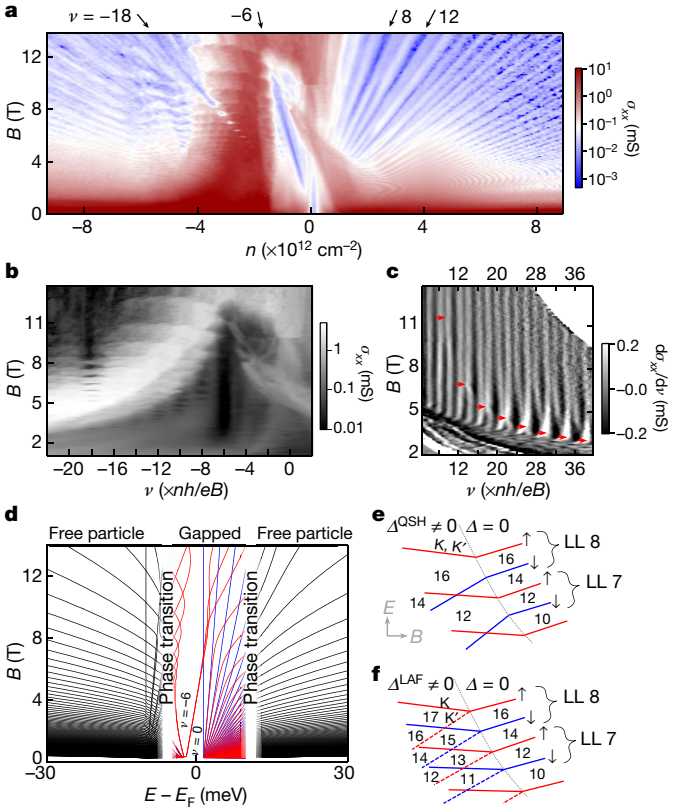

Fig. 3 | Quantum Hall effect in RG. a, Map of longitudinal conductivity $\sigma_{xx}(n, B)$ for device 1; $D = 0$; $T = 20$ mK. Arrows and numbers indicate the filling factors of quantum Hall states. **b**, $\sigma_{xx}(\nu, B)$ for the hole side (same data as in **a**). **c**, Differential $d\sigma_{xx}/d\nu(\nu, B)$ map for the electron side (data from **a**). Red arrows mark the positions of LL crossings. **d**, Calculated spectra of LLs in multilayer RG, using gapped and gapless band structures at low (coloured curves) and high (black) energies, respectively. The free-particle and gapped regions are separated by phase transitions. Red and blue lines, depending on the order parameter, correspond to electronic states with opposite spins (quantum spin Hall) or of opposite valleys (layer antiferromagnetism). E_F, Fermi energy. **e**, Effect of quantum spin Hall order parameter on the Landau spectrum. Numbers indicate the filling factors. LL 7 and LL 8 refer to the orbital indices of the zeroth LL. ↑ (red lines) and ↓ (blue lines) label spin-split LLs. Δ_{QSH} is the QSH order parameter, and K and K′ are the opposite valleys. The dotted line demarcates the transition between gapped and free-particle regimes. **f**, Same as in **e** but for layer antiferromagnetism. Solid (dashed) coloured lines refer to K (K′) valleys.

and transverse (ρ_{xy}) resistivities of device 1 are shown in Extended Data Fig. 3a as a function of B at $n = 2.3 \times 10^{12}$ cm^{-2} and $D = 0$. Shubnikov–de Haas oscillations emerge at $B \approx 1$ T, and well-quantized ρ_{xy} plateaux develop for $B > 3$ T manifesting the onset of the quantum Hall effect (QHE), such that under a strong magnetic field the electronic spectrum of 2D surface states collapses into a series of discrete Landau levels (LLs), leading to quantized ρ_{xy}. In high B (see, for example, Extended Data Fig. 3b for $B = 10$ T), $\rho_{xy}(n)$ plateaux appear at even fractions of h/e^2, indicating a two-fold (valley) degeneracy of the LLs. To examine the quantization, Fig. 3a shows the Landau fan diagram $\sigma_{xx}(n, B)$ for device 1 at $D = 0$. We note strong electron–hole asymmetry in the diagram: the electron side exhibits straight LLs (blue lines follow the slopes $B/n = h/e\nu$, where ν is the filling factor) fanning out from the neutrality point, while the hole side shows a criss-cross pattern. We observed similar behaviour in RG devices of different thicknesses, which is consistent with the surface origin of the LLs (Extended Data Fig. 4). The QHE has also been reported in thin films of Bernal-stacked graphite[23]. In the latter case, the quantization was due to the formation of standing waves in the bulk. In contrast, our multilayer RG has a gapped bulk but conducting surfaces, which should exhibit the QHE if their electronic quality is sufficiently high.

In N-layer RG, a Berry phase $\pm N\pi$ around the opposite K points leads to N-degenerate zero-energy LLs for each spin and valley, which are localized on the opposite surfaces for opposite valleys[24,25]. A free-particle spectrum of LLs in RG calculated using the same method as in ref. [26] is plotted in Extended Data Fig. 4a. Typically for semimetals, conduction- and valence-band LLs make numerous crossings at moderate B, which for multilayer RG happens on the hole side of the spectrum. In the absence of a displacement field, all LLs are valley degenerate. In addition, low-index valence-band LLs are triply degenerate, reflecting the triply degenerate maxima of the valence band (Fig. 1b). They are split at higher B where the three Fermi surfaces of the valence band merge into one. For device 1 (9 layers) in Fig. 3a, the total number of the zeroth LLs is 36 (2 spins, 2 valleys and 9 orbitals), and the lines corresponding to filling factors up to ±18 come from these zeroth LLs. Lines on the electron side, which trace $\nu = 8, 12, 16, \ldots$ are well pronounced. These filling factors in multiples of 4 can be explained by relatively large Zeeman gaps between two-fold degenerate orbital levels of zeroth LLs. A pronounced gap at $\nu = -18$ followed by a series of crossings below 8 T could be traced back to the crossings between the $2N$-fold degenerate zeroth LL and the valence-band LLs. The robust $\nu = -18$ state emerges when these crossings stop (Extended Data Fig. 4a). When only a single gate is used (Extended Data Fig. 5), the valley degeneracy becomes lifted, and a robust gap appears at $\nu = -7$ (for 7-layer-thick device 7), $\nu = -9$ (for 9-layer device 1) and at $\nu = -11$ (for 11-layer device 6). This provides additional support for our assignment of the observed spectrum to the N-degenerate zeroth LL, which is in turn a manifestation of an $N\pi$ Berry phase in N-layer RG.

Although the free-particle theory adequately describes the experimental results at high doping (Fig. 3a, d above $|n| > 2.5 \times 10^{12}$ cm^{-2}), it fails to explain the pronounced gaps observed at $\nu = 0$ and $\nu = -6$ (Fig. 3a). Apart from the crisscross pattern on the hole side (Fig. 3b), which agrees with the free-particle theory, there is a series of crossing points on the electron side at the symmetry broken states $\nu = 10, 14, 18, 22\ldots$ The crossings are better seen if we replot the Landau fan as a function of ν (Fig. 3c; the crossing points are marked with red arrows). These crossings also cannot be explained using the free-particle picture. To account for the latter features, we suggest a spontaneous appearance of an interaction-induced spin and/or valley symmetry-breaking order parameter. It leads to a bandgap when the resulting band splitting exceeds the single-particle overlap between the conduction and valence bands, thus allowing the observation of quantum Hall states at $\nu = 0$ and -6 (Fig. 3a, d). With increasing B, the gap switches from $\nu = 0$ to $\nu = -6$. This can be explained by large orbital magnetic moments that have opposite signs for opposite spins (or valleys) and lead to closure of the $\nu = 0$ gap, as shown in Fig. 3d. The bandgap disappears with increasing doping, but the observed crossings on the electron side (Fig. 3c, and also Extended Data Fig. 4c, d for 3.3-nm-thick device 5) suggest that a small interaction-induced order parameter remains present up to $n \approx 2.5 \times 10^{12}$ cm^{-2}.

The interplay between the orbital, valley and spin degrees of freedom leads to several possible states with spontaneously broken symmetry in multilayer RG. They include quantum valley Hall, quantum anomalous Hall, layer antiferromagnetic insulator and quantum spin Hall states[3] (see Methods). The crossing points on the electron side (Fig. 3c, and Extended Data Fig. 4d for similar results in device 5) can be explained by the phase transition from spin-polarized states due to Zeeman splitting at higher electron concentration to quantum spin Hall states at electron concentration $n < 2.5 \times 10^{12}$ cm^{-2} (Fig. 3e). The quantum spin Hall phase is accompanied by a giant Berry curvature and a related giant orbital magnetic moment (the same in both valleys but opposite for the two spin directions)[3]. The observed crossings cannot be explained by any other of the conjectured phases listed above. For instance, the

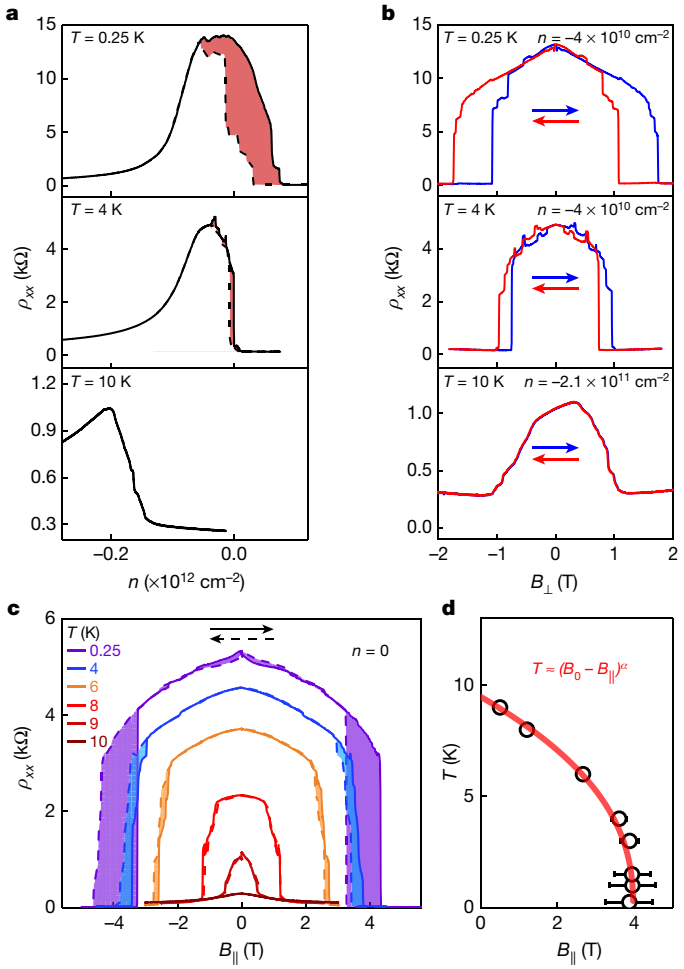

Fig. 4 | Hysteretic behaviour of the insulating state in multilayer RG. **a**, $\rho_{xx}(n)$ of dual-gated device 5 (RG about 3.3 nm thick) at $D = 0$; data were taken at three different temperatures (top, 0.25 K; middle, 4 K; bottom, 10 K). The solid (dashed) curves indicate positive (negative) sweep directions; the coloured areas highlight the hysteresis. **b**, Hysteresis in $B_\perp$ of the same device used in **a**. Panels show $\rho_{xx}(B_\perp)$; the data were taken at the same three temperatures as in **a**, with n values shown at the top right of each panel. Coloured arrows show sweep directions. **c**, Hysteresis in $B_\parallel$ for device 6 (single-gated RG about 3.6 nm thick). $\rho_{xx}(B_\parallel)$ is shown for six different temperatures; the coloured areas highlight the hysteresis. **d**, Phase diagram of the critical behaviour in **c**: the temperature at which the insulating state appears depends on $B_\parallel$ (error bars are due to hysteresis). The red curve is the fit $T \approx (B_0 - B_\parallel)^\alpha$, where $B_0 \approx 4$ T is the critical field at $T = 0$ K, and $\alpha \approx 0.4$ is the critical exponent.

layer antiferromagnetic phase leads to lifted valley degeneracy and the presence of gaps and crossings at both even and odd filling factors (Fig. 3f), which contradicts the experiment. Note that there is no evidence that the observed quantum spin Hall phase becomes stronger towards zero doping, because the development of another competing order cannot be excluded.

In the absence of a magnetic field, thin (<4 nm) RG devices reveal an intrinsic insulating state at the neutrality point (Fig. 1d, e). Extended Data Fig. 6a shows the temperature dependence of $\rho_{xx}(n)$ around the insulating state at $D = 0$ in another RG device about 3.3 nm thick. At T below 10 K, the resistance shoots up by orders of magnitude, showing thermal activation behaviour consistent with a gap of 2–3 meV (Extended Data Fig. 6a). We note that this value represents an effective transport gap, after accounting for the lifted overlap of about $2\gamma_4\gamma_1/\gamma_0$ (Extended Data Fig. 9).

Surprisingly, pronounced hysteretic behaviour is observed in the resistivity of multilayer RG around the neutrality point as a function of doping (see Fig. 4a and Extended Data Fig. 6a, b). The hysteresis rapidly decreases with increasing T and disappears if the RG enters a metallic state. Note that the hysteresis strongly favours electron doping, reflecting the electron–hole asymmetry of the RG band structure. In addition to the hysteresis as a function of n, we also observed pronounced hysteresis in response to both perpendicular ($B_\perp$) and parallel ($B_\parallel$) magnetic fields. $B_\perp$ suppresses the insulating state (Fig. 4b) but the accompanying Landau quantization unfortunately complicates analysis of the observed T dependence. In contrast, measurements in $B_\parallel$ (Fig. 4c), where the orbital degree of freedom remains unaffected, provide a clearer picture. With increasing T, both the hysteresis and the transition field rapidly decrease, and the $B_\parallel$–T phase diagram follows the power-law $T \approx (B_0 - B_\parallel)^\alpha$ where $\alpha \approx 0.4$ is the critical exponent (Fig. 4d). Our fit is comparable to those reported for the 'hidden order' phase in strongly correlated heavy fermion systems like[27] URu_2Si_2. The pronounced hysteretic behaviour with abrupt switching hints at spontaneous formation of insulating electronic phases that are separated into domains, similar to those observed in other correlated systems such as manganites, cuprates, and transition metal oxides[28]. The hysteresis as a function of both electric and magnetic fields is characteristic of multiferroic materials, and advanced scanning probe techniques could be helpful in identifying the nature of those electronic domains in future.

The present work offers a novel experimental system in which to explore strongly correlated phenomena that does not rely on spin–orbit or exchange interactions in transition metal oxides[28] or on precise structuring of graphene superlattices[29–32]. Electronic coupling between top and bottom surfaces in thin RG films is similar to that observed in thin films of topological insulators[33,34] and could be responsible for the spontaneous gap opening in our case. However, this coupling cannot explain the observed hysteretic behaviour. We believe that multilayer RG provides an interesting system in which to explore strong correlations, quantum criticality and other many-body phenomena, usually reserved to *f*-element-based heavy fermions or *d*-element-based transition metal oxides.

Online content

Any methods, additional references, Nature Research reporting summaries, source data, extended data, supplementary information, acknowledgements, peer review information; details of author contributions and competing interests; and statements of data and code availability are available at https://doi.org/10.1038/s41586-020-2568-2.

1. Kopnin, N. B., Ijäs, M., Harju, A. & Heikkilä, T. T. High-temperature surface superconductivity in rhombohedral graphite. *Phys. Rev. B* **87**, 140503(R) (2013).
2. Otani, M., Koshino, M., Takagi, Y. & Okada, S. Intrinsic magnetic moment on (0001) surfaces of rhombohedral graphite. *Phys. Rev. B* **81**, 161403(R) (2010).
3. Zhang, F., Jung, J., Fiete, G. A., Niu, Q. & MacDonald, A. H. Spontaneous quantum Hall states in chirally stacked few-layer graphene systems. *Phys. Rev. Lett.* **106**, 156801 (2011).
4. Pamuk, B., Baima, J., Mauri, F. & Calandra, M. Magnetic gap opening in rhombohedral-stacked multilayer graphene from first principles. *Phys. Rev. B* **95**, 075422 (2017).
5. Muñoz, W. A., Covaci, L. & Peeters, F. M. Tight-binding description of intrinsic superconducting correlations in multilayer graphene. *Phys. Rev. B* **87**, 134509 (2013).
6. Xu, D. H. et al. Stacking order, interaction, and weak surface magnetism in layered graphene sheets. *Phys. Rev. B* **86**, 201404(R) (2012).
7. Yang, Y. et al. Stacking order in graphite films controlled by van der Waals technology. *Nano Lett.* **19**, 8526–8532 (2019).
8. Ho, C. H., Chang, C. P. & Lin, M. F. Evolution and dimensional crossover from the bulk subbands in ABC-stacked graphene to a three-dimensional Dirac cone structure in rhombohedral graphite. *Phys. Rev. B* **93**, 075437 (2016).
9. Haering, R. R. Band structure of rhombohedral graphite. *Can. J. Phys.* **36**, 352–362 (1958).
10. Mcclure, J. W. Electron energy band structure and electronic properties of rhombohedral graphite. *Carbon* **7**, 425–432 (1969).
11. Xiao, R. J. et al. Density functional investigation of rhombohedral stacks of graphene: topological surface states, nonlinear dielectric response, and bulk limit. *Phys. Rev. B* **84**, 165404 (2011).
12. Xiao, D., Chang, M. C. & Niu, Q. Berry phase effects on electronic properties. *Rev. Mod. Phys.* **82**, 1959–2007 (2010).
13. Velasco, J. et al. Transport spectroscopy of symmetry-broken insulating states in bilayer graphene. *Nat. Nanotechnol.* **7**, 156–160 (2012).

14. Lee, Y. et al. Competition between spontaneous symmetry breaking and single-particle gaps in trilayer graphene. *Nat. Commun*. **5**, 5656 (2014).
15. Myhro, K. et al. Large tunable intrinsic gap in rhombohedral-stacked tetralayer graphene at half filling. *2D Mater*. **5**, 045013 (2018).
16. Chen, G. et al. Evidence of a gate-tunable Mott insulator in a trilayer graphene moiré superlattice. *Nat. Phys*. **15**, 237–241 (2019).
17. Lee, Y. et al. Gate tunable magnetism and giant magnetoresistance in ABC-stacked few-layer graphene. Preprint at http://arXiv.org/abs/1911.04450 (2019).
18. Henni, Y. et al. Rhombohedral multilayer graphene: a magneto-Raman scattering study. *Nano Lett*. **16**, 3710–3716 (2016).
19. Henck, H. et al. Flat electronic bands in long sequences of rhombohedral-stacked graphene. *Phys. Rev. B* **97**, 245421 (2018).
20. Shi, Y. et al. Tunable Lifshitz transitions and multiband transport in tetralayer graphene. *Phys. Rev. Lett*. **120**, 096802 (2018).
21. Nakasuga, T. et al. Low-energy band structure in Bernal stacked six-layer graphene: Landau fan diagram and resistance ridge. *Phys. Rev. B* **99**, 085404 (2019).
22. Koshino, M. Interlayer screening effect in graphene multilayers with ABA and ABC stacking. *Phys. Rev. B* **81**, 125304 (2010).
23. Yin, J. *et al*. Dimensional reduction, quantum Hall effect and layer parity in graphite films. *Nature Phys*. **15**, 437–442 (2019).
24. Koshino, M. & McCann, E. Trigonal warping and Berry's phase Nπ in ABC-stacked multilayer graphene. *Phys. Rev. B* **80**, 165409 (2009).
25. Min, H. K. & MacDonald, A. H. Chiral decomposition in the electronic structure of graphene multilayers. *Phys. Rev. B* **77**, 155416 (2008).
26. Slizovskiy, S., McCann, E., Koshino, M. & Fal'ko, V. I. Films of rhombohedral graphite as two-dimensional topological semimetals. *Commun. Phys*. **2**, 164 (2019).
27. Ran, S. et al. Phase diagram of $URu_{2-x}Fe_xSi_2$ in high magnetic fields. *Proc. Natl Acad. Sci. USA* **114**, 9826–9831 (2017).
28. Dagotto, E. Complexity in strongly correlated electronic systems. *Science* **309**, 257–262 (2005).
29. Cao, Y. et al. Correlated insulator behaviour at half-filling in magic-angle graphene superlattices. *Nature* **556**, 80–84 (2018).
30. Cao, Y. et al. Unconventional superconductivity in magic-angle graphene superlattices. *Nature* **556**, 43–50 (2018).
31. Sharpe, A. L. et al. Emergent ferromagnetism near three-quarters filling in twisted bilayer graphene. *Science* **365**, 605–608 (2019).
32. Serlin, M. et al. Intrinsic quantized anomalous Hall effect in a moiré heterostructure. *Science* **367**, 900–903 (2020).
33. Zhang, Y. et al. Crossover of the three-dimensional topological insulator Bi_2Se_3 to the two-dimensional limit. *Nat. Phys*. **6**, 584–588 (2010); erratum **6**, 712 (2010).
34. Neupane, M. et al. Observation of quantum-tunnelling-modulated spin texture in ultrathin topological insulator Bi_2Se_3 films. *Nat. Commun*. **5**, 3841 (2014).

Methods

Device fabrication

The RG films were obtained by mechanical exfoliation of natural graphite flakes (Graphenium Flakes 25–30 mm, NGS Naturgraphit) onto a SiO_2 (290 nm)/Si wafer. Exfoliated graphite films often show domains of various stacking orders, which can be identified by Raman spectroscopy. By mapping the ratio of the integrated area of the low-frequency component (ranging around 2,670–2,700 cm^{-1}) and the high-frequency component (ranging around 2,700–2,730 cm^{-1}) of the Raman 2D band, we can visualize the distribution of rhombohedral stacking in the films[7]. Raman spatial maps were taken with a step size of 0.5 μm.

RG films often revert back into Bernal stacking during the flake transfer process, and only a small region of the flake remains in the original stacking order. The transition between rhombohedral stacking and Bernal stacking occurs during the shift of graphene layers along armchair directions, whereas it does not happen along zig-zag directions. To retain the high electronic quality of RG, we used a directional van der Waals assembly technique[7] as follows. First, we identified the crystal orientation of graphite from the edge chirality of graphite films using Raman spectroscopy. Next, we used a polymer (a polymethylmethacrylate (PMMA)/polydimethylsiloxane (PDMS) stack mounted on a glass slide)-mediated dry transfer method to encapsulate RG films in hexagonal boron nitride (hBN). During the encapsulation process, the pressing-down direction of the PDMS/PMMA layers was controlled along the zig-zag direction of the graphite films, so that the stacking transformation could be avoided. Then, we used the above-mentioned Raman-ratio map again to confirm that rhombohedral stacking was retained in the hBN-encapsulated graphite. Finally, multiterminal Hall bar devices were made from the hBN/RG films/hBN heterostructures using standard electron-beam lithography. Examples of our Raman analysis during device fabrication are presented in Extended Data Fig. 7 for device 6 (3.6-nm-thick RG).

Surface and bulk contributions

Extended Data Figure 8 shows the temperature dependence of resistivity, $\rho_{xx}(T)$, at $n = 0$ for 16.5-and 3.3-nm-thick RG (devices 4 and 5, respectively). In contrast to the metallic behaviour of Bernal-stacked graphite[23], we observed a semiconductor-to-metal-transition with decreasing temperature. We attribute this transition to the interplay between three parallel conduction channels: the bulk and the two surfaces. Infinitely thick RG has 3D Dirac cones in its bulk energy spectrum[8], but in films of a finite thickness (with N layers), these Dirac cones are gapped by $\Delta \approx 2.1$ eV per N (see below). At high temperatures, the RG bulk conducts as a result of thermal activation across this gap, and this conductivity dominates over the 2D surface states. With decreasing T, the bulk contribution decreases and, finally, below some critical temperature T_c (about 20 K and 40 K for 16.5-nm and 3.3-nm RG, respectively), the contribution from the surfaces dominates, and $\rho_{xx}(T)$ shows metallic behaviour. This temperature behaviour of resistivity is similar to that observed in 3D topological insulators, which is also ascribed to competing conductances of bulk and surface states[35]. The observed T_c is smaller for thicker samples, in agreement with the expected $1/N$ dependence of the bulk gap. The observed T dependence indicates that at low temperatures ($T < T_c$), the conductivity through 3D bulk bands is suppressed and mostly 2D surface states contribute to electron transport. Thermal activation within the RG bulk limits the interval of exponential T dependence, preventing us from evaluating the bulk gaps at high D.

Tight-binding model

To describe multilayer RG, we employ the Slonczewski–Weiss–McClure (SWMC) parameterization of graphite[10,24,26,36], with interlayer hopping parameters that take into account the lattice arrangement of rhombohedral graphite, as shown in Fig. 1a. Multilayer RG has bulk subbands shifted away from zero energy, leading to a bulk gap of about $3\pi\gamma_1/N$ for N layers, making only the surface bands relevant for electronic transport at low T. The surface states have shallow dispersion for quasi-momenta $p < p_c = \gamma_1/v$, where v is the Dirac velocity determined by intralayer nearest-neighbour hopping γ_0. There is also a quadratic term in the dispersion of surface states[26], $p^2/(2\,m_*)$ with $m_*^{-1} = 2\,v^2/\gamma_1(2\,\gamma_4/\gamma_0 + \delta/\gamma_1) \approx (0.4\,m_e)^{-1}$, which breaks the electron–hole symmetry, and trigonal warping terms controlled by γ_2 and γ_3. Here m_e is the free electron mass. Since the SWMC parameters are poorly known for RG, we use the conventional HG values[23,36] for the larger hopping amplitudes ($\gamma_0 = 3.16$ eV, $\gamma_1 = 0.39$ eV, $\gamma_3 = 0.25$ eV) while tuning the unknown γ_2 to −0.01 eV and m_* to $0.4m_e$ to better describe the experiment. We also set the energy difference of dimerized (that carry bulk states) and non-dimerized (that carry surface states) sublattices to zero, $\delta = 0$, and tuned γ_4 to about 0.13 eV. These parameter values have been chosen by comparing Fig. 3a with Extended Data Fig. 4a and matching the electron density of the first crossing of valence and conduction bands ($n = -6.3 \times 10^{12}$ cm^{-2}), which corresponds to the valence-band population where the chemical potential is at the bottom of the conduction band. Other crossings lead to extra constraints that can be satisfied reasonably well at positive filling factors ($4 < \nu < 40$, where crossings are in the range 5 T > B > 2 T), while the matching becomes worse near zero filling and at larger magnetic fields, suggesting an increased role of interaction effects.

Bandgap induced by displacement field

Introducing a vertical electric displacement field D via asymmetric gating leads to a potential difference $\tilde{\Delta}$ between the top and the bottom layers, resulting in a density redistribution that strongly screens the external electric field. The dispersion of surface states with non-zero $\tilde{\Delta}$ is shown in Extended Data Fig. 9. Note that the difference between the energies of valence- and conduction-band states at the K point equals $\tilde{\Delta}$ (only γ_1 vertical hopping and the $\tilde{\Delta}$ potential contribute to the Hamiltonian at K points, leading to states localized at A_1 and B_N sublattices with energies $\pm\tilde{\Delta}/2$, while all the other states belong to dimers, connected by γ_1 vertical hopping and having energies $\pm\gamma_1$). After calculating the energy dispersion, the screening electron density accumulated at layer i is calculated as

$$n_i = 2\int_{\mathrm{BZ}} \frac{\mathrm{d}^2k}{(2\pi)^2} \sum_{l=1}^{2N} [(|\Psi^l_{\mathrm{A}_i}(k)|^2 + |\Psi^l_{\mathrm{B}_i}(k)|^2) f(\varepsilon_l - E_\mathrm{F}) - 1]$$

where i is the layer number in N-layer RG, the integration is over the Brillouin zone (BZ), l stands for band index, $\Psi^l_{\mathrm{A}_i}(k)$ and $\Psi^l_{\mathrm{B}_i}(k)$ are normalized wavefunctions of two sublattices in layer i, f is the Fermi function, E_F is the Fermi level, ε_l is the energy of band l, and −1 subtracts a homogeneous charge jelly that neutralizes the Fermi sea electron density. Denoting the total screening charge accumulated near the top and bottom surfaces by $n_\mathrm{t}^{\mathrm{scr}}(\tilde{\Delta})$ and $n_\mathrm{b}^{\mathrm{scr}}(\tilde{\Delta})$ respectively, we relate the displacement field to the charge density and the potential asymmetry as

$$\frac{-e[n_\mathrm{t} - n_\mathrm{b}]}{2\,\varepsilon_0} \equiv D = \frac{e[n_t^{\mathrm{scr}}(\tilde{\Delta}) - n_\mathrm{b}^{\mathrm{scr}}(\tilde{\Delta})]}{2\,\varepsilon_0} + \frac{\varepsilon\tilde{\Delta}}{d}$$

where e is the electron charge, d is the thickness of the graphite film, and ε_0 is the vacuum permittivity. We employed the Hartree approximation and used the fact that the dominant screening charge is localized at the surface layers. By varying the potential difference of the surface layers, tuning the chemical potential to maintain overall charge neutrality, and finding the electron density distribution, we determined the relation between the bandgap and applied external displacement field, as shown in Fig. 2f inset. The bandgap Δ, defined as the difference between the conduction-band minimum and the valence-band maximum, is shown in Extended Data Fig. 9.

In the absence of displacement field D, the conduction and valence bands of RG overlap. Therefore, one has to apply a field D larger than some critical D_{crit} so that the potential asymmetry exceeds the bandwidth of overlapping, and drives the system from a semimetallic to a semiconducting phase, Extended Data Fig. 9. Calculated values of D_{crit} are shown in Fig. 2e and compared to experimental results. When the total electron concentration is zero, $n_t - n_b = 0$, the Fermi level is in the gap, resulting in the experimentally observed transport gap presented in the main text.

Possibility of stacking faults

It is important to have a reliable method to check for possible stacking faults in the sample. Apart from Raman[7] (Extended Data Fig. 1a–d) and electronic Raman scattering signatures[37], measurements of an in-plane transport gap opened by the vertical displacement field (asymmetric gating) provides another diagnostic tool (Extended Data Fig. 1e–g). Our calculations reveal that it is impossible to open a transport gap if stacking faults or thicker inclusions of ABA stacking are present. We considered the most elementary A**BCB**A stacking fault that joins ABC stacking with its mirror-image CBA stacking (Extended Data Fig. 2a); a Bernal stacking fault that joins two ABC multilayers, as shown in Extended Data Fig. 2d for the A**BCBC**A multilayer; and surface stacking fault AB**CAC** (Extended Data Fig. 2g). The bold characters indicate the type and position of stacking faults.

At the K points of the Brillouin zone of RG, the in-plane hoppings γ_0 destructively interfere, leaving only γ_1 as a high-energy scale. For the twin-boundary stacking, the low-energy states are localized on sublattices A_1, A_5 and B_3, and on a zero-energy eigenstate $(\Psi_{B_2}, \Psi_{B_4}) = \left(\frac{1}{\sqrt{2}}, -\frac{1}{\sqrt{2}}\right)$ of a $B_2A_3B_4$ trimer, which we denote as $B_2 - B_4$, Extended Data Fig. 2a. Away from the K point, chiral decomposition[25] leads to the appearance of effective 2- and 3-layer ABC chiral subsystems with obvious generalization to films thicker than 5 graphene layers. So, there are four low-energy sub-bands: two with energies growing away from the K point (conduction-band type) and two with energies decreasing away from the K point (valence-band-type). Similarly to RG discussed before, the hopping γ_4 leads to an overlap of valence and conduction sub-bands of the order of 20 meV. Application of the vertical electric field (creating layer potentials $U_1 < U_2 < \ldots < U_5$) splits the four almost degenerate sub-bands into two outer valence and conduction bands, localized on A_1 and A_5 (with energies U_1 and U_5 at the K point), and two inner valence and conduction bands, localized on B_3 and $B_2 - B_4$ (with energies U_3 and $(U_2 + U_4)/2$ at the K point). The energy splitting of the two inner bands is $U_3 - (U_2 + U_4)/2 = \frac{e^2 d_1 n_{B_3}}{2\varepsilon_0}$, where $d_1 = 0.335$ nm is the distance between layers, and it only depends on the charge density of the third layer, n_{B_3}.

For the A**BCBC**A stacking fault in Extended Data Fig. 2d, the low-energy states at the K point are localized on sublattices A_1, B_3, A_4 and B_6, with the splitting of the inner band determined by the electric field between layers 3 and 4. In both A**BCB**A and A**BCBC**A stacking fault cases, to open a gap one requires a displacement field sufficient to overcome the doubled screening of four low-energy bands and, additionally, to create a potential difference of about 20 meV between the two consecutive layers forming a stacking fault. Such displacement fields would strongly exceed the values plotted in Fig. 2e, and are beyond our experimental reach. Large but experimentally attainable displacement fields would split the inner B_3 and A_4 bands at the K point, as shown in Extended Data Fig. 2e, f, but such high fields would also substantially increase the dispersion of these bands, resulting in band overlap near $p = p_c$, thus closing the gap. As for the ABA surface stacking fault in Extended Data Fig. 2g–i, the ABA surface bands overlap with a Dirac cone having velocity $v/\sqrt{2}$, which shunts the gapped state.

Thus we conclude that any stacking faults make opening of a transport gap impossible. We also note that stacking faults would, generically, lead to asymmetric behaviour with respect to reversal of the direction of D. Calculated dispersions with non-zero displacement field are shown for the twin-boundary defect in Extended Data Fig. 2b, c; for the stacking fault buried inside the ABC bulk in Extended Data Fig. 2e, f; and for the surface stacking fault in Extended Data Fig. 2h, i. Examples of transport data for multilayer graphite devices with stacking faults are shown in Extended Data Fig. 1. The presence of faults is established by measuring Raman spectra.

Landau levels in multilayer RG

We have calculated the LL spectrum by employing the same method as in ref. [26]. Numerical diagonalization is performed in a regularized finite basis consisting of oscillator states for each sublattice component, namely $(\phi_0, \phi_1, \ldots, \phi_{N_0+n-1})$ for sublattice A_n and $(\phi_0, \phi_1, \ldots, \phi_{N_0+n})$ for B_n where $N_0 = 250$ is a cut-off LL index, sufficient for convergence at $B > 0.5$ T.

To qualitatively understand the LL spectrum, let us start with the minimal model[24] with only the nearest-neighbour in-plane (γ_0) and interlayer (γ_1) hoppings. In the absence of a displacement field ($D = 0$), the low-energy LL spectrum consists of $4N$-degenerate levels at zero energy, which we refer to as zeroth LLs (where 4 is due to double-spin and double-valley degeneracy, and N comes from N-fold orbital degeneracy), plus four-fold degenerate levels arising from the conduction and valence bands that disperse as $E^{\pm} \approx \pm B^{N/2}$. Within the two-band model, the vector wavefunctions of zeroth LLs of one valley reside on one (for example, the top) surface, $\Psi_{K^+,i} = \begin{pmatrix} \varphi_i \\ 0 \end{pmatrix}$, $i = 0, \ldots, N-1$, while for the other valley the wavefunctions sit on the opposite (for example, the bottom) surface, $\Psi_{K^-,i} = \begin{pmatrix} 0 \\ \varphi_i \end{pmatrix}$. Therefore, for zeroth LLs the valley degeneracy is equivalent to the top/bottom surface degeneracy.

The minimal model is insufficient to describe the experimental results, making it necessary to consider further electron hopping amplitudes. The presence of inter-layer same-sublattice hopping γ_4 leads to strong electron–hole asymmetry and breaks the orbital degeneracy of zeroth LLs, leading to dispersion $E_n^0 = n\hbar\omega_c$, $n = 0, \ldots, N-1$, with $\omega_c = eB/m_*$, $m_* \approx 0.4\, m_e$. The conduction-band LLs continue the sequence of four-fold degenerate LLs as $E_n^+ = n\hbar\omega_c$, $n = N, N+1, \ldots$. The valence-band dispersion is non-monotonic and produces a series of four-fold degenerate LLs $E_n^- = n\hbar\omega_c$, $n = 1, 2, \ldots$ near zero energy, as well as a sequence of 12-fold degenerate levels at higher energies, originating from the three equivalent valence-band maxima caused by trigonal warping (hoppings γ_3, γ_2).

At moderate B, valence-band LLs bend down, forming numerous crossings with zeroth LLs and conduction-band LLs[24]. This explains the multiple crossings of the LLs on the hole side in Fig. 3a, b. The two-fold degeneracy of the filling factors (for example, $\nu = 6, 8, 10\ldots$) at $D = 0$ can be attributed to the preserved valley degeneracy, while the gaps are given by combination of the orbital splitting ($\nu = 6, 10, 14\ldots$ for odd N and $\nu = 4, 8, 12, 16\ldots$ for even N) and spin splitting ($\nu = 4, 8, 12, 16\ldots$ for odd N and $\nu = 6, 10, 14\ldots$ for even N). Although the theory qualitatively agrees with the experiment, it predicts a twice higher value of B at which the last crossings occur. This discrepancy can be attributed to exchange interactions.

The filling factor at a specified chemical potential is determined as the number of filled LLs in the regularized basis, with half the total number of levels subtracted to account for the background charge neutralizing the Fermi sea. Normally, this would place the zero electron density between LLs originating from valence and conduction bands that form the pairs related by approximate electron–hole symmetry $(\Psi_A, \Psi_B) \rightarrow (\Psi_A, -\Psi_B)$. However, there are N additional (spin and valley degenerate) zero LLs (numbered as $0, \ldots, N-1$) with wavefunctions localized only on one of the sublattices. At low B, zero LLs overlap with valence-band LLs, leading to complicated counting of the filling factors but, for $B \gtrsim 10$ T, conventional valence-band LLs are below the zero energy, leading to zero electron density ($\nu = 0$) located in the middle point of zeroth LLs. This middle point is located either in between the

Zeeman-split zeroth LLs with index $(N-1)/2$ for odd N, or between the orbital-split zeroth LLs with indices $N/2-1$ and N/2 for even N.

Spin- and valley-polarized states

Coulomb and phonon-mediated interactions between electrons can lead to a multitude of patterns for spontaneous symmetry breaking. These include breaking a 'top–bottom' symmetry of the two surfaces, a spin/valley symmetry, a six-fold rotation symmetry (nematic phase), a lattice translational symmetry (charge density wave), or a U(1) gauge symmetry (superconductivity)[38–40]. The presented experiments provide evidence that symmetry breaking occurs for a limited range of sample thicknesses (<10 layers), hinting at the importance of interaction between the surfaces, which suggests a 'top–bottom' type of symmetry breaking order. The candidates are thus the quantum valley Hall (VH; ferroelectric) phase with order parameter $\Delta^{\mathrm{VH}} = \lambda\, \sigma_z^{\mathrm{layer}}$, quantum layer antiferromagnetism (LAF) $\Delta^{\mathrm{LAF}} = \lambda\, \sigma_z^{\mathrm{layer}} \otimes \sigma_z^{\mathrm{spin}}$, the quantum spin Hall (QSH) phase (also called the 'spin flux' phase) $\Delta^{\mathrm{QSH}} = \lambda\, \sigma_z^{\mathrm{layer}} \otimes \sigma_z^{\mathrm{spin}} \otimes \sigma_z^{\mathrm{valley}}$, or the quantum anomalous Hall (AH) phase $\Delta^{\mathrm{AH}} = \lambda\, \sigma_z^{\mathrm{layer}} \otimes \sigma_z^{\mathrm{valley}}$. Here, σ_z is a Pauli matrix. In the absence of a B field, only the relative orientation of spins matters, while the presence of a B field lifts this degeneracy to fix an optimal 'canted' orientation of spins[41]. The AH phase breaks the time-reversal symmetry and implies a Hall signal at $B = 0$, which has not been observed. The VH phase is the one induced by displacement field and discussed above, but it is not continuously connected to the observed spontaneous insulating phase, and, instead, competes with it. So we are left with two candidates: LAF and the QSH effect. Both phases lead to giant Berry curvatures and, consequently, to large orbital magnetic moments, which peak near the three degenerate maxima of the valence band[17]. The orbital magnetic moment has opposite signs in the two valleys for Δ^{LAF} or for the gate-induced displacement field. In the case of Δ^{QSH}, the orbital moment becomes the same in both valleys but opposite for the two spin directions. The orbital moment leads to pronounced lifting of the 12-fold degeneracy of LLs originating from valence-band maxima, which results in two groups of six-fold LLs. This explains the observed robust gap at $\nu = -6$ (Fig. 3a, b, d). The six unoccupied valence-band LLs lead to the layer-antiferromagnet (three K↑ and three K′↓ levels) in the case of the quantum LAF order parameter and to a ferromagnet (three K↑ and three K′↑) in the case of QSH ordering. Canting effects can be neglected since the magnitude of the order parameter is much larger than the Zeeman splitting.

The effect of order parameters on the spectrum of zeroth LLs amounts to valley-/spin-dependent shifts for LAF/QSH phases, which follows from localization of zeroth LLs on the top/bottom surfaces in the K/K′ valleys. Hence, Δ^{LAF} breaks the valley degeneracy, leading to the appearance of gaps at odd filling factors (Fig. 3f) whereas the valley degeneracy remains intact for Δ^{QSH} (Fig. 3e). The experimental data in Fig. 3c are consistent with the QSH order for electron doping below $2.5 \times 10^{12}\ \mathrm{cm}^{-2}$, where the orbital and spin magnetic moments align. Note that a QSH order parameter fits finite magnetic field data at substantial electron doping, and does not necessarily connect to the observed spontaneous gap near charge neutrality.

Data availability

The data that support the findings of this study are available from the corresponding author upon reasonable request.

35. Cai, S. et al. Independence of topological surface state and bulk conductance in three-dimensional topological insulators. *npj Quantum Mater*. **3**, 62 (2018).
36. Dresselhaus, M. S. & Dresselhaus, G. Intercalation compounds of graphite. *Adv. Phys*. **51**, 1–186 (2002).
37. García-Ruiz, A., Slizovskiy, S., Mucha-Kruczynski, M. & Fal'ko, V. I. Spectroscopic signatures of electronic excitations in Raman scattering in thin films of rhombohedral graphite. *Nano Lett*. **19**, 6152–6156 (2019).
38. Zhang, F. & MacDonald, A. H. Distinguishing spontaneous quantum Hall states in bilayer graphene. *Phys. Rev. Lett*. **108**, 186804 (2012).
39. Lemonik, Y., Aleiner, I. & Fal'ko, V. I. Competing nematic, antiferromagnetic, and spin-flux orders in the ground state of bilayer graphene. *Phys. Rev. B* **85**, 245451 (2012).
40. Kharitonov, M. Canted antiferromagnetic phase of the $\nu = 0$ quantum Hall state in bilayer graphene. *Phys. Rev. Lett*. **109**, 046803 (2012).
41. Kharitonov, M. Antiferromagnetic state in bilayer graphene. *Phys. Rev. B* **86**, 195435 (2012).

Acknowledgements This work was supported by the EU Graphene Flagship Program, the European Research Council, the Royal Society, and the Engineering and Physical Sciences Research Council (EPSRC). A.M. acknowledges the support of an EPSRC Early Career Fellowship (EP/N007131/1). S.V.M. was supported by the RFBR (20-02-00601). This work was partially supported by the French National Research Agency (ANR) in the framework of a RhomboG grant (ANR-17-CE24-0030).

Author contributions A.M. conceived the presented idea and directed the project. Y.S., S.V.M., S.O., C.M., J.B., J.Y., A.I.B. and B.A.P. performed transport measurements. S.X., Y.Y. and S.-K.S. fabricated devices. Y.S., S.O., C.M. and J.Y. performed data analysis. S.S. and V.I.F. developed the theory and performed theoretical calculations. Y.S., S.O., A.K.G., V.I.F. and A.M. contributed to the interpretation of data. K.W. and T.T. grew hBN single crystals. A.M., Y.S., A.K.G., S.S., V.I.F. and K.S.N. contributed to the writing of the manuscript. All authors discussed the results and commented on the manuscript.

Competing interests The authors declare no competing interests.

Additional information

Correspondence and requests for materials should be addressed to A.M.

Peer review information *Nature* thanks Dmitri Efetov and the other, anonymous, reviewer(s) for their contribution to the peer review of this work.

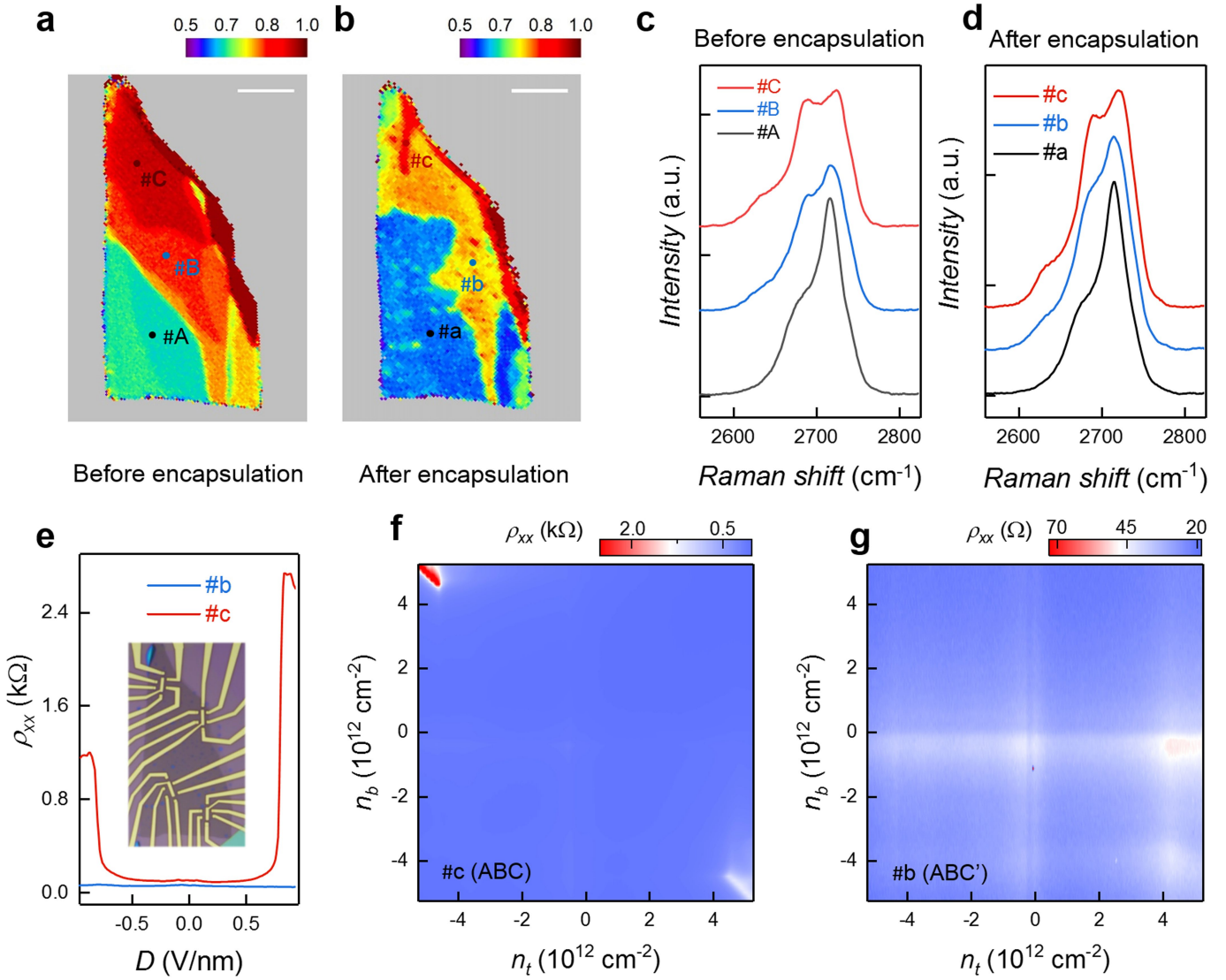

Extended Data Fig. 1 | Effect of stacking sequence on the displacement-field-induced bandgap. a, **b**, Raman maps of device 3, a 6.5-nm graphite flake with domains of differing local stacking sequence, shown before (**a**) and after (**b**) encapsulation. The colour coding indicates the ratio of the integrated area of the low-frequency component of the graphite Raman 2D band (ranging around 2,670–2,700 cm^{-1}) to that of the high-frequency component (ranging around 2,700–2,730 cm^{-1}). Coloured dots in **a** and **b** mark the positions where the Raman spectra shown in **c** and **d** respectively were taken. Scale bars, 10 µm. **c**, **d**, Typical 2D Raman peaks of HG (black curves A and a), RG (red curves C and c) and graphite of mixed ABA and ABC stacking (blue curves B and b), before (**c**) and after (**d**) encapsulation. Laser wavelength, 532 nm. **e**, ρ_{xx} as a function of D for Hall bar devices made using domains at point b (light blue) and point c (red), respectively, $T = 1.6$ K. Inset, optical micrograph of the devices before shaping them into the Hall bar geometry. **f**, **g**, Resistivity maps $\rho_{xx}(n_t, n_b)$ of graphite with ABC stacking (**f**) and mixed stacking (**g**); $T = 1.6$ K, $B = 0$ T.

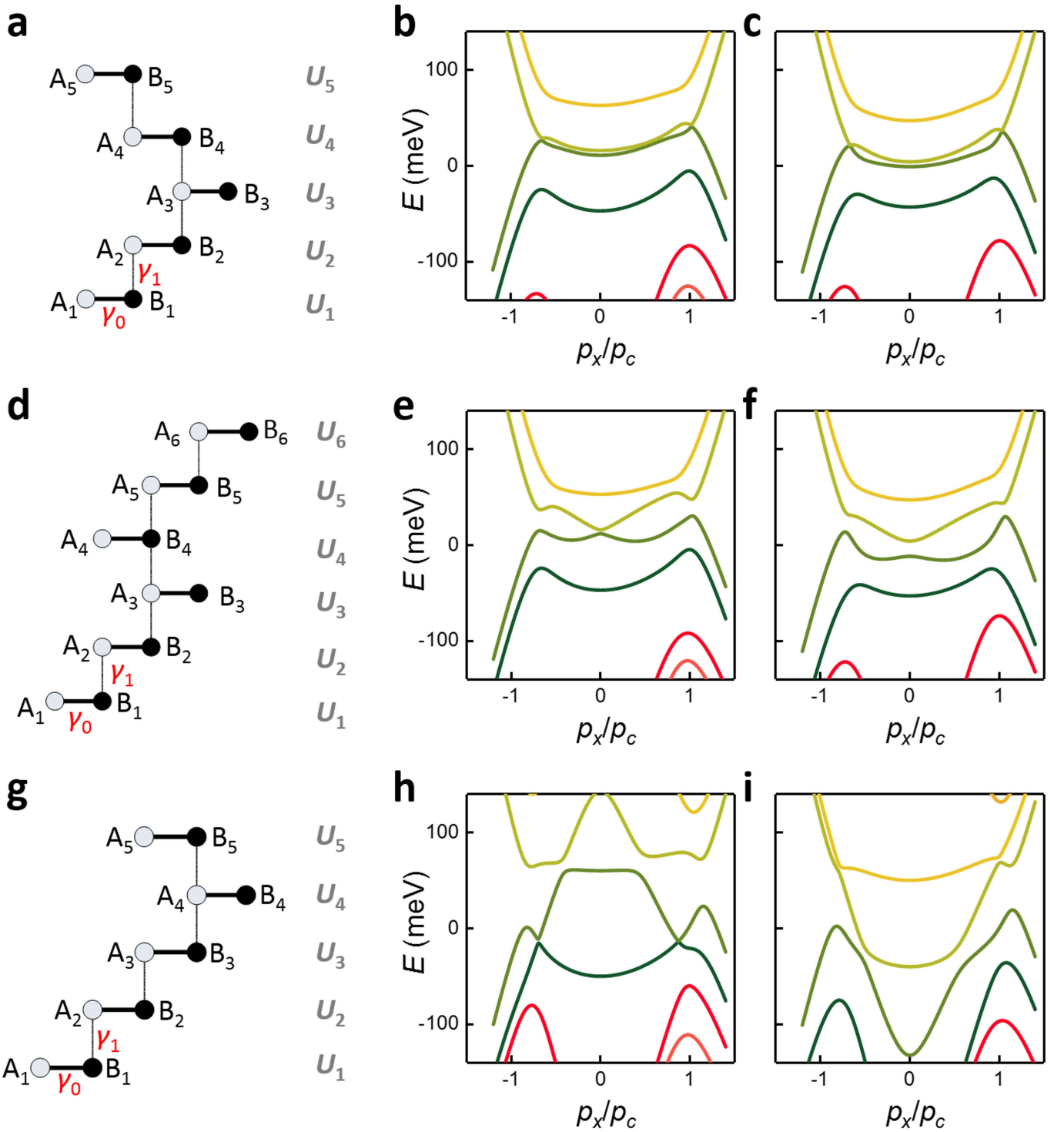

Extended Data Fig. 2 | Band structures of multilayer RG with stacking faults. a, Schematic of twin-boundary defect. **b**, **c**, Calculated spectra for the ABCABC**ABA**CBACBACBA sequence at positive (**b**) and negative (**c**) D. **d**, Schematic of a buried Bernal stacking fault A**BCBC**A. **e**, **f**, Calculated band structure for such a defect: ABCABC**ABAB**CABCABCA sequence at positive (**e**) and negative (**f**) D. **g**, Schematic of surface stacking fault ABCAC. **h**, **i**, Spectra for the ABCABCABCABCABC**ABA** sequence at positive (**h**) and negative (**i**) D. In all the calculations we used $D = \pm 1$ V nm^{-1}. See Methods section 'Possibility of stacking faults' for details of nomenclature used in **a**, **d**, **g**. E is the band energy, p_x is the in-plane momentum, and $p_c = \gamma_1/v$, where v is the Dirac velocity.

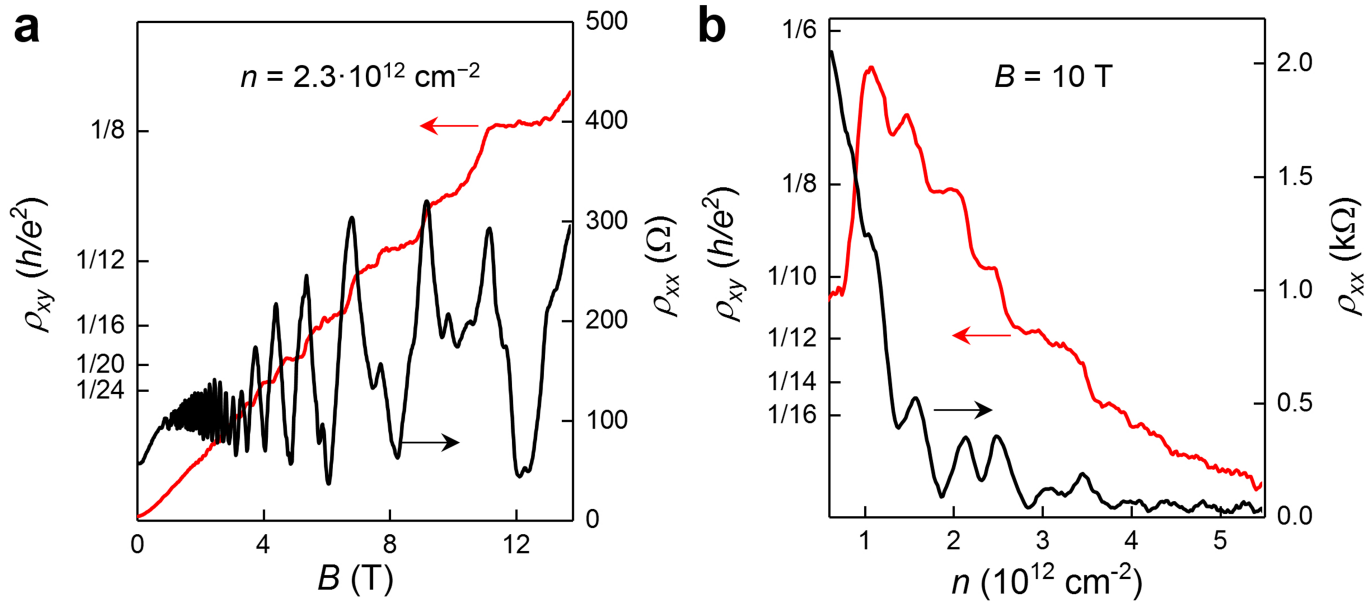

Extended Data Fig. 3 | The quantum Hall effect in thin RG. a, Hall resistivity ρ_{xy} (red curve) and longitudinal resistivity ρ_{xx} (black curve) as a function of magnetic field B measured at 20 mK for the same device as in main text Fig. 3 (device 1); $n = 2.3 \times 10^{12}$ cm^{-2}, $D = 0$ V nm^{-1}. **b**, ρ_{xy} and ρ_{xx} as a function of n for the same device as in **a**; $D = 0$, $B = 10$ T, $T = 20$ mK.

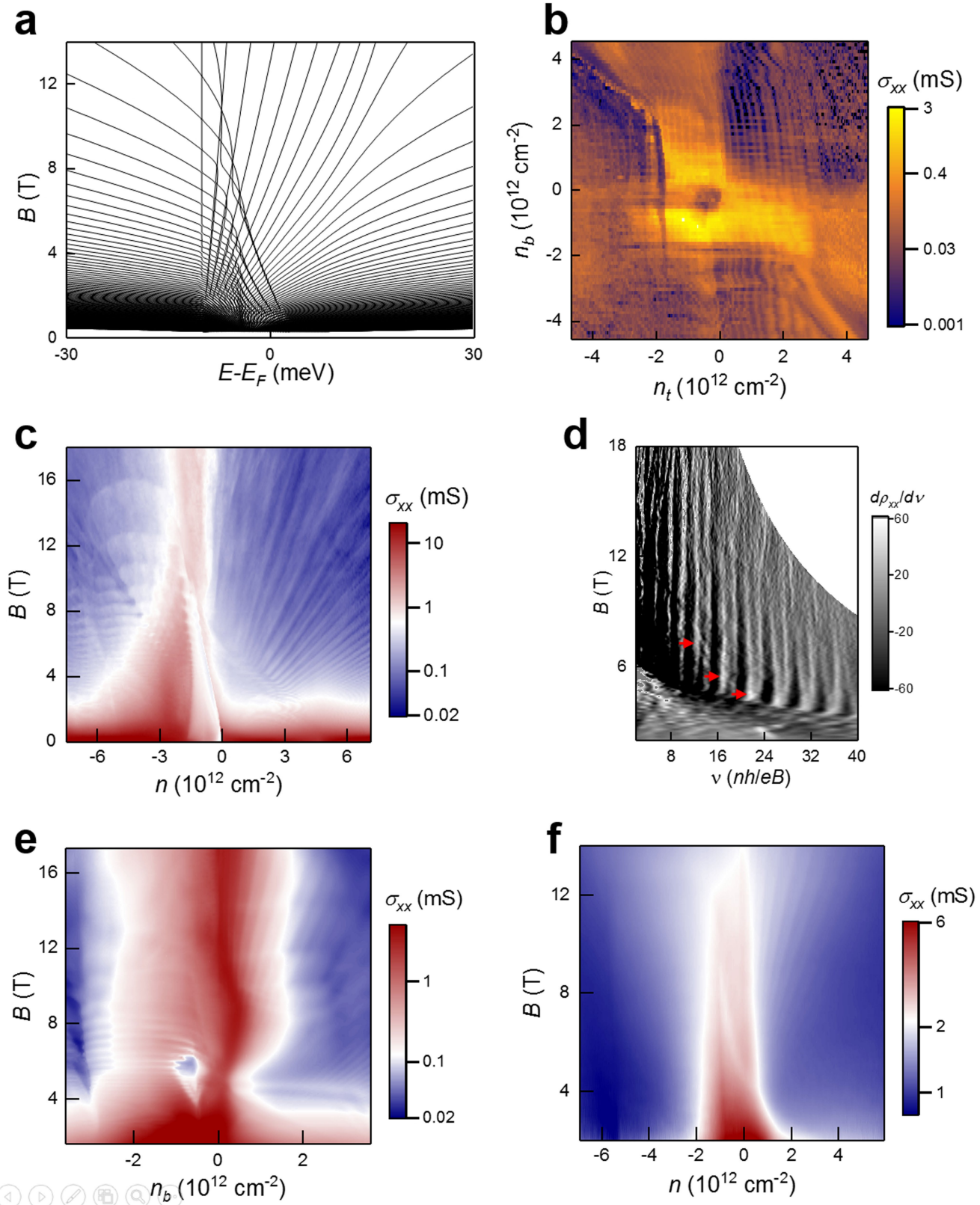

Extended Data Fig. 4 | Landau levels from surface states of multilayer RG. **a**, Calculated free-particle spectrum. **b**, Conductivity map $\sigma_{xx}(n_t, n_b)$ for 3-nm-thick RG (device 1) measured at $B = 9$ T and $T = 20$ mK. Note that, for two independent surfaces, LLs should form sets of horizontal and vertical lines. The observed behaviour suggests that top and bottom surfaces of our RG devices are nearly independent 2D systems. **c**, Landau fan $\sigma_{xx}(n, B)$ for device 5 (3.3-nm-thick RG); $D = 0$, $T = 0.25$ K. **d**, Differential $d\rho_{xx}/d\nu(\nu, B)$ map on the electron side (same device as in **c**). The red arrows indicate LL crossings. **e**, $\sigma_{xx}(n_b, B)$ for device 8 (7.2-nm-thick RG) measured at $T = 1.7$ K. **f**, $\sigma_{xx}(n, B)$ for device 4 (16.5-nm-thick RG) at $D = 0$ and $T = 0.25$ K.

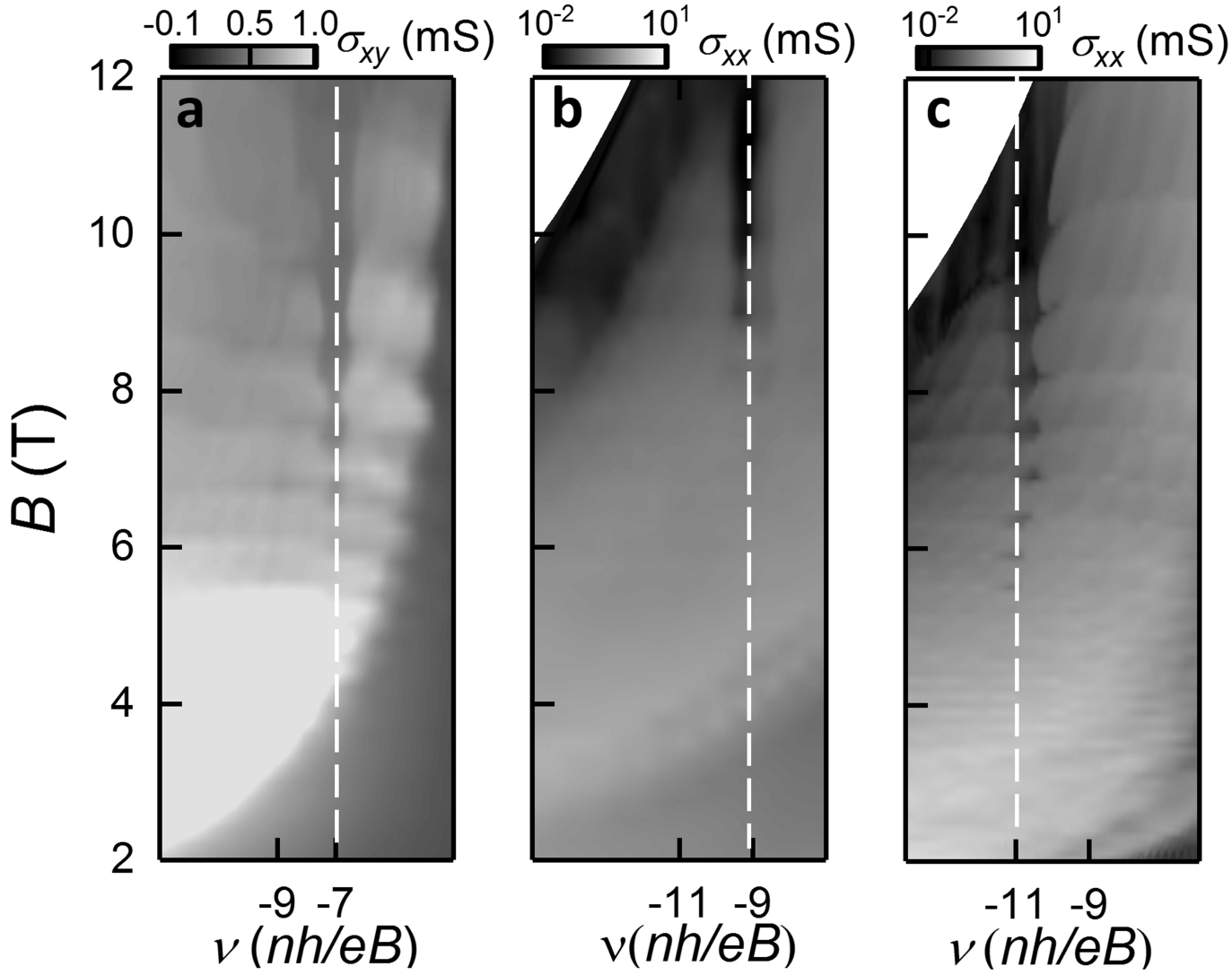

Extended Data Fig. 5 | Single-gate ($D \neq 0$) Landau fan diagrams highlighting the robust $\nu = -N$ quantum Hall state in N-layer-thick RG. a, Conductivity map $\sigma_{xy}(\nu, B)$ for 7-layer-thick RG (device 7). **b**, Conductivity map $\sigma_{xx}(\nu, B)$ for 9-layer-thick RG (device 1). **c**, $\sigma_{xx}(\nu, B)$ for 11-layer-thick RG (device 6).

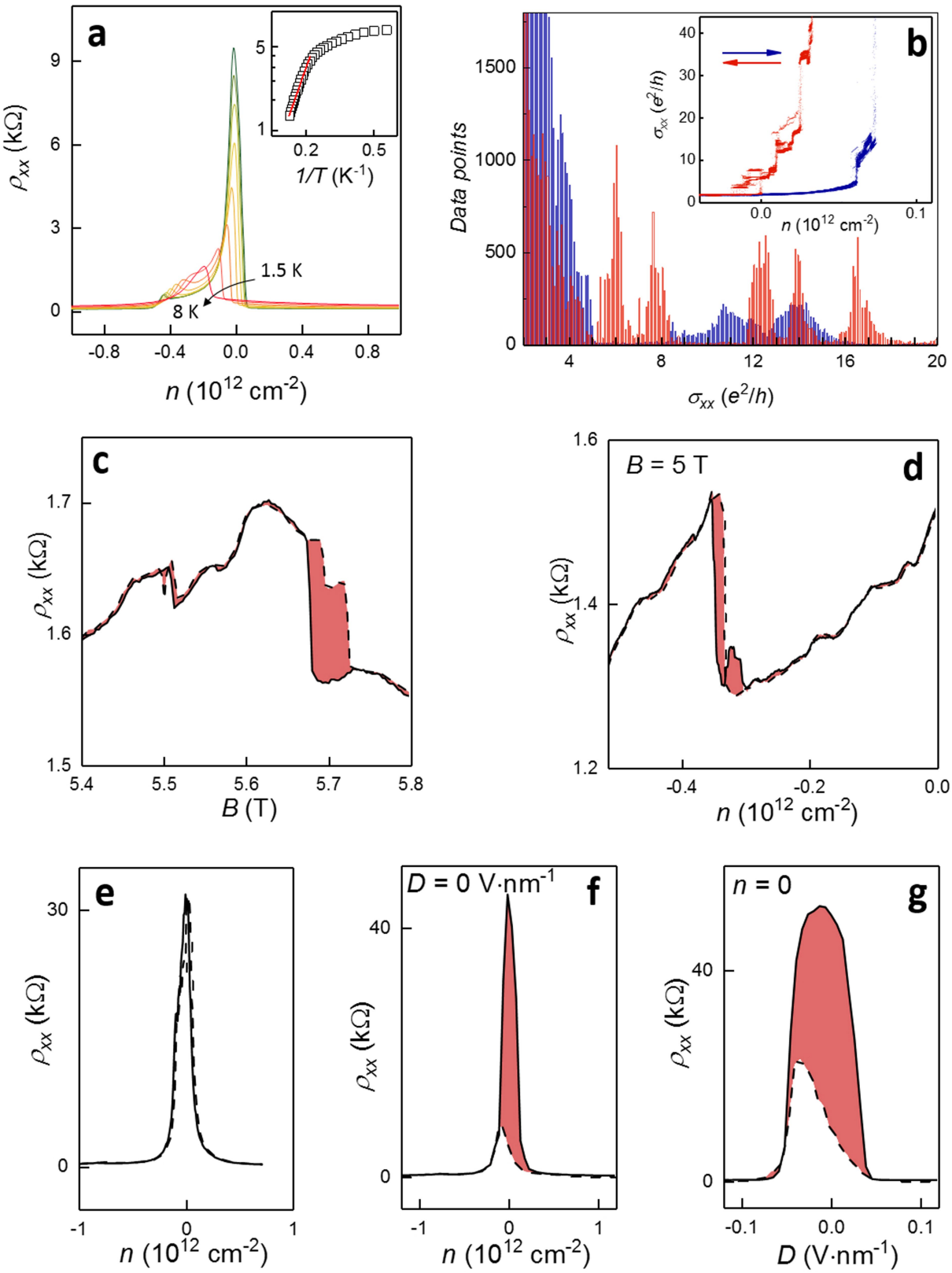

Extended Data Fig. 6 | See next page for caption.

Extended Data Fig. 6 | Insulating states and hysteretic behaviour in multilayer RG. a, **b**, Additional data for 3.3-nm-thick RG (device 5, same as in main text Fig. 4a, b). **a**, Main panel, temperature dependence of $\rho_{xx}(n)$ around the insulating state, $B = 0$ T. Inset, Arrhenius plot for the peak resistivity, indicating the presence of a bandgap of about 2–3 meV. The y axis shows peak resistivity, and red line indicates the fit. **b**, Main panel, histogram of the conductivity values found on the hysteretic curves $\sigma_{xx}(n)$, such as those shown in the inset. Eighty-three such curves were used to make the histogram, where data from forward and backward sweeps are plotted in blue and red, respectively. $D = 0$, $T = 250$ mK, $B = 0$. **c**, Hysteresis (shaded red) in $\rho_{xx}(B)$ observed in device 7 (2.3-nm-thick RG) at the charge neutrality point; **d**, hysteresis (shaded red) in $\rho_{xx}(n)$ at $B = 5$ T. For **c** and **d**, $T = 250$ mK. **e**–**g**, Hysteretic behaviour of device 1 for different cooling cycles. No noticeable hysteresis was found for the first cooling event (**e**). Hysteresis in $\rho_{xx}(n)$ (**f**) and $\rho_{xx}(D)$ (**g**) is clearly seen after another cooling. Solid (dashed) lines indicate positive (negative) sweep directions and the coloured areas highlight the difference between the sweep directions. $T = 20$ mK; $B = 0$ T.

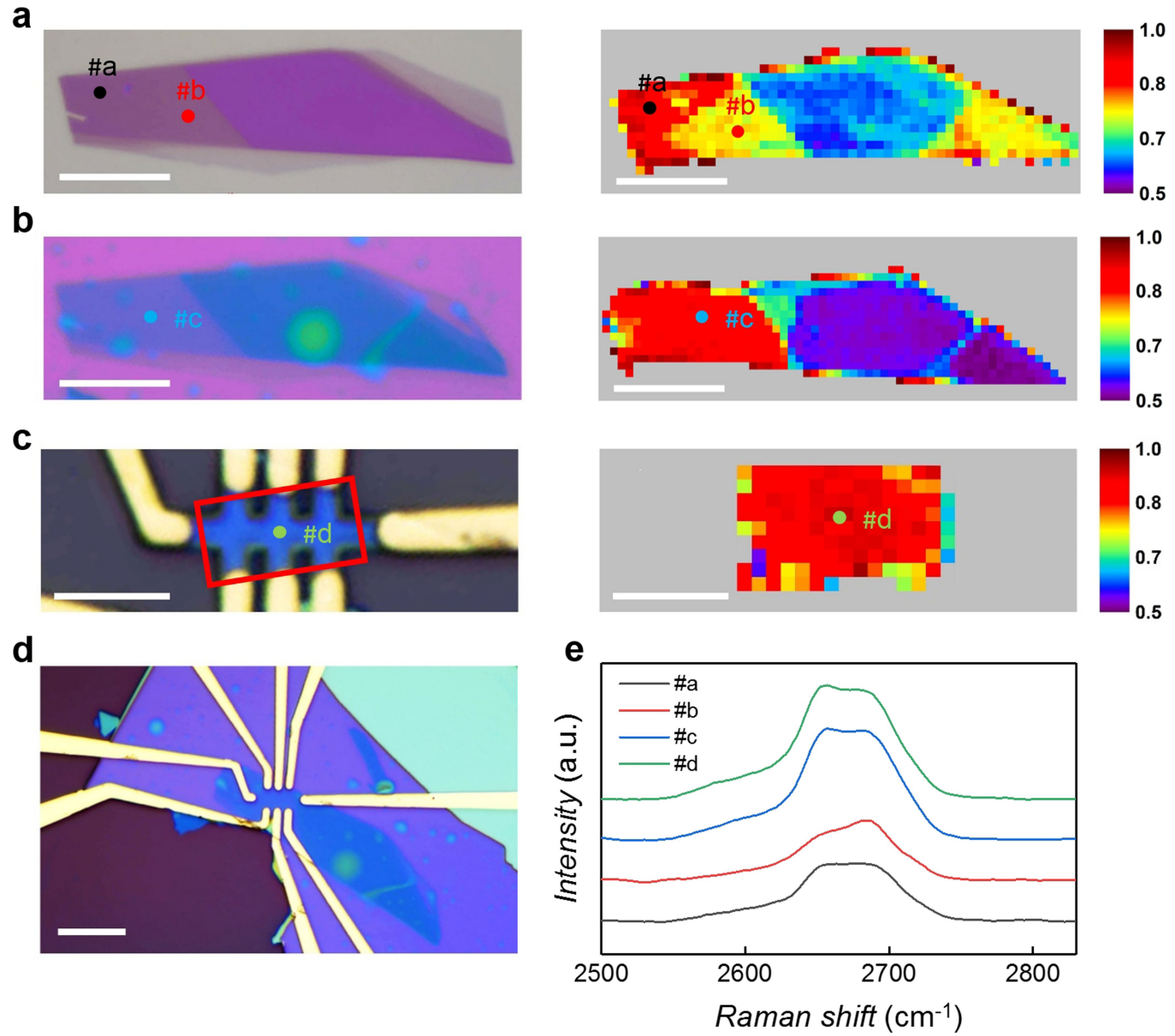

Extended Data Fig. 7 | Stacking order of device 6 at different fabrication stages. a, Optical image of the graphite flake (left) and the corresponding Raman map with a step size of 0.8 µm × 0.8 µm (right). Scale bar, 10 µm. **b**, Optical image of the graphite flake encapsulated by hBN (left) and the corresponding Raman map with a step size of 0.7 µm × 0.7 µm (right). Scale bar, 10 µm. **c**, Optical image of the finished Hall bar (left) and the corresponding Raman map with a step size of 0.5 µm × 0.5 µm (right). Scale bar, 4 µm. The colour coding of the Raman maps in **a**–**c** indicates the ratio of the integrated area of the low-frequency component (ranging around 2,635–2,665 cm^{-1}) to that of the high-frequency component (ranging around 2,665–2,695 cm^{-1}) of the graphite Raman 2D band. The coloured dots in **a**–**c** mark the positions where the Raman spectra shown in **e** were taken. **d**, Optical image showing that the Hall bar device is made from the ABC stacked region. Scale bar, 10 µm. **e**, Typical 2D Raman peaks of RG (dots a, c and d) and of graphite of mixed ABA and ABC stacking (dot b). Laser excitation wavelength, 633 nm.

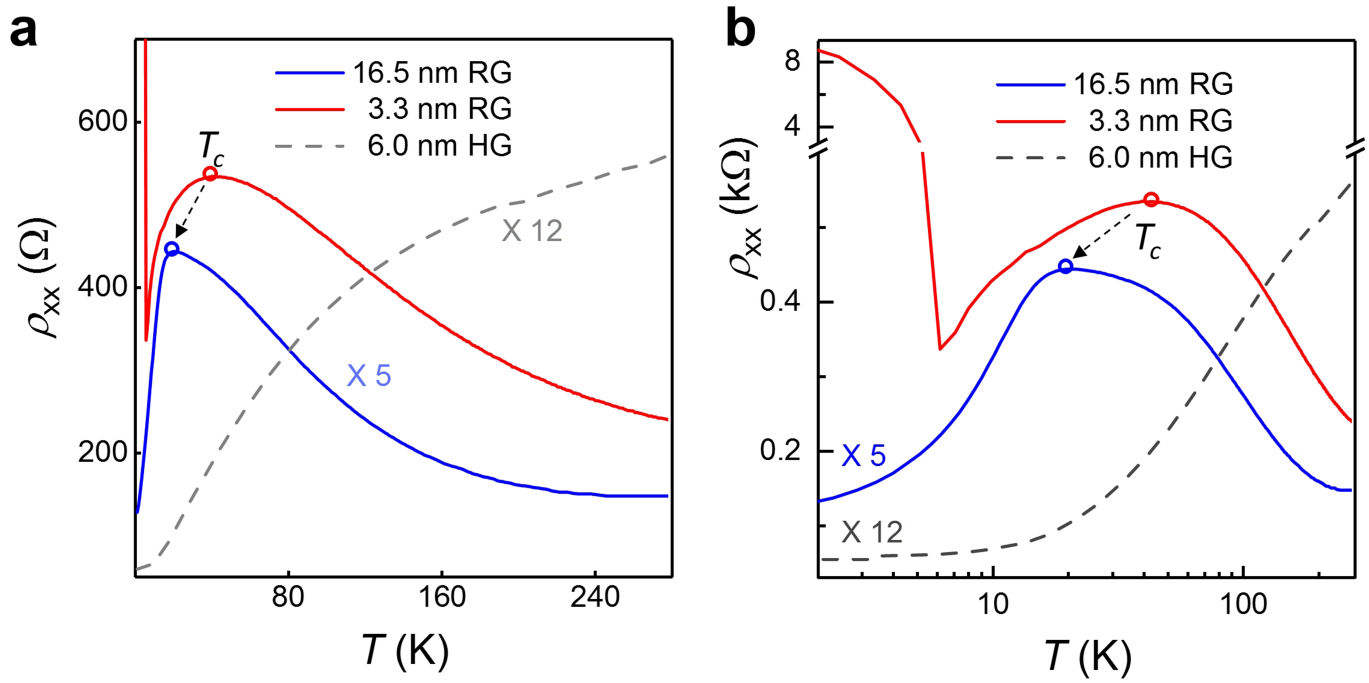

Extended Data Fig. 8 | Temperature dependence of resistivity. a, ρ_{xx} as a function of T at zero gate doping for RG device 4 with a thickness of 16.5 nm (blue solid curve), for RG device 5 with a thickness of 3.3 nm (red solid curve), and for 6-nm HG (grey dashed line). **b**, Same data as **a** but plotted on a log scale. While cooling down, ρ_{xx} of RG first increases for $T > T_c$, and then decreases, in sharp contrast to the monotonic decrease of ρ_{xx} for HG. The critical temperature T_c decreases with increasing thickness of RG. Besides the presence of T_c, ρ_{xx} of the 3.3-nm RG device 5 shows a sharp increase for $T < 6$ K owing to the phase transition to the insulating state.

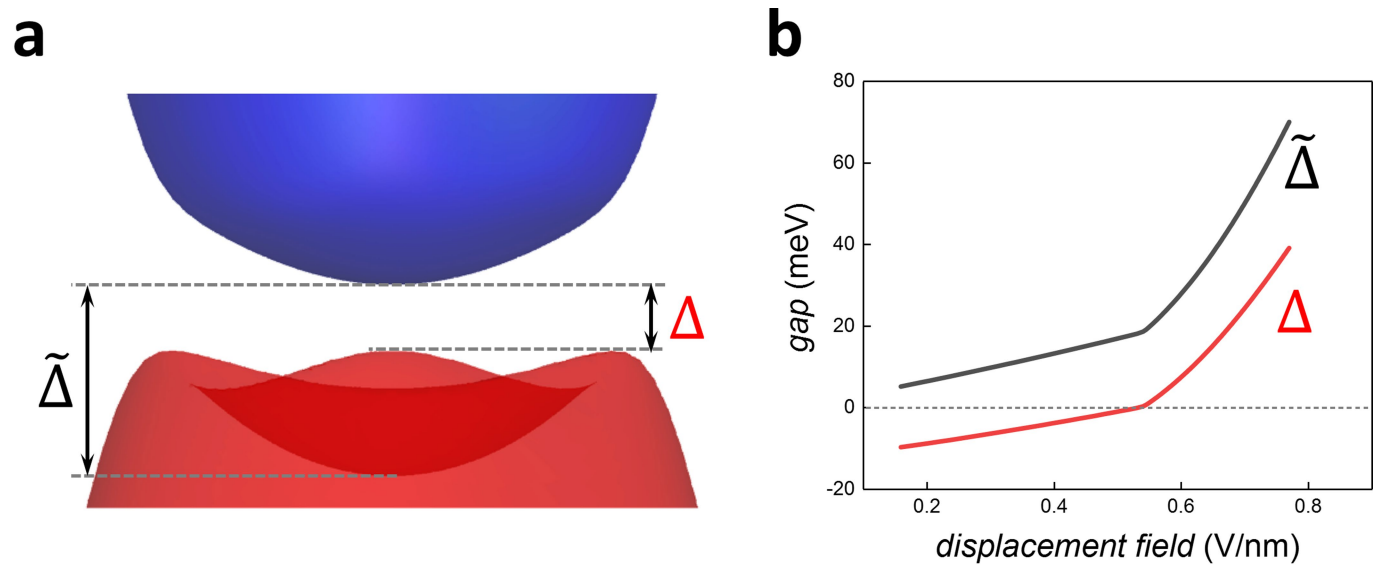

Extended Data Fig. 9 | Bandgap opening by displacement field. a, Band dispersion of RG under an applied displacement field; bandgap $\tilde{\Delta}$ is masked by a bandwidth of $2\gamma_4\gamma_1/\gamma_0$ such that only the effective gap $\Delta = \tilde{\Delta} - 2\gamma_4\gamma_1/\gamma_0$ is visible in transport measurements. **b**, Calculated dependence of $\tilde{\Delta}$ and Δ on displacement field for $N = 9$ layers.

Chapter 7: In situ technique for van der Waals twistronics

7.1 Introduction

The discovery of correlated flat bands in magic angle twisted bilayer stimulated intensive researches covering many van der Waals systems demonstrating a plethora of interaction-induced effects including Mott insulating states, superconductivity and magnetism, etc. Tuning of twist angle became a viable tool to control the topology and electron interactions in 2D materials. In this chapter, we present a novel technique enabling *in situ* dynamical rotation and manipulation of 2D materials in van der Waals heterostructures. We demonstrate this technique by fabricating heterostructures with perfect alignment between graphene and encapsulating layers of hexagonal boron nitride, forming double moiré superlattices at the two interfaces. In this technique, an epitaxial polymer layer patterned onto a target 2D flake by a standard electron-beam lithography process is the key to realize a precise control of the manipulation. The epitaxial polymer layer limits the contact area of the polymer gel manipulator precisely to the patterned shape, allowing a much larger controlling force threshold. This work greatly facilitates the accurate rotation and manipulation of 2D crystals and opens up a new strategy in designing van der Waals materials with novel electronic properties, which should have a significant impact on the field of twistronics.

7.2 *In situ* manipulation of van der Waals heterostructures for twistronics

Publication: In situ manipulation of van der Waals heterostructures for twistronics

Journal reference: Science Advances, 2020, 6, 49, eabd3655.

DOI: 10.1126/sciadv.abd3655

My contribution to this work: developed the technique of *in situ* manipulation of van der Waals heterostructures, conceived the idea of applying the *in situ* technique to twistronics, prepared all the samples, performed Raman measurement, analysed the transport data, prepared the figures and wrote the manuscript.

Full author list: Yaping Yang, Jidong Li, Jun Yin, Shuigang Xu, Ciaran Mullan, Takashi Taniguchi, Kenji Watanabe, Andre K. Geim, Konstantin S. Novoselov, Artem Mishchenko.

Author contributions: A.M. developed the concept of the experiment and supervised the project. Y.Y. carried out the experiments, fabricated the devices, interpreted data with help from C.M. and wrote the manuscript. J.L. and S.X. gave critical suggestions to the presented idea. J.Y. performed transport measurement. T.T. and K.W. synthesized the hBN crystals. A.K.G and K.S.N. advised on the experiments. All authors discussed the results and commented on the manuscript.

CONDENSED MATTER PHYSICS

In situ manipulation of van der Waals heterostructures for twistronics

Yaping Yang[1,2]*, Jidong Li[3], Jun Yin[3], Shuigang Xu[2], Ciaran Mullan[1], Takashi Taniguchi[4], Kenji Watanabe[4], Andre K. Geim[1,2], Konstantin S. Novoselov[1,2,5], Artem Mishchenko[1,2]*

In van der Waals heterostructures, electronic bands of two-dimensional (2D) materials, their nontrivial topology, and electron-electron interactions can be markedly changed by a moiré pattern induced by twist angles between different layers. This process is referred to as twistronics, where the tuning of twist angle can be realized through mechanical manipulation of 2D materials. Here, we demonstrate an experimental technique that can achieve in situ dynamical rotation and manipulation of 2D materials in van der Waals heterostructures. Using this technique, we fabricated heterostructures where graphene is perfectly aligned with both top and bottom encapsulating layers of hexagonal boron nitride. Our technique enables twisted 2D material systems in one single stack with dynamically tunable optical, mechanical, and electronic properties.

INTRODUCTION

Rotational misalignment caused by a twist angle between adjacent layers of two-dimensional (2D) materials results in symmetry breaking and strain effects, leading to enhanced or suppressed interlayer coupling and electronic band structure reconstruction (*1*–*4*). Moiré superlattices formed by rotational misalignment and lattice mismatch have been under intense scrutiny, and an abundance of new phenomena has been observed (*5*–*24*). Graphene placed on hexagonal boron nitride (hBN) represents a prototypical system of a twisted heterobilayer. In this system, when at a small twist angle, mono- or few-layer graphene in a quantizing magnetic field exhibits a fractal energy spectrum known as Hofstadter's butterfly (*5*–*7*). This system has been reported to bear topological bands and strong correlations, exhibiting a number of fascinating many-body phenomena, such as correlated insulating states and superconductivity reported in trilayer graphene on hBN (*8*, *9*), and fractional Chern insulators observed in bilayer graphene on hBN (*10*). In twisted homobilayers, strongly correlated phenomena including correlated insulating states, unconventional superconductivity, and ferromagnetism have been observed in twisted bilayer graphene (*11*–*14*) and twisted bilayer-bilayer graphene systems (*15*–*18*). A variety of other systems, such as twisted transition metal dichalcogenide layers (*19*–*22*), graphene/WS_2 bilayer (*23*), and twisted bilayer graphene aligned to hBN (*24*), have also manifested many intriguing phenomena.

In twistronics, accurate positioning, rotation, and manipulation of 2D materials are needed to fabricate a system with desired twist angles. To this end, several techniques have been developed, including optical alignment of crystal edges (*7*, *25*), tear-and-stack technique for twisted homobilayers (*26*), and in situ rotation mediated by atomic force microscopy (AFM) tips (*27*). Here, we present a new experimental strategy to dynamically manipulate layered heterostructures in situ with precise control, allowing investigation of optical, mechanical, and electronic properties of a system with tunable twist angles between individual layers.

RESULTS

For our in situ twistronics technique, we use a glass slide with a droplet of polydimethylsiloxane (PDMS) as a manipulator, which is cured and naturally shaped into a hemisphere geometry. For a carefully fabricated PDMS hemisphere, the contact area between the manipulator and a 2D crystal can be as small as a few tens of micrometers (*26*, *28*), which depends on the hemisphere radius and is highly sensitive to the contact force, making it difficult to precisely control the target flake. To solve this problem, we developed a critical step, where we intentionally deposited an epitaxial polymethyl methacrylate (PMMA) patch on top of a target flake through a standard electron beam lithography (EBL) process. The concept is illustrated in Fig. 1. The epitaxial PMMA patch can be designed into an arbitrary shape that fits the target flake, and its thickness is normally a few hundred nanometers, which can be further increased by spin coating double layers of PMMA or by reducing the spinning speed, while the height of the PDMS manipulator can be adjusted with a high accuracy in most of the micromanipulator-based transfer systems. Thereby, the contact area between the PDMS hemisphere and the flake can be precisely limited to the area of the epitaxial PMMA patch without PDMS touching beyond the target flake at a much larger contact force threshold.

This strategy facilitates the accurate manipulation of the target flake. Figure 1 (B to D) shows the cartoon schematics of how the in situ manipulation of heterostructures works. To manipulate the target flake of the hBN/graphene/hBN heterostructure, first, by lowering down the polymer gel handle, PDMS hemisphere is brought in contact with the PMMA patch, which is prepatterned onto top hBN. When they touch, there is a color change in the PMMA patch, which can be easily distinguished under an optical microscope (see fig. S1). Figure 1E shows the top view when the PDMS hemisphere touches the PMMA patch, where the interference rings imply that the PDMS hemisphere is in the proximity of the flake without touching it. In incommensurate state, the top hBN and the underneath

[1]School of Physics and Astronomy, University of Manchester, Oxford Road, Manchester M13 9PL, UK. [2]National Graphene Institute, University of Manchester, Oxford Road, Manchester M13 9PL, UK. [3]State Key Laboratory of Mechanics and Control of Mechanical Structures and MOE Key Laboratory for Intelligent Nano Materials and Devices, College of Aerospace Engineering, Nanjing University of Aeronautics and Astronautics, Nanjing 210016, China. [4]National Institute for Materials Science, 1-1 Namiki, Tsukuba 305-0044, Japan. [5]Centre for Advanced 2D Materials, National University of Singapore, 117546, Singapore.
*Corresponding author. Email: ypyang0916@gmail.com (Y.Y.); artem.mishchenko@gmail.com (A.M.)

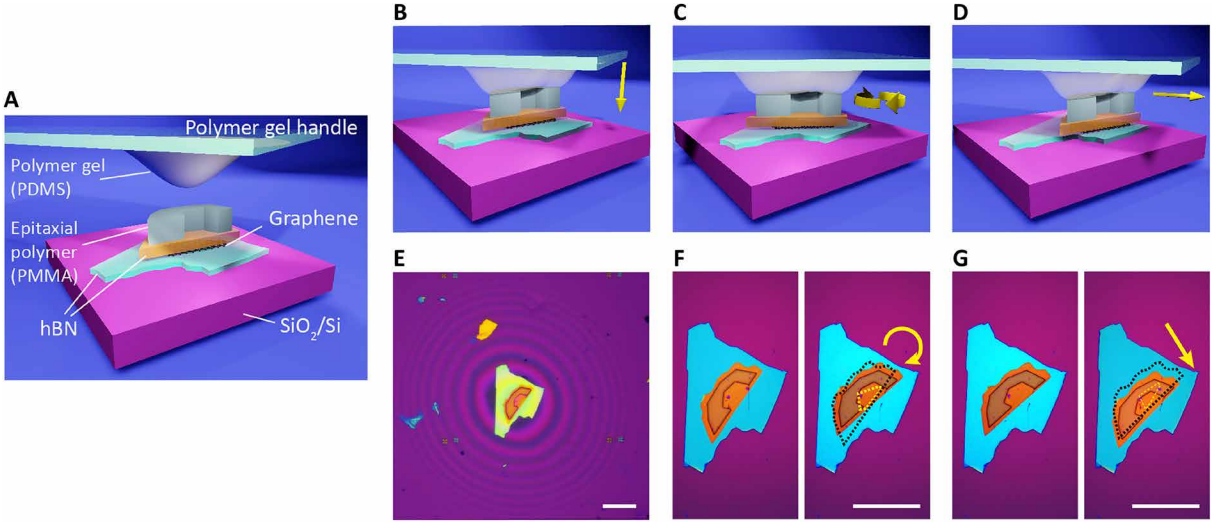

Fig. 1. In situ manipulation of van der Waals heterostructures. (**A**) Schematic of polymer (PMMA)–mediated in situ manipulation technique. (**B**) Schematic of the polymer gel handle (PDMS handle) touching PMMA. (**C**) Schematic of rotating a 2D material stack. (**D**) Schematic of sliding a 2D material stack. (**E**) Optical image of the stack covered by a polymer (PMMA) patch in contact with the polymer gel (PDMS). The interference rings show the proximity of the PDMS hemisphere to the substrate. (**F**) Optical images of the stack before (left) and after (right) rotation. The yellow arrow shows the rotation direction. (**G**) Optical images of the stack before (left) and after (right) translation manipulation. The yellow arrow shows the translation direction. The dashed lines in the right panels of (F) and (G) indicate the original position of the graphene and top hBN. Scale bars, 40 μm.

graphene can both slide and rotate freely on the surface of the bottom hBN under the control of the PDMS hemisphere (Fig. 1, C, D, F, and G, and movies S1 and S2). Figure 1 (F and G) shows that the PMMA patch is in good adhesion to the top hBN and does not delaminate during the manipulation process. We discuss, in detail, the motion mechanism of incommensurately stacked 2D materials in section S2. Briefly, sliding of the crystallites is governed by the friction forces at graphene/top hBN and graphene/bottom hBN interfaces. In incommensurate state, kinetic friction forces at the two interfaces are markedly reduced, which is the so-called superlubricity (*29*, *30*), and could be slightly different from each other depending on the twist angles θ_t and θ_b, as well as the interface conditions; therefore, the graphene can rotate or slide with the movement of the top hBN.

The manipulation technique presented here enables continuous modification of the twist angle between the layers even after the heterostructure is already assembled. To perform in situ optical measurements such as Raman spectroscopy after each manipulation step, the PMMA patch was intentionally designed not to cover the graphene so that it can give a strong enough signal (Fig. 1, F and G). Compared with previous in situ rotation technique mediated by an AFM tip (*27*), our manipulation technique is convenient and reproducible since the PMMA patch can be easily washed away by acetone and repatterned by EBL. In addition, our technique can manipulate flakes regardless of their thickness, whereas an AFM tip might destroy thin flakes.

To demonstrate the potential of the manipulation technique in twistronics, we fabricated another hBN/graphene/hBN heterostructure (sample 1) where the graphene layer was aligned to both the top and bottom hBN layers. We first assembled the heterostructure intentionally with $0 < \theta_t, \theta_b < \theta_{tb} < 60°$ (Fig. 2D), where θ_t, θ_b, and θ_{tb} are twist angles between graphene and top hBN, graphene and bottom hBN, and top hBN and bottom hBN, as shown in Fig. 2 (A and B). Then, we used our technique to rotate the top hBN layer, by making sure that the rotating PMMA patch is patterned within the top layer (Fig. 2D). The twist angles θ_t and θ_b varied simultaneously as the rotation progressed until either of them reached 0° where the graphene layer was locked to one of the hBN layers, that is, the graphene/hBN interface went through a transition from an incommensurate to a commensurate state (*31*, *32*). At a certain moment, the smooth rotation stacks and the PMMA delaminates from the top hBN layer (Fig. 2E). We associate these conditions with θ_t and θ_b both being ≈0°, indicating that graphene is aligned to both hBN layers. At this stage, the two hBN layers are aligned to each other as well, with θ_{tb} also reaching 0°, as shown in Fig. 2E. The delamination of PMMA after all the 2D layers are locked to each other indicates that the interaction between the 2D materials at the commensurate state is stronger than that between the PMMA and the top 2D crystal (see section S2). Such a self-locking mechanism is inevitable in commensurately stacked 2D materials and hinders further rotation and tuning of twist angles (*33*). If one imposes a larger external driving force to further rotate or move the crystals after locking, it might risk destroying the 2D crystals (see example shown in fig. S2, where we slightly etched the top hBN and then deposited the PMMA patch so that it will not delaminate from the top hBN). For other 2D systems where the commensurate state does not happen (see fig. S6), the twist angle can be reversibly tuned even at marginal values.

In principle, there are two types of alignment in a doubly aligned hBN/graphene/hBN heterostructure, that is, $\theta_t = \theta_b = \theta_{tb} = 0°$ and $\theta_t = 0°$, $\theta_b = \theta_{tb} = 60°$. The state of the resulting stack is determined by the initial settings of θ_t and θ_b and the rotation direction. Scenarios for various θ_t and θ_b are presented in fig. S3, where the cases in fig. S3A (initial alignment) and fig. S3E (final alignment) match Fig. 2D and Fig. 2E. The initial settings of the twist angles rely on the known crystal orientation of graphene and hBN layers, which is normally

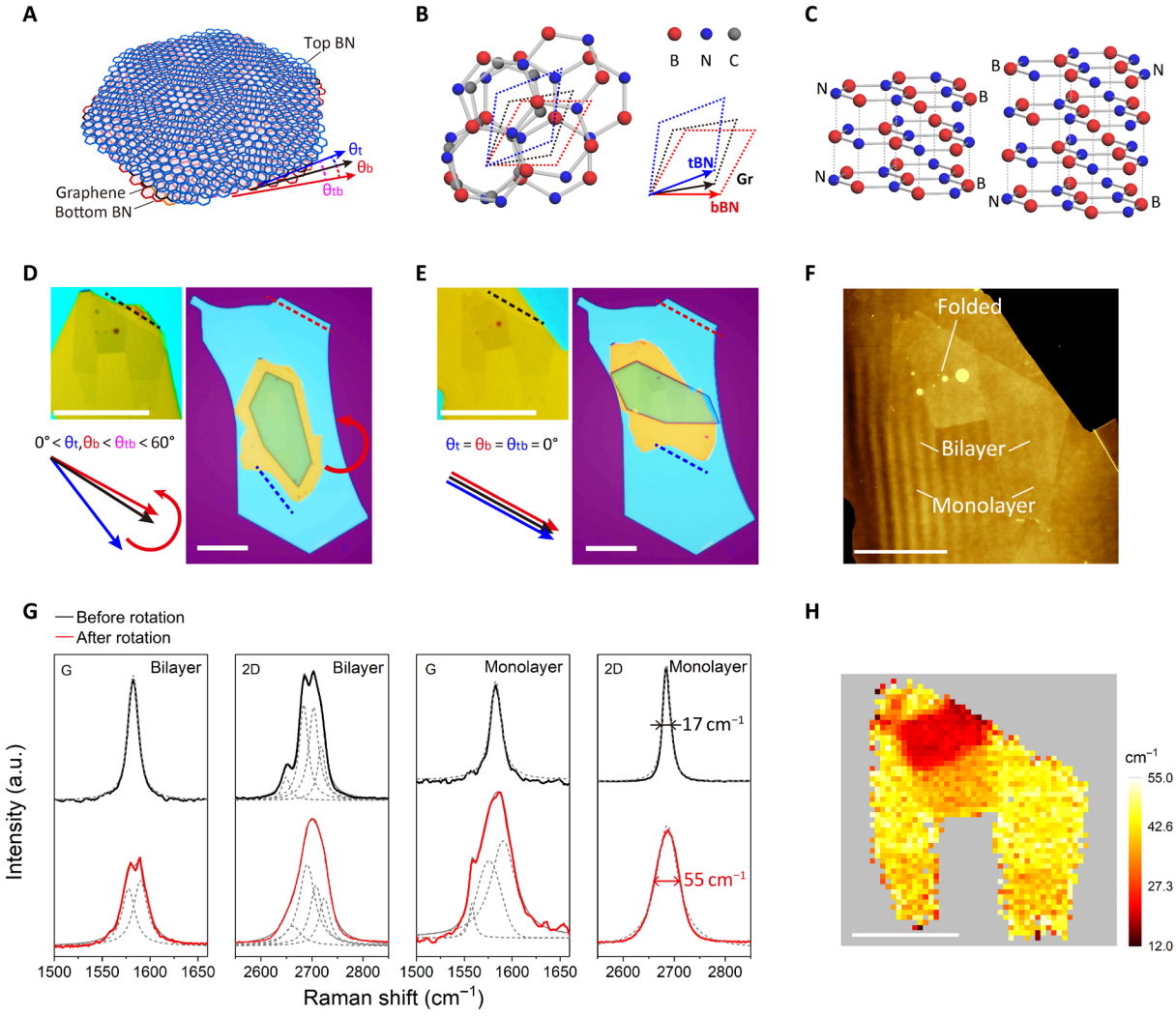

Fig. 2. Encapsulated graphene perfectly aligned to both the top and bottom hBN using in situ rotation technique. (**A**) Schematic of graphene encapsulated by hBN, with twist angles θ_t, θ_b, and θ_{tb} between the layers. (**B**) Lattice structure of graphene encapsulated by hBN and the corresponding lattice vectors of each layer. (**C**) Atomic structure of hBN, with odd (left) and even (right) numbers of layers. (**D** and **E**) Optical images of the stack, before (D) and after (E) rotation, which belong to the scenarios in fig. S3A (before rotation) and fig. S3E (after rotation). The top left panels increase the contrast to show the position of graphene. The bottom left panels show the relative crystal orientations of each layer. The red arc arrow highlights the rotation direction. The dashed lines indicate the crystal edges of graphene and hBN layers, which were aligned after the PMMA patch delaminated from the top hBN, as shown in (E). Scale bars, 20 μm. (**F** and **H**) AFM topography and 2D bandwidth Raman map of the stack after rotation, respectively. Scale bars, 10 μm. (**G**) Raman spectra of graphene at the monolayer and bilayer regions before and after rotation. a.u., arbitrary units.

distinguished by straight long edges of the flake. Since hBN crystals are threefold rotationally symmetric, using hBN flakes from the same exfoliated crystal can help to secure the crystal orientations. However, for hBN, the symmetry between the top and bottom atomic layers depends on whether the number of layers in hBN is odd or even (Fig. 2C). This ambiguity can, in principle, be circumvented by using the same surface, either top or bottom, of the original hBN crystal for alignment. To demonstrate how this can be done, we fabricated sample 2 with $\theta_t = 0°$, $\theta_b = \theta_{tb} = 60°$ in the final stack (see section S2 and figs. S4 and S5).

DISCUSSION

To confirm the alignment of graphene to both hBN layers, we carried out Raman characterization, as shown in Fig. 2 (G and H). The graphene layer in sample 1 originally contained monolayer and bilayer regions (Fig. 2F). For the monolayer region, the full width at half maximum of 2D peak ($FWHM_{2D}$) increases from 17 to 55 cm^{-1} after rotation; G peak width also broadens with the emergence of lower-frequency components (Fig. 2G). These results are consistent with previous reports (*34*, *35*). The broadening of 2D peak by near 40 cm^{-1} and the appearance of lower-frequency components in G peak signify near-perfect alignment between the hBN and graphene crystals and arise from graphene coupling to the moiré potentials from both top and bottom hBN crystals (*27*, *35*). For the bilayer region, the splitting of 2D peak is strongly enhanced when graphene is misaligned to both hBN layers, whereas after rotation, these components broaden and shift toward each other, resulting in a prominent change in the line shape of 2D peak. In contrast, G peak splits into two distinct components after rotation. These results for doubly

aligned bilayer graphene have not been reported before, and we ascribe the change in Raman spectra to the periodic strain field induced by moiré patterns (see section S3). Figure 2H shows the 2D peak width Raman map of the graphene layer after rotation. It clearly demonstrates the homogeneous distribution of $FWHM_{2D}$ among different regions of the graphene layer, indicating a spatially uniform twist angle in the stack. The AFM topography (Fig. 2F) here shows that the rotation process did not damage or crease the graphene layer.

To further quantify the existence of two moiré superlattices at both sides of the graphene layer in this heterostructure, we made it into a device and investigated its transport properties. We will now focus on our bilayer device (Fig. 3). Figure 3A shows the longitudinal resistivity ρ_{xx} and transverse resistivity ρ_{xy} as a function of charge carrier density n at nonquantizing magnetic field of $B = 0.03$ T. We observed both broadened resistivity peak at the primary Dirac point (PDP) and satellite resistivity peaks at finite densities situated symmetrically with respect to PDP. The Hall resistivity ρ_{xy} near each satellite peak changes sign, suggesting that they are moiré-induced secondary Dirac points (SDPs).

In quantizing magnetic fields, the presence of moiré potential splits the Landau levels into a fractal structure: the Hofstadter minibands separated by a hierarchy of self-similar minigaps, to which the corresponding densities follow linear trajectories according to the Diophantine equation: $n/n_0 = t\,(\phi/\phi_0) + s$, where s and t are integers denoting the superlattice miniband filling index and quantized Hall conductivity of the gapped state, respectively; ϕ_0 is the magnetic flux quantum; and n_0 is the total number of electron states per area of a completely filled Bloch band (*36*). Existence of two moiré patterns should result in two sets of these self-similar bands. Figure 3D is a simplified Wannier diagram showing the positions of the most prominent σ_{xx} zeroes in the measured Landau fan diagram (Fig. 3B). We find that the Landau fans originate from PDP at $n = 0$ and from the two sets of SDPs at $n_{s1} = \pm 2.15 \times 10^{12}$ cm^{-2} and

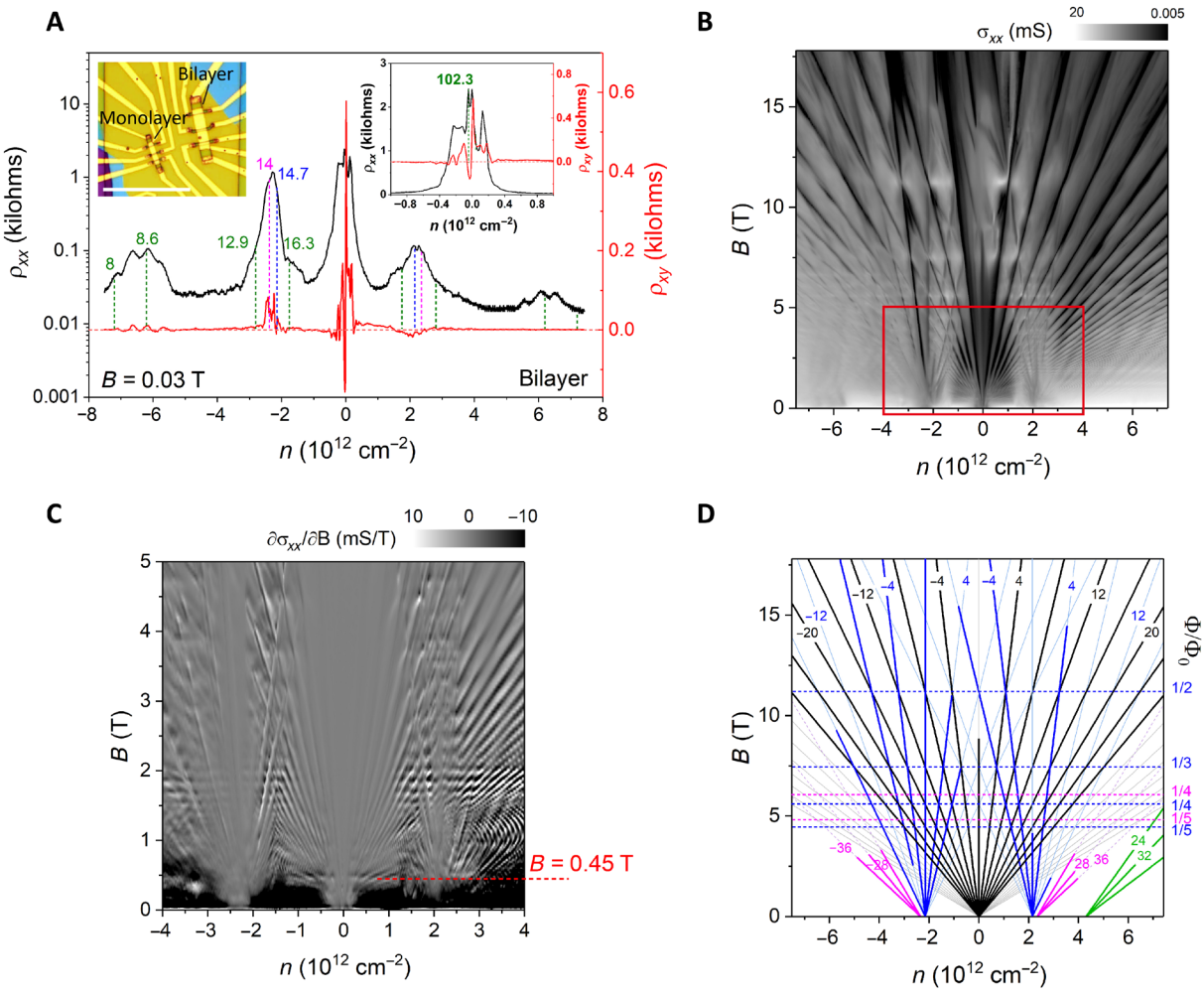

Fig. 3. Hofstadter's butterfly and Brown-Zak oscillations in bilayer graphene double moiré superlattices. (**A**) ρ_{xx} and ρ_{xy} as a function of n. $T = 0.3$ K, $B = 0.03$ T. The blue, magenta, and green dashed lines and numbers mark n_{s1}, n_{s2}, and n_{sm}, with moiré wavelengths λ_{s1}, λ_{s2}, and λ_{sm}, respectively. Left inset shows device micrograph. Scale bar, 20 μm. Right inset highlights the low carrier density region of (A). (**B**) Map $\sigma_{xx}(n,B)$ measured at $T = 0.3$ K. (**C**) Map $\partial\sigma_{xx}/\partial B(n,B)$ highlighting Brown-Zak (BZ) oscillations in part (red rectangle) of (B). The feature at $B = 0.45$ T originates from the BZ state of the super-moiré pattern with $\lambda_{sm} \approx 102.3$ nm. (**D**) Wannier diagram labeling the quantum Hall states identified in (B). The solid lines show quantum oscillations emerging from PDP and SDPs, with $\nu = \pm 4, \pm 8, \pm 12, \ldots$ for PDP (black), $t = \pm 4, \pm 8, \pm 12, \ldots$ for SDP n_{s1} (blue), $t = \pm 20, \pm 28, \pm 36$ for SDP n_{s2} (magenta), and $s = 2$, $t = 24, 32, 44$ for SDP n_{s1} (green). The horizontal dashed lines and numbers on the right show the most prominent BZ oscillations of SDPs n_{s1} (blue) and n_{s2} (magenta), with different values of p/q for $\phi = (p/q)\,\phi_0$.

$n_{s2} = \pm 2.34 \times 10^{12}$ cm^{-2} (corresponding to the moiré wavelengths of λ_{s1} = 14.7 nm and λ_{s2} = 14.0 nm, respectively). To identify the two SDPs more clearly, we plot $\partial\sigma/\partial n$ versus B and n in fig. S9 (A, C, and D).

In the fractal superlattice spectra, the self-similar minigaps occur at $\phi = \phi_0 p/q$, where $\phi = BA$ is the magnetic flux per superlattice unit cell, A is the superlattice unit cell area, ϕ_0 is the magnetic flux quantum, and p and q are co-prime integers. The strongest minigaps arise at $\phi = \phi_0/q$, resulting in Brown-Zak (BZ) magneto-oscillations (*37*) with the periodicity of $1/B = A/\phi_0$. These minigaps also correspond to the intersections between the central and satellite fans in the Landau fan diagram (*5*, *6*). We observe BZ oscillations (horizontal streaks visible in Fig. 3B) belonging to the two sets of satellite fans, as shown by the horizontal blue and magenta dashed lines in Fig. 3D, which provides independent confirmation of the two distinct moiré periods. BZ oscillations are more clearly seen in $\partial\sigma/\partial B(B,n)$ maps in fig. S9 (B, E, and F), in which we observed other p/q fractions. High temperature suppresses cyclotron oscillations, making the BZ oscillations more visible (fig. S10). At electron doping where BZ oscillations are more pronounced (*37*), two sets of maxima, corresponding to the two periodicities, 15.2 and 14.7 nm, are clearly seen (fig. S10, B and D). This independently verifies the existence of two moiré superlattices with different wavelengths at both sides of the graphene layer.

These coexisting moiré patterns with different wavelengths should, in principle, interfere, resulting in a second-order (composite) moiré pattern, as reported in experimental (*38*–*40*) and theoretical studies (*41*, *42*). From the two SDPs, we calculated the corresponding twist angles to be 0.24° and 0.38° (see Materials and Methods). Using the method described in (*38*, *39*), we obtained six possible composite moiré wavelengths (λ_{sm}; see section S4) and observed satellite peaks in ρ_{xx} near most of the corresponding carrier densities n_{sm} required to reach the first Brillouin zone edge of the six possible composite moiré patterns, which are marked by green dashed lines and numbers in Fig. 3A. The n_{sm} of the largest $\lambda_{sm} \approx 102.3$ nm is in the range of $\pm 0.04 \times 10^{12}$ to $\pm 0.05 \times 10^{12}$ cm^{-2} (right inset of Fig. 3A). Notably, in the plot of $\partial\sigma_{xx}/\partial B(n,B)$ within $|n| < \pm 2 \times 10^{12}$ cm^{-2}, we observe a prominent horizontal streak at B = 0.45 T (Fig. 3C), which perfectly matches the magnetic field of the first-order magnetic Bloch state originating from the composite moiré pattern when $BA = \phi_0$ (where q = 1). The results for the bilayer graphene region discussed above are similar to what was found in the monolayer graphene region (figs. S11 to S13).

The manipulation technique presented here proves success in making the hBN/graphene/hBN heterostructures with perfect alignment between graphene and the two hBN layers with a high twist angle homogeneity. In contrast, optical alignment of crystal edges or heating of the final stack cannot consistently guarantee perfect alignment with the twist angle of <1° in a single stack (*5*–*7*, *10*, *38*, *40*). Among the samples we have made, we selected top hBN, which is smaller than bottom hBN, in the heterostructures so that the movement of the top 2D layers can be seen more clearly. However, for purposes of device fabrication, the top hBN is not necessarily always smaller than the bottom hBN. Even if top hBN is larger than the bottom hBN with some small regions touching the silicon substrate, according to our observations, the movement of the top 2D layers is not hindered.

In conclusion, we introduce an in situ manipulation of van der Waals heterostructures mediated by patterning a polymer resist patch onto target flakes, which can precisely and dynamically control the rotation and positioning of 2D materials by a simple gel stamp manipulator. Using this technique, we realized a perfect alignment of graphene with respect to hBN layers with a much higher success rate compared with conventional optical alignment of crystal edges during micromechanical transfer. Our technique can be easily generalized to other 2D material systems (as shown in fig. S6) and allows for reversible manipulation in any 2D systems away from commensurate regime (where it becomes irreversible). We believe our technique has the potential for in situ twistronics using micromanipulators or microelectromechanical systems inside the cryogenic measurement systems, thus opening up a new strategy in device engineering and finding its applications in research of 2D quasi-crystals (*43*, *44*), magic-angle flat bands (*11*–*14*), devices with AB/BA domain walls (*45*), and other topologically nontrivial systems.

MATERIALS AND METHODS

Van der Waals assembly

All heterostructures were assembled using standard dry-transfer technique (*46*) using a PMMA coated on a PDMS stamp, and SiO_2 (290 nm)/Si as a substrate. The devices made from the monolayer and bilayer graphene regions are in a Hall bar geometry, with electrical contacts made by Cr/Au (3 nm/80 nm). The graphene flakes were obtained by mechanical exfoliation of bulk graphite (NGS naturgraphit; Graphenium Flakes, 25 to 30 mm).

Raman characterization

The Raman spectra were acquired by the Renishaw Raman System with 1800 lines/mm grating, using linearly polarized laser radiation at the wavelength of 532 nm. The laser power was kept below 5 mW. The Raman spatial maps were taken with a step size of 0.5 μm. To extract the peak width of the 2D band, we fit the spectrum at each pixel in the spatial mapping to a single Lorentzian function.

Transport measurements

Transport measurements were carried out in a four-terminal geometry with a low-frequency ac excitation of 100 nA using standard lock-in technique at the base temperature of 0.3 K (BZ oscillations were measured at 70 K). The devices were gated to control a charge carrier density (n) and a displacement field (D) by applying bias voltages to the metal top gate (V_t) and the doped silicon substrate (V_b). The charge carrier density is determined by $n = (D_b - D_t)/e$, the vertical displacement field D is set by $D = (D_b + D_t)/2$. Here, $D_b = \varepsilon_b(V_b - V_b^0)/d_b$, and $D_t = -\varepsilon_t(V_t - V_t^0)/d_t$, where $\varepsilon_{t,b}$ and $d_{t,b}$ are the dielectric constants and thicknesses of the top and bottom dielectric layers, respectively, and V_b^0 and V_t^0 are the effective offset voltages caused by environment-induced doping.

Calculation of moiré wavelength, twist angle, and super-moiré wavelength

The moiré wavelength λ is calculated using the geometric relation $n_s = 4/\frac{\sqrt{3}}{2}\lambda^2$, where n_s is the charge density at full filling of the moiré miniband (at the density of four electrons per superlattice unit cell). The relation between twist angle θ and moiré superlattice wavelength λ in the hBN/graphene/hBN heterostructure is given by (*47*)

$$\lambda = \frac{(1+\delta)\,a}{\sqrt{2(1+\delta)(1-\cos\theta)+\delta^2}}$$

$$\tan\varphi = \frac{\sin\theta}{(1+\delta)-\cos\theta}$$

where a is the graphene lattice constant; δ is the lattice mismatch between hBN and graphene, which is 1.65% [we used the value calculated by (*34*, *39*)]; and φ is the relative orientation of the two moiré patterns with respect to the graphene lattice (φ_1 and φ_2, respectively).

Using the method described previously (*38*), for super-moiré wavelength Λ, in analogy to the equation above, the relation between Λ and the twist angle Θ between the constituent moiré patterns (the wavelengths being λ_1 and λ_2; $\lambda_1 \geq \lambda_2$) is given by

$$\Lambda = \frac{(1+\Delta)\lambda_2}{\sqrt{2(1+\Delta)(1-\cos\Theta)+\Delta^2}}$$

where Δ is the mismatch between the constituent moiré patterns, given by

$$\Delta = \frac{\lambda_1 - \lambda_2}{\lambda_2}$$

and the twist angle Θ is given by

$$\Theta = (|\varphi_1 - \varphi_2| - 30°) \bmod (60°) - 30°$$

The modular division used here to find Θ reproduces the output of the piecewise conditional reported in (*38*).

SUPPLEMENTARY MATERIALS

Supplementary material for this article is available at http://advances.sciencemag.org/cgi/content/full/6/49/eabd3655/DC1

REFERENCES AND NOTES

1. Y.-H. Zhang, D. Mao, Y. Cao, P. Jarillo-Herrero, T. Senthil, Nearly flat Chern bands in moiré superlattices. *Phys. Rev. B* **99**, 075127 (2019).
2. S. Carr, D. Massatt, S. Fang, P. Cazeaux, M. Luskin, E. Kaxiras, Twistronics: Manipulating the electronic properties of two-dimensional layered structures through their twist angle. *Phys. Rev. B* **95**, 075420 (2017).
3. F. Wu, T. Lovorn, E. Tutuc, I. Martin, A. H. MacDonald, Topological insulators in twisted transition metal dichalcogenide homobilayers. *Phys. Rev. Lett.* **122**, 086402 (2019).
4. X. Chen, J. R. Wallbank, A. A. Patel, M. Mucha-Kruczyński, E. McCann, V. I. Fal'ko, Dirac edges of fractal magnetic minibands in graphene with hexagonal moiré superlattices. *Phys. Rev. B* **89**, 075401 (2014).
5. L. A. Ponomarenko, R. V. Gorbachev, G. L. Yu, D. C. Elias, R. Jalil, A. A. Patel, A. Mishchenko, A. S. Mayorov, C. R. Woods, J. R. Wallbank, M. Mucha-Kruczynski, B. A. Piot, M. Potemski, I. V. Grigorieva, K. S. Novoselov, F. Guinea, V. I. Fal'ko, A. K. Geim, Cloning of Dirac fermions in graphene superlattices. *Nature* **497**, 594–597 (2013).
6. C. R. Dean, L. Wang, P. Maher, C. Forsythe, F. Ghahari, Y. Gao, J. Katoch, M. Ishigami, P. Moon, M. Koshino, T. Taniguchi, K. Watanabe, K. L. Shepard, J. Hone, P. Kim, Hofstadter's butterfly and the fractal quantum Hall effect in moiré superlattices. *Nature* **497**, 598–602 (2013).
7. B. Hunt, J. D. Sanchez-Yamagishi, A. F. Young, M. Yankowitz, B. J. LeRoy, K. Watanabe, T. Taniguchi, P. Moon, M. Koshino, P. Jarillo-Herrero, R. C. Ashoori, Massive Dirac fermions and Hofstadter butterfly in a van der Waals heterostructure. *Science* **340**, 1427–1430 (2013).
8. G. Chen, L. Jiang, S. Wu, B. Lyu, H. Li, B. L. Chittari, K. Watanabe, T. Taniguchi, Z. Shi, J. Jung, Y. Zhang, F. Wang, Evidence of a gate-tunable Mott insulator in a trilayer graphene moiré superlattice. *Nat. Phys.* **15**, 237–241 (2019).
9. G. Chen, A. L. Sharpe, P. Gallagher, I. T. Rosen, E. J. Fox, L. Jiang, B. Lyu, H. Li, K. Watanabe, T. Taniguchi, J. Jung, Z. Shi, D. Goldhaber-Gordon, Y. Zhang, F. Wang, Signatures of tunable superconductivity in a trilayer graphene moiré superlattice. *Nature* **572**, 215–219 (2019).
10. E. M. Spanton, A. A. Zibrov, H. Zhou, T. Taniguchi, K. Watanabe, M. P. Zaletel, A. F. Young, Observation of fractional Chern insulators in a van der Waals heterostructure. *Science* **360**, 62–66 (2018).
11. A. L. Sharpe, E. J. Fox, A. W. Barnard, J. Finney, K. Watanabe, T. Taniguchi, M. A. Kastner, D. Goldhaber-Gordon, Emergent ferromagnetism near three-quarters filling in twisted bilayer graphene. *Science* **365**, 605–608 (2019).
12. Y. Cao, V. Fatemi, A. Demir, S. Fang, S. L. Tomarken, J. Y. Luo, J. D. Sanchez-Yamagishi, K. Watanabe, T. Taniguchi, E. Kaxiras, R. C. Ashoori, P. Jarillo-Herrero, Correlated insulator behaviour at half-filling in magic-angle graphene superlattices. *Nature* **556**, 80–84 (2018).
13. Y. Cao, V. Fatemi, S. Fang, K. Watanabe, T. Taniguchi, E. Kaxiras, P. Jarillo-Herrero, Unconventional superconductivity in magic-angle graphene superlattices. *Nature* **556**, 43–50 (2018).
14. M. Yankowitz, S. Chen, H. Polshyn, Y. Zhang, K. Watanabe, T. Taniguchi, D. Graf, A. F. Young, C. R. Dean, Tuning superconductivity in twisted bilayer graphene. *Science* **363**, 1059–1064 (2019).
15. C. Shen, Y. Chu, Q. Wu, N. Li, S. Wang, Y. Zhao, J. Tang, J. Liu, J. Tian, K. Watanabe, T. Taniguchi, R. Yang, Z. Y. Meng, D. Shi, O. V. Yazyev, G. Zhang, Correlated states in twisted double bilayer graphene. *Nat. Phys.* **16**, 520–525 (2020).
16. A. Kerelsky, C. Rubio-Verdú, L. Xian, D. M. Kennes, D. Halbertal, N. Finney, L. Song, S. Turkel, L. Wang, K. Watanabe, T. Taniguchi, J. Hone, C. Dean, D. Basov, A. Rubio, A. N. Pasupathy, Moiré-less correlations in ABCA graphene. *arXiv:1911.00007* (2019).
17. X. Liu, Z. Hao, E. Khalaf, J. Y. Lee, Y. Ronen, H. Yoo, D. Haei Najafabadi, K. Watanabe, T. Taniguchi, A. Vishwanath, P. Kim, Tunable spin-polarized correlated states in twisted double bilayer graphene. *Nature* **583**, 221–225 (2020).
18. Y. Cao, D. Rodan-Legrain, O. Rubies-Bigorda, J. M. Park, K. Watanabe, T. Taniguchi, P. Jarillo-Herrero, Tunable correlated states and spin-polarized phases in twisted bilayer-bilayer graphene. *Nature* **583**, 215–220 (2020).
19. E. M. Alexeev, D. A. Ruiz-Tijerina, M. Danovich, M. J. Hamer, D. J. Terry, P. K. Nayak, S. Ahn, S. Pak, J. Lee, J. I. Sohn, M. R. Molas, M. Koperski, K. Watanabe, T. Taniguchi, K. S. Novoselov, R. V. Gorbachev, H. S. Shin, V. I. Fal'ko, A. I. Tartakovskii, Resonantly hybridized excitons in moiré superlattices in van der Waals heterostructures. *Nature* **567**, 81–86 (2019).
20. K. L. Seyler, P. Rivera, H. Yu, N. P. Wilson, E. L. Ray, D. G. Mandrus, J. Yan, W. Yao, X. Xu, Signatures of moiré-trapped valley excitons in $MoSe_2/WSe_2$ heterobilayers. *Nature* **567**, 66–70 (2019).
21. L. Wang, E.-M. Shih, A. Ghiotto, L. Xian, D. A. Rhodes, C. Tan, M. Claassen, D. M. Kennes, Y. Bai, B. Kim, K. Watanabe, T. Taniguchi, X. Zhu, J. Hone, A. Rubio, A. N. Pasupathy, C. R. Dean, Correlated electronic phases in twisted bilayer transition metal dichalcogenides. *Nat. Mater.* **19**, 861–866 (2020).
22. L. An, X. Cai, D. Pei, M. Huang, Z. Wu, Z. Zhou, J. Lin, Z. Ying, Z. Ye, X. Feng, R. Gao, C. Cacho, M. Watson, Y. Chen, N. Wang, Interaction effects and superconductivity signatures in twisted double-bilayer WSe_2. *Nanoscale Horiz.* **5**, 1309–1316 (2020).
23. S. Ulstrup, R. J. Koch, S. Singh, K. M. McCreary, B. T. Jonker, J. T. Robinson, C. Jozwiak, E. Rotenberg, A. Bostwick, J. Katoch, J. A. Miwa, Direct observation of minibands in a twisted graphene/WS_2 bilayer. *Sci. Adv.* **6**, eaay6104 (2020).
24. M. Serlin, C. L. Tschirhart, H. Polshyn, Y. Zhang, J. Zhu, K. Watanabe, T. Taniguchi, L. Balents, A. F. Young, Intrinsic quantized anomalous Hall effect in a moiré heterostructure. *Science* **367**, 900–903 (2020).
25. C. R. Woods, L. Britnell, A. Eckmann, R. S. Ma, J. C. Lu, H. M. Guo, X. Lin, G. L. Yu, Y. Cao, R. V. Gorbachev, A. V. Kretinin, J. Park, L. A. Ponomarenko, M. I. Katsnelson, Y. N. Gornostyrev, K. Watanabe, T. Taniguchi, C. Casiraghi, H.-J. Gao, A. K. Geim, K. S. Novoselov, Commensurate–incommensurate transition in graphene on hexagonal boron nitride. *Nat. Phys.* **10**, 451–456 (2014).
26. K. Kim, M. Yankowitz, B. Fallahazad, S. Kang, H. C. P. Movva, S. Huang, S. Larentis, C. M. Corbet, T. Taniguchi, K. Watanabe, S. K. Banerjee, B. J. LeRoy, E. Tutuc, van der Waals heterostructures with high accuracy rotational alignment. *Nano Lett.* **16**, 1989–1995 (2016).
27. R. Ribeiro-Palau, C. Zhang, K. Watanabe, T. Taniguchi, J. Hone, C. R. Dean, Twistable electronics with dynamically rotatable heterostructures. *Science* **361**, 690–693 (2018).
28. Y. Wakafuji, R. Moriya, S. Masubuchi, K. Watanabe, T. Taniguchi, T. Machida, 3D manipulation of 2D materials using microdome polymer. *Nano Lett.* **20**, 2486–2492 (2020).
29. X. Feng, S. Kwon, J. Y. Park, M. Salmeron, Superlubric sliding of graphene nanoflakes on graphene. *ACS Nano* **7**, 1718–1724 (2013).
30. A. Vanossi, N. Manini, M. Urbakh, S. Zapperi, E. Tosatti, *Colloquium*: Modeling friction: From nanoscale to mesoscale. *Rev. Mod. Phys.* **85**, 529–552 (2013).
31. Z. Liu, J. Yang, F. Grey, J. Z. Liu, Y. Liu, Y. Wang, Y. Yang, Y. Cheng, Q. Zheng, Observation of microscale superlubricity in graphite. *Phys. Rev. Lett.* **108**, 205503 (2012).
32. E. Koren, U. Duerig, Moiré scaling of the sliding force in twisted bilayer graphene. *Phys. Rev. B* **94**, 045401 (2016).
33. K. Yao, N. R. Finney, J. Zhang, S. L. Moore, L. Xian, N. Tancogne-Dejean, F. Liu, J. Ardelean, X. Xu, D. Halbertal, K. Watanabe, T. Taniguchi, H. Ochoa, A. Asenjo-Garcia, X. Zhu, D. N. Basov, A. Rubio, C. R. Dean, J. Hone, P. J. Schuck, Nonlinear twistoptics at symmetry-broken interfaces. *arXiv:2006.13802* (2020).
34. N. R. Finney, M. Yankowitz, L. Muraleetharan, K. Watanabe, T. Taniguchi, C. R. Dean, J. Hone, Tunable crystal symmetry in graphene-boron nitride heterostructures with coexisting moiré superlattices. *Nat. Nanotechnol.* **14**, 1029–1034 (2019).
35. A. Eckmann, J. Park, H. Yang, D. Elias, A. S. Mayorov, G. Yu, R. Jalil, K. S. Novoselov, R. V. Gorbachev, M. Lazzeri, A. K. Geim, C. Casiraghi, Raman fingerprint of aligned graphene/h-BN superlattices. *Nano Lett.* **13**, 5242–5246 (2013).

36. A. H. MacDonald, Landau-level subband structure of electrons on a square lattice. *Phys. Rev. B* **28**, 6713–6717 (1983).
37. R. Krishna Kumar, X. Chen, G. H. Auton, A. Mishchenko, D. A. Bandurin, S. V. Morozov, Y. Cao, E. Khestanova, M. Ben Shalom, A. V. Kretinin, K. S. Novoselov, L. Eaves, I. V. Grigorieva, L. A. Ponomarenko, V. I. Fal'ko, A. K. Geim, High-temperature quantum oscillations caused by recurring Bloch states in graphene superlattices. *Science* **357**, 181–184 (2017).
38. L. Wang, S. Zihlmann, M.-H. Liu, P. Makk, K. Watanabe, T. Taniguchi, A. Baumgartner, C. Schönenberger, New generation of moiré superlattices in doubly aligned hBN/graphene/hBN heterostructures. *Nano Lett.* **19**, 2371–2376 (2019).
39. Z. Wang, Y. B. Wang, J. Yin, E. Tóvári, Y. Yang, L. Lin, M. Holwill, J. Birkbeck, D. J. Perello, S. Xu, J. Zultak, R. V. Gorbachev, A. V. Kretinin, T. Taniguchi, K. Watanabe, S. V. Morozov, M. Anđelković, S. P. Milovanović, L. Covaci, F. M. Peeters, A. Mishchenko, A. K. Geim, K. S. Novoselov, V. I. Fal'ko, A. Knothe, C. R. Woods, Composite super-moiré lattices in double-aligned graphene heterostructures. *Sci. Adv.* **5**, eaay8897 (2019).
40. M. Onodera, K. Kinoshita, R. Moriya, S. Masubuchi, K. Watanabe, T. Taniguchi, T. Machida, Cyclotron resonance study of monolayer graphene under double moiré potentials. *Nano Lett.* **20**, 4566–4572 (2020).
41. N. Leconte, J. Jung, Commensurate and incommensurate double moire interference in graphene encapsulated by hexagonal boron nitride. *2D Mater.* **7**, 031005 (2020).
42. M. Andelkovic, S. P. Milovanovic, L. Covaci, F. M. Peeters, Double Moiré with a twist: Supermoiré in encapsulated graphene. *Nano Lett.* **20**, 979–988 (2019).
43. S. J. Ahn, P. Moon, T. H. Kim, H. W. Kim, H. C. Shin, E. H. Kim, H. W. Cha, S. J. Kahng, P. Kim, M. Koshino, Y. W. Son, C. W. Yang, J. R. Ahn, Dirac electrons in a dodecagonal graphene quasicrystal. *Science* **361**, 782–786 (2018).
44. P. Moon, M. Koshino, Y.-W. Son, Quasicrystalline electronic states in 30° rotated twisted bilayer graphene. *Phys. Rev. B* **99**, 165430 (2019).
45. S. G. Xu, A. I. Berdyugin, P. Kumaravadivel, F. Guinea, R. Krishna Kumar, D. A. Bandurin, S. V. Morozov, W. Kuang, B. Tsim, S. Liu, J. H. Edgar, I. V. Grigorieva, V. I. Fal'ko, M. Kim, A. K. Geim, Giant oscillations in a triangular network of one-dimensional states in marginally twisted graphene. *Nat. Commun.* **10**, 4008 (2019).
46. T. Uwanno, Y. Hattori, T. Taniguchi, K. Watanabe, K. Nagashio, Fully dry PMMA transfer of graphene onh-BN using a heating/cooling system. *2D Mater.* **2**, 041002 (2015).
47. M. Yankowitz, J. Xue, D. Cormode, J. D. Sanchez-Yamagishi, K. Watanabe, T. Taniguchi, P. Jarillo-Herrero, P. Jacquod, B. J. LeRoy, Emergence of superlattice Dirac points in graphene on hexagonal boron nitride. *Nat. Phys.* **8**, 382–386 (2012).
48. Y. Song, D. Mandelli, O. Hod, M. Urbakh, M. Ma, Q. Zheng, Robust microscale superlubricity in graphite/hexagonal boron nitride layered heterojunctions. *Nat. Mater.* **17**, 894–899 (2018).
49. B. Cheng, P. Wang, C. Pan, T. Miao, Y. Wu, T. Taniguchi, K. Watanabe, C. N. Lau, M. Bockrath, Raman spectroscopy measurement of bilayer graphene's twist angle to boron nitride. *Appl. Phys. Lett.* **107**, 033101 (2015).
50. M. Huang, H. Yan, C. Chen, D. Song, T. F. Heinz, J. Hone, Phonon softening and crystallographic orientation of strained graphene studied by Raman spectroscopy. *Proc. Natl. Acad. Sci. U.S.A.* **106**, 7304–7308 (2009).
51. T. M. G. Mohiuddin, A. Lombardo, R. R. Nair, A. Bonetti, G. Savini, R. Jalil, N. Bonini, D. M. Basko, C. Galiotis, N. Marzari, K. S. Novoselov, A. K. Geim, A. C. Ferrari, Uniaxial strain in graphene by Raman spectroscopy: Gpeak splitting, Grüneisen parameters, and sample orientation. *Phys. Rev. B* **79**, 205433 (2009).
52. L. J. McGilly, A. Kerelsky, N. R. Finney, K. Shapovalov, E. M. Shih, A. Ghiotto, Y. Zeng, S. L. Moore, W. Wu, Y. Bai, K. Watanabe, T. Taniguchi, M. Stengel, L. Zhou, J. Hone, X. Zhu, D. N. Basov, C. Dean, C. E. Dreyer, A. N. Pasupathy, Visualization of moiré superlattices. *Nat. Nanotechnol.* **15**, 580–584 (2020).
53. A. Das, S. Pisana, B. Chakraborty, S. Piscanec, S. K. Saha, U. V. Waghmare, K. S. Novoselov, H. R. Krishnamurthy, A. K. Geim, A. C. Ferrari, A. K. Sood, Monitoring dopants by Raman scattering in an electrochemically top-gated graphene transistor. *Nat. Nanotechnol.* **3**, 210–215 (2008).
54. S. Pisana, M. Lazzeri, C. Casiraghi, K. S. Novoselov, A. K. Geim, A. C. Ferrari, F. Mauri, Breakdown of the adiabatic Born-Oppenheimer approximation in graphene. *Nat. Mater.* **6**, 198–201 (2007).
55. J. R. Wallbank, A. A. Patel, M. Mucha-Kruczyński, A. K. Geim, V. I. Fal'ko, Generic miniband structure of graphene on a hexagonal substrate. *Phys. Rev. B* **87**, 245408 (2013).

Acknowledgments

Funding: This work was supported by EPSRC Early Career Fellowship EP/N007131/1 and ERC Consolidator Grant 865590. **Author contributions:** A.M. developed the concept of the experiment and supervised the project. Y.Y. carried out the experiments, fabricated the devices, interpreted data with help from C.M., and wrote the manuscript. J.L. and S.X. gave critical suggestions to the presented idea. J.Y. performed transport measurements. T.T. and K.W. synthesized the hBN crystals. A.K.G. and K.S.N. advised on the experiments. All authors discussed the results and commented on the manuscript. **Competing interests:** The authors declare that they have no competing interests. **Data and materials availability:** All data needed to evaluate the conclusions in the paper are present in the paper and/or the Supplementary Materials. Additional data related to this paper may be requested from the corresponding authors upon reasonable request.

Submitted 16 June 2020
Accepted 22 October 2020
Published 4 December 2020
10.1126/sciadv.abd3655

Citation: Y. Yang, J. Li, J. Yin, S. Xu, C. Mullan, T. Taniguchi, K. Watanabe, A. K. Geim, K. S. Novoselov, A. Mishchenko, In situ manipulation of van der Waals heterostructures for twistronics. *Sci. Adv.* **6**, eabd3655 (2020).

Science Advances
AAAS

advances.sciencemag.org/cgi/content/full/6/49/eabd3655/DC1

Supplementary Materials for

In situ manipulation of van der Waals heterostructures for twistronics

Yaping Yang*, Jidong Li, Jun Yin, Shuigang Xu, Ciaran Mullan, Takashi Taniguchi, Kenji Watanabe, Andre K. Geim, Konstantin S. Novoselov, Artem Mishchenko*

*Corresponding author. Email: ypyang0916@gmail.com (Y.Y.); artem.mishchenko@gmail.com (A.M.)

Published 4 December 2020, *Sci. Adv.* **6**, eabd3655 (2020)
DOI: 10.1126/sciadv.abd3655

The PDF file includes:

Other Supplementary Material for this manuscript includes the following:

(available at advances.sciencemag.org/cgi/content/full/6/49/eabd3655/DC1)

Supplementary information

1. Identification of the initial contact between polymer gel and epitaxial polymer

In our manipulation technique, the critical step to precisely control the movement of 2D flakes is the identification of the initial contact between the polymer gel (PDMS) and the epitaxial polymer patch (PMMA). The signature of the contact is a color change in the PMMA patch and an appearance of a sharpened edge of the contact area between the PDMS gel and PMMA patch, which is easily distinguished under optical microscope, Fig. S1.

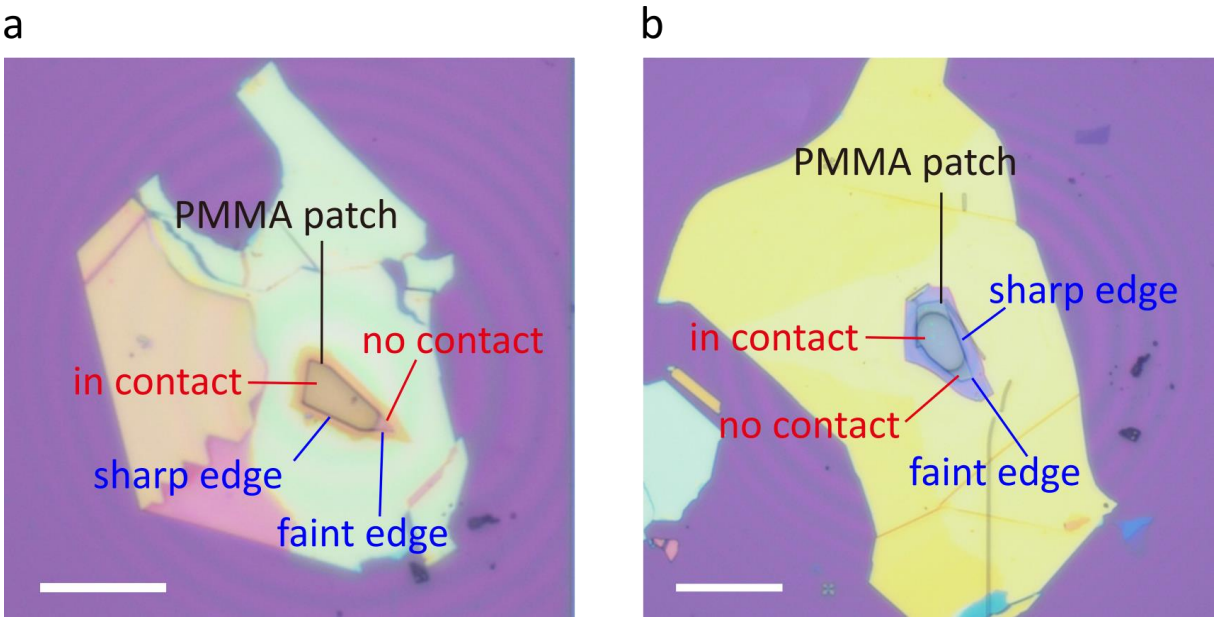

Fig. S1. Micrographs showing the moment when polymer gel (PDMS) is brought into contact with epitaxial polymer (PMMA). (a) PDMS gel is in contact with most of the PMMA patch, only in a small region on the right corner the contact is absent. The region in contact shows a different color from the no-contact region. (b) PDMS gel touches the center of the PMMA patch, with the in-contact area limited to the PMMA patch. In both images, the edges of the in-contact regions are thicker than the edges of no-contact regions. The scale bars are 50 µm.

2. The motion of incommensurately stacked 2D materials

In our manipulation technique, the motion of 2D materials in the van der Waals heterostructure depends on the balance between external driving force and the adhesion between PMMA patch and the top 2D layer, as well as the kinetic friction originating from the van der Waals force between the adjacent 2D layers. The kinetic friction between 2D layers is dramatically reduced in the incommensurate state due to the cancellation of lateral corrugation forces between two crystals in the sliding direction, the so called superlubricity where the 2D flakes can move smoothly. Inversely, in commensurate state, the two adjacent 2D layers are locked together due to pinning of the boundaries that separate local regions of the commensurate phase (*25, 29, 30*), thus the friction is significantly higher. Such boundaries, either topological defects or misfit dislocations, are caused by the lattice mismatch and twist angle between adjacent layers.

The sliding of crystalline interfaces is governed by the friction between the layers. The kinetic friction between graphene and hBN shows rotational anisotropy and six-fold symmetry with respect to the rotation

angle between graphene and hBN (*48*). In incommensurate state where kinetic friction is extremely small, it still varies slightly with the rotation angle (*48*). Therefore, the friction forces at graphene/top hBN and graphene/bottom hBN interfaces are comparable but slightly different from each other depending on the twist angles θ_t and θ_b, which could lead to simultaneous rotation of both top hBN and graphene. Most likely, due to the superlubricity, as the top hBN rotates under the control of PMMA patch, graphene remains static until top hBN clicks to it, and then with further rotation, the top hBN together with graphene clicks to bottom hBN. More realistically, the interface conditions vary among the whole stack. There could be polymer residues or other contaminants adsorbed on the surface of bottom hBN, causing difference in frictions at the two interfaces, thereby graphene can rotate with top hBN simultaneously.

For graphene/hBN and hBN/hBN interfaces, the commensurate state occurs at a small twist angle between the layers, since these two interfaces already satisfy the condition of a small lattice mismatch (1.65% (*34, 39*) for graphene/hBN interface and 0% for hBN/hBN interface). At commensurate state, the locking of the graphene/hBN and hBN/hBN interfaces limits further motion of the flakes (*33*), thereby when the external driving force is large enough, the PMMA patch/hBN/graphene/hBN stack will break at the weaker coupled PMMA patch/hBN interface, in agreement with the delamination of PMMA patch when graphene is aligned to both hBN layers after rotation (Fig. 2e in the main text and Fig. S4c). By slightly etching the top hBN and then depositing the polymer patch, the adhesion between PMMA and the top hBN can be dramaticaly improved and PMMA will not delaminate from the top hBN. Then, if one imposes a larger external driving force in order to further rotate or move the crystals after locking, the 2D crystals will be destroyed, as shown in Fig. S2, where we used hBN/graphite flake/hBN stack as an example. Rotation of the top two layers of hBN/graphene/hBN heterostructure with different initial settings of θ_t and θ_b should result in the final stack with commensurate or incommensurate states at the two interfaces, as shown in Fig. S3 and Table S1. The scenarios are based on the fact that graphene can rotate with top hBN simultaneously. Here we consider both the 0^o and 60^o alignment of graphene and hBN layer, since these two types of alignment have distinct symmetry and affect electronic structure of graphene differently (*34, 41*).

We fabricated hBN/graphene/hBN heterostructure (sample 2) with the manipulation process matching the cases in Fig. S3b (initial alignment) and Fig. S3j (final alignment). To make sure that the crystal orientation of the flakes is known, we first identified hBN fakes which have fractured into two pieces during the mechanical exfoliation procedure (Fig. S4a). Note that for hBN crystals with odd numbers of layers, the top and bottom layers have the same crystal orientation, whereas for hBN crystals with even numbers of layers, the top and bottom layers are of mirror symmetry (Fig. 2c in the main text). Therefore, the common edges of the fractured hBN pieces indicate the same crystal orientation of the atomic layer belonging to the same surface, either top or bottom, of the original crystal. Then we used one of the fractured hBN piece to pick up graphene and flipped over the other fractured piece as the bottom hBN layer, so that the hBN atomic layers adjacent to graphene come from the same crystal surface. See Fig. S5 for the details of this procedure. Next, the initial θ_t and θ_b were set according to Fig. S3b and the following rotation direction led to the final stack with $\theta_t=0^o$, $\theta_b=\theta_{tb}=60^o$ (Fig. S4c), which is the case of Fig. S3j.

We carried out Raman spectroscopy to prove the alignment of graphene and hBN in sample 2, as shown in Fig. S4d and e. The behavior of Raman spectra in monolayer and bilayer graphene regions are similar to those observed in sample 1. Whereas the full width at half maximum of 2D peak ($FWHM_{2D}$) increased from 17 cm^{-1} to 48.5 cm^{-1} after rotation, smaller than that in the perfect alignment case, which means that the twist angles θ_t and θ_b are larger than those in sample 1. Figure S4e shows the distribution of $FWHM_{2D}$ among the graphene flake after rotation, indicating a spatially uniform twist angle in both monolayer and bilayer regions. The AFM topography (Fig. S4f) here shows that the rotation process did not damage or crease the graphene layer.

The assembly process of sample 2 is illustrated in Fig. S5. The details of the process are as follows. **Step 1**, we used PMMA coated PDMS block mounted on a glass slide to pick-up one of the fractured hBN pieces as the top hBN (hBN piece 1). **Step 2**, we used polypropylene carbonate (PPC) coated PDMS block mounted on another glass slide to pick-up the other fractured hBN piece (hBN piece 2), which serves as the bottom hBN. **Step 3**, the target graphene flake is picked up by PDMS/PMMA/hBN piece 1. Now the graphene flake is in contact with the bottom surface of hBN piece 1. **Step 4**, the PDMS/PPC block is flipped over so that the bottom surface of hBN piece 2 faces upwards, as indicated by the red line in the figure. Then the PDMS/PMMA/ hBN piece 2 is rotated in order to align the shared crystal edges of hBN piece 1 and 2 under microscope. **Step 5**, hBN piece 2 is picked up by PMMA/hBN piece 1 /graphene at temperature above 75^{o}. When temperature is high enough, the adhesion between PPC and hBN is smaller than the adhesion between PMMA and hBN. Thereby the bottom hBN (hBN piece 2) can be easily picked up by PMMA/hBN piece 1 /graphene. **Step 6**, the final stack hBN piece 1/graphene/ hBN piece 2 is released onto a new silicon wafer by dissolving away PMMA using acetone. In the final stack, graphene flake is in contact with both the bottom surfaces of hBN piece 1 and hBN piece 2. Since the bottom surfaces of hBN piece 1 and hBN piece 2 are originally from the same atomic layer, we can guarantee the settings of θ_t and θ_b if the alignment of the shared edges is based on the same surface of the fractured hBN pieces.

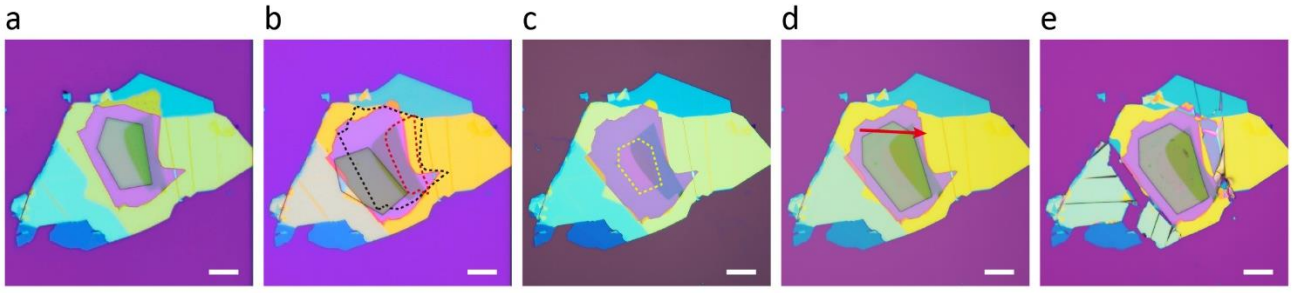

Fig. S2. Displacement of hBN/graphite/hBN stack after commensurate locking. (a) hBN/graphite/hBN stack deposited with PMMA patch. (b) Top hBN and graphite rotated with PMMA patch, and then PMMA patch delaminated from top hBN after the 2D layers lock with each other. The black and red dashed polygons indicate the original position of top hBN and graphite, respectively. (c) Slightly etched top hBN. The yellow dashed polygon indicates the etched region, which shows color difference from non-etched region. (d) A new PMMA patch deposited onto the top hBN, covering the etched region. The red arrow implies the displacement direction. (e) Bottom hBN was broken after the displacement, without delamination of PMMA patch. The scale bars are 20 μm.

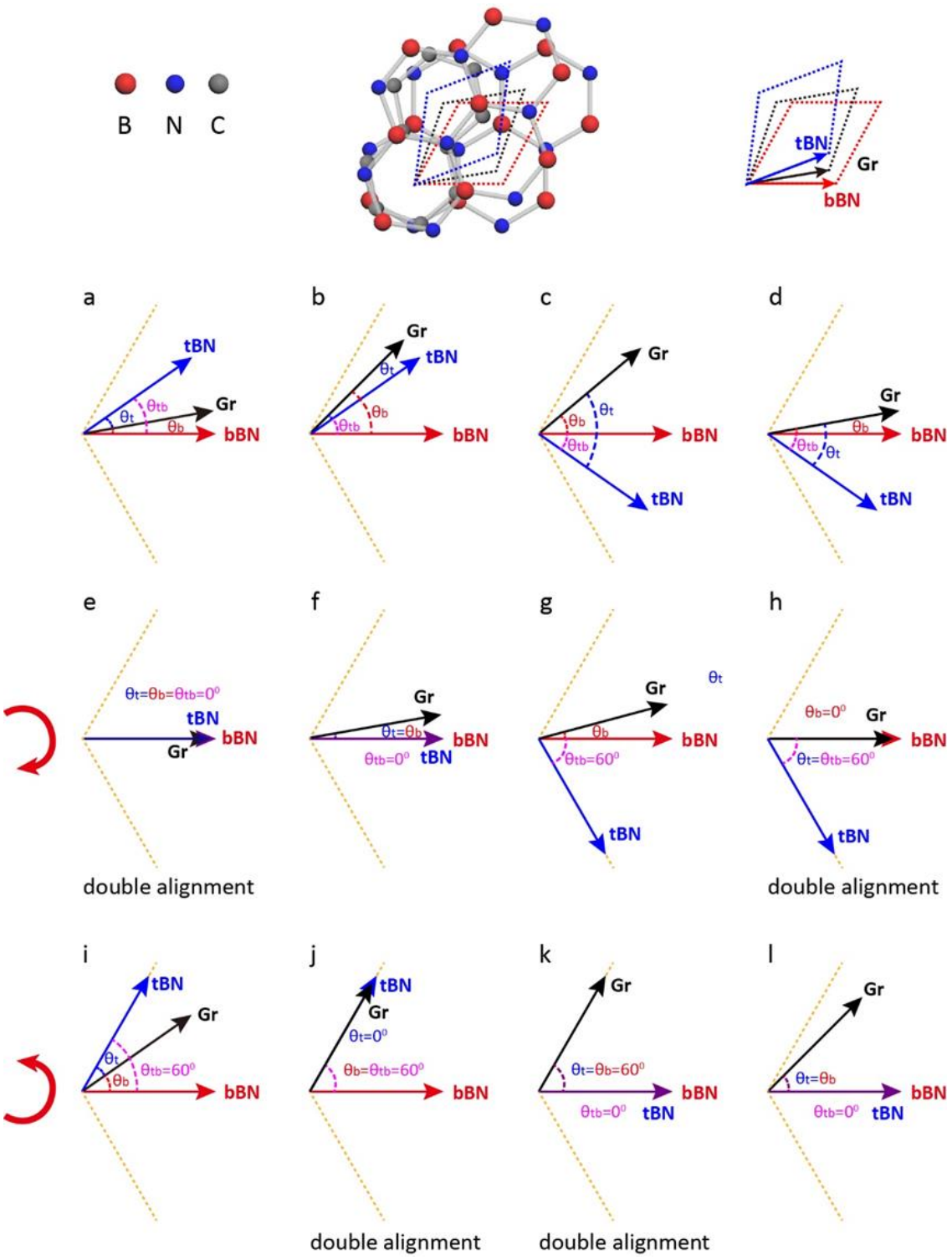

Fig. S3. The resulting alignment of hBN/graphene/hBN stack under different rotation directions. (a) to (d) hBN/graphene/hBN stack with different initial settings of θ_t and θ_b. (e) to (h) The final stacks corresponding to (a) to (d) with different types of alignment after clockwise rotating. (i) to (l) The final stacks corresponding to (a) to (d) with different types of alignment after anti-clockwise rotating. The red, black and blue arrows indicate the crystal orientation of bottom hBN, graphene and top hBN, respectively. The red arc arrows on the left show the rotation direction. During the rotation process, the bottom hBN layer remains at original position and only the top hBN and graphene rotate under the control of polymer gel manipulator. Orange dashed lines mark ±60° with respect to red arrows (bottom hBN), the rotations will stack at these lines as top hBN goes into AA' stacking with bottom hBN.

Table S1. Resulting stack with different initial settings of θ_t and θ_b as shown in Fig. S3.

Panels in Fig. S3	Initial setting of twist angles (°)	Resulting stack	
		Rotation direction	
		clockwise	anticlockwise
a	$0<\theta_t, \theta_b<\theta_{tb}<60^o$	$\theta_t=0^o, \theta_b=0^o, \theta_{tb}=0^o$ double alignment	$\theta_t\neq0^o, \theta_b\neq0^o, \theta_{tb}=60^o$, misalignment
b	$0<\theta_t, \theta_{tb}<\theta_b<60^o$	$\theta_t=\theta_b\neq0^o, \theta_{tb}=60^o$, misalignment	$\theta_t=0^o, \theta_b=\theta_{tb}=60^o$, double alignment
c	$-60^o<\theta_{tb}<0<\theta_b<60^o, \lvert60^o-\theta_{tb}\rvert<\theta_b$	$\theta_t=\theta_b\neq0^o, \theta_{tb}=60^o$, misalignment	$\theta_t=\theta_b=60^o, \theta_{tb}=0^o$, double alignment
d	$-60^o<\theta_{tb}<0<\theta_b<60^o, \lvert60^o-\theta_{tb}\rvert>\theta_b$	$\theta_b=0^o, \theta_t=\theta_{tb}=60^o$, double alignment	$\theta_t=\theta_b\neq0^o, \theta_{tb}=0^o$, misalignment

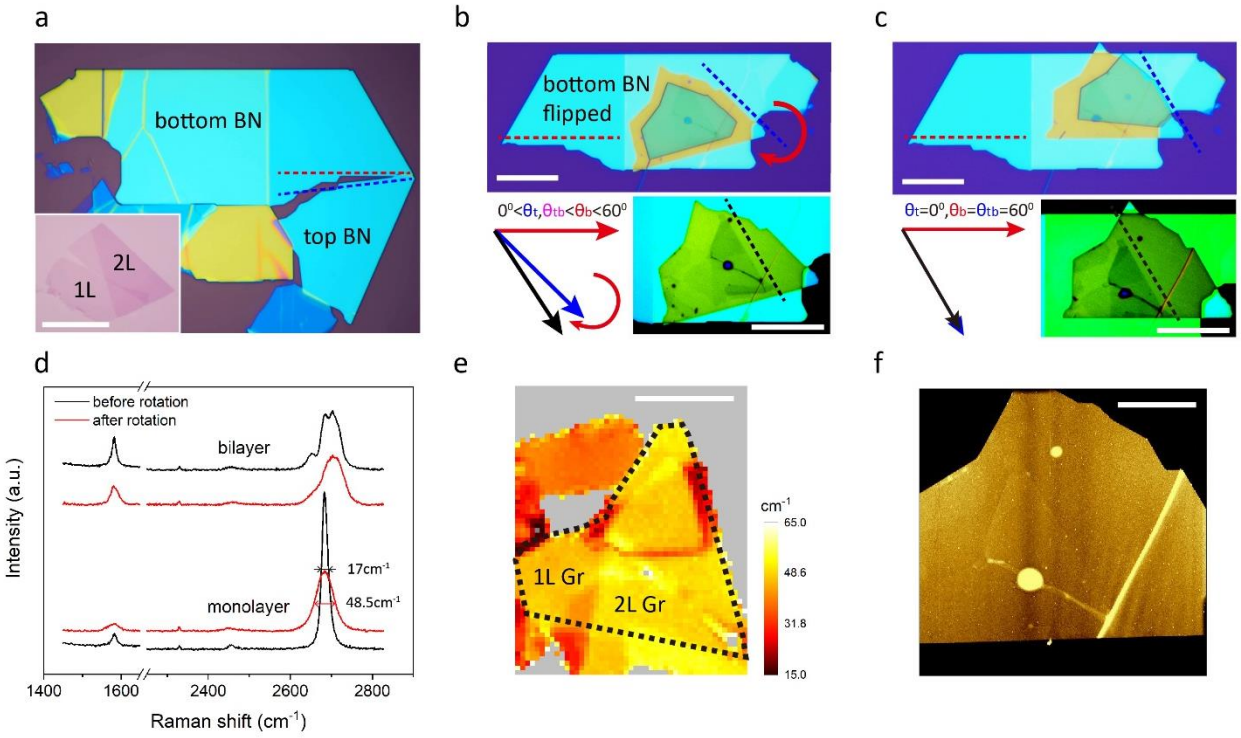

Fig. S4. Encapsulated graphene aligned to both top and bottom hBN, with $\theta_t=0^o$, $\theta_b=\theta_{tb}=60^o$. (a) Optical image of an hBN flake with a crack after mechanical exfoliation. The bottom inset shows the graphene flake containing monolayer and bilayer region. (b) Bottom hBN was flipped over before the release of top hBN/graphene stack. The final heterostructure was intentionally designed with the relative crystal orientations $0<\theta_t, \theta_{tb}<\theta_b<60^o$, as shown in left bottom inset, which matches the case in Fig. S3b. The red arc arrow implies the rotation direction. (c) The heterostructure after rotation, with $\theta_t=0^o$, $\theta_b=\theta_{tb}=60^o$ as shown in left bottom inset, which matches the

case in Fig. S3j. The PMMA patch delaminated from top hBN after all the crystals were aligned to each other. The right bottom insets of (b) and (c) increase the contrast to show the position of graphene. The red, blue and black dashed lines in (a-c) indicate the crystal orientation of bottom hBN, top hBN and graphene respectively. (d) Raman spectra of graphene at the monolayer and bilayer region before and after rotation, respectively. (e) 2D band width Raman map of the stack after rotation. The dashed line shows the region where graphene is covered by top hBN. (f) AFM topography of the stack after rotation. The scale bars in (a) to (c) are 20 μm. The scale bars in (e) and (f) are 10 μm.

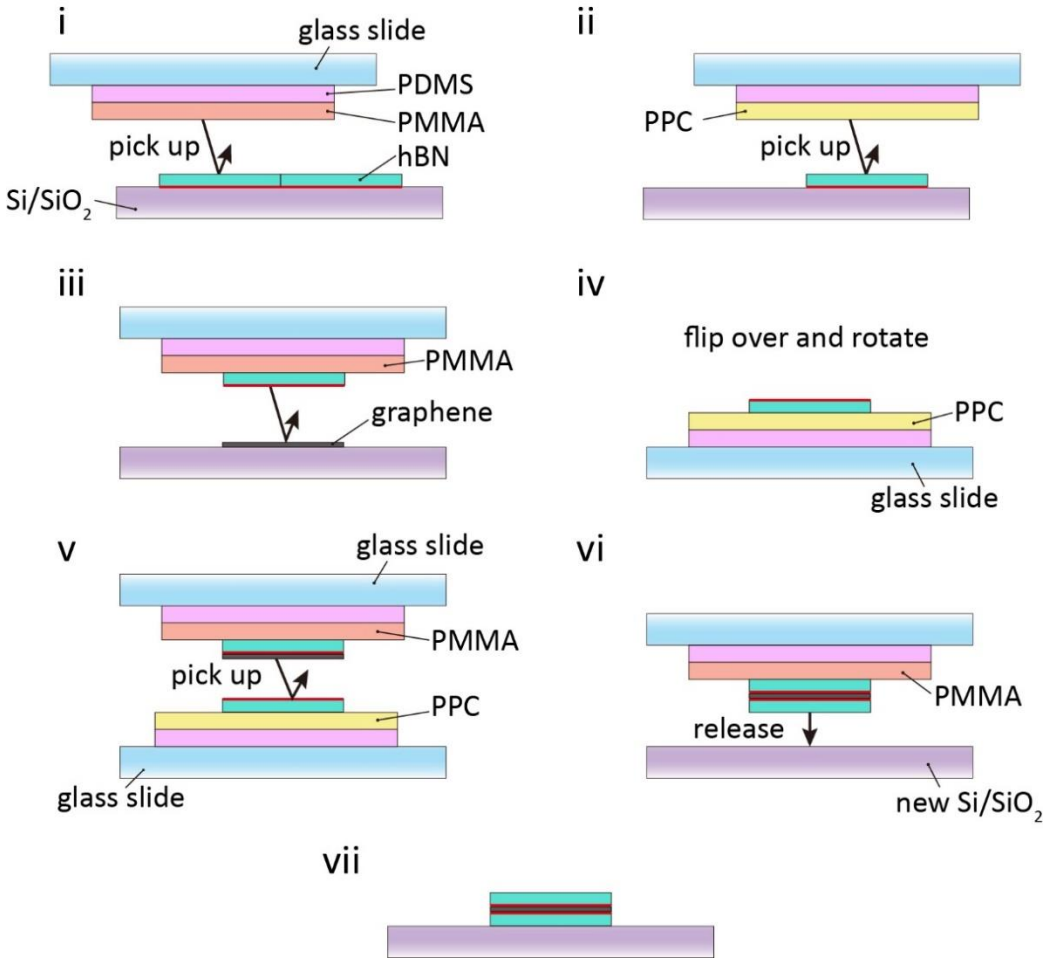

Fig. S5. Schematic process flow for graphene encapsulated by the same hBN crystal. In the final stack, the hBN atomic layers adjacent to graphene belong to the same surface of the original crystal, as highlighted by the red lines.

For other interfaces where the adjacent layers have larger lattice mismatch, such as MoS_2/hBN interface, a small or even zero twist angle will not result in the commensurate state. The kinetic friction between the 2D layers always remains at an extremely low value, thereby the 2D flake can move and rotate smoothly even when passing through the point where twist angle is zero without the delamination of PMMA patch, as shown in Fig. S6.

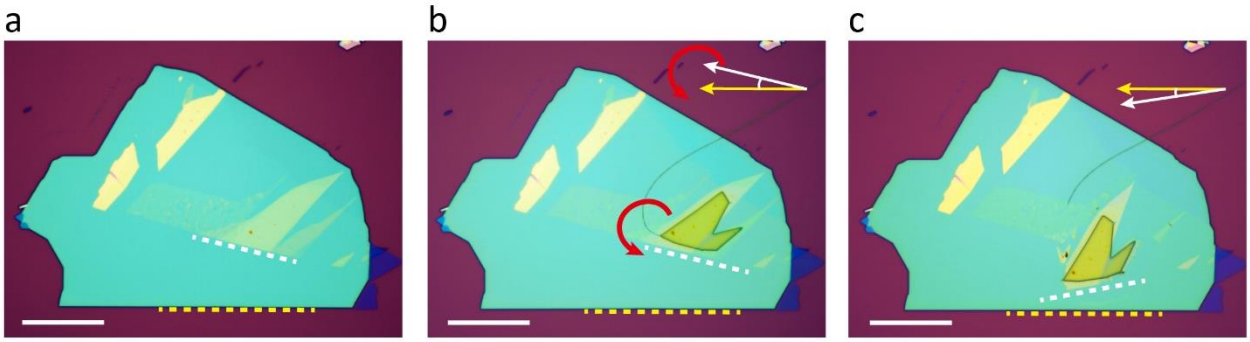

Fig. S6. Rotation of MoS_2 on top of hBN. (a) Optical image of MoS_2/hBN stack before rotation. The white and yellow dashed lines indicate the crystal orientations of MoS_2 and hBN crystal, respectively. (b) PMMA patch patterned onto MoS_2 flake. The white and yellow arrows show the twist angle between MoS_2 and hBN crystal. The red arc arrow implies the rotation direction. (c) Rotation of MoS_2 flake with the twist angle passing through 0^o, without PMMA being delaminated from MoS_2 flake, confirming that there is no commensurate state at a small twist angle of MoS_2 and hBN crystal. The scale bars are 20 μm.

3. Raman spectra of graphene in the monolayer and bilayer regions before and after rotation

Raman spectra of graphene are strongly modified when graphene is subjected to double moiré superlattices (Fig. 2g). In our sample, for monolayer graphene region, G peak changes its shape from a narrow peak centered at 1582 cm^{-1} with $FWHM_G$ ≈14.5 cm^{-1} to a broadened asymmetric peak after rotation. The presence of a low energy shoulder at ≈1558 cm^{-1} of G peak after rotation is attributed to a TO phonon, similar to what was observed in graphene aligned to only one hBN crystal (*35*). For 2D peak, the broadening effect is strongly enhanced in double-moiré superlattice compared to a simple aligned graphene/hBN heterostructure: ≈20 cm^{-1} increase in FWHM for graphene in a single moiré superlattice (*27, 35*) and ≈40 cm^{-1} increase in FWHM for our doubly-aligned sample, indicating that the double moiré superlattices induce a much stronger periodic inhomogeneity originated from charge accumulation, strain, etc.

For bilayer graphene region, G peak splits into two components in the presence of double moiré superlattices. For 2D peak, the four components broadened and their position differences reduced, which is similar to what was reported in bilayer graphene aligned to only one hBN crystal (*49*).

We found an overall downshift of around 2cm^{-1} for both G peak and 2D peak among the whole flake after rotation (Fig. S7 a-d), which contradicts the results of previous studies (*27, 34*). Similar behavior is found in Sample 2 (Fig. S8). Near the corner of the folded region (as indicated by the arrows), before rotation, the peak positions of G and 2D peaks are slightly lower than those of the nearby region. We attribute this phonon softening to the strain caused by folding (*50*). Whereas after rotation, peak position near the corner of the folded region shows an upshift behavior, and is higher than that of the nearby region. Note that during the rotation, the folded graphene rotated as well, therefore we expect an enhanced strain effect near this region. However the abnormal behavior of the peak position implies a mechanism beyond strain effect.

To further look into the line shape of G peak after rotation, we fit G peak with two Lorentzian peaks for

both bilayer and monolayer graphene regions and plot the maps of the peak position difference and intensity ratio of the two components, as shown in Fig. S7e and f. The maps show that the G peak splitting is homogeneous for both bilayer and monolayer graphene regions, which is around 13 cm^{-1} and 22 cm^{-1}, respectively. The intensity ratio of the two components is around 1 for the bilayer region, which means that they have comparable weight, and is around 0.6 for the monolayer region.

The overall downshift and broadening of the peak positions for G and 2D peaks and splitting of G peak remind one of the effects of strain. Under uniaxial strain, the doubly degenerate E_{2g} mode splits into two components, one along the strain direction and the other perpendicular, which leads to the splitting of G peak (*51*). Tensile strain usually gives phonon softening, while compressive strain usually leads to phonon stiffening. In the presence of moiré superlattice, the spatial strain distribution is periodically modulated, and tension and compression of graphene lattice should coexist. The combined effect of the opposite types of strain could explain the observed behavior of the Raman peaks.

Alternatively, the shift of G and 2D peaks could be related to a change in the Kohn anomalies associated with the phonon dispersion at Γ and K. For instance, the aligned hBN layers in the hBN/graphene/hBN heterostructure could have built-in electric fields (*52*) which can dope graphene and thereby shift the Raman peak positions. However, this scenario is unlikely, as previous studies show that the presence of electrostatic doping causes non-adiabatic removal of the Kohn anomaly from the Γ point, leading to the stiffening of G band and 2D band (*53, 54*). Thus, most likely, the main factor that causes the change in Raman spectra is the periodic strain field induced by moiré patterns.

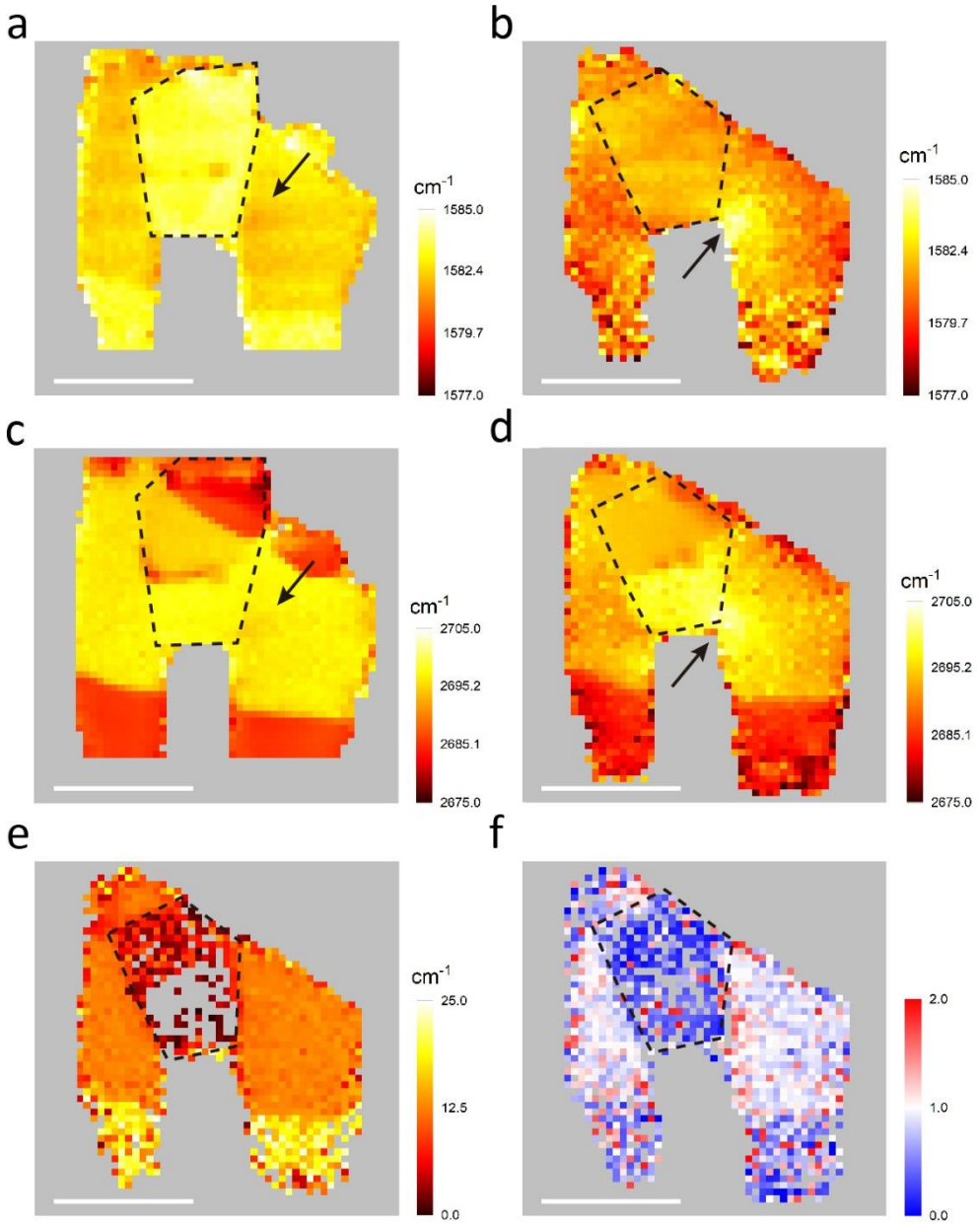

Fig. S7. Raman maps of sample 1 before and after rotation. (a) G peak position map before rotation. (b) G peak position map after rotation. (c) 2D peak position map before rotation. (d) 2D peak position map after rotation. G and 2D peaks of (a) to (d) were fitted by a single Lorentzian. (e) Map of the position difference of the two components of G peak after rotation. (f) Map of the peak intensity ratio of G peak components after rotation. G peak of (e) and (f) was fitted by two Lorentzian peaks. The scale bars are 10 μm. The black dashed lines show the folded region. The black arrows indicate a higher strain level near the folded corner.

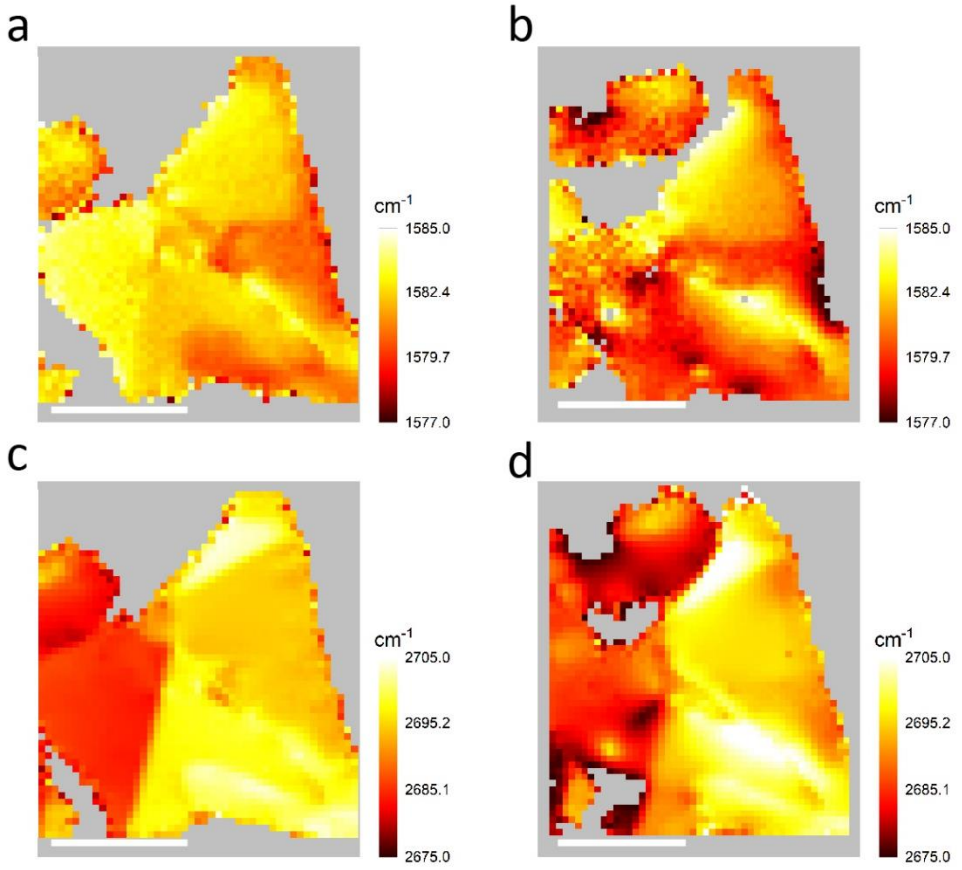

Fig. S8. Raman maps of sample 2 before and after rotation. (a) G peak position map before rotation. (b) G peak position map after rotation. (c) 2D peak position map before rotation. (d) 2D peak position map after rotation. G and 2D peaks were fitted by a single Lorentzian. The scale bars are 10 µm.

4. Transport properties of graphene in double moiré superlattices.

In commensurate magnetic field and periodic moiré potential, the fractal energy spectrum of electron in graphene exhibits a self-similar recursive behavior, where the superlattice minibands show a gapped Dirac-like spectrum at $\phi = \phi_0 p/q$ and express Landau level (LL) characteristics of Dirac fermions (*55*). Therefore we expect to observe quantized Hall conductivity associated with each minigap, similar to what is observed in the usual quantum Hall effect where $\sigma_{xy} = \nu e^2/h$, ν is a filling factor of a particular LL. Accordingly, when σ_{xx} is plotted in a map vs *n* and *B* (fan diagram), the gaps between Landau levels (the zeroes in the σ_{xx}) should trace linear trajectories emerging from primary Dirac point (PDP) as well as secondary Dirac points (SDPs) induced by moiré superlattice. For the fans emerging from PDP, the trajectories follows $B = n\phi_0/\nu$. For the fans emerging from SDPs, substituting ϕ with BA and $n_0=1/A$ in the Diophantine equation $\phi/\phi_0 = (n/n_0\text{-}s)/t$ yields $B\text{-}(-s/t)\phi_0/A = n\phi_0/t$ (which can be viewed as the quantization of minibands at an effective magnetic field of $B_{eff} = B\text{-}(-s/t)\phi_0/A$ or $B_{eff} = B\text{-}(p/q)\phi_0/A$, where *p* and *q* are co-prime integers). Thus we can deduce the corresponding carrier density to SDP from fan diagram.

Based on the Raman spectra of the hBN/graphene/hBN heterostructure, we estimate that the twist angles θ_t and θ_b should be both close to 0°, thereby in the transport properties, we expect to see two sets of SDPs close to each other apart from the PDP. For both bilayer and monolayer graphene devices, in longitudinal resistivity (ρ_{xx}) vs carrier density (*n*) dependence, we observed broadened (and with a complex structure) satellite peaks located around $n = \pm 2\times10^{12}$ cm^{-2} (Fig. 3a in the main text and Fig. S11a). At small B = 0.03 T where the Landau quantization is not yet developed, the transversal resistivity ρ_{xy} changes sign in the carrier density regions of these satellite peaks, indicating that they are moiré superlattice induced SDPs. These SDPs are more prominent in the hole side compared to the electron side, which is consistent with previous studies (*5, 6*).

In the Landau fan diagram at high magnetic fields, by tracing the linear trajectories we observed two sets of SDPs induced by the two independent moiré patterns for both bilayer and monolayer device. For bilayer device, the SDPs are at $n_{s1} = \pm 2.15\times10^{12}$ cm^{-2}, and $n_{s2} = \pm 2.34\times10^{12}$ cm^{-2} (Fig. 3a, b and d in the main text and Fig. S9a, c and d), corresponding to the moiré wavelengths of λ_{s1} = 14.7 nm and λ_{s2} = 14.0 nm, and the twist angles of 0.24° and 0.38°, respectively. For monolayer device, the SDPs are at $n_{s1} = \pm 2.10\times10^{12}$ cm^{-2}, $n_{s2} = \pm 2.44\times10^{12}$ cm^{-2} (Fig. S11 and Fig. S12a, c and d), corresponding to the moiré wavelengths of λ_{s1} = 14.8 nm and λ_{s2} = 13.8 nm, and the twist angles of 0.2° and 0.43°, respectively. In addition to the Raman map in Fig. 2h in main text, the similar values of the two sets of SDPs obtained from the bilayer and the monolayer devices, confirm that top and bottom twist angles are spatially uniform in the stack.

In the fan diagram $\partial\sigma/\partial B(n,B)$, we observed Brown-Zak (BZ) oscillations originating from the first order magnetic Bloch states ($\phi/\phi_0=1/q$) for the two sets of SDPs in both bilayer and monolayer devices (Fig. S9b, e, f and Fig. S12b, e, f). The first order magnetic Bloch states formed by the two moiré superlattices are also prominent at high temperature (T = 70 K, where the Landau quantization is suppressed), as indicated by the arrows in Figs. S10 and S13. We also observed high order magnetic Bloch states ($\phi/\phi_0 = 3/q$) belonging to the two moiré superlattices, as shown in Fig. S9e, f and Fig. S12e, f.

In principle, the super-moiré pattern generated by the two original moiré patterns should have six possible reciprocal lattice vectors, as described in the previous study (*39*), whereas the method in Ref (*38*) only considers one possible reciprocal lattice vector with the largest super-moiré pattern wavelength (λ_{sm} = 102.3 nm). If we take into account other possible reciprocal lattice vectors, we will get six possible second-order moiré wavelengths in total. For bilayer graphene device, the other five super-moiré wavelengths are 16.3 nm, 12.9 nm, 8.6 nm, 8 nm and 7.2 nm. The corresponding carrier densities n_{sm} of the first Brillouin zone edge are $\pm1.75\times10^{12}$ cm^{-2}, $\pm2.8\times10^{12}$ cm^{-2}, $\pm6.2\times10^{12}$ cm^{-2}, $\pm7.2\times10^{12}$ cm^{-2} and $\pm9\times10^{12}$ cm^{-2}. For monolayer graphene device, the six super-moiré wavelengths are 64.7 nm, 17.8 nm, 12.1 nm, 8.9 nm, 7.8 nm and 7.2 nm. The corresponding carrier densities n_{sm} of the first Brillouin zone edge are $\pm0.11\times10^{12}$ cm^{-2}, $\pm1.46\times10^{12}$ cm^{-2}, $\pm3.14\times10^{12}$ cm^{-2}, $\pm5.8\times10^{12}$ cm^{-2}, $\pm7.5\times10^{12}$ cm^{-2} and $\pm8.9\times10^{12}$ cm^{-2}. We observed satellite peaks in ρ_{xx} near most of these carrier densities n_{sm} (Fig. 3a in the main text and Fig. S11a). Note that near n_{sm} corresponding to these resistivity peaks, most of the low-B ρ_{xy} regions have sign reversal. In addition, similar to bilayer device, in the plot of $\partial\sigma_{xx}/\partial B(n,B)$ of monolayer device, we observe prominent horizontal streaks at B = 1.14 T and 0.57 T, which perfectly matches the magnetic field of the first and second order magnetic Bloch state originating from the super-moiré pattern when $BA = \phi_0$ (where q = 1) and $BA = \phi_0/2$ (where q = 2), respectively. These features allow us to attribute the origin of the observed carrier densities n_{sm} to the super-moiré pattern with different wavelengths.

4.1 Bilayer graphene in double moiré superlattices.

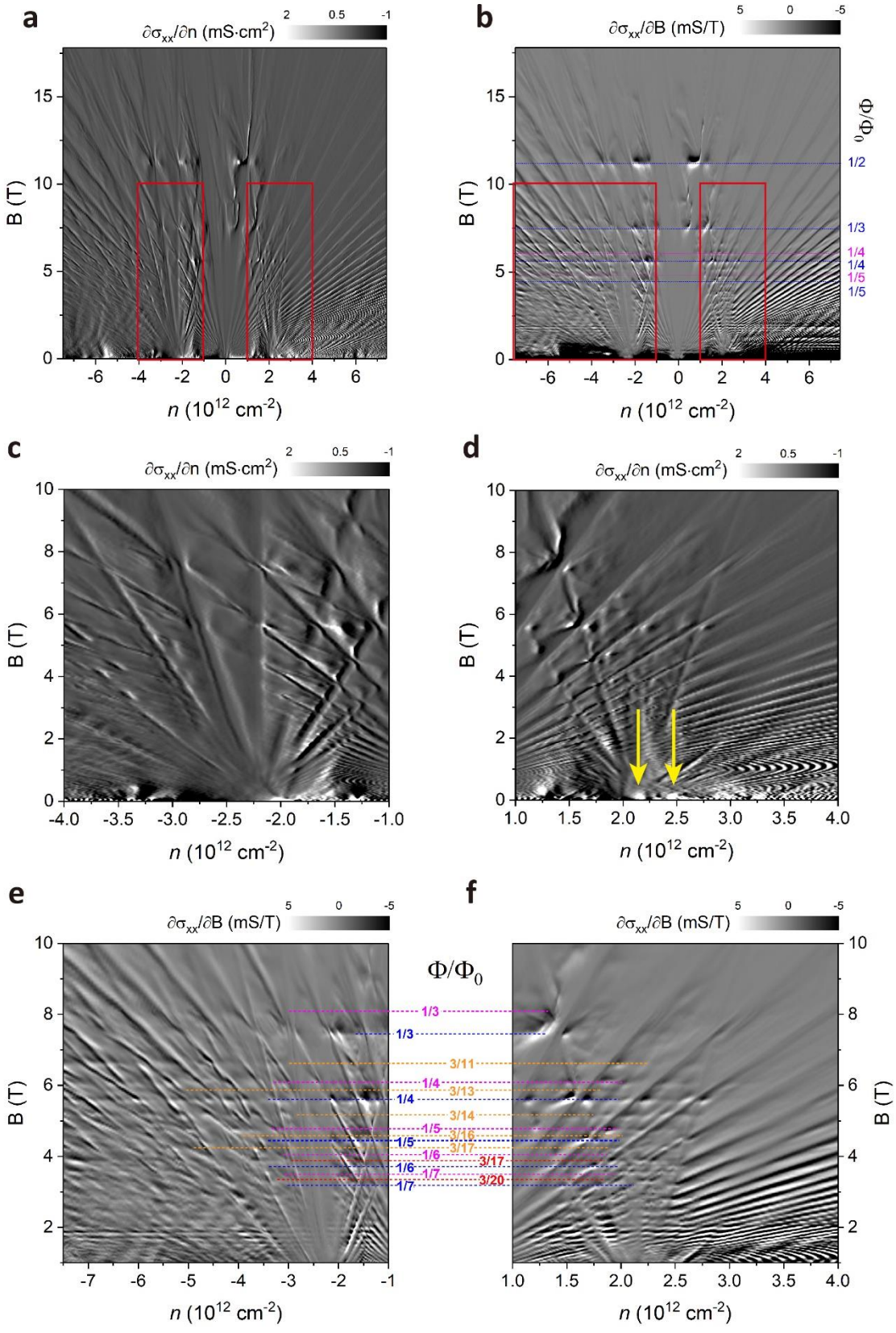

Fig. S9. Fractal Landau fan diagrams of bilayer graphene in double moiré superlattices. (a) Fan diagram $\partial\sigma_{xx}/\partial n(n,B)$ at T = 0.3 K. (b) Fan diagram $\partial\sigma_{xx}/\partial B(n,B)$. (c) and (d) are part of (a) for hole and electron doping

(marked in (a) by red rectangles), respectively, near secondary Dirac points (SDPs). Yellow arrows indicate the two sets of SDPs. (e) and (f) are part of (b) for hole and electron doping (marked in (b) by red rectangles), respectively, near SDPs. The blue and red dashed lines show the Brown-Zak oscillations belonging to the SDP at n_{s1} = ±2.14×10^{12} cm^{-2}, whereas magenta and orange dashed lines belong to the SDP at n_{s2} = ±2.34×10^{12} cm^{-2}. The numbers on the dashed lines show the values of p/q for oscillations at $\phi = (p/q)\phi_0$.

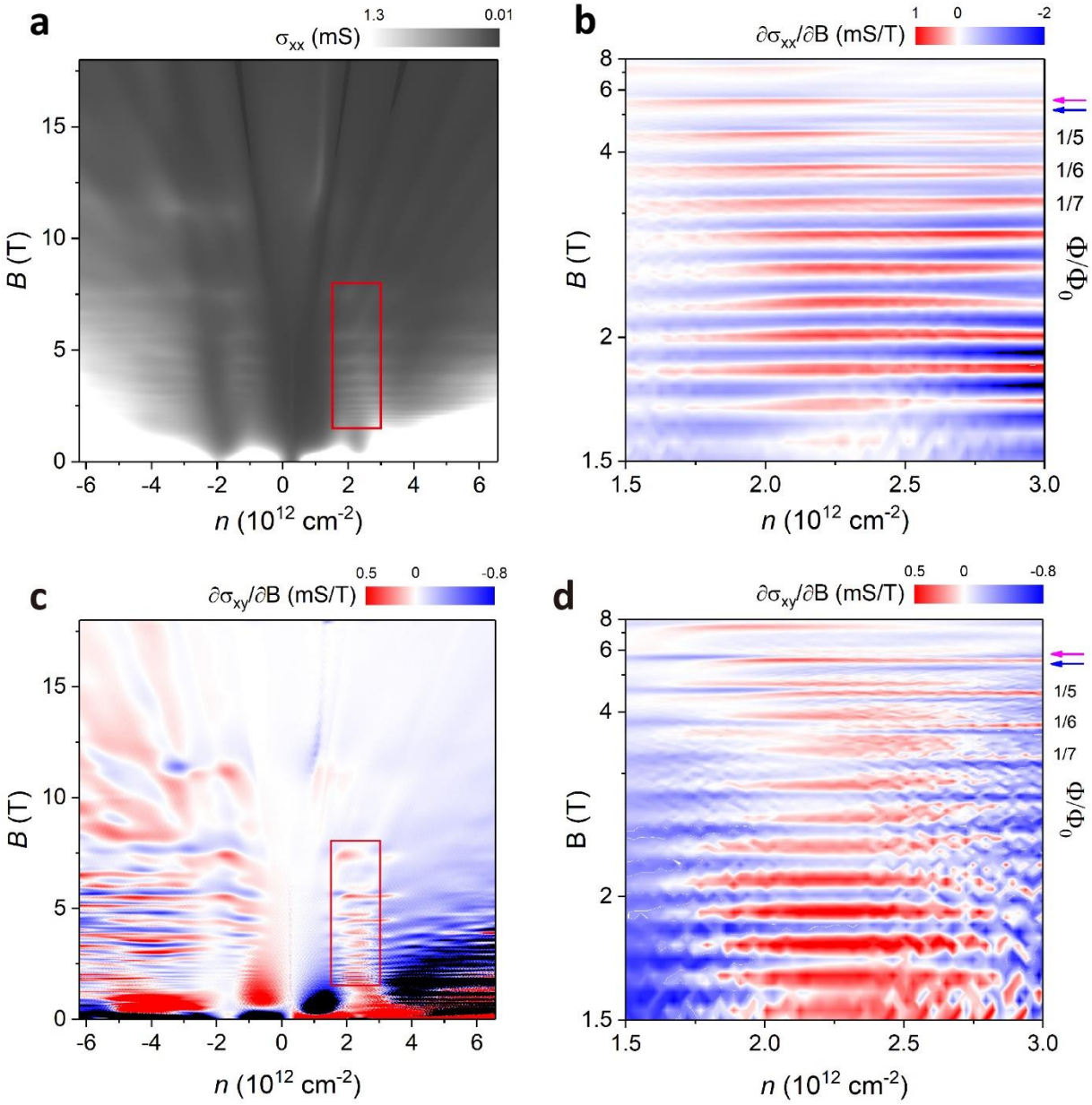

Fig. S10. Brown-Zak oscillations in double moiré bilayer graphene at T = 70 K. (a) Longitudinal conductivity σ_{xx} as a function of n and B, $\sigma_{xx}(n,B)$. (b) $\partial\sigma_{xx}/\partial B(n,B)$ for part of (a) near the SDPs for electron doping (marked in (a) by a red rectangle). (c) $\partial\sigma_{xy}/\partial B(n,B)$. (d) Region of (c) near the SDPs for electron doping (marked in (c) by a red rectangle). The blue and magenta arrows show the Brown-Zak oscillations belonging to the SDPs at n_{s1} = ±2.14×10^{12} cm^{-2}, and n_{s2} = ±2.34×10^{12} cm^{-2}, respectively. The numbers on the right in (b) and (d) indicate $\phi = (1/q)\,\phi_0$ with q = 5 to 7. At low magnetic fields, the resolution in B is not sufficient to distinguish the two sets of oscillations.

4.2 Monolayer graphene in double moiré superlattices.

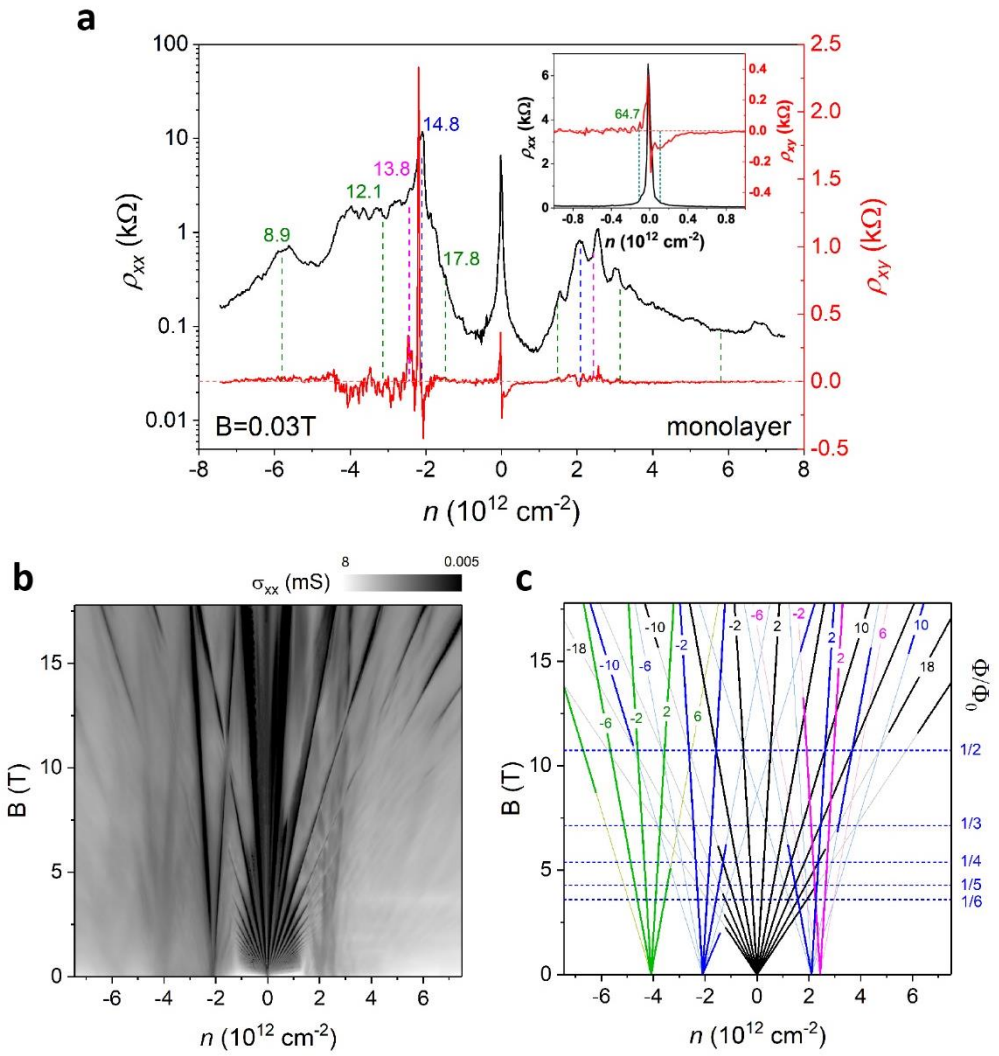

Fig. S11. Electronic transport and Landau quantization of monolayer graphene in double moiré superlattices. (a) Longitudinal resistivity ρ_{xx} and transverse resistivity ρ_{xy} of the monolayer region as a function of charge carrier density n after rotation. T = 0.3 K, B = 0.03 T. The dashed lines and numbers show the satellite peaks and the corresponding moiré wavelengths λ (see Methods). The blue and magenta dashed lines mark the SDPs at n_{s1} and n_{s2} corresponding to moiré patterns formed at both sides of graphene, respectively. The green dashed lines mark the n_{sm} required to reach the first Brillouin zone edge of super-moiré pattern with different wavelengths. The right inset is the zoomed-in figure of (a). (b) Fan diagram $\sigma_{xx}(n,B)$ measured at T = 0.3 K. (c) Simplified Wannier diagram labelling the quantum hall effect states identified in (b). Black lines show quantum oscillations with dominant sequence of Landau level filling factors ν = ±2, ±6, ±10, ... emerging from the PDP. Blue lines show quantum oscillations of t = ±2, ±6, ±10, emerging from SDP n_{s1}. Magenta lines show quantum oscillations of t = ±2 emerging from SDP n_{s2}. Green lines are another set of gap trajectories (s = 2) from the same moiré superlattice as SDP n_{s1} according to the Diophantine equation, with quantum oscillations of t = ±2, ±6. The blue horizontal dashed lines and numbers on the right show the most prominent BZ oscillations belonging to the SDP ns_1, with different values of p/q for $\phi = (p/q)\,\phi_0$.

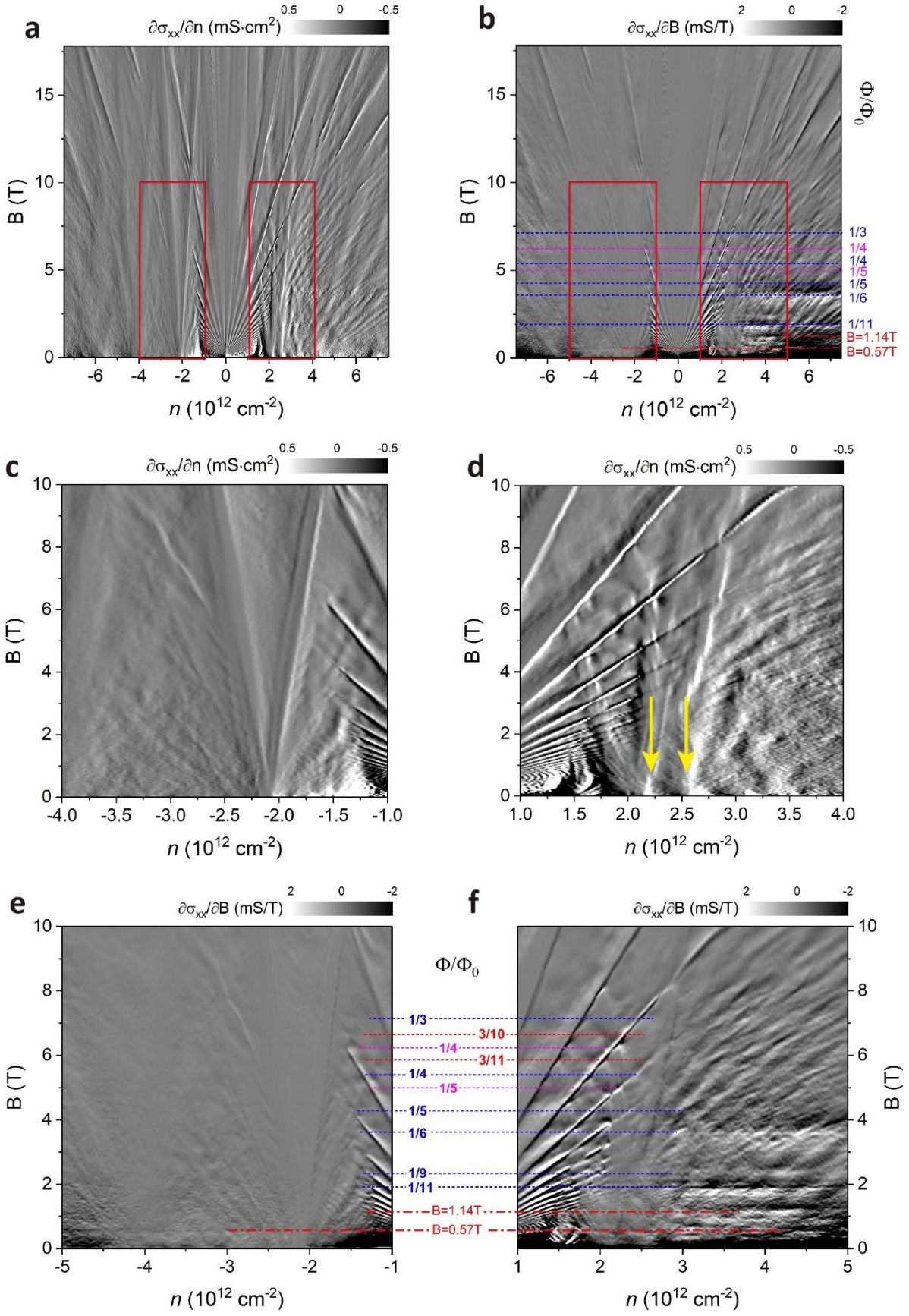

Fig. S12. Fractal Landau fan diagrams of monolayer graphene in double moiré superlattices. (a) Fan diagram $\partial\sigma_{xx}/\partial n(n,B)$ at T = 0.3 K. (b) Fan diagram $\partial\sigma_{xx}/\partial B(n,B)$. (c) and (d) are part of (a) for hole and electron doping

near SDPs (marked in (a) by red rectangles), respectively. Yellow arrows indicate the two sets of SDPs. (e) and (f) are part of (b) for hole and electron doping (marked in (b) by red rectangles), respectively, near SDPs. The blue and red dashed lines show the BZ oscillations belonging to the SDP at $n_{s1} = \pm 2.10\times10^{12}$ cm^{-2}. The magenta dashed lines show the BZ oscillations belonging to the SDP $n_{s2} = \pm 2.44\times10^{12}$ cm^{-2}. The numbers on the dashed lines show the values of p/q for oscillations at $\phi = (p/q)\phi_0$. The BZ feature at B = 1.14 T and 0.57 T originates from the first and second order magnetic Bloch state of the super-moiré pattern with the largest $\lambda_{sm} \approx$ 64.7 nm at $\phi = \phi_0$ and $\phi = \phi_0/2$, respectively.

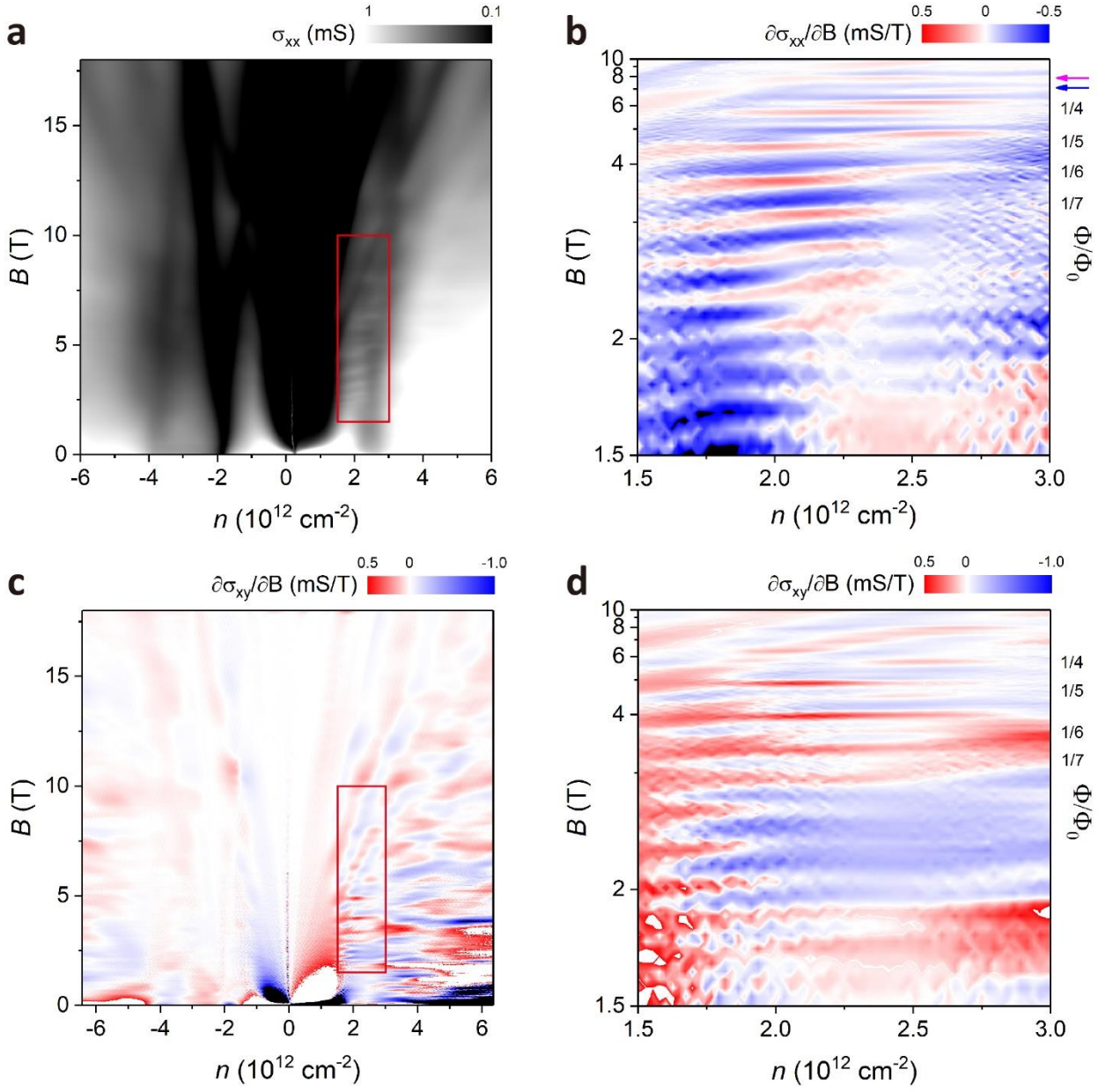

Fig. S13. Brown-Zak oscillations in double moiré monolayer graphene at T = 70 K. (a) Longitudinal conductivity σ_{xx} as a function of n and B, $\sigma_{xx}(n,B)$. (b) $\partial\sigma_{xx}/\partial B(n,B)$ in part of (a) near the SDPs for electron doping (marked in (a) by a red rectangle). The blue and magenta arrows show the Brown-Zak oscillations belonging to the SDPs at $n_{s1} = \pm 2.10\times10^{12}$ cm^{-2}, and $n_{s2} = \pm 2.44\times10^{12}$ cm^{-2}, respectively. (c) $\partial\sigma_{xy}/\partial B(n,B)$. (d) Part of (c) near the SDPs for electron doping (marked in (c) by a red rectangle). The numbers on the right in (b) and (d) indicate $\phi = (1/q)\ \phi_0$ with q = 4 to 7.

Supplementary Movies

Supplementary Movie S1. Rotation of van der Waals heterostructure. The movie shows the rotation of top hBN and graphene in an hBN/graphene/hBN stack under the control of PMMA patch deposited on top of the top hBN. The PMMA patch detached from top hBN after the clicking between top hBN, graphene and bottom hBN.

Supplementary Movie S2. Displacement of van der Waals heterostructure. The movie shows the displacement of top hBN and graphene in the same hBN/graphene/hBN stack under the control of PMMA patch deposited on top of the top hBN.

REFERENCES AND NOTES

1. Y.-H. Zhang, D. Mao, Y. Cao, P. Jarillo-Herrero, T. Senthil, Nearly flat Chern bands in moiré superlattices. *Phys. Rev. B* **99**, 075127 (2019).

2. S. Carr, D. Massatt, S. Fang, P. Cazeaux, M. Luskin, E. Kaxiras, Twistronics: Manipulating the electronic properties of two-dimensional layered structures through their twist angle. *Phys. Rev. B* **95**, 075420 (2017).

3. F. Wu, T. Lovorn, E. Tutuc, I. Martin, A. H. MacDonald, Topological insulators in twisted transition metal dichalcogenide homobilayers. *Phys. Rev. Lett.* **122**, 086402 (2019).

4. X. Chen, J. R. Wallbank, A. A. Patel, M. Mucha-Kruczyński, E. McCann, V. I. Fal'ko, Dirac edges of fractal magnetic minibands in graphene with hexagonal moiré superlattices. *Phys. Rev. B* **89**, 075401 (2014).

5. L. A. Ponomarenko, R. V. Gorbachev, G. L. Yu, D. C. Elias, R. Jalil, A. A. Patel, A. Mishchenko, A. S. Mayorov, C. R. Woods, J. R. Wallbank, M. Mucha-Kruczynski, B. A. Piot, M. Potemski, I. V. Grigorieva, K. S. Novoselov, F. Guinea, V. I. Fal'ko, A. K. Geim, Cloning of Dirac fermions in graphene superlattices. *Nature* **497**, 594–597 (2013).

6. C. R. Dean, L. Wang, P. Maher, C. Forsythe, F. Ghahari, Y. Gao, J. Katoch, M. Ishigami, P. Moon, M. Koshino, T. Taniguchi, K. Watanabe, K. L. Shepard, J. Hone, P. Kim, Hofstadter's butterfly and the fractal quantum Hall effect in moiré superlattices. *Nature* **497**, 598–602 (2013).

7. B. Hunt, J. D. Sanchez-Yamagishi, A. F. Young, M. Yankowitz, B. J. LeRoy, K. Watanabe, T. Taniguchi, P. Moon, M. Koshino, P. Jarillo-Herrero, R. C. Ashoori, Massive Dirac fermions and Hofstadter butterfly in a van der Waals heterostructure. *Science* **340**, 1427–1430 (2013).

8. G. Chen, L. Jiang, S. Wu, B. Lyu, H. Li, B. L. Chittari, K. Watanabe, T. Taniguchi, Z. Shi, J. Jung, Y. Zhang, F. Wang, Evidence of a gate-tunable Mott insulator in a trilayer graphene moiré superlattice. *Nat. Phys.* **15**, 237–241 (2019).

9. G. Chen, A. L. Sharpe, P. Gallagher, I. T. Rosen, E. J. Fox, L. Jiang, B. Lyu, H. Li, K. Watanabe, T. Taniguchi, J. Jung, Z. Shi, D. Goldhaber-Gordon, Y. Zhang, F. Wang, Signatures of tunable superconductivity in a trilayer graphene moiré superlattice. *Nature* **572**, 215–219 (2019).

10. E. M. Spanton, A. A. Zibrov, H. Zhou, T. Taniguchi, K. Watanabe, M. P. Zaletel, A. F. Young, Observation of fractional Chern insulators in a van der Waals heterostructure. *Science* **360**, 62–66 (2018).

11. A. L. Sharpe, E. J. Fox, A. W. Barnard, J. Finney, K. Watanabe, T. Taniguchi, M. A. Kastner, D. Goldhaber-Gordon, Emergent ferromagnetism near three-quarters filling in twisted bilayer graphene. *Science* **365**, 605–608 (2019).

12. Y. Cao, V. Fatemi, A. Demir, S. Fang, S. L. Tomarken, J. Y. Luo, J. D. Sanchez-Yamagishi, K. Watanabe, T. Taniguchi, E. Kaxiras, R. C. Ashoori, P. Jarillo-Herrero, Correlated insulator behaviour at half-filling in magic-angle graphene superlattices. *Nature* **556**, 80–84 (2018).

13. Y. Cao, V. Fatemi, S. Fang, K. Watanabe, T. Taniguchi, E. Kaxiras, P. Jarillo-Herrero, Unconventional superconductivity in magic-angle graphene superlattices. *Nature* **556**, 43–50 (2018).

14. M. Yankowitz, S. Chen, H. Polshyn, Y. Zhang, K. Watanabe, T. Taniguchi, D. Graf, A. F. Young, C. R. Dean, Tuning superconductivity in twisted bilayer graphene. *Science* **363**, 1059–1064 (2019).

15. C. Shen, Y. Chu, Q. Wu, N. Li, S. Wang, Y. Zhao, J. Tang, J. Liu, J. Tian, K. Watanabe, T. Taniguchi, R. Yang, Z. Y. Meng, D. Shi, O. V. Yazyev, G. Zhang, Correlated states in twisted double bilayer graphene. *Nat. Phys.* **16**, 520–525 (2020).

16. A. Kerelsky, C. Rubio-Verdú, L. Xian, D. M. Kennes, D. Halbertal, N. Finney, L. Song, S. Turkel, L. Wang, K. Watanabe, T. Taniguchi, J. Hone, C. Dean, D. Basov, A. Rubio, A. N. Pasupathy, Moiré-less correlations in ABCA graphene. *arXiv:1911.00007* (2019).

17. X. Liu, Z. Hao, E. Khalaf, J. Y. Lee, Y. Ronen, H. Yoo, D. Haei Najafabadi, K. Watanabe, T. Taniguchi, A. Vishwanath, P. Kim, Tunable spin-polarized correlated states in twisted double bilayer graphene. *Nature* **583**, 221–225 (2020).

18. Y. Cao, D. Rodan-Legrain, O. Rubies-Bigorda, J. M. Park, K. Watanabe, T. Taniguchi, P. Jarillo-Herrero, Tunable correlated states and spin-polarized phases in twisted bilayer-bilayer graphene. *Nature* **583**, 215–220 (2020).

19. E. M. Alexeev, D. A. Ruiz-Tijerina, M. Danovich, M. J. Hamer, D. J. Terry, P. K. Nayak, S. Ahn, S. Pak, J. Lee, J. I. Sohn, M. R. Molas, M. Koperski, K. Watanabe, T. Taniguchi, K. S. Novoselov, R. V. Gorbachev, H. S. Shin, V. I. Fal'ko, A. I. Tartakovskii, Resonantly hybridized excitons in moiré superlattices in van der Waals heterostructures. *Nature* **567**, 81–86 (2019).

20. K. L. Seyler, P. Rivera, H. Yu, N. P. Wilson, E. L. Ray, D. G. Mandrus, J. Yan, W. Yao, X. Xu, Signatures of moiré-trapped valley excitons in $MoSe_2/WSe_2$ heterobilayers. *Nature* **567**, 66–70 (2019).

21. L. Wang, E.-M. Shih, A. Ghiotto, L. Xian, D. A. Rhodes, C. Tan, M. Claassen, D. M. Kennes, Y. Bai, B. Kim, K. Watanabe, T. Taniguchi, X. Zhu, J. Hone, A. Rubio, A. N. Pasupathy, C. R. Dean, Correlated electronic phases in twisted bilayer transition metal dichalcogenides. *Nat. Mater.* **19**, 861–866 (2020).

22. L. An, X. Cai, D. Pei, M. Huang, Z. Wu, Z. Zhou, J. Lin, Z. Ying, Z. Ye, X. Feng, R. Gao, C. Cacho, M. Watson, Y. Chen, N. Wang, Interaction effects and superconductivity signatures in twisted double-bilayer WSe_2. *Nanoscale Horiz.* **5**, 1309–1316 (2020).

23. S. Ulstrup, R. J. Koch, S. Singh, K. M. McCreary, B. T. Jonker, J. T. Robinson, C. Jozwiak, E. Rotenberg, A. Bostwick, J. Katoch, J. A. Miwa, Direct observation of minibands in a twisted graphene/WS_2 bilayer. *Sci. Adv.* **6**, eaay6104 (2020).

24. M. Serlin, C. L. Tschirhart, H. Polshyn, Y. Zhang, J. Zhu, K. Watanabe, T. Taniguchi, L. Balents, A. F. Young, Intrinsic quantized anomalous Hall effect in a moiré heterostructure. *Science* **367**, 900–903 (2020).

25. C. R. Woods, L. Britnell, A. Eckmann, R. S. Ma, J. C. Lu, H. M. Guo, X. Lin, G. L. Yu, Y. Cao, R. V. Gorbachev, A. V. Kretinin, J. Park, L. A. Ponomarenko, M. I. Katsnelson, Y. N. Gornostyrev, K. Watanabe, T. Taniguchi, C. Casiraghi, H.-J. Gao, A. K. Geim, K. S. Novoselov, Commensurate–incommensurate transition in graphene on hexagonal boron nitride. *Nat. Phys.* **10**, 451–456 (2014).

26. K. Kim, M. Yankowitz, B. Fallahazad, S. Kang, H. C. P. Movva, S. Huang, S. Larentis, C. M. Corbet, T. Taniguchi, K. Watanabe, S. K. Banerjee, B. J. LeRoy, E. Tutuc, van der Waals heterostructures with high accuracy rotational alignment. *Nano Lett.* **16**, 1989–1995 (2016).

27. R. Ribeiro-Palau, C. Zhang, K. Watanabe, T. Taniguchi, J. Hone, C. R. Dean, Twistable electronics with dynamically rotatable heterostructures. *Science* **361**, 690–693 (2018).

28. Y. Wakafuji, R. Moriya, S. Masubuchi, K. Watanabe, T. Taniguchi, T. Machida, 3D manipulation of 2D materials using microdome polymer. *Nano Lett.* **20**, 2486–2492 (2020).

29. X. Feng, S. Kwon, J. Y. Park, M. Salmeron, Superlubric sliding of graphene nanoflakes on graphene. *ACS Nano* **7**, 1718–1724 (2013).

30. A. Vanossi, N. Manini, M. Urbakh, S. Zapperi, E. Tosatti, *Colloquium*: Modeling friction: From nanoscale to mesoscale. *Rev. Mod. Phys.* **85**, 529–552 (2013).

31. Z. Liu, J. Yang, F. Grey, J. Z. Liu, Y. Liu, Y. Wang, Y. Yang, Y. Cheng, Q. Zheng, Observation of microscale superlubricity in graphite. *Phys. Rev. Lett.* **108**, 205503 (2012).

32. E. Koren, U. Duerig, Moiré scaling of the sliding force in twisted bilayer graphene. *Phys. Rev. B* **94**, 045401 (2016).

33. K. Yao, N. R. Finney, J. Zhang, S. L. Moore, L. Xian, N. Tancogne-Dejean, F. Liu, J. Ardelean, X. Xu, D. Halbertal, K. Watanabe, T. Taniguchi, H. Ochoa, A. Asenjo-Garcia, X. Zhu, D. N. Basov, A. Rubio, C. R. Dean, J. Hone, P. J. Schuck, Nonlinear twistoptics at symmetry-broken interfaces. *arXiv:2006.13802* (2020).

34. N. R. Finney, M. Yankowitz, L. Muraleetharan, K. Watanabe, T. Taniguchi, C. R. Dean, J. Hone, Tunable crystal symmetry in graphene-boron nitride heterostructures with coexisting moiré superlattices. *Nat. Nanotechnol.* **14**, 1029–1034 (2019).

35. A. Eckmann, J. Park, H. Yang, D. Elias, A. S. Mayorov, G. Yu, R. Jalil, K. S. Novoselov, R. V. Gorbachev, M. Lazzeri, A. K. Geim, C. Casiraghi, Raman fingerprint of aligned graphene/h-BN superlattices. *Nano Lett.* **13**, 5242–5246 (2013).

36. A. H. MacDonald, Landau-level subband structure of electrons on a square lattice. *Phys. Rev. B* **28**, 6713–6717 (1983).

37. R. Krishna Kumar, X. Chen, G. H. Auton, A. Mishchenko, D. A. Bandurin, S. V. Morozov, Y. Cao, E. Khestanova, M. Ben Shalom, A. V. Kretinin, K. S. Novoselov, L. Eaves, I. V. Grigorieva, L. A. Ponomarenko, V. I. Fal'ko, A. K. Geim, High-temperature quantum oscillations caused by recurring Bloch states in graphene superlattices. *Science* **357**, 181–184 (2017).

38. L. Wang, S. Zihlmann, M.-H. Liu, P. Makk, K. Watanabe, T. Taniguchi, A. Baumgartner, C. Schönenberger, New generation of moiré superlattices in doubly aligned hBN/graphene/hBN heterostructures. *Nano Lett.* **19**, 2371–2376 (2019).

39. Z. Wang, Y. B. Wang, J. Yin, E. Tóvári, Y. Yang, L. Lin, M. Holwill, J. Birkbeck, D. J. Perello, S. Xu, J. Zultak, R. V. Gorbachev, A. V. Kretinin, T. Taniguchi, K. Watanabe, S. V. Morozov, M. Anđelković, S. P. Milovanović, L. Covaci, F. M. Peeters, A. Mishchenko, A. K. Geim, K. S. Novoselov, V. I. Fal'ko, A. Knothe, C. R. Woods, Composite super-moiré lattices in double-aligned graphene heterostructures. *Sci. Adv.* **5**, eaay8897 (2019).

40. M. Onodera, K. Kinoshita, R. Moriya, S. Masubuchi, K. Watanabe, T. Taniguchi, T. Machida, Cyclotron resonance study of monolayer graphene under double moiré potentials. *Nano Lett.* **20**, 4566–4572 (2020).

41. N. Leconte, J. Jung, Commensurate and incommensurate double moire interference in graphene encapsulated by hexagonal boron nitride. *2D Mater.* **7**, 031005 (2020).

42. M. Andelkovic, S. P. Milovanovic, L. Covaci, F. M. Peeters, Double Moiré with a twist: Supermoiré in encapsulated graphene. *Nano Lett.* **20**, 979–988 (2019).

43. S. J. Ahn, P. Moon, T. H. Kim, H. W. Kim, H. C. Shin, E. H. Kim, H. W. Cha, S. J. Kahng, P. Kim, M. Koshino, Y. W. Son, C. W. Yang, J. R. Ahn, Dirac electrons in a dodecagonal graphene quasicrystal. *Science* **361**, 782–786 (2018).

44. P. Moon, M. Koshino, Y.-W. Son, Quasicrystalline electronic states in 30° rotated twisted bilayer graphene. *Phys. Rev. B* **99**, 165430 (2019).

45. S. G. Xu, A. I. Berdyugin, P. Kumaravadivel, F. Guinea, R. Krishna Kumar, D. A. Bandurin, S. V. Morozov, W. Kuang, B. Tsim, S. Liu, J. H. Edgar, I. V. Grigorieva, V. I. Fal'ko, M. Kim, A. K. Geim, Giant oscillations in a triangular network of one-dimensional states in marginally twisted graphene. *Nat. Commun.* **10**, 4008 (2019).

46. T. Uwanno, Y. Hattori, T. Taniguchi, K. Watanabe, K. Nagashio, Fully dry PMMA transfer of graphene onh-BN using a heating/cooling system. *2D Mater.* **2**, 041002 (2015).

47. M. Yankowitz, J. Xue, D. Cormode, J. D. Sanchez-Yamagishi, K. Watanabe, T. Taniguchi, P. Jarillo-Herrero, P. Jacquod, B. J. LeRoy, Emergence of superlattice Dirac points in graphene on hexagonal boron nitride. *Nat. Phys.* **8**, 382–386 (2012).

48. Y. Song, D. Mandelli, O. Hod, M. Urbakh, M. Ma, Q. Zheng, Robust microscale superlubricity in graphite/hexagonal boron nitride layered heterojunctions. *Nat. Mater.* **17**, 894–899 (2018).

49. B. Cheng, P. Wang, C. Pan, T. Miao, Y. Wu, T. Taniguchi, K. Watanabe, C. N. Lau, M. Bockrath, Raman spectroscopy measurement of bilayer graphene's twist angle to boron nitride. *Appl. Phys. Lett.* **107**, 033101 (2015).

50. M. Huang, H. Yan, C. Chen, D. Song, T. F. Heinz, J. Hone, Phonon softening and crystallographic orientation of strained graphene studied by Raman spectroscopy. *Proc. Natl. Acad. Sci. U.S.A.* **106**, 7304–7308 (2009).

51. T. M. G. Mohiuddin, A. Lombardo, R. R. Nair, A. Bonetti, G. Savini, R. Jalil, N. Bonini, D. M. Basko, C. Galiotis, N. Marzari, K. S. Novoselov, A. K. Geim, A. C. Ferrari, Uniaxial strain in graphene by Raman spectroscopy: Gpeak splitting, Grüneisen parameters, and sample orientation. *Phys. Rev. B* **79**, 205433 (2009).

52. L. J. McGilly, A. Kerelsky, N. R. Finney, K. Shapovalov, E. M. Shih, A. Ghiotto, Y. Zeng, S. L. Moore, W. Wu, Y. Bai, K. Watanabe, T. Taniguchi, M. Stengel, L. Zhou, J. Hone, X. Zhu, D. N. Basov, C. Dean, C. E. Dreyer, A. N. Pasupathy, Visualization of moiré superlattices. *Nat. Nanotechnol.* **15**, 580–584 (2020).

53. A. Das, S. Pisana, B. Chakraborty, S. Piscanec, S. K. Saha, U. V. Waghmare, K. S. Novoselov, H. R. Krishnamurthy, A. K. Geim, A. C. Ferrari, A. K. Sood, Monitoring dopants by Raman scattering in an electrochemically top-gated graphene transistor. *Nat. Nanotechnol.* **3**, 210–215 (2008).

54. S. Pisana, M. Lazzeri, C. Casiraghi, K. S. Novoselov, A. K. Geim, A. C. Ferrari, F. Mauri, Breakdown of the adiabatic Born-Oppenheimer approximation in graphene. *Nat. Mater.* **6**, 198–201 (2007).

55. J. R. Wallbank, A. A. Patel, M. Mucha-Kruczyński, A. K. Geim, V. I. Fal'ko, Generic miniband structure of graphene on a hexagonal substrate. *Phys. Rev. B* **87**, 245408 (2013).

Chapter 8: Conclusions and outlook

8.1 Conclusions

In this thesis, dedication is given to devising creative vdW technologies that enable devices with remarkable performance, so that we could approach intrinsic electronic properties of the thermodynamically less stable rhombohedral graphite or achieve powerful dynamic control over the properties of vdW heterostructures through therotational degree of freedom.

Regarding the validity of the two vdW technologies, they all proved to satisfy the demand and goals of fabricating high-quality devices and should greatly promote the investigation of the physical properties of the related material. The first vdW technique is described in detail in **Chapter 5**. It aims at increasing the success rate of the heterostructure where rhombohedral graphite encapsulated by hBN retains its stacking order. The strong tendency of stacking order transition from rhombohedral to Bernal graphite has long time been the obstacle to fabricating high-quality devices of ABC-stacked graphite films. Our work first came up with an effective solution to this problem and should give inspiration to similar problems regarding structural phase transition of other materials. In this work, we found that when the hBN encapsulation direction is controlled parallel to the graphite zigzag edges, ABC stacking was well preserved. Whereas encapsulation along the armchair edges easily led to the transformation of ABC stacking into ABA stacking. The underlying mechanism of the technique is that the stacking transformation happens along armchair directions much more easily than zigzag directions.

Chapter 7 presents the elaborate procedure of the second vdW technique, which is committed to accurately positioning, rotating, and manipulating 2D crystals in the vdW heterostructures. Mediated by polymer resist patch patterned onto target flakes, the technique is a breakthrough method that allows precise fine-tuning of the 'twist' between atom-thin 2D materials layers stacked in a superlattice structure and therefore dynamical control of optical, mechanical, and electronic properties of van der Waals materials. We used this technique to rotate and slide the top hBN together with graphene on the bottom hBN through a polymer patch deposited onto the top hBN. We found that for crystals with comparable lattice constants, the smooth rotation or displacement got stuck at the commensurate state. This phenomenon helps to get a heterostructure where graphene and hBN are well aligned with each other, i.e. forming a moiré superlattice at the interface with a small twist angle. Compared to other manipulation techniques of 2D materials [18,177], the

technique in our work is non-destructive, more precise, more convenient and applies to any 2D material systems away from commensurate regime without limitation to their thickness.

In terms of the electronic properties of the devices we have made, these devices all proved to work with good performance and boast exciting and unusual physical phenomena. In the study of rhombohedral graphite, the prerequisite for investigating its electronic properties is to fully understand the atomic structure of graphite films and to efficiently search regions of rhombohedral stacking in the films. Comprehensive characterization of graphite stacking order is presented in **Chapter 5**.We found that there exist domains of mixed rhombohedral and Bernal stacking in graphite films. These domains exhibited distinct responses in the Raman modes, mechanical properties, and infrared plasmon reflection, depending on the exact stacking sequences. Thus they can be visualized using corresponding characterization methods.

In **Chapter 6** we presented the intriguing electronic properties of the rhombohedral graphite devices. For pure ABC stacked N -layer graphite, as is predicted theoretically, it possesses gapped bulk states and topologically protected surface states which are nearly flat. At high temperatures, the bulk of RG conducts as a result of thermal activation of 3D bands across the gap. At low temperature, the 2D surface states dominate and exhibit quantum Hall effect in a magnetic field, with phase transitions between a trivial gapless semimetal and a gapped quantum spin Hall insulator with a Berry phase of $\pm N\pi$. The surface states can open an energy gap in an external electric field due to broken inversion symmetry. However, the gap cannot be opened if stacking faults reside in the bulk. For graphite thinner than around four nanometres, an insulating state appears at the neutrality point with pronounced hysteresis as a function of the electric field as well as perpendicular and parallel magnetic fields. These features are attributed to the emergence of strongly correlated electronic surface states.

In **Chapter 7**, the Raman characterization and electronic transport study of the obtained heterostructure with perfect alignment between graphene and the two encapsulating layers of hBN, demonstrate the potential of the manipulation technique in twistronics applications. We observed pronounced changes in Raman responses before and after rotation. Specifically, for monolayer graphene, G peak evolved into a broadened asymmetric peak and 2D peak broadened a lot. For bilayer graphene, G peak split into two components and 2D peak components tended to merge into an asymmetric peak. These effects are attributed to the much stronger periodic inhomogeneity of charges and strain caused by the double moiré superlattices. For electronic properties, we observed two sets of secondary Dirac points and Brown-Zak oscillations originating from the two moiré superlattices. In addition, we observed the signature of the first-order magnetic Bloch state of the super-moiré pattern

generated by the double moiré superlattices. These results in turn prove the perfect alignment of graphene and hBN layers and thus indicate the effectiveness of the vdW technique.

8.2 Outlook

The first vdW technology to micromechanically control the crystal structure of graphite allows to prepare high-quality devices of hBN encapsulated rhombohedral graphite and is expected to greatly facilitate electronic transport studies of this exciting material. For rhombohedral graphite, even though the observation of surface states and gapped bulk states is in agreement with theoretical predictions from tight-binding model and the recent scanning tunnelling microscopy and spectroscopy (STM/STS) measurement results[178], the appearance of the intrinsic insulating state at the neutrality point for thinner samples remains unclear and cannot be explained by the free particle picture. The near-flat surface states exhibit strong correlations[37] and can potentially host magnetic state[9,38] and surface superconducting state[6,10], which are not observed in our samples. Future work should focus on investigating the strong correlations and explaining the emergence of the intrinsic insulating state in thinner rhombohedral graphite samples.

The second vdW technology presents a new strategy in device engineering that could lead to autonomous robotic manipulation. It could be further developed in the following two research directions. First, the potential for twistronics, through micromanipulators or micro-electro-mechanical systems inside the cryogenic measurement systems. The topology and electron interactions in a twisted 2D material system are highly dependent on the twist angles. Thus robust, universal and efficient techniques for controlling twist angles are demanded. The technique demonstrated in our work perfectly satisfies the desire and applies not only to graphene based heterostructures, but to other 2D material systems, finding its applications in research of 2D quasicrystals[179,180], magic-angles flat bands[181-183], and other topologically nontrivial systems. It is a validated route towards realizing continuously tunable twist angle that would facilitate the investigation of phase transitions and, potentially, of other emergent phenomena.

Second, the study of superlubricity, a highly interesting area of tribology. Combined with atomic force microscopy, the technique demonstrated in our research could be developed into a new method for testing frictions between 2D crystals[113,115,185]. Thus the discovery of combinations of different 2D materials and investigations of their excellent tribological properties could be greatly expedited[115,186]. On the other hand, with the ability to precisely slide and rotate the 2D materials, our technique will motivate the design of novel nano-functionalized interfaces for friction control in micro/nano-electro-mechanical systems[187].

Bibliography

1 Feynman, R. P. There's Plenty of Room at the Bottom. *Eng. Sci.* **23**, (1960), 22-36.

2 Onodera, M. *et al.* Assembly of van der Waals heterostructures: exfoliation, searching, and stacking of 2D materials. *Japanese Journal of Applied Physics* **59**, (2020).

3 Fan, S. *et al.* Transfer assembly for two-dimensional van der Waals heterostructures. *2D Materials* **7**, (2020).

4 Yankowitz, M. *et al.* van der Waals heterostructures combining graphene and hexagonal boron nitride. *Nature Reviews Physics* **1**, (2019), 112-125.

5 Liu, Y. *et al.* Van der Waals heterostructures and devices. *Nature Reviews Materials* **1**, (2016).

6 Kopnin, N. B. *et al.* High-temperature surface superconductivity in rhombohedral graphite. *Physical Review B* **87**, (2013).

7 Otani, M. *et al.* Intrinsic magnetic moment on (0001) surfaces of rhombohedral graphite. *Physical Review B* **81**, (2010).

8 Zhang, F. *et al.* Spontaneous quantum Hall states in chirally stacked few-layer graphene systems. *Phys Rev Lett* **106**, (2011), 156801.

9 Pamuk, B. *et al.* Magnetic gap opening in rhombohedral-stacked multilayer graphene from first principles. *Physical Review B* **95**, (2017).

10 Muñoz, W. A. *et al.* Tight-binding description of intrinsic superconducting correlations in multilayer graphene. *Physical Review B* **87**, (2013).

11 Xu, D.-H. *et al.* Stacking order, interaction, and weak surface magnetism in layered graphene sheets. *Physical Review B* **86**, (2012).

12 Charlier, J. C. *et al.* First-principles study of the stacking effect on the electronic properties of graphite(s). *Carbon* **32**, (1994), 289-299.

13 Carr, S. *et al.* Electronic-structure methods for twisted moiré layers. *Nature Reviews Materials* **5**, (2020), 748-763.

14 Tran, K. *et al.* Moiré and beyond in transition metal dichalcogenide twisted bilayers. *2D Materials*, (2020).

15 Balents, L. *et al.* Superconductivity and strong correlations in moiré flat bands. *Nature Physics* **16**, (2020), 725-733.

16 Novoselov, K. S. *et al.* 2D materials and van der Waals heterostructures. *Science* **353**, (2016), aac9439.

17 Geim, A. K. & Grigorieva, I. V. Van der Waals heterostructures. *Nature* **499**, (2013), 419-425.

18 Ribeiro-Palau, R. *et al.* Twistable electronics with dynamically rotatable heterostructures. *Science* **361**, (2018), 690-693.

19 Yankowitz, M. *et al.* Dynamic band-structure tuning of graphene moire superlattices with pressure. *Nature* **557**, (2018), 404-408.

20 Dean, C. R. *et al.* Boron nitride substrates for high-quality graphene electronics. *Nat Nanotechnol* **5**, (2010), 722-726.

21 Zeng, Y. *et al.* High-Quality Magnetotransport in Graphene Using the Edge-Free Corbino Geometry. *Phys Rev Lett* **122**, (2019), 137701.

22 Young, A. F. *et al.* Spin and valley quantum Hall ferromagnetism in graphene. *Nature Physics* **8**, (2012), 550-556.

23 Novoselov, K. S. *et al.* Two-dimensional gas of massless Dirac fermions in graphene. *Nature* **438**, (2005), 197-200.

24 Zhang, Y. *et al.* Experimental observation of the quantum Hall effect and Berry's phase in graphene. *Nature* **438**, (2005), 201-204.

25 Dean, C. R. *et al.* Multicomponent fractional quantum Hall effect in graphene. *Nature Physics* **7**, (2011), 693-696.

26 Chen, S. *et al.* Competing Fractional Quantum Hall and Electron Solid Phases in Graphene. *Phys Rev Lett* **122**, (2019), 026802.

27 Polshyn, H. *et al.* Quantitative Transport Measurements of Fractional Quantum Hall Energy Gaps in Edgeless Graphene Devices. *Phys Rev Lett* **121**, (2018), 226801.

28 Liu, X. *et al.* Quantum Hall drag of exciton condensate in graphene. *Nature Physics* **13**, (2017), 746-750.

29 Li, J. I. A. *et al.* Pairing states of composite fermions in double-layer graphene. *Nature Physics* **15**, (2019), 898-903.

30 Sunku, S. S. *et al.* Photonic crystals for nano-light in moire graphene superlattices. *Science* **362**, (2018), 1153-1156.

31 Ni, G. X. *et al.* Plasmons in graphene moire superlattices. *Nat Mater* **14**, (2015), 1217-1222.

32 Dean, C. R. *et al.* Hofstadter's butterfly and the fractal quantum Hall effect in moire superlattices. *Nature* **497**, (2013), 598-602.

33 Hunt, B. *et al.* Massive Dirac fermions and Hofstadter butterfly in a van der Waals heterostructure. *Science* **340**, (2013), 1427-1430.

34 Ponomarenko, L. A. *et al.* Cloning of Dirac fermions in graphene superlattices. *Nature* **497**, (2013), 594-597.

35 Xiao, R. *et al.* Density functional investigation of rhombohedral stacks of graphene: Topological surface states, nonlinear dielectric response, and bulk limit. *Physical Review B* **84**, (2011).

36 Ho, C.-H. *et al.* Evolution and dimensional crossover from the bulk subbands in ABC-stacked graphene to a three-dimensional Dirac cone structure in rhombohedral graphite. *Physical Review B* **93**, (2016).

37 Lee, Y. *et al.* Competition between spontaneous symmetry breaking and single-particle gaps in trilayer graphene. *Nat Commun* **5**, (2014), 5656.

38 Olsen, R. *et al.* Ferromagnetism in ABC-stacked trilayer graphene. *Physical Review B* **87**, (2013).

39 Cousins, C. S. G. Elasticity of carbon allotropes. IV. Rhombohedral graphite: Elasticity, zone-center optic modes, and phase transformation using transferred Keating parameters. *Physical Review B* **67**, (2003).

40 Cao, Y. *et al.* Correlated insulator behaviour at half-filling in magic-angle graphene superlattices. *Nature* **556**, (2018), 80-84.

41 Cao, Y. *et al.* Unconventional superconductivity in magic-angle graphene superlattices. *Nature* **556**, (2018), 43-50.

42 Kim, K. *et al.* van der Waals Heterostructures with High Accuracy Rotational Alignment. *Nano Lett* **16**, (2016), 1989-1995.

43 Feng, X. *et al.* Superlubric sliding of graphene nanoflakes on graphene. *ACS Nano* **7**, (2013), 1718-1724.

44 Kawai, S. *et al.* Superlubricity of graphene nanoribbons on gold surfaces. *Science* **351**, (2016), 957-961.

45 Wilson, M. Electrons in atomically thin carbon sheets behave like massless particles. *Physics Today* **59**, (2006), 21-23.

46 Wallace, P. R. The Band Theory of Graphite. *Physical Review* **71**, (1947), 622-634.

47 Kuzmenko, A. B. *et al.* Determination of the gate-tunable band gap and tight-binding parameters in bilayer graphene using infrared spectroscopy. *Physical Review B* **80**, (2009).

48 Lipson, H. & Stokes, A. R. The structure of graphite. *Proceedings of the Royal Society of London. Series A. Mathematical and Physical Sciences* **181**, (1997), 101-105.

49 Nery, J. P. *et al.* Long-Range Rhombohedral-Stacked Graphene through Shear. *Nano Lett* **20**, (2020), 5017-5023.

50 Min, H. & MacDonald, A. H. Chiral decomposition in the electronic structure of graphene multilayers. *Physical Review B* **77**, (2008).

51 Dresselhaus, M. S. & Dresselhaus, G. Intercalation compounds of graphite. *Advances in Physics* **51**, (2002), 1-186.

52 Yang, Y. P. *et al.* Stacking Order in Graphite Films Controlled by van der Waals Technology. *Nano Letters* **19**, (2019), 8526-8532.

53 Koshino, M. & McCann, E. Trigonal warping and Berry's phase Nπ in ABC-stacked multilayer graphene. *Physical Review B* **80**, (2009).

54 Slizovskiy, S. *et al.* Films of rhombohedral graphite as two-dimensional topological semimetals. *Communications Physics* **2**, (2019).

55 McCann, E. & Fal'ko, V. I. Landau-level degeneracy and quantum Hall effect in a graphite bilayer. *Phys Rev Lett* **96**, (2006), 086805.

56 Guinea, F. *et al.* Electronic states and Landau levels in graphene stacks. *Physical Review B* **73**, (2006).

57 Hyart, T. *et al.* Two Topologically Distinct Dirac-Line Semimetal Phases and Topological Phase Transitions in Rhombohedrally Stacked Honeycomb Lattices. *Journal of Low Temperature Physics* **191**, (2018), 35-48.

58 Heikkilä, T. T. & Volovik, G. E. Dimensional crossover in topological matter: Evolution of the multiple Dirac point in the layered system to the flat band on the surface. *JETP Letters* **93**, (2011), 59-65.

59 Schnyder, A. P. & Ryu, S. Topological phases and surface flat bands in superconductors without inversion symmetry. *Physical Review B* **84**, (2011).

60 Cai, S. *et al.* Independence of topological surface state and bulk conductance in three-dimensional topological insulators. *npj Quantum Materials* **3**, (2018).

61 Burkov, A. A. Topological semimetals. *Nat Mater* **15**, (2016), 1145-1148.

62 Koshino, M. & McCann, E. Multilayer graphenes with mixed stacking structure: Interplay of Bernal and rhombohedral stacking. *Physical Review B* **87**, (2013).

63 Landau, L. D. Zur Theorie der phasenumwandlungen II. *Phys. Z. Sowjetunion* **11**, (1937), 26-35.

64 Yoshioka, D. *The Quantum Hall Effect*. (2002).

65 Klitzing, K. v. *et al.* New Method for High-Accuracy Determination of the Fine-Structure Constant Based on Quantized Hall Resistance. *Physical Review Letters* **45**, (1980), 494-497.

66 McClure, J. W. Diamagnetism of Graphite. *Physical Review* **104**, (1956), 666-671.

67 Ferry, D. K. *Transport in Semiconductor Mesoscopic Devices*. (2015).

68 Sondhi, S. L. *et al.* Continuous quantum phase transitions. *Reviews of Modern Physics* **69**, (1997), 315-333.

69 Ando, T. *et al.* Berry's Phase and Absence of Back Scattering in Carbon Nanotubes. *Journal of the Physical Society of Japan* **67**, (1998), 2857-2862.

70 Novoselov, K. S. *et al.* Unconventional quantum Hall effect and Berry's phase of 2π in bilayer graphene. *Nature Physics* **2**, (2006), 177-180.

71 Mikitik, G. P. & Sharlai, Y. V. The Berry phase in graphene and graphite multilayers. *Low Temperature Physics* **34**, (2008), 794-800.

72 Taguchi, Y. *et al.* Spin chirality, Berry phase, and anomalous Hall effect in a frustrated ferromagnet. *Science* **291**, (2001), 2573-2576.

73 Shen, S.-Q. Spin Hall effect and Berry phase in two-dimensional electron gas. *Physical Review B* **70**, (2004).

74 Sheng, D. N. *et al.* Quantum spin-Hall effect and topologically invariant Chern numbers. *Phys Rev Lett* **97**, (2006), 036808.

75 Nayak, A. K. *et al.* Large anomalous Hall effect driven by a nonvanishing Berry curvature in the noncolinear antiferromagnet Mn3Ge. *Sci Adv* **2**, (2016), e1501870.

76 Xiao, D. *et al.* Berry phase effects on electronic properties. *Reviews of Modern Physics* **82**, (2010), 1959-2007.

77 Berry, M. E. Quantal phase factors accompanying adiabatic changes. *Proceedings of the Royal Society of London. A. Mathematical and Physical Sciences* **392**, (1997), 45-57.

78 Mikitik, G. P. & Sharlai, Y. V. Manifestation of Berry's Phase in Metal Physics. *Physical Review Letters* **82**, (1999), 2147-2150.

79 Mikitik, G. P. & Sharlai, Y. V. Berry phase and de Haas-van Alphen effect in LaRhIn5. *Phys Rev Lett* **93**, (2004), 106403.

80 Roth, L. M. Semiclassical Theory of Magnetic Energy Levels and Magnetic Susceptibility of Bloch Electrons. *Physical Review* **145**, (1966), 434-448.

81 Onsager, L. Interpretation of the de Haas-van Alphen effect. *The London, Edinburgh, and Dublin Philosophical Magazine and Journal of Science* **43**, (2010), 1006-1008.

82 Sharapov, S. G. *et al.* Magnetic oscillations in planar systems with the Dirac-like spectrum of quasiparticle excitations. *Physical Review B* **69**, (2004).

83 Luk'yanchuk, I. A. & Kopelevich, Y. Phase analysis of quantum oscillations in graphite. *Phys Rev Lett* **93**, (2004), 166402.

84 Zhang, F. *et al.* Band structure ofABC-stacked graphene trilayers. *Physical Review B* **82**, (2010).

85 Zak, J. Magnetic Translation Group. II. Irreducible Representations. *Physical Review* **134**, (1964), A1607-A1611.

86 Brown, E. Bloch Electrons in a Uniform Magnetic Field. *Physical Review* **133**, (1964), A1038-A1044.

87 Hofstadter, D. R. Energy levels and wave functions of Bloch electrons in rational and irrational magnetic fields. *Physical Review B* **14**, (1976), 2239-2249.

88 MacDonald, A. H. Landau-level subband structure of electrons on a square lattice. *Physical Review B* **28**, (1983), 6713-6717.

89 Wannier, G. H. A Result Not Dependent on Rationality for Bloch Electrons in a Magnetic Field. *Physica Status Solidi (b)* **88**, (1978), 757-765.

90 Wallbank, J. R. *et al.* Generic miniband structure of graphene on a hexagonal substrate. *Physical Review B* **87**, (2013), 245408.

91 Park, C. H. *et al.* New generation of massless Dirac fermions in graphene under external periodic potentials. *Phys Rev Lett* **101**, (2008), 126804.

92 Yankowitz, M. *et al.* Emergence of superlattice Dirac points in graphene on hexagonal boron nitride. *Nature Physics* **8**, (2012), 382-386.

93 Chen, X. *et al.* Dirac edges of fractal magnetic minibands in graphene with hexagonal moiré superlattices. *Physical Review B* **89**, (2014), 075401.

94 Krishna Kumar, R. *et al.* High-temperature quantum oscillations caused by recurring Bloch states in graphene superlattices. *Science* **357**, (2017), 181-184.

95 Watanabe, K. *et al.* Direct-bandgap properties and evidence for ultraviolet lasing of hexagonal boron nitride single crystal. *Nat Mater* **3**, (2004), 404-409.

96 Cassabois, G. *et al.* Hexagonal boron nitride is an indirect bandgap semiconductor. *Nature Photonics* **10**, (2016), 262-266.

97 Xue, J. *et al.* Scanning tunnelling microscopy and spectroscopy of ultra-flat graphene on hexagonal boron nitride. *Nat Mater* **10**, (2011), 282-285.

98 Zhang, Y. *et al.* Origin of spatial charge inhomogeneity in graphene. *Nature Physics* **5**, (2009), 722-726.

99 Pease, R. S. Crystal structure of boron nitride. *Nature* **165**, (1950), 722-723.

100 Warner, J. H. *et al.* Atomic resolution imaging and topography of boron nitride sheets produced by chemical exfoliation. *ACS Nano* **4**, (2010), 1299-1304.

101 Constantinescu, G. *et al.* Stacking in bulk and bilayer hexagonal boron nitride. *Phys Rev Lett* **111**, (2013), 036104.

102 Cao, Y. *et al.* Quality Heterostructures from Two-Dimensional Crystals Unstable in Air by Their Assembly in Inert Atmosphere. *Nano Lett* **15**, (2015), 4914-4921.

103 Mishchenko, A. *et al.* Nonlocal Response and Anamorphosis: The Case of Few-Layer Black Phosphorus. *Nano Lett* **15**, (2015), 6991-6995.

104 Wang, L. *et al.* One-dimensional electrical contact to a two-dimensional material. *Science* **342**, (2013), 614-617.

105 Banszerus, L. *et al.* Ballistic Transport Exceeding 28 mum in CVD Grown Graphene. *Nano Lett* **16**, (2016), 1387-1391.

106 Israelachvili, J. N. *Intermolecular and Surface Forces*. (2011).

107 Kittel, C. *Introduction to Solid State Physics*. (Wiley, 2004).

108 Vanossi, A. *et al.* Colloquium: Modeling friction: From nanoscale to mesoscale. *Reviews of Modern Physics* **85**, (2013), 529-552.

109 Lee, C. *et al.* Frictional characteristics of atomically thin sheets. *Science* **328**, (2010), 76-80.

110 Braun, O. M. & Kivshar, Y. S. *The Frenkel-Kontorova Model*. (2004).

111 Bak, P. Commensurate phases, incommensurate phases and the devil's staircase. *Reports on Progress in Physics* **45**, (1982), 587-629.

112 Peyrard, M. & Aubry, S. Critical behaviour at the transition by breaking of analyticity in the discrete Frenkel-Kontorova model. *Journal of Physics C: Solid State Physics* **16**, (1983), 1593-1608.

113 Koren, E. *et al.* Surface science. Adhesion and friction in mesoscopic graphite contacts. *Science* **348**, (2015), 679-683.

114 Berman, D. *et al.* Friction. Macroscale superlubricity enabled by graphene nanoscroll formation. *Science* **348**, (2015), 1118-1122.

115 Song, Y. *et al.* Robust microscale superlubricity in graphite/hexagonal boron nitride layered heterojunctions. *Nat Mater* **17**, (2018), 894-899.

116 Li, H. *et al.* Superlubricity between MoS2 Monolayers. *Adv Mater* **29**, (2017).

117 Hirth, J. P. & Lothe, J. *Theory of dislocations*. 2nd edn, (Krieger Publishing Company, 1982).

118 Hattendorf, S. *et al.* Networks of ABA and ABC stacked graphene on mica observed by scanning tunneling microscopy. *Surface Science* **610**, (2013), 53-58.

119 Jiang, L. *et al.* Soliton-dependent plasmon reflection at bilayer graphene domain walls. *Nat Mater* **15**, (2016), 840-844.

120 Yoo, H. *et al.* Atomic and electronic reconstruction at the van der Waals interface in twisted bilayer graphene. *Nat Mater* **18**, (2019), 448-453.

121 Weston, A. *et al.* Atomic reconstruction in twisted bilayers of transition metal dichalcogenides. *Nat Nanotechnol* **15**, (2020), 592-597.

122 Delavignette, P. & Amelinckx, S. Dislocation patterns in graphite. *Journal of Nuclear Materials* **5**, (1962), 17-66.

123 Jiang, L. *et al.* Manipulation of domain-wall solitons in bi- and trilayer graphene. *Nat Nanotechnol*, (2018).

124 Yankowitz, M. *et al.* Electric field control of soliton motion and stacking in trilayer graphene. *Nat Mater* **13**, (2014), 786-789.

125 Gong, L. *et al.* Reversible loss of Bernal stacking during the deformation of few-layer graphene in nanocomposites. *ACS Nano* **7**, (2013), 7287-7294.

126 Read, W. T. & Shockley, W. Dislocation Models of Crystal Grain Boundaries. *Physical Review* **78**, (1950), 275-289.

127 Liao, X. *et al.* Deformation twinning in hexagonal materials. *MRS Bulletin* **41**, (2016), 314-319.

128 Rooney, A. P. *et al.* Anomalous twin boundaries in two dimensional materials. *Nat Commun* **9**, (2018), 3597.

129 Wijk, M. M. v. *et al.* Relaxation of moiré patterns for slightly misaligned identical lattices: graphene on graphite. *2D Materials* **2**, (2015).

130 Lin, X. *et al.* Shear instability in twisted bilayer graphene. *Physical Review B* **98**, (2018).

131 Dai, S. *et al.* Twisted Bilayer Graphene: Moire with a Twist. *Nano Lett* **16**, (2016), 5923-5927.

132 Nam, N. N. T. & Koshino, M. Lattice relaxation and energy band modulation in twisted bilayer graphene. *Physical Review B* **96**, (2017).

133 Gargiulo, F. & Yazyev, O. V. Structural and electronic transformation in low-angle twisted bilayer graphene. *2D Materials* **5**, (2017).

134 Alden, J. S. *et al.* Strain solitons and topological defects in bilayer graphene. *Proc Natl Acad Sci U S A* **110**, (2013), 11256-11260.

135 Butz, B. *et al.* Dislocations in bilayer graphene. *Nature* **505**, (2014), 533-537.

136 Lin, J. *et al.* AC/AB stacking boundaries in bilayer graphene. *Nano Lett* **13**, (2013), 3262-3268.

137 Woods, C. R. *et al.* Commensurate–incommensurate transition in graphene on hexagonal boron nitride. *Nature Physics* **10**, (2014), 451-456.

138 Lin, X. & Ni, J. Effective lattice model of graphene moiré superlattices on hexagonal boron nitride. *Physical Review B* **100**, (2019).

139 van Wijk, M. M. *et al.* Moire patterns as a probe of interplanar interactions for graphene on h-BN. *Phys Rev Lett* **113**, (2014), 135504.

140 Novoselov, K. S. *et al.* Electric field effect in atomically thin carbon films. *Science* **306**, (2004), 666-669.

141 Blake, P. *et al.* Making graphene visible. *Applied Physics Letters* **91**, (2007).

142 Gorbachev, R. V. *et al.* Hunting for monolayer boron nitride: optical and Raman signatures. *Small* **7**, (2011), 465-468.

143 You, Y. *et al.* Edge chirality determination of graphene by Raman spectroscopy. *Applied Physics Letters* **93**, (2008), 163112.

144 Finney, N. R. *et al.* Tunable crystal symmetry in graphene-boron nitride heterostructures with coexisting moire superlattices. *Nat Nanotechnol* **14**, (2019), 1029-1034.

145 Kretinin, A. V. *et al.* Electronic properties of graphene encapsulated with different two-dimensional atomic crystals. *Nano Lett* **14**, (2014), 3270-3276.

146 Bertolazzi, S. *et al.* Stretching and breaking of ultrathin MoS2. *ACS Nano* **5**, (2011), 9703-9709.

147 Uwanno, T. *et al.* Fully dry PMMA transfer of graphene onh-BN using a heating/cooling system. *2D Materials* **2**, (2015), 041002.

148 Pizzocchero, F. *et al.* The hot pick-up technique for batch assembly of van der Waals heterostructures. *Nat Commun* **7**, (2016), 11894.

149 Zomer, P. J. *et al.* Fast pick up technique for high quality heterostructures of bilayer graphene and hexagonal boron nitride. *Applied Physics Letters* **105**, (2014), 013101.

150 Purdie, D. G. *et al.* Cleaning interfaces in layered materials heterostructures. *Nat Commun* **9**, (2018), 5387.

151 Frisenda, R. *et al.* Recent progress in the assembly of nanodevices and van der Waals heterostructures by deterministic placement of 2D materials. *Chem Soc Rev* **47**, (2018), 53-68.

152 Liu, Y. *et al.* Recent Progress in the Fabrication, Properties, and Devices of Heterostructures Based on 2D Materials. *Nano-Micro Letters* **11**, (2019).

153 Kim, K. *et al.* Tunable moire bands and strong correlations in small-twist-angle bilayer graphene. *Proc Natl Acad Sci U S A* **114**, (2017), 3364-3369.

154 Haigh, S. J. *et al.* Cross-sectional imaging of individual layers and buried interfaces of graphene-based heterostructures and superlattices. *Nat Mater* **11**, (2012), 764-767.

155 Ferrari, A. C. & Basko, D. M. Raman spectroscopy as a versatile tool for studying the properties of graphene. *Nat Nanotechnol* **8**, (2013), 235-246.

156 Yan, J. A. *et al.* Phonon dispersions and vibrational properties of monolayer, bilayer, and trilayer graphene: Density-functional perturbation theory. *Physical Review B* **77**, (2008).

157 Tan, P. H. *et al.* The shear mode of multilayer graphene. *Nat Mater* **11**, (2012), 294-300.

158 Lui, C. H. *et al.* Observation of layer-breathing mode vibrations in few-layer graphene through combination Raman scattering. *Nano Lett* **12**, (2012), 5539-5544.

159 Malard, L. M. *et al.* Raman spectroscopy in graphene. *Physics Reports* **473**, (2009), 51-87.

160 Gupta, A. *et al.* Raman scattering from high-frequency phonons in supported n-graphene layer films. *Nano Lett* **6**, (2006), 2667-2673.

161 Ferrari, A. C. *et al.* Raman spectrum of graphene and graphene layers. *Phys Rev Lett* **97**, (2006), 187401.

162 Maultzsch, J. *et al.* Double-resonant Raman scattering in graphite: Interference effects, selection rules, and phonon dispersion. *Physical Review B* **70**, (2004).

163 Cançado, L. G. *et al.* Geometrical approach for the study ofG'band in the Raman spectrum of monolayer graphene, bilayer graphene, and bulk graphite. *Physical Review B* **77**, (2008).

164 Graf, D. *et al.* Spatially resolved Raman spectroscopy of single- and few-layer graphene. *Nano Lett* **7**, (2007), 238-242.

165 Beams, R. *et al.* Raman characterization of defects and dopants in graphene. *J Phys Condens Matter* **27**, (2015), 083002.

166 Wirtz, L. & Rubio, A. The phonon dispersion of graphite revisited. *Solid State Communications* **131**, (2004), 141-152.

167 Koshino, M. Interlayer screening effect in graphene multilayers withABAandABCstacking. *Physical Review B* **81**, (2010).

168 Cancado, L. G. *et al.* Influence of the atomic structure on the Raman spectra of graphite edges. *Phys Rev Lett* **93**, (2004), 247401.

169 Casiraghi, C. *et al.* Raman spectroscopy of graphene edges. *Nano Lett* **9**, (2009), 1433-1441.

170 Girit, C. O. *et al.* Graphene at the edge: stability and dynamics. *Science* **323**, (2009), 1705-1708.

171 Kobayashi, Y. *et al.* Observation of zigzag and armchair edges of graphite using scanning tunneling microscopy and spectroscopy. *Physical Review B* **71**, (2005).

172 *Introduction to Bruker's ScanAsyst and PeakForce Tapping AFM Technology*, <https://www.bruker.com/fileadmin/user_upload/8-PDF-Docs/SurfaceAnalysis/AFM/ApplicationNotes/Introduction_to_Brukers_ScanAsyst_and_PeakForce_Tapping_Atomic_Force_Microscopy_Technology_AFM_AN133.pdf>

173 Pittenger, B. *et al.* in *Nanomechanical Analysis of High Performance Materials Solid Mechanics and Its Applications* Ch. Chapter 2, 31-51 (2014).

174 Franken, L. E. *et al.* A Technical Introduction to Transmission Electron Microscopy for Soft ‐ Matter: Imaging, Possibilities, Choices, and Technical Developments. *Small* **16**, (2020).

175 *MyScope*, <https://myscope.training/legacy/tem/background/concepts/imagegeneration/diffraction/beam/>

176 Zhang, Y. *et al.* Direct observation of a widely tunable bandgap in bilayer graphene. *Nature* **459**, (2009), 820-823.

177 Wakafuji, Y. *et al.* 3D Manipulation of 2D Materials Using Microdome Polymer. *Nano Lett* **20**, (2020), 2486-2492.

178 Alexander, K. *et al.* Moiré-less Correlations in ABCA Graphene. *arXiv:1911.00007*.

179 Ahn, S. J. *et al.* Dirac electrons in a dodecagonal graphene quasicrystal. *Science* **361**, (2018), 782-786.

180 Moon, P. *et al.* Quasicrystalline electronic states in 30^{o} rotated twisted bilayer graphene. *Physical Review B* **99**, (2019), 165430.

181 Uri, A. *et al.* Mapping the twist-angle disorder and Landau levels in magic-angle graphene. *Nature* **581**, (2020), 47-52.

182 Sharpe, A. L. *et al.* Emergent ferromagnetism near three-quarters filling in twisted bilayer graphene. *Science* **365**, (2019), 605-608.

183 Yankowitz, M. *et al.* Tuning superconductivity in twisted bilayer graphene. *Science* **363**, (2019), 1059-1064.

184 Xu, S. G. *et al.* Giant oscillations in a triangular network of one-dimensional states in marginally twisted graphene. *Nat Commun* **10**, (2019), 4008.

185 Liu, Z. *et al.* Observation of microscale superlubricity in graphite. *Phys Rev Lett* **108**, (2012), 205503.

186 Ru, G. *et al.* Interlayer friction and superlubricity in bilayer graphene and MoS2/MoSe2 van der Waals heterostructures. *Tribology International* **151**, (2020).

187 Hinchet, R. *et al.* Recent Progress on Flexible Triboelectric Nanogenerators for Self Powered Electronics. *ChemSusChem* **8**, (2015), 2327-2344.